Exploring Radio WISE Selected Galaxies:

An investigation into the properties of the most extreme galaxies in the universe.

Emily R. Ferris

A thesis presented for the degree of Doctor of Philosophy

Astrophysics Division

School of Physics and Astronomy

University of Leicester

UK

Submitted December 2021

Abstract

This thesis presents analysis of ISAAC photometric and X-shooter spectroscopic observations of 30 selected high redshift galaxies at z = 0.880 - 2.853. Uncovered through cross matching sources from the WISE All-Sky catalogue with the NVSS radio source catalogue, Radio selected WISE Galaxies (RWGs) are extremely luminous with bolometric luminosities exceeding $10^{13}\,L_{\odot}$. With expected reddening of E(B-V) $>$ 0.9 magnitudes, this dusty and obscured population of new and unique radio intermediate galaxies are critical to our understanding of the properties and evolution of high redshift, ultra luminous IR galaxies. Theorised to be a new stage galaxy evolution, RWGs represent a super active BH growth and feedback phase, which all AGN may experience, therefore allowing us to observe these sources and their environments the most extreme state, increasing our knowledge of this peak phase in galaxy and quasar evolution.

I first measure the J and K_s band flux densities of 30 RWGs and use the `MAGPHYS` code to fit their SEDs, aiming to understand the size of the sources. I then present detections and spectral fitting of four broad multi-component emission lines (Hα, Hβ, [OIII]λ5007 and CIV) across 18 RWGs, with three independent methods used to determine black hole and host galaxy masses. Following on, I discuss the assumptions made when calculating my black hole masses, aiming to quantify the expected super Eddington ratios of RWGs and the effect that high visual extinctions have on these measured masses, in order to fully understand how extreme and unique these sources are. Finally, I make use of the full 300 - 2480 nm wavelength range of X-shooter's three spectroscopic arms and fit multi Gaussian models to a total of 100 individual line profiles across 15 line variants and 23 RWGs. I use these measured emission and absorption line properties to investigate the characteristics of the line profiles in order to compare RWGs to a standard quasar population. Throughout this investigation I also find that RWGs remain a distinct population from similarly detected HotDOGs and are $\sim$ 1 dex smaller in mass and therefore likely a shorter evolutionary phase. Finally, I aim to uncover the driving mechanisms behind these unique radio galaxies by placing them on BPT diagrams and find a new selection criteria that can be used to help determine future RWGs.

Declaration

I hereby declare that no part of this thesis has been previously submitted to this or any other University as part of the requirement for a higher degree. The work herein was conducted by the undersigned except for contributions as acknowledged in the text.

Emily R. Ferris

Acknowledgements

There are many people I need to thank for supporting me throughout the last four years and the creation of this thesis.

Firstly I feel I must thank Andrew and Mike for providing a range of feedback and the STFC for funding my studentship.

Next I would like to thank all my office mates in G17 (and the late G13) for keeping me sane, distracted and being great at decorating the office during Christmas time.

Thank you to Jordan for being the biggest help, writing translator and best office mate when I started. Without him I would have been extremely lost for the first couple of years and wouldn't have had half as many distractions.

I would next like to thank my mum and dad for always being supportive, there to listen and ready to read anything even if they don't understand a word. Thank you for always being my biggest encouragement, looking after me and letting me go home whenever I need to.

Finally there's one person left whom I must thank. Rob, for the last four years you have been at my side, always looking after me and always being my biggest supporter. Thank you for never letting me quit even when I begged you too and for always making me grateful that I started this journey, even though it has definitely not been easy. You are my constant and I cant wait to continue on to the next stages of our lives together.

I love you Snuggs.

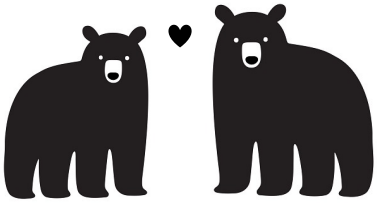

Contents

List of Figures

List of Tables

Chapter 1

Introduction

1.1 Overview and Motivation

Throughout this thesis I aimed to investigate the properties of extremely luminous and obscured radio intermediate galaxies. Radio WISE Galaxies (RWGs) are a new unique and population of galaxies selected through a cross match between NVSS radio sources (Becker et al., 1995) and the WISE All-sky survey catalogue (Cutri et al., 2013). Targeted as extremely luminous Infra Red (IR) galaxies, RWGs are radiatively efficient Active Galactic Nuclei (AGNs), with WISE band colours distinctly redder than the main WISE population. Due to their obscured nature RWGs are selected to be in their peak fuelling phase and as radio intermediate sources, they are likely compact with young radio jets that are still confined to their host galaxies (Lonsdale et al., 2015; Lonsdale et al., 2016).

The NASA Wide-field Infrared Survey Explorer (WISE) (Wright et al., 2010) discovered $\sim$ 1000 rare, extremely luminous Infra-Red (IR) galaxies, selected using mid-IR colours, including radio-selected WISE galaxies (Lonsdale et al., 2015; Silva et al., 2015; Jones et al., 2015). These radio AGN have been selected by combining mid-IR WISE and NVSS radio data meaning RWGs have compact radio emission still confined within their hosts, with young radio jets potentially exciting their ISM. With Spectral Energy Distributions dominated by thermal emission from hot/warm dust in the optical to mid-IR, RWGs are likely radiatively efficient, in their peak fuelling phase and perhaps undergoing powerful feedback processes (Hopkins et al., 2006). They are highly-obscured systems that remain distinct from other very luminous active galaxy populations and provide a new opportunity to uncover some of the most extreme AGN in the universe, in their most dramatic black hole (BH) growth and feedback phase. RWGs' internal structure and morphologies may provide insight into a brief, key, peak phase in galaxy and quasar evolution.

Follow up campaigns with the Atacama Large Millimeter/Submillimeter Array (ALMA)

(Lonsdale et al., 2015; Silva et al., 2015; Tsai et al., 2015; Díaz-Santos et al., 2016, 2018) have revealed a wide range of AGN spectral diagnostics, and complex morphologies in the ISM of RWGs. With well established radio galaxies apparently found in proto-clusters (Wylezalek et al., 2013; Hatch et al., 2014), and the environments of RWGs showing a 4-6 times overdensity of ultraluminous, dusty, high-redshift 850 -μm -selected galaxies on the sky (SMGs, e.g. Blain et al., 2002; Casey et al., 2014) as compared with typical blank fields (Jones et al., 2015; Silva et al., 2015), and a more modest overdensity of red Spitzer-IRAC-selected galaxies (Penney et al., 2019a). This is potentially consistent with RWGs, and these ultra-luminous, dusty AGNs in general, being found in an active, extended still-virializing filamentary proto-cluster environments over scales in excess of five arcmin (3 Mpc) consistent with theoretical models (e.g. Chiang et al., 2017).

RWGs, being potential sites of the most powerful and intense AGN fuelling and feedback, provide a unique opportunity to study the AGN phenomenon in extremes, and to determine whether RWGs are distinct from other AGN classifications. This is the case for other WISE discovered sources including Extremely Luminous IR Galaxies (ELIRGs) (Tsai et al., 2015, 2018). In addition, the extremely luminous nature of our sources ($L_{bol} \sim 10^{47}\,\mathrm{erg\,s^{-1}}$), suggests that these luminous RWGs will be at their peak of activity. In a substantial increase in depth compared to previous large telescope IR spectroscopy of RWGs (Kim et al., 2013), this thesis discusses high-resolution near-IR spectra of 27 RWGs, with near-IR imaging of 30 sources, taken in good seeing ($\sim$ 0.8"), in order to determine the BH, host and galaxy stellar masses. Specifically, the availability of virial mass estimates, based on scaling relations matched to reverberation-mapped samples (Kaspi et al., 2000), and the relation between the stellar velocity dispersion of the host galaxy bulge and BH mass ($M_{BH} - \sigma_*$, Magorrian et al., 1998a; Ferrarese & Merritt, 2000; Gebhardt et al., 2000), enables the calculation of the BH and host galaxy masses.

Defined as having masses $\geq 10^5\,M_\odot$, supermassive BH masses can now be determined in various ways using high-resolution spectroscopy. In this thesis spectroscopic data then allows me demonstrate different approaches to determine RWG BH masses, including using both a virial mass estimate based on the Balmer line properties, or an assumed Eddington ratio and the [OIII]λ5007 luminosity as a proxy for the bolometric luminosity. With the evolution of BHs and their hosts appearing closely linked, and AGN-driven outflows and feedback thought to be the crucial joining mechanism, these masses are vital properties to determine, and can test the validity of these scaling relations in the most dramatic cases. Determination of visual extinction and Eddington ratios also helps to determine whether these galaxies lie in excess of the local mass relations or accrete above the Eddington limit. Analysis of common emission lines and

placement on BPT diagrams also aims to confirm both the AGN and obscured nature of these galaxies.

This thesis aimed to demonstrate the importance of studying these highly luminous and dusty radio galaxies by presenting the results of photometric and spectroscopic observations of 30 RWGs. RWGs represent some of the universe's most extreme galaxies and as a newly selected population, it is yet to be determined where they lie in the context of other galaxies. Aiming to understand what place these galaxies have among others, analysis of these galaxy properties will help to determine which are common between all sources in my sample, any similarities to HotDOGs and therefore determine which properties may be used as indicators in an aim to classify future RWGs.

1.2 Thesis Structure

This thesis is structured as described below. Chapter two provides background information on AGN, including the differences between galaxy types, galaxy formation and evolution, along with detailing the conclusions made by previous works (Kim et al., 2013; Lonsdale et al., 2015; Jones et al., 2015) during their investigations into RWGs. I also detail the properties of other extremely luminous and comparable WISE selected populations, Hot Dust Obscured Galaxies (HotDOGs, Wu et al., 2012; Stern et al., 2014; Assef et al., 2015) and Lyα emitters (Bridge et al., 2013). Chapter three details and describes the different instruments used throughout my analysis including the data reduction methods applied to the raw data obtained through observations by these instruments.

Chapters four, five and six present my research and analysis into RWGs. I firstly detail the photometric and spectroscopic Very Large Telescope (VLT) observations of RWGs, and use a multi Gaussian model to fit my detected NIR emission lines, using the measured fluxes and widths to derive measurements of BH and host galaxy masses. My second research chapter investigates the assumptions made when calculating my BH mass measurements, determining the Eddington ratio of my RWGs, quantifying the amount of dust obscuration and determining the effects that these properties have on my mass measurements. My final research chapter aims to make use of the remaining spectroscopic data from X-shooter's UVB and VIS arms, measuring the emission and absorption properties of 100 total line detections. I use these spectral properties to classify RWGs as AGNs through their placement on BPT (Baldwin et al., 1981) diagrams and investigate measurable asymmetry and velocity offsets.

I then close this thesis with my final conclusions, future prospects and thoughts on RWGs and their place among other galaxy populations.

Please note that throughout this thesis the following cosmological parameters are used: $H_0 = 71\,\mathrm{kms^{-1}\,Mpc^{-1}}$, $\Omega_\Lambda = 0.73$ and $\Omega_M = 0.27$.

Chapter 2

A Review of Extreme Galaxies

2.1 Introduction

Galaxies are gravitationally bound systems of stars, gas, dust and dark matter, with an estimated 2×10^{11} galaxies (Lauer et al., 2021) and 1×10^{24} stars (Marov, 2015) making up the Universe. With different visual morphologies, sizes and formation mechanisms, individual galaxies are grouped or clustered together forming a bigger part of the universe's substructure. This chapter will first discuss different types of galaxy, with a focus on AGNs and galaxy evolution, before moving on to a lengthier discussion of new galaxy populations discovered using WISE band colour selection criteria. There I discuss three different populations of galaxies all selected using WISE band colours, and present the most interesting and recent discoveries made from observations of these new galaxy populations.

As RWGs are theorised to be a new stage of galaxy evolution, understanding their extreme properties and how long lived this phase is of utmost importance in the understanding of where in evolution they sit. Understanding their differences from the similarly selected HotDOGs will also confirm whether they are the same population and therefore part of the same evolutionary stage, or are they two different galaxy types. This chapter discusses different types of galaxies and the current understanding of their evolutionary path. This will hep in the understanding of how unique RWGs are, how they differ from other galaxy populations and where in evolution they sit, during a merging process or otherwise.

2.2 Different Types of Galaxies

Galaxies have been classified by their visual morphology since the 1920s when Edwin Hubble observed a diverse galaxy population (Hubble, 1926; Hubble, 1929), ultimately leading to the development of the Hubble sequence (Hubble, 1936). This "tuning fork" like diagram, shown in

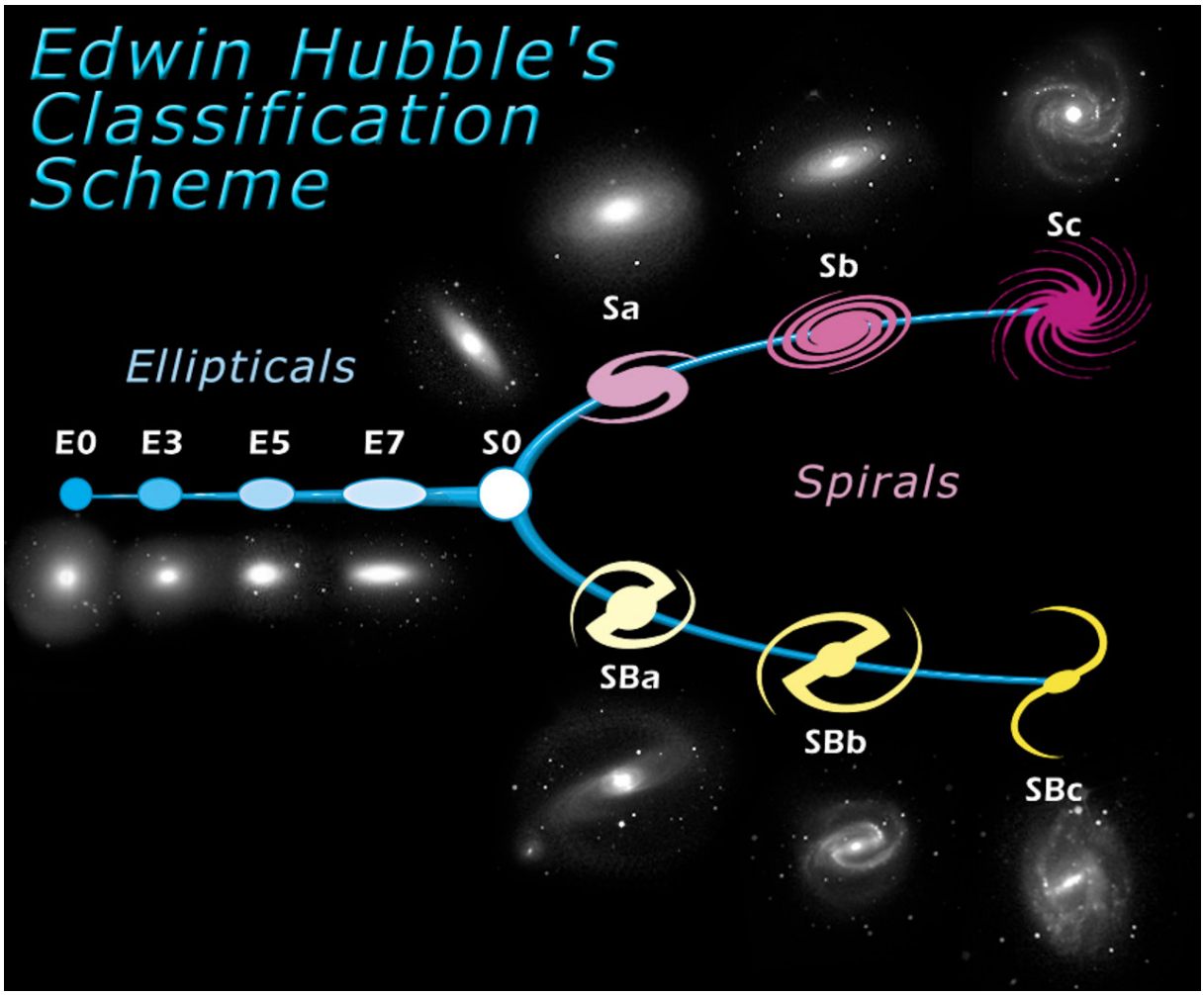

Figure 2.1: The Hubble sequence used to classify galaxies based in their visual morphology's, differentiating mainly between spiral and elliptical shaped galaxies. Credit:ESA/Hubble

Figure 2.1, is a simplistic classification system that can separate the majority of galaxies into one of three classes; elliptical galaxies, spiral galaxies and lenticular galaxies.

Elliptical galaxies have smooth and relatively featureless light distributions of stars, appearing as ellipses in the sky. They are categorised by their ellipticity, with the naming convention of En, with n $\sim 10 \times e$ and $e = 1 - \frac{b}{a}$, where a and b are the semi-major and semi-minor axis of an ellipse. Therefore an E0 galaxy is very round, whilst an E7 galaxy has an extremely elongated shape.

Spiral galaxies, on the other hand, consist of a flat rotating disc of stars, gas and dust, with arms spiralling out from the centre and concentrated around a central bulge. They can be separated into two classifications of barred and non-barred spiral galaxies, in addition to a,b and c type spirals, with a type spirals having closely bound arms in comparison to b and c types. Spiral galaxies make up $\sim$ 60% of the universe's galaxies (Loveday, 1996) with approximately half of these spiral galaxies being barred.

Lenticular, or S0, galaxies consist of a bright central bulge, with no visible spiral arms nor extended structure, and hence lie at the merging point of elliptical and spiral galaxies on the Hubble sequence. It was originally theorised that the Hubble sequence was a evolutionary track with elliptical galaxies evolving into spirals and lenticular galaxies being the midpoint of this transition, though this thought process has been since altered.

There are also additional galaxy types that do not fit on the Hubble sequence. Irregular galaxies have neither a disc nor elliptical structure but likely asymmetric profiles and therefore sit apart from galaxies on the Hubble sequence. These differences in galaxy morphology are likely driven by the motions of dust and gas within the galaxies, in addition to internal processes and interactions with the surrounding environments (Barnes & Hernquist, 1996). Understanding these processes is therefore an important step in the understanding the differences in morphology and properties between different galaxy types.

2.3 History of Active Galactic Nuclei

Active Galactic Nuclei (AGN) are some of the most luminous sources in the universe (Assef et al., 2015; Tsai et al., 2015) and have been detected to emit strong levels of non thermal radiation across the electromagnetic spectrum, from X-rays to radio. The earliest observations of AGN signatures were performed by Edward Fath (1909) who detected the first spectroscopic emission lines through observations of NG1068 and M81. Rather than the continuous spectra of stellar absorption lines they expected to observe, they instead detected both bright emission and absorption lines across a range of various frequencies. Further observations taken in the following 30 years (Slipher, 1917; Humason, 1932; Mayall, 1934, 1939) also detected the presence of these emission lines in their observations, publishing the emission line spectra of various extra galactic nebulae.

In 1943, Carl Seyfert (1943) published his observations of broadened nuclear emission lines found in six spiral nebulae, observing a correlation between source and line brightness, with the strongest emission lines present in the two brightest galaxies observed. Similar galaxies to those originally observed by Carl Seyfert are now known as Seyfert galaxies. Consisting of high luminosity cores and emission lines, Seyfert galaxies are one of the main populations of active galaxies and account for $\sim 10\%$ galaxies in the entire universe (Maiolino & Rieke, 1995). Further investigation into these highly luminous sources throughout the following decades led to many breakthrough discoveries of new techniques and different population types of AGN. Examples of this include the first use of detected nuclear emission lines to determine the redshift of a galaxy (Schmidt, 1963a) and the suggestion that accretion of gas on to a Super Massive Black Hole

(SMBH) (Salpeter, 1964; Shields, 1999) could be the driving mechanism behind quasars.

2.3.1 Powering an AGN

In 1969 Donald Lynden-Bell suggested that a dead quasar lay in the centre of some nearby galaxies taking the form of a SMBH with a mass $\sim 10^7 - 10^9\,\mathrm{M}_\odot$ and argued that accretion on to this SMBH was the source of the powerful non stellar emission found in these galaxies (Lynden-Bell, 1969). Since this first suggestion, fifty years ago it has now been determined that accretion of mass on to the SMBH is the main mechanism powering AGN. AGN are extremely luminous sources reaching $\mathrm{L_{bol}} \approx 3.5 \times 10^{14}\,\mathrm{L}_\odot$ in the case of W2246 the most luminous galaxy in the universe (Assef et al., 2015; Tsai et al., 2015), and mass accretion on to the SMBH is the most efficient way to convert energy into radiation, especially as a massive BH has a high Eddington luminosity.

The Eddington luminosity, or Eddington limit, is defined as the maximum luminosity a radiating body can achieve whilst remaining in hydrostatic equilibrium. Balancing the radiative and gravitational forces, Equation 2.1 gives the Eddington luminosity for a body of a given mass M, where G is the gravitational constant ($6.67 \times 10^{-1}\,\mathrm{m^3\,kg^{-1}\,s^{-2}}$), m_p is the mass of a proton ($1.67 \times 10^{-27}\,\mathrm{kg}$), c is the speed of light ($\sim 3 \times 10^8\,\mathrm{km\,s^{-1}}$) and σ_T is the Thompson scattering cross section.

$$L_{Edd} = \frac{4\pi G M m_p c}{\sigma_T} \tag{2.1}$$

For Hydrogen, Equation 2.1 reduces to $\mathrm{L_{Edd}} \approx 1.26 \times 10^{38} \left(\frac{\mathrm{M}}{\mathrm{M}_\odot}\right) \mathrm{erg\,s^{-1}} \approx 3.2 \times 10^4 \left(\frac{\mathrm{M}}{\mathrm{M}_\odot}\right) \mathrm{L}_\odot$. To achieve an Eddington luminosity of $3.5 \times 10^{13}\,\mathrm{L}_\odot$, equal to that of W2246 (Assef et al., 2015; Tsai et al., 2015), a SMBH mass of $1.1 \times 10^9\,\mathrm{M}_\odot$ would be required. Super Eddington luminosities, achieved by galaxies accreting at rates greater than allowed by the Eddington limit, would require an even smaller BH mass to achieve this extremely bright luminosity.

2.4 Galaxy Formation and Evolution

The ΛCDM cosmological model is the simplest model in agreement with observed phenomena that describes the expansion of the universe after the Big Bang, including the formation of galaxies. Based on three main parameters; a cosmological constant (Λ), Cold Dark Matter (CDM) and normal matter, it aims to explain the underlying structure in the distribution of galaxies, the observed abundances of H, He and Li, structure of the cosmic microwave background

and the accelerating expansion of the universe. Any accepted model also has to be able to explain any observations and match predictions about how galaxies form and evolve.

Edwin Hubble's galaxy classification system (Hubble, 1926; Hubble, 1929; Hubble, 1936) separated elliptical, spiral and lenticular galaxies with any formation model needing to explain the differences between these galaxy types. Blue, star forming spiral galaxies are thin, dense and fast rotating whilst red elliptical galaxies tend to have randomly orientated orbits. Whilst it was initially believed that this tuning fork sequence (see Figure 2.1) was an evolutionary track, it is now accepted that this is unlikely to be the case with only galaxy complexity increasing as you move left to right along the tracks. In fact it has been suggested that disc galaxies with spiral arms are the first stage of galaxy evolution.

2.4.1 Formation of Disc Galaxies

In 1962, Eggen et al. proposed that disc galaxies were formed through a gas cloud collapse with clumps of dark matter gravitationally interacting and gaining angular momentum. They theorised that, as this matter cools and contracts, the central region increases rotation speed, conserving angular momentum, until it forms into a tight disc. Once cooled, they argue that the gas no longer remains gravitationally bound and breaks apart forming smaller gas clouds and stars, with dark matter distributed outside the disc in a halo. Observations however proved this theory too simplistic, showing stars located outside of the disc with Searle & Zinn (1978) suggesting that galaxies form though smaller progenitors coalescing. An opposite theory was later suggested, with smaller gas clouds and matter clumps gravitationally drawn together to form galaxy clusters, instead of a giant gas cloud fracturing apart (White & Rees, 1978). This model still produces a disc like distribution of matter surrounded by a dark matter halo. Whilst the ΛCDM model predicts some observed properties of the universe remarkably well it under estimates the observed numbers of these thin disc galaxies (Steinmetz & Navarro, 2002).

2.4.2 Galaxy Evolution

The evolution of galaxies happens on timescales of billions of years, going through stages of star formation, AGN activity and interactions with galaxies in nearby environments. Whilst galaxy mergers are theorised to evolve spiral galaxies into ellipticals, galaxies can also passively evolve turning from blue star forming to red galaxies through galaxy quenching.

Galaxy Mergers

The evolution of galaxies through merger events is the most violent galaxy interaction possible, and is theorised to be responsible for the evolution of elliptical galaxies (Barnes, 1989), spiral galaxies and local ultra luminous IR galaxies (Toomre & Toomre, 1972). Any galaxy is expected to be formed via the merging of successive dark matter halos, with N-body simulations (Lacey & Cole, 1993; Kauffmann et al., 1993; Roukema et al., 1993, 1997) used to create galaxy merger history "trees" which combined estimated galaxy population evolution and star formation rates to yield expected luminosity functions at various epochs. Mutual tidal capture of two separate disc galaxies were first simulated using N-bodies by Holmberg (1941) who later rejected the idea that repeated tidal interactions could cause galaxies to merge. Later simulations by Zwicky (1959), however, were the first to propose that multiple encounters of two systems could lead to disruptions of both systems or a mutual capture/merger (Barnes & Hernquist, 1992).

The effects of galaxy mergers depend on various parameters including the number of galaxies, size of galaxies, galaxy composition, relative position and angle etc. There are two main types of galaxy merger: major and minor. Major mergers are defined as collisions between two or more galaxies (Barnes & Hernquist, 1992) of similar luminosities, that collide in a way such that the dust and gas is driven away, likely leaving behind an elliptical galaxy as the end stage of the merger process. Throughout this process a variety of feedback mechanisms draw out the dust and gas which is expected to lead to AGN activity and is likely the main cause of quasars as major mergers are thought to be the main supply of gas and dust that galaxies accrete onto their SMBH (Eggen et al., 1962).

A bottom up theory of major galaxy mergers suggests that the first galaxies would have formed from fragments of the matter density field collapsing from gravitational attraction, before becoming gravitationally bound together and forming larger cosmic structures (Rees, 1978). The resulting merged galaxy will have significant property differences including enhanced activity of the central SMBH and a changing star formation rate (Toomre & Toomre, 1972). Understanding these major galaxy mergers can be of vital importance in understanding the formation and evolution of highly luminous $z \sim 2$ galaxies (Tacconi et al., 2008), with major mergers of galaxies of similar luminosities being the most efficient at triggering new star formation (Lambas et al., 2012; Alonso et al., 2012).

Minor mergers are the most common type of merger and occur when there is a significant size difference between the merging galaxies. Lambas et al. (2012) use the luminosity threshold of $L2/L1 \leq 0.33$ to distinguish minor mergers, using the luminosity ratios as a proxy for the differences in galaxy mass. Whilst minor mergers are more frequent, Lambas et al. (2012) classify

only $\sim$ 45% of their 1095 SDSS galaxy sample (z $<$ 0.3) (York et al., 2000) as minor mergers measuring a greater number of major interactions. They conclude that galaxy mergers are the key mechanism in regulating galaxy properties, with the luminosity ratios of the prevent merging galaxies, an important factor in determining the resultant star formation and galaxy colours (Lambas et al., 2012).

Galaxy mergers may also be classified due to the amount of gas present in the merging galaxies, although this classification system is less common. A wet merger occurs between two or more gas rich blue galaxies and dominate merging events between z = 0.2 - 1.2 as shown by Lin et al. (2008). They typically produce resultant galaxies with large amounts of star formation, though are also thought to be responsible for intermediate mass red galaxies. High mass red galaxies are thought to evolve through dry mergers (Lin et al., 2008), a merger between gas poor red galaxies, which has little effect on star formation and is responsible for only 8% of galaxy mergers at $z \sim 1.1$. In the middle sits a damp merger, a merger between gas rich blue and gas poor red galaxies, possessing enough resultant gas to fuel significant levels of star formation, though insufficient gas mass for the formation of globular clusters (Forbes et al., 2007).

Galaxy Quenching

A successful theory of galaxy evolution needs to account for the shut off of star formation along with the excess of galaxies switching from the red to the blue sequence, in addition to galaxy mergers (Faber et al., 2007). Galaxy quenching occurs when there is no more cold gas for stars to form (Blanton, 2006; Gabor et al., 2010), in a timescale quicker than it would take for a galaxy to use up its supply. There are two hypothesised mechanisms responsible for this quenching; preventative feedback mechanisms that stop cold gas entering a galaxy and forming stars, or ejective feedback mechanisms which remove cold gas from galaxies before star formation can occur.

The strangulation mechanism (Peng et al., 2015) is an example of a preventative mechanism that causes quenching in lower mass galaxies (local galaxies with $>10^{11}$ $M_{\odot}$) through interactions with nearby galaxies that prevent gas accretion. Ejective feedback mechanisms may however be responsible for the quenching of more massive galaxies in simulations (Di Matteo et al., 2005; Kereš et al., 2009) suggesting that released energy from high energy jets, formed via gas accreting onto the SMBH, are able to expel enough cold gas to enable galaxy quenching.

2.5 Different Types of AGN

This next section will discuss the different types of AGN and how their defining characteristics are used for classification purposes. With the different AGN types observed across the electromagnetic spectrum, models have been detailed to describe their observational differences.

2.5.1 Type 1 vs Type 2 AGN

AGNs can be classified as type one or type two AGN based on their observed emission line properties. Type one or broad line AGN (Villarroel & Korn, 2014; Zou et al., 2019) have at least one broad emission line measuring a Full Width Half Maximum (FWHM) $>2000\,\mathrm{km\,s^{-1}}$ and are observed face on with the central nucleus visible. They produce both broad and narrow emission lines with a bright continuum. Type two AGN, or narrow line AGN, only posses narrow emission lines due to their respective orientation when observed, where the broad line emission is blocked by the obscuring torus (Netzer, 2013). They emit faint narrow line emission, from the narrow line emitting clouds, and have weak continuum. The unification model of AGN from Urry & Padovani (1995) suggests that type one and type two AGN are exactly the same, where the only differences between the two AGN types is the orientation of the obscuring torus with respect to the observer. Figure 2.2 shows this unified model of AGN from Urry & Padovani (1995) where the observed viewing angles between type one and two AGN are opposites with respect to the positioning of the obscuring torus. Whilst this model suggests that all AGN consist of the same inner most structure of a central nucleus surrounded by an accretion disc, this unified model can not explain all the differences between AGN types as discussed further on.

2.5.2 Radio Loud AGN

Whilst AGNs can be classified as type one or type two AGN, they can also be more generally classified as radio loud or radio quiet. Radio loud AGN poses radio emission from both the radio jet and radio lobes, which dominates the AGN luminosity at radio, and in some cases all, wavelengths. In contrast, radio quiet AGN can neglect any jet based radio emission at all observed wavelengths. The population of radio loud AGN can be split into three different categories; radio galaxies, quasars and blazars.

Radio Galaxies

Radio galaxies, as indicated by their name, show both nuclear and extended radio emission and are very luminous at radio wavelengths and almost exclusively found in elliptical galaxies. They can emit radio luminosities $\geq 1 \times 10^{47}\,\mathrm{erg\,s^{-1}}$ at frequencies of 10 MHz to 100 GHz (Fanaroff

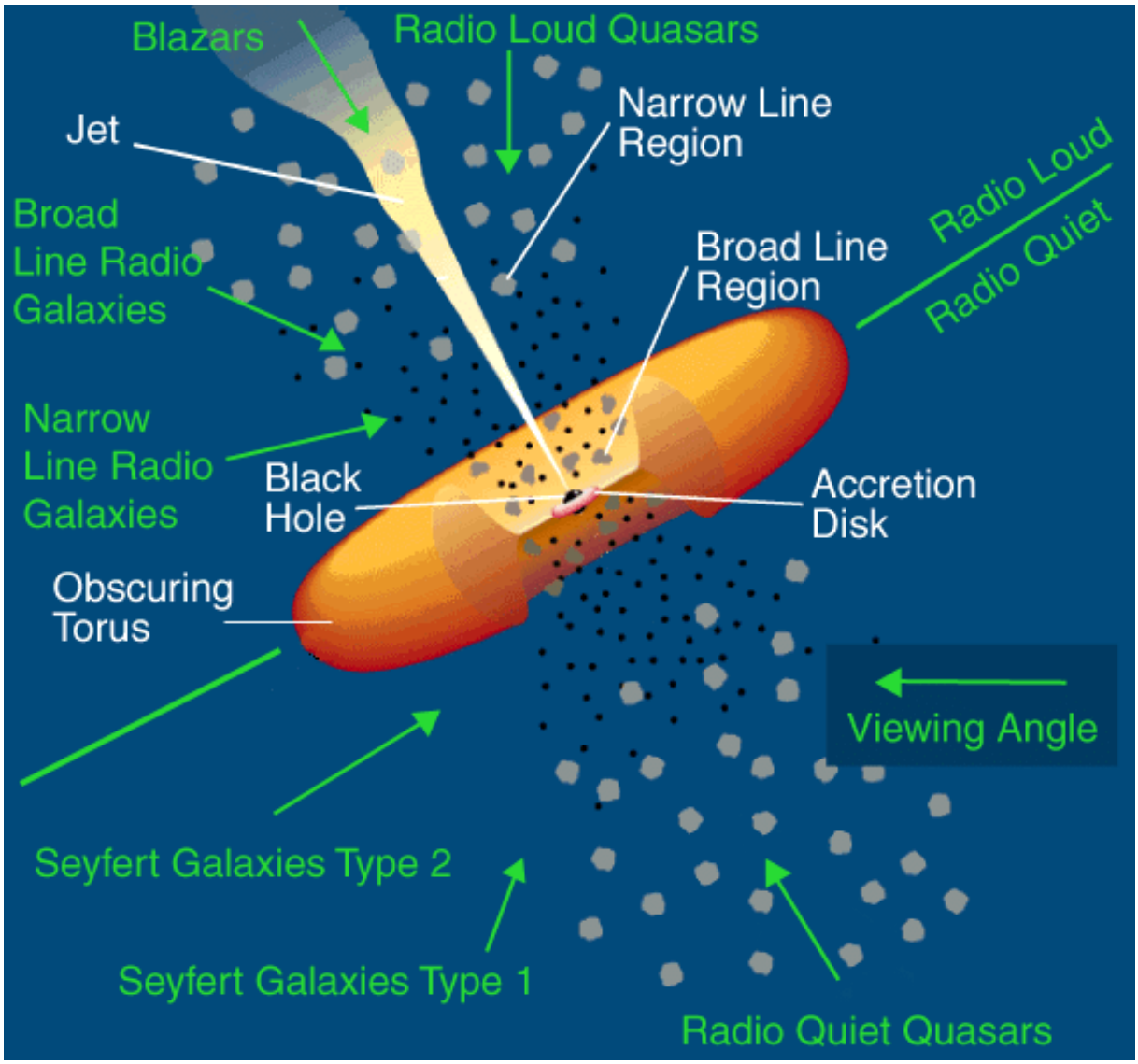

Figure 2.2: The unified model of the AGN where the viewing angle obtained by the observer changes the observed characteristics of the AGN. The different green arrows represent different viewing angles showing the types of AGN observed along that line of sight. Credit: Coloured version of Figure one from Urry & Padovani (1995).

& Riley, 1974) and show detections of both broad and narrow emission lines. Fanaroff & Riley (1974) subdivided their observed radio galaxies into two classes FRI and FRII; where FRI galaxies are brightest at their centre compared to FRII galaxies which are brightest towards the galaxy edge. They additionally also noticed a luminosity divide with FRII galaxies being the brightest of the two classes.

Radio emission is powered by synchrotron radiation in radio jets where charged particles, including protons and positrons, are accelerated in magnetic fields causing emitted radiation. Interactions between the Inter-Galactic Medium (IGM) and twin radio jets are responsible for observed radio emission, with the observed luminosities of the individual jets dependent on the orientation of the jet with respect to the observer. This effect is called relativistic beaming where the apparent luminosity of an object moving close to the speed of light is modified. In the case of twin radio jets, the jet facing the observer appears brighter than the other, as demonstrated by the AGN jets of M87 (Sparks et al., 1992) where only one of the radio jets is visible.

Quasars

Quasars are extremely luminous AGN that consist of a SMBH surrounded by an accretion disc. They are intense point like sources of radio emission with optical counterparts. Quasars were first observed with the start of radio astronomy in the 1950s, possessing unexpected features in comparison to the currently known population of nebula. These sources were extremely luminous at a range of frequencies across the radio band, and possessed unexpected emission lines. They were however expected to be no bigger than the solar system due to their rapidly varying optical and X-ray luminosities, on timescales of hours to months. Because of this rapid variability they were coined as quasi stellar (meaning star like) radio sources, or Quasi Stellar Objects (QSOs). Quasars were first observed in the late 1950s as part of radio surveys (Matthews & Sandage, 1963; Schmidt, 1963b) with radio sources 3C48 and 3C273 confirmed as the first observed quasars (Matthews & Sandage, 1963; Schmidt, 1963b). The term quasars was coined one year later as a short hand by Chiu (1964).

Hubble Space Telescope (HST) imaging of quasars show that they occur in the centre of galaxies (Bahcall et al., 1997) and are compact sources. They posses broad Ultra Violet (UV) emission lines with [OIII]λ5007 luminosities that are systematically higher than observed radio galaxies (Urry & Padovani, 1995). With $>$ 750,000 known quasars (Lyke et al., 2020) in the SDSS DR16 quasar catalogue, quasars with larger redshifts ($z > 3$) can be used as indicators of early galaxy formation, aiding with the discovery of properties of the early universe. For example the most distant radio quasar has a redshift of $z = 6.823$ (Bañados et al., 2021). There

are different sub classes of quasars, including both radio loud and radio quiet quasars, with only $\sim 10\%$ of quasars possessing powerful radio jets.

Blazars

Blazars were first discovered along with the early quasars, but unlike quasars they posses no narrow emission lines and only weak broad line features (Rees, 1978). They are also extremely luminous AGN, with the the central AGN jet axis observed close to or exactly at the observers line of sight. Blazars are affected by relativistic beaming enhancing their observed emission (Urry & Padovani, 1995), and are luminous across the electromagnetic spectrum. In addition they are sources of high energy photons and neutrinos, the latter of which has been used to trace the origin of a blazar (IceCube Collaboration, 2018). Blazars can be sub divided into two categories; BL Lacertaes (BL Lacs) and Optically Violently Variable (OVV) quasars (Urry & Padovani, 1995). Both classes are characterised by rapid variability, high and variable polarisation and high brightness temperatures. Under the AGN unification model, they are thought to be low and high luminosity radio galaxies respectively (Urry & Padovani, 1995; Willott et al., 2000), whilst the term blazar was first used in 1978 to describe a combination of these two classes.

2.5.3 Radio Quiet AGN

Radio quiet AGN lack any jet based radio emission at all observed wavelengths making them simpler than their radio loud counterparts. Whilst radio quiet quasars male up $\sim 90\%$ of the quasar population, below I will only briefly discuss two populations of radio quiet AGN; Seyfert galaxies and Low-Ionisation Nuclear Emission-line Regions (LINERs).

Seyferts

Seyfert galaxies were discovered by, and named after, Carl Seyfert in 1943 (Seyfert, 1943). Consisting of $\sim 10\%$ of all galaxies in the entire universe (Maiolino & Rieke, 1995), along with quasars Seyfert galaxies are one of the two most populous populations of AGN, though in general they are less luminous than quasars. When observed at visible wavelengths Seyfert galaxies appear as normal spiral galaxies, though when observed in the IR they have extremely luminous cores and show bright Doppler broadened emission lines of H and O (Osterbrock, 1989).

Seyfert galaxies can be sub-divided into two classes; Type I and Type II. Type I Seyfert galaxies possess both broad (> 1000 km s^{-1}) and narrow (≤ 1000 km s^{-1}) emission lines of ionised gas, whereas type II Seyfert galaxies only show narrow line emission. In reality, the spectra of Seyfert galaxies is not this simple with additions of type 1.5, 1.8 and 1.9 Seyfert

galaxies existing which show decreasing strengths of some (eg. Hα and Hβ) broad emission lines (Osterbrock, 1989). These findings have led to the suggestion that all type II Seyfert galaxies are truly type I, but in cases where the broad line emission is difficult to detect due to the observers viewing angle and the dusty torus obscuring these emission lines (Singh et al., 2011). In the case of the Seyfert galaxy NGC 1068, a polarised spectrum showed broad H emission lines that were previously undetected with normal spectroscopy, providing evidence for the theory that the broad emission lines of types II Seyfert galaxies are simply obscured (Bailey et al., 1988). This implied that previously undetected line types, were simply obscured and type I and type II Seyfert galaxies were the same population. This then provided evidence for the unification of AGN, which states that all AGN are the same and their observed differences and due to the viewing angle of the observer.

LINERS

LINERs are similar to Seyfert galaxies possessing both broad and narrow emission lines with spectra that include the weakly ionised atoms O, O^+, N^+ and S^+. They can be almost indistinguishable from low luminosity Seyfert galaxies though possess a less dense broad line emitting region (Ho, 1996). Initially discovered in 1980 (Heckman, 1980) LINER galaxies are extremely common and make up $\sim \frac{1}{3}$ of all nearby galaxies within 20 - 40 Mpc (Ho et al., 1997).

2.5.4 Unification of AGN

The unification model of AGN suggests that all AGN classes are the same population with their differences explained by the viewing angle of the observer (Antonucci, 1993; Urry & Padovani, 1995). This paradigm is demonstrated by Figure 2.2 which shows how the viewing angle effects the object class seen. Seyfert II galaxies may actually be type I with their broad emission lines obscured by a dusty torus. Similarly LINERS may appear as Seyfert galaxies though with specific spectral features. Radio galaxies show evidence of obscuration in comparison to quasars, and the similarly bright blazars, which are viewed face on to the radio jet. Whilst this unification model suggests that all AGN are the same, it does not explain all difference between the AGN sub-classes including the different environments these sources reside in (Donoso et al., 2014). For example a sample of WISE selected AGN was found to sit in overdense environments of SMGs (Jones et al., 2014; Penney et al., 2019b) in comparison to similarly selected sources.

2.6 WISE Selected Galaxy Populations

Beginning on 14th January 2010, the WISE mission completed all sky coverage in July 2014 observing the whole sky in four IR bands. With the main science objective of finding the most luminous, dusty galaxies achieved interesting outlier populations were quickly discovered through stringent constraints on target selection based on WISE colour selection criteria. With quick follow-up observations, discoveries were made for various properties of these new galaxy populations including HotDOGs (Eisenhardt et al., 2012) and RWGs Lonsdale et al. (2015). The following sections will briefly discuss three new populations of WISE galaxies, and their most important discoveries.

2.6.1 Radio WISE Galaxies

Radio WISE Galaxies (RWG's), previously referred to as radio powerful WISE galaxies, are a population of radio intermediate WISE galaxies defined by the selection criteria of Lonsdale et al. (2015). They are highly luminous and obscured galaxies, defined apart from other populations of WISE galaxies (to be later discussed) by their possession of radio jets. The original selection criteria for RWGs will be briefly discussed here along with their most exciting discoveries. As analyses of RWG observations are the focus of this thesis; part of a continuation of ongoing studies into this rare and extreme galaxy population, they will be the first population to be discussed.

The population of RWGs was selected from the WISE All-sky survey by Lonsdale et al. (2015) with the aim of addressing the impact of young, moderately powerful radio jets from luminous obscured radio AGNs on the disruption of the Inter Stellar Medium (ISM) and star formation in their hosts. Focusing on redshifts of $z \sim 1-3$, their selection criteria were carefully chosen with each additional criterion chosen to target a favourable property. The high Mid-IR (MIR) luminosity of RWGs implies radiatively efficient AGNs, compact radio sources favour young radio sources still confined to their hosts whilst selecting very red optical to MIR AGNs targets obscured systems likely in their peak fuelling stages.

The target selection criteria of RWGs will be reiterated later when discussing the observations that are the focus of this thesis, however they will also be briefly discussed here as to provide context into the properties of RWGs and the main science results published so far. A cross match of the National Radio Astronomy Observatory (NRAO) Very Large Array (VLA) Sky Survey (NVSS) (Becker et al., 1995) to point sources in the WISE All-sky catalogue selected all radio sources in the WISE catalogue north of $\delta = -40°$, with extra positional information provided by the Faint Images of the Radio Sky at Twenty centimetres (FIRST) catalogue allowing exclusion

of sources $\pm 10°$ from the galactic plane. The *ext* WISE All-sky catalogue flag was used to reject extended WISE sources from the subset of galaxies defined by this initial selection cut.

Unlike for previously selected WISE galaxy populations (see the sections below) a MIR colour selection criteria was not applied in order to select the reddest sources in the WISE population. Instead, and in order to remove any bias due to the fact that the observed MIR spectral shapes are complex and strongly redshift dependent, a colour selection criteria was used to gather all sources that lie significantly redward of the main WISE population. The condition $(W2-W3)+1.25(W1-W2) > 7$ was used, with W1, W2 and W3 referring to the 3.4, 4.6 and 12 μm wavebands observed by WISE. The unique selection criteria for RWGs, $\log(f_{22\mu m}/f_{20cm}) < 0$ is used to reject radio quiet sources, differing from the populations of HotDOGs (see section 2.6.2) and Lyα Blobs (LABs - see section 2.6.3). Figure 2.3 shows these criteria in comparison to the WISE population and the AGN selection criteria used by Laor & Stern (2012). Finally visual inspections of Sloan Digital Sky Survey (SDSS) images were used to inspect the candidates rejecting low redshift and outlier sources along with galaxies whose size put them at $z < 0.5$.

Application of these criteria by Lonsdale et al. (2015) yielded 708 sources, only 1.3% of the initial cross matched catalogues. A Signal to Noise Ratio (SNR) SNR > 7 consideration left 703 sources in the W3 waveband and 269 sources in W4. This was reduced to Lonsdale et al. (2015)'s final subset of 156 RWGs by applying a flux density threshold of 7 mJy. With a Right Ascension (RA) of 03:00:00 $<$ RA $<$ 08:30:00 and 13:00:00 $<$ RA $<$ 21:00:00 Lonsdale et al. (2015) presented Atacama Large Millimeter/submillimeter Array (ALMA) observations of 49 RWGs, 30 of which will be discussed in detail during my own work.

Aiming to fit SEDs to their ALMA fluxes (and the WISE W1, 2, 3, and 4 band fluxes) they used SED templates previously designed to fit the Ultra Luminous IR Galaxy (ULIRG) Arp220, the dusty broad line QSO Mk231 and the starburst galaxy M82 (Polletta et al., 2006, 2007). The majority of their SED fits show the RWGs have a unique SED shape of flux dominated in the mid-IR by warm dust but then a sharp decline into the sub-mm. The SED of multiple sources suggest a high excitation obscured AGN (Lonsdale et al., 2015). They further conclude that the rest frame MIR - Sub-mm SEDs are dominated by AGN emission in the mid-IR.

Most comparable to the research presented in this thesis are the BH mass estimates made using AGN luminosity from their SED's as unlike now, there was no spectroscopic indicator available at the time. Assuming an Eddington ratio of $\lambda_{Edd} = 0.25$ (as typical of z $\sim$ 2 quasars - Kormendy & Ho (2013)) gives $\mathrm{L_{Edd}} = 3.3 \times 10^4\,\mathrm{M_{BH}}$ and allows the BH masses to be derived from the $\mathrm{L_{AGN}}$ from their fitted SEDs. They measure $\log(\mathrm{M_{BH}}) = 8.20 - 10.23\,\mathrm{M_\odot}$ across the 49 RWGs from $\mathrm{L_{AGN}} = 11.58 - 13.61\,\mathrm{L_\odot}$. However, it has been suggested that RWGs, similar

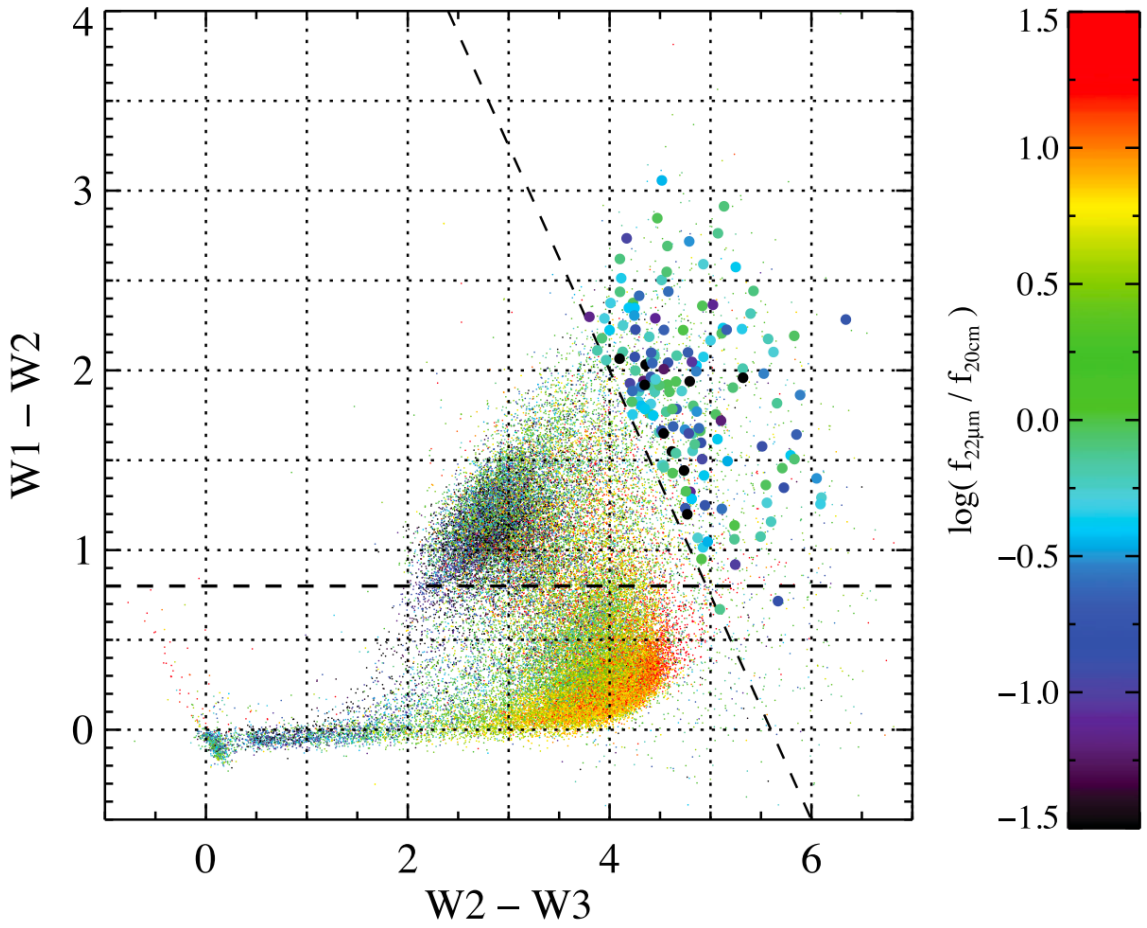

Figure 2.3: WISE 3.4–4.6–12 μm (W1−W2−W3) colour–colour plot (using Vega magnitudes) showing the full WISE-NVSS sample of 54,457 sources, colour- coded by radio loudness shown by the colour bar on the right. The sequence at the bottom is the sequence of normal spirals and starbursts. The flux-limited ultra-red sample of 156 sources is highlighted above the dashed line with larger symbols. The horizontal dashed line shows the AGN colour selection criterion used by Laor & Stern (2012): $(W1 - W2) > 0.8$, for comparison to the ultra-red selection criterion. Credit: Caption and figure from Figure one from Lonsdale et al. (2015).

to other WISE populations, may accrete at super Eddington rates (Kim et al., 2013; Assef et al., 2015) leaving these as overestimates of the BH mass. Contrastingly, these may also be underestimates of the true BH masses as they exclude emission not traced by dust in the X-ray and optical as well as extreme mid-IR extinction being a possibility.

Comparatively Kim et al. (2013) estimate larger BH masses for three out of six comparable sources due to either by underestimations by Lonsdale et al. (2015) or shocks and outflows boosting the line strengths used to estimate the other BH masses. Kim et al. (2013) obtained NIR spectra on 24 sources taken from the Lonsdale et al. (2015) sample with the instrument Folded port Infra-Red Echellette (FIRE) on the Baade 6.5m telescope. Only seven of the 24 sources provided usable spectroscopic Hα or Hβ lines and no broad line detections were made. Fitting single Gaussian components to the H_β and surrounding [OIII]$\lambda\lambda 4959, 5007$ lines and integrating the Hα flux allowed the emission line luminosities to be calculated at these wavelengths. They measure $L_{OIII_{\lambda 5007}} \approx 10^{43} - 10^{44}\ \mathrm{erg\,s^{-1}}$ and with a correction factor of $L_{bol} = 3200 L_{OIII}$ (Shen et al., 2011), take the [OIII]λ5007 luminosity as a proxy for the bolometric luminosity. Assuming $\lambda_{Edd} = 1$ they obtain lower limits to their BH masses of $\log(M_{BH}) \geq 8.9 - 9.3\,M_\odot$, with some of these lower limits being significantly in excess of masses predicted by Lonsdale et al. (2015). They use the Balmer decrement to calculate the extinction for three of their sources ($\log A_V \approx 0 - 1.3$ mag), however do not correct their presented fluxes for extinction, again meaning that the true flux and BH mass values are likely larger than presented.

Analysis of hot, dusty and luminous radio powered galaxies is of the utmost importance as it allows confirmation of the AGN nature of MIR selected sources and provides details into the evolution of these newly discovered galaxy populations. However, in comparison to other WISE populations there has been little interest in RWGs with only the works by Lonsdale et al. (2015) and Kim et al. (2013) presenting dedicated research. Other similarly selected WISE populations have been the focus of more complete investigations and will be discussed below.

2.6.2 Hot Dust Obscured Galaxies

Hot Dust Obscured Galaxies (HotDOGs), initially termed W1W2-dropouts, are the most well known and observed population of WISE galaxies, uncovered by similar WISE colour selection criteria to RWGs. Whilst HotDOGs are easily detected in the WISE W3 and W4 (12 and 22 μm), they have faint or undetectable fluxes in the W1 and W2 bands (3.4 and 4.6 μm). Spectroscopy of HotDOGs (Eisenhardt et al., 2012; Wu et al., 2012) has shown that HotDOGs exist at high redshifts, 65% with z $>$ 1.5, and with high W4 flux densities HotDOGs have the potential to be hyper-luminous and indeed this population contains the universe's most luminous galaxy -

W2246 (Assef et al., 2015). Follow up observations of HotDOGs were quickly obtained by Wu et al. (2012) and Eisenhardt et al. (2012) with their results presented in 2012.

The W1W2-dropout selection criteria to select HotDOGs was first outlined by Eisenhardt et al. (2012) and also used by Wu et al. (2012) when selecting their targets for follow up observation. The HotDOG selection criteria is as follows: $17.4 < \mathrm{W1} < 34$ μJy, with the conditions $6.9 < \mathrm{W4} < 7.7$ mJy and $\mathrm{W2} - \mathrm{W4} > 8.2$ mJy or both $1.7 < \mathrm{W3} < 10.6$ mJy and $\mathrm{W2} - \mathrm{W3} > 5.3$ mJy needing to be met. Additionally targets had to be further than 30° from the galactic centre, more than 10° from the galactic plane, pass quality control checks in the WISE pipeline and also pass a rigorous visual inspection of individual exposures among other selection criteria.

Figure 2.4 demonstrates the rarity of HotDOGs, by showing the distribution of HotDOGs in WISE W1-W2-W3 colour space. HotDOGs occupy the upper right hand of the plot with the $\mathrm{W2} - \mathrm{W3} > 5.3$ mJy selection criteria being easily seen to select the reddest galaxies. They plot 226,017 sources representing 8% of all WISE catalogue sources in the selected region, in comparison to the 907 plotted W1W2-dropouts selected over the entire sky - demonstrating that this is clearly a rare population, though not on the same scale as RWGs. Their inserted histogram shows the redshift distribution of the selected HotDOGs, with a peak at z = 2.5, demonstrating well the success of WISE at finding these most luminous objects at high redshifts.

At the time of its discovery in May 2010, WISE J1814+3412, hereafter W1814, was one of only 37 sources with follow up observations and was found to be the most luminous source in W4. Presented as the first hyper-luminous infrared galaxy discovered by WISE (Eisenhardt et al., 2012) follow-up imaging was done in multiple wavelengths, from optical with the Multi-Object Spectrograph for Astrophysics, Intergalactic medium studies and Cosmology (MOSAIC) to radio with the European Very Large Array (EVLA). An assumption of two power laws was successfully used to fit an SED model to the WISE W3 and W4 flux densities along with 350 μm observations done by the Submillimeter High Angular Resolution Camera (SHARC-II) (Dowell et al., 2003), obtaining an estimate for the bolometric luminosity of W1814 as $\mathrm{L_{bol}} = 3.7 \times 10^{13}\,\mathrm{L_\odot}$. Whilst their estimate does not include luminosity at shorter wavelengths, they did take into account reddening corrections by applying extinction laws (Cardelli et al., 1989; Gordon & Clayton, 1998) and at a standard R value of $R_V = 3.1$. At this luminosity, W1814 easily qualifies as a hyper-luminous IR galaxy, classified by $L_{IR} > 10^{13}$ $\mathrm{L_\odot}$, though sources later presented in Wu et al. (2012) were found to be even more luminous. These results by Eisenhardt et al. (2012) successfully demonstrated the importance of follow-up observations made using the W1W2-dropout selection criteria and led the way for a number of papers to follow presenting their interesting discoveries made using this same selection criteria.

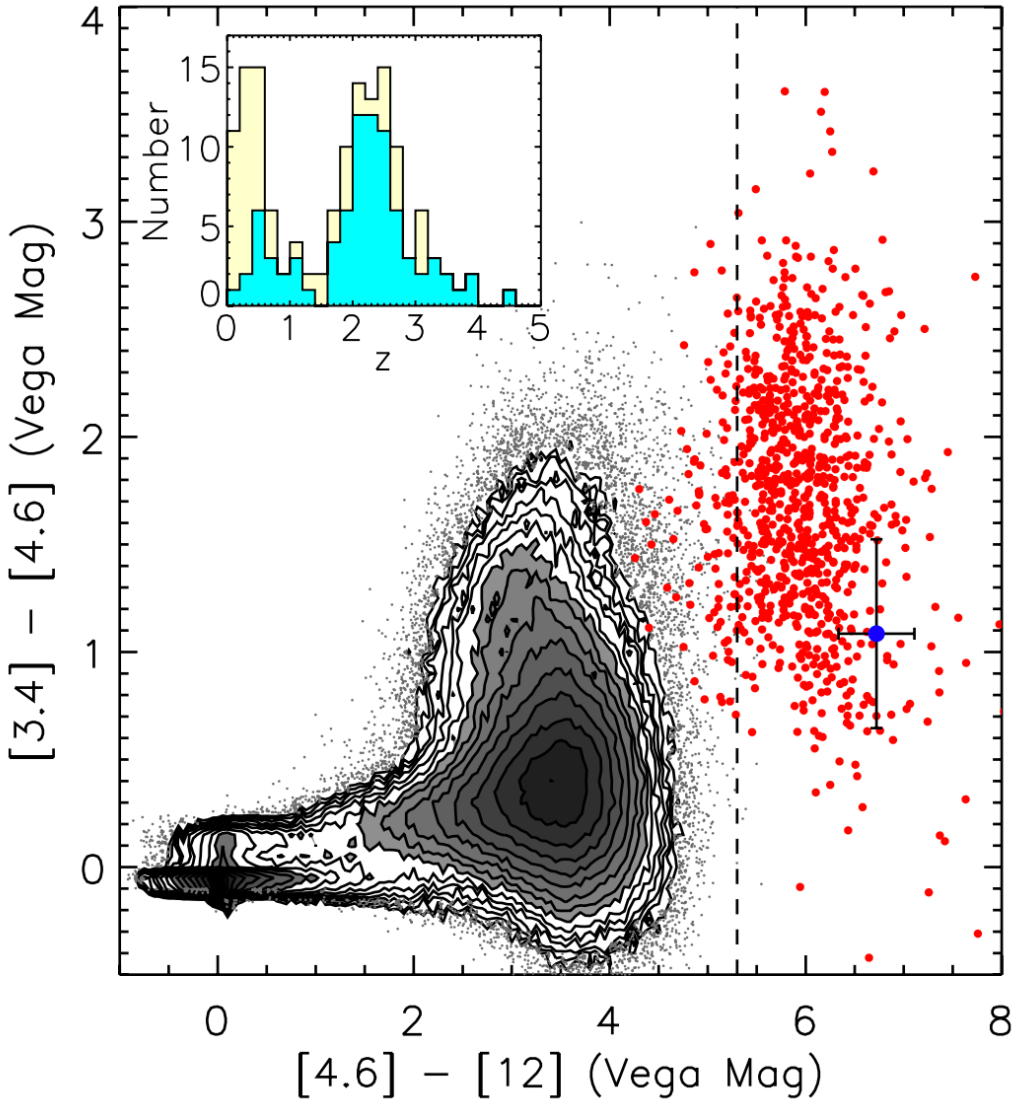

Figure 2.4: WISE colour–colour plot of the 226,017 sources with <0.3 mag errors in W1 (3.4μm), W2 (4.6μm), and W3 (12μm), in the 313.4 deg^2 area of the all-sky release catalogue. The larger red points are for 907 W1W2-dropouts (Eisenhardt et al., 2012) selected over the whole sky, excluding the Galactic plane and bulge, an area ∼100 times larger, illustrating the rarity of the W12 drop population. The inset shows the histogram of available redshifts for the W1W2-dropout sample, with the cyan shading corresponding to W1W2-dropouts not seen in the optical digitised sky survey. Credit: Figure and caption from Figure 1 of Eisenhardt et al. (2012).

Using data from the same observation runs as Eisenhardt et al. (2012), Wu et al. (2012) extended their analysis to include an additional 14 galaxies. Observations of these 14 HotDOGs, all with z $>$ 1.7, were taken with SHARC-II at 350 μm yielding nine detections, with an additional 18 sources observed with Bolocam (Glenn et al., 1998) at 1.1 mm yielding five detections. Multiple power laws were used to construct mid-IR - mm SEDs using the photometric follow-up data from Bolocam, SHARC-II and warm Spitzer observations. The multiple targets observed revealed a consistent SED shape of a power law from the mid-IR, but then apparently flat from the mid-IR to the sub mm and further into the mm wavelengths. This SED shape clearly indicated a new population of galaxies as it could not be well fitted by existing model templates. Figure 2.5 shows this SED shape poorly fitted with AGN dust torus (Polletta et al., 2006), QSO and starburst galaxy models (Polletta et al., 2007) with SED points completely missed. Newer works (Assef et al., 2020) suggest that this SED shape is due to excess UV emission from extreme, unobscured star formation.

Wu et al. (2012) derive total SED luminosities of 1.7×10^{13} $L_\odot$ - 1.8×10^{14} $L_\odot$, easily classifying these HotDOGs as Hyper Luminous Infra-Red Galaxies (HyLIRGs). Assuming that their energy output is dominated by IR emission it can be assumed that the IR luminosity is approximately equal to the bolometric luminosity. A modified blackbody of $S_\nu \propto \nu^{1.5} \times B_\nu(T)$ provided dust temperature estimates of 60 - 120K. Although this is noticeably hotter than previous IR galaxies, they notice a colder dust component not dissimilar to that found in starburst galaxies. Whilst termed W1W2-dropout galaxies in these two works (Eisenhardt et al., 2012; Wu et al., 2012), all of these observed sources also fall under the HotDOGs classification (Assef et al., 2011), yet are rarer and more luminous by factors 1000 and 10 respectively. The high luminosities and dust temperatures mean that these objects are of great interest to study in the context of galaxy formation and evolution.

In the years that followed a number of papers were published presenting follow-up observations of HotDOGs and below I summarise the most important and interesting findings from these papers.

Mid and far IR observations of 20 HotDOGs with $L_{bol} > 10^{14}L_\odot$ (Extremely Luminous Infra-Red Galaxies - ELIRGs) were presented in Tsai et al. (2015). These 20 sources made up 15% of the known HotDOG sample possessing spectroscopic redshifts making this a significant sample. Photometry from the All-WISE data release (Cutri et al., 2013) along with MIR data obtained with the Infra-Red Array Camera (IRAC), and Far Infra-Red (FIR) data from Herschel was used to create the full sample of photometric observations. In an attempt to answer some of the unknowns in quasar evolution including if these ELIRGs were a new stage in quasar evolution,

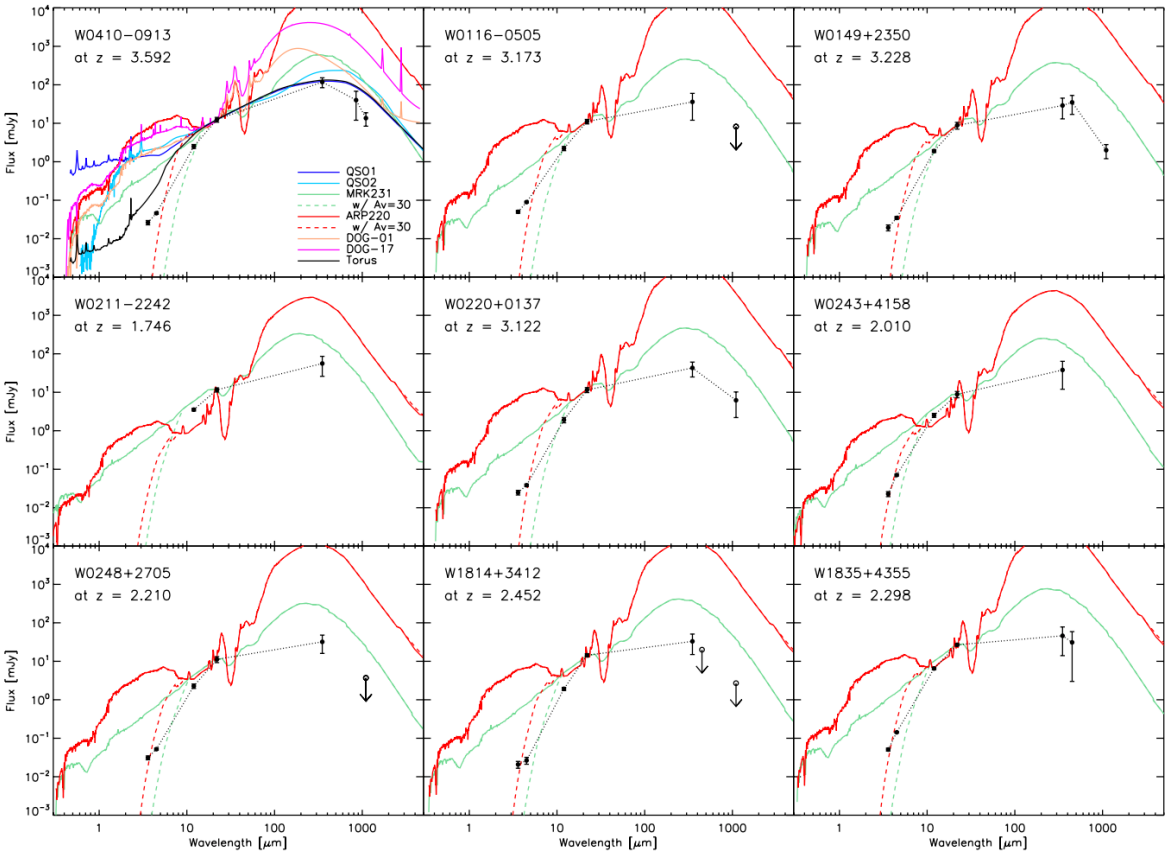

Figure 2.5: The SEDs for SHARCII detected W1W2-dropout galaxies with measured photometry, overlaid on a variety of standard SED templates at their spectroscopic redshifts (Polletta et al., 2006, 2007; Narayanan et al., 2010), normalised at 22 μm. Additional visual extinction must be added in order to account for the extremely red mid-IR colours of the W1W2-dropout galaxies. Black dotted lines in the figure demonstrate the method to connect SED points with power-laws to approximate the total luminosity. Credit: Caption and figure from Figure 3 of Wu et al. (2012).

these WISE ELIRGs were compared to a sample of 116 optically-selected quasars of the same luminosity ($L_{bol} > 10^{14} L_{\odot}$). In comparison to these quasars they find that the ELIRG HotDOGs are redder in the 4.6 - 12 μm colour by $\sim$ 2 - 3 magnitudes and span a narrower redshift range, though this later point may be a selection effect. Additionally, the rest frame luminosities of the selected HotDOGs at 5.8 and 7.8 μm are between 30 and 80% greater than the obscured quasars with no evidence of beaming or lensed systems, helping to find out what is powering these galaxies.

A companion paper to Tsai et al. (2015), Assef et al. (2015) present SED fits from follow-up with IRAC, and NIR observations from the Wide Field IR Camera (WIRC). Optical spectroscopy of a core sample of 53 targets was also obtained using the Keck-I telescope. Following a previous approach (Eisenhardt et al., 2012), templates of low resolution AGN, galaxy SED, and an AGN reddening component were used to fit the SED from the optical through to the mid-IR. Well modelled by a luminous obscured AGN that dominates the rest-frame emission at $\lambda > 1\,\mu m$ and a bolometric luminosity that combined with a host galaxy that is less luminous but dominates the rest frame optical and UV emission, stellar mass estimates are made by multiplying their rest K band host luminosity by the mass-to-light ratio of that band. They measure stellar mass estimates of $10^{11} - 10^{12}\,M_{\odot}$ with high IR luminosities. Whilst they measure no BH masses, they conclude that these stellar mass estimates lead to consequences for any BH mass estimates; with either HotDOGs radiating above the Eddington limit or measured BH masses likely in excess of local relations (Assef et al., 2015).

Maintaining the theme of the most luminous galaxies, presented in Díaz-Santos et al. (2016) are ALMA [C_{II}] 157.7 μm observations of W2246–0526, hereafter W2246, - the most luminous galaxy in the known universe. At a redshift of z = 4.601 and with a bolometric luminosity of $L_{bol} = 3.5 \times 10^{14}\,L_{\odot}$, W2246 is classified as a HotDOG based on its luminosity and dust temperature hosting a deeply buried AGN / SMBH. They investigated the ISM of W2246, adding additional information to the known HotDOG population. The instability of injected energy and momentum into the ISM may provide information on the evolution of these galaxies as this suggests that gas is being blown away from the system isotropically. An integrated [C_{II}] to far-IR emission ratio of 2×10^{-4} is seen only in the most obscured nuclei of local LIRG dusty systems, yet with a greater [C_{II}] luminosity and velocity dispersion when compared to Mrk 231 (a dust enshrouded AGN) a more massive and highly turbulent medium is implied (Díaz-Santos et al., 2016). In this work they emphasise the importance of studying systems like this to model gas kinematics under strong feedback at early times in the universe and in more extreme environments.

Wu et al. (2018) present a pilot survey to measure the SMBH masses of five HotDOGs - an extension of the work done in Assef et al. (2015) who did not give individual BH estimates. Measurement of these BH masses is of great importance in the quest to to understand these galaxies, as predicted by Assef et al. (2015), either the BH masses inferred are well above local relations or they accrete at high Eddington ratios that exceed the Eddington limit. Their five targets all have secure redshifts of $z \sim 2$ and well-sampled SEDs. NIR spectroscopy was obtained using MOSFIRE and FLAMINGOS-2 leading to detections of broad Hα emission lines from all five targets. Following previous approaches (Greene & Ho, 2005), they use a combination of multiple Gaussian components to obtain a FWHM measurement for the broad Hα line in order to estimate BH mass and use a Monte Carlo (Assef et al., 2011) approach to estimate the error of FWHM measurements, with two main fitting concerns of the blending of broad AGN emission lines with narrow line regions and possible contamination from outflows.

Since the discovery of the tight correlation between BH mass and the stellar velocity dispersion of the host galaxies bulge, there has been renewed interest in determining the BH masses of AGN (Ferrarese & Merritt, 2000). Magorrian et al. (1998b) derived the relation $M_{BH} \sim 0.006 M_{Bulge}$ based on observations of 36 quiescent galaxies observed with HST, implying a direct feedback relation between the growth of a supermassive BH and the stellar velocity dispersion despite processes such as galaxy mergers that may disrupt this correlation. This correlation is maintained through a feedback mechanism driven by momentum transfer (King, 2003) and most of the BH's energy is lost due to radiation. The discovery of this tight correlation allowed BH masses to be inferred from much easier measurements. Reverberation mapping techniques (Blandford & McKee, 1982) can then be used to estimate the radius of an AGN's broad line region and therefore derive virial BH masses.

As $M_{BH} \propto v^2 R_{BLR}/G$ and $R_{BLR} \propto L_{5100}^{0.5}$ with $L_{5100} = \lambda L_\lambda$ at $\lambda = 5100\,\text{Å}$, Wu et al. (2018) derive the relation in Equation 2.2, where f is a scale factor (of order unity) depending on the structure, kinematics and inclination of the BLR (Assef et al., 2011; Collin et al., 2006). Assuming $f = 1.17$ (Assef et al., 2011) they estimates of $M_{BH} \sim 10^9\,\mathrm{M}_\odot$ with Eddington ratios close to unity, that are comparable to obscured quasars, consistent with the theory that HotDOGs represent a transitional phase in quasar evolution. This clearly demonstrates the need for accurate BH mass estimates to help understand the evolution of such objects.

$$\mathrm{M_{BH}} = 7.8 \times 10^6\,\mathrm{f} \left(\frac{\mathrm{FWHM_{H\alpha}}}{10^3\,\mathrm{km\,s^{-1}}}\right)^{2.06} \times \left(\frac{\mathrm{L_{5100}}}{10^{44}\,\mathrm{erg\,s^{-1}}}\right)^{0.52} \mathrm{M_\odot} \tag{2.2}$$

Jun et al. (2020) also presented BH mass estimates of 10 $z \sim 2$ HotDOGs through use of X-shooter UV spectra, aiming to determine the presence of ionised gas outflows. They find evidence

for these outflows in eight of their sources through observing broad, blue shifted [OIII]λ5007 emission line profiles. They derive outflow rates of $> 10^3\,\mathrm{M_\odot yr^{-1}}$ greater than BH accretion rates, with feedback efficiencies of $\sim 0.1 - 1$ that are consistent with merger driven quasar activity. As in Wu et al. (2018), they also measure Eddington ratios of ~ 1 for their HotDOGs, but conclude that previous BH mass estimates may have significant uncertainties due to outflows, that have not previously been taken into account.

In the past 10 years our knowledge of HotDOGs has been greatly expanded with the HotDOG selection criteria extensively tested and successfully used to select extremely luminous and interesting galaxies. We have learnt that are rare sources (0.3% of WISE catalogue sources in the matched area), they sit in the upper left of a WISE WISE colour plot and exist at high redshifts with 65% of HotDOGs detected at z $>$ 1.5. They are HyLIRGs with $L_{bol} > 10^{14}\mathrm{L_\odot}$ with measured stellar masses of $M_{BH} \sim 10^{12}\,\mathrm{M_\odot}$ and BH masses of $M_{BH} \sim 10^{9}\,\mathrm{M_\odot}$. It has also been shown that they exhibit a constant SED shape of power law from the mid-IR and flatter mid-IR to mm, assisting with the determination of the properties discussed above.

2.6.3 Lyα Emitters and Blobs

The final WISE selected population to be discussed are Lyman α emitters (LAEs) and Lyman α Blobs (LABs). These rare AGN are extremely dusty and have emission extended on scales of 30-100 kpc. A mid-IR colour selection criteria of W2 - W3 $\geq$ 4.8 is used by Bridge et al. (2013) to identify radio quiet LAEs at a redshift range of 1.6 $<$ z $<$ 4.6. This criteria is successful at identifying LAE's with a 78% success rate, and $\geq$ 37% of these sources also classified as LABs as the spatial extent of their Lyα emission was $\geq 30\,kpc$.

The populations of LAEs and dusty IR galaxies should be largely separate as dust easily extinguishes Lyα photons due to the resonant scattering of atomic hydrogen, however observations of high redshift LAE/LABs are important as Lyα can be used as a tracer of star formation. Hot, dusty WISE selected LAE/LABs, WLAE/WLABS (Bridge et al., 2013) lie in a specific region of a WISE - WISE colour plot as shown by Figure 2.6. In addition to the MIR colour selection of $W2 - W3 \geq 4.8$, additional criterion of $S/N \geq 5$ for W3 and W4 observations, were used to select these WLAE/WLABs. Again excluded were sources within 30° of the galactic centre and 10° of the galactic plane, with no detections in SDSS required to avoid low redshift star forming galaxies.

Bridge et al. (2013) present optical spectroscopy of 92 WISE-selected targets with Keck I Low Resolution Imaging Spectrometer (LRIS) along side follow up photometry with Herschel, with measured luminosities $> 10^{13}\,L_\odot$ classifying these WLABs as HyLIRGs. They hypothesise that

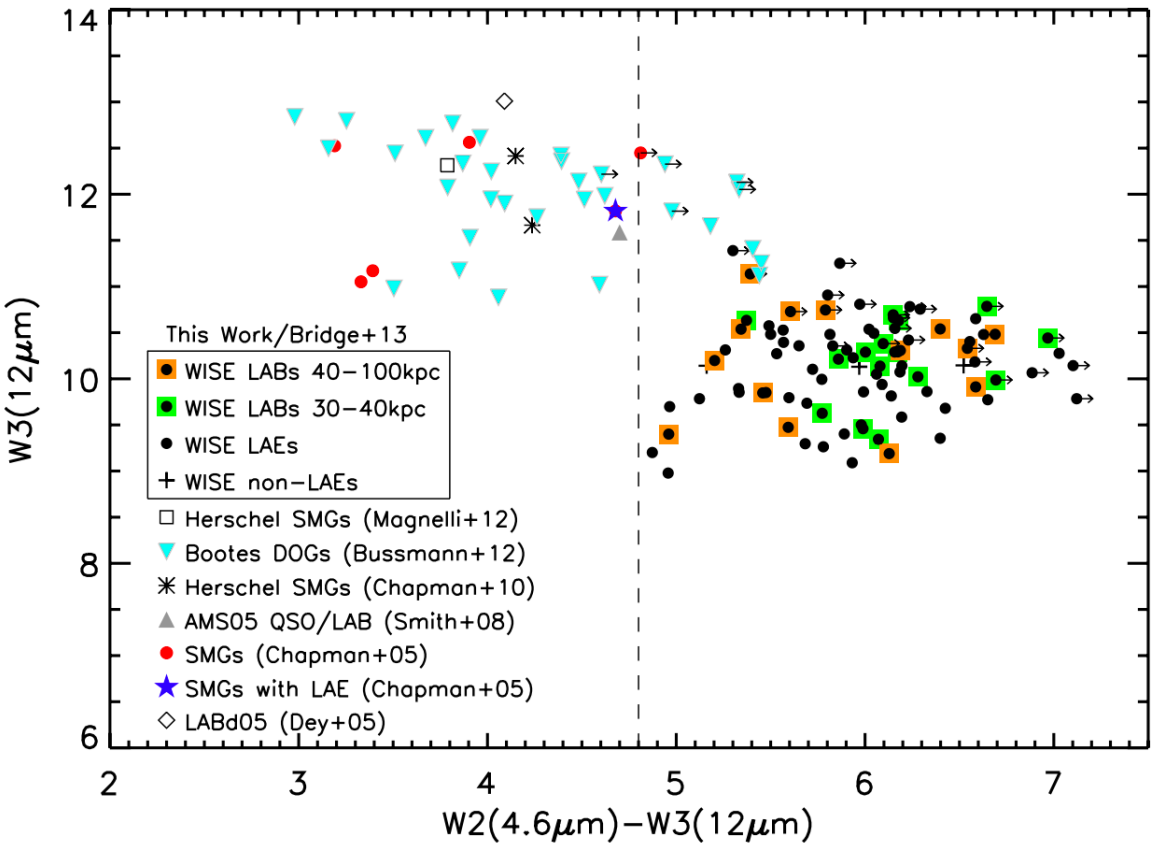

Figure 2.6: WISE W3(12 μm) vs. WISE W2–W3 (4.5–12 μm) colour for all sources in the sample with spectroscopic redshifts between $1.6 > z > 4.6$. WLAEs (black circles), 30–40 kpc WLABs (green squares), and 40–100 kpc WLABs (orange squares) are plotted. For comparison, z = 2–3 WISE detected SMGs/DOGs are highlighted: Magnelli et al. (2012): open squares, Bussmann et al. (2012): cyan downward triangle, Chapman et al. (2010): black asterisks, Smith et al. (2009): grey triangle and Chapman et al. (2010): blue star and red circle. Credit: Caption and figure from Figure 2 of Bridge et al. (2013)

.

the differences between WLABs and LABs means that they are likely at different evolutionary or environmental stages and with no overlap between the two populations, they select no previously known LABs with this new WISE colour based selection criteria. Any population overlap or indeed lack of, from different WISE colour selection criteria can provide new information about the possible evolutionary stages of these hot, dusty galaxies. Two thirds of the LAB sources are undetected by the FIRST and NVSS radio surveys; the selection criteria for RWGs detailed in Lonsdale et al. (2015). Comparatively to HotDOGs (Eisenhardt et al., 2012) there is a substantial overlap in z $>$ 2 selected sources noticing that the WLAB criteria is twice as effective at selecting high redshift galaxies (Bridge et al., 2013), and is clearly an interesting new WISE based selection criteria that has successfully discovered a new, rare galaxy population missed in previous narrow area surveys.

2.6.4 Measured Overdensities of WISE Galaxies

A final noteworthy subset of publications focus on the environments surrounding these previously discussed WISE selected galaxies, including analysis of both RWGs and HotDOGs. Jones et al. (2014) present Submillimetre Common-User Bolometer Array (SCUBA-2) 850μm sub mm follow-up observations of ten classified HotDOGs chosen for their known redshifts. Following previous works the photometric observations are fitted using SED templates (Polletta et al., 2007) commonly noting the steep red IR power law, mid-IR peak and flatter mid-IR to sub mm shape noted by Wu et al. (2012) and in contradiction to the SED shapes found for the Lyα Blobs (Bridge et al., 2013) which have a far-IR peak.

Most novel is the discovery of a number of serendipitous sources surrounding the target. With previous studies having provided evidence that in the environments of high redshift, far and mid-IR luminous galaxies there is an increase in the galaxy density, Jones et al. (2014) compare the number of serendipitous sources in the Hot DOG fields to two blank sub mm surveys fields in an aim to investigate clustering. If found clustering could provide evidence for large dark-matter halos associated with Sub Mm Galaxies (SMGs, Cooray et al., 2010). Comparing the number of sources within 1.5' circles centred on HotDOGs they report a relative over-density of SMGs by a factor $\approx 2.8 \pm 1.1$, though find no evidence for angular clustering.

Presenting a similar analysis, Silva et al. (2015) report on the over-density of sources in the environments of WISE / NVSS selected galaxies (RWGs). Following the selection criteria of Lonsdale et al. (2015), with an added constraint of $\log(f_{22\mu m}/f_{20cm}) < 1$ to avoid radio loud systems, they analyse ALMA observations of 49 targets, 26 of which were detected at $\geq 3\sigma$. A comparison of source counts outside of a 1.5' radius centred on the RWGs yields a relative over

density $\geq 10\times$ in comparison with blank field surveys. This over-density is significantly larger than reported for other WISE selected sources (Jones et al., 2014, 2015) though Silva et al. (2015) also find no evidence of angular clustering. Information on clustering may help in the understanding of these new galaxy populations as an over-density in SMGs implies significant star formation, with an over density of these WISE selected sources suggesting that they exist in over dense regions but they are not yet in fully formed clusters.

Following on in a similar manner, Jones et al. (2015) also present observations of RWGs in order to search for over-density of sources in the surrounding environments. They present SCUBA-2 observations of thirty galaxies taken from the Lonsdale et al. (2015) sample and count the number of SMGs within 1.5' regions centred around the targeted RWG. They report a relative over-density factor of 6.3 ± 1.1 when compared to blank field surveys. This factor is $\sim 1.6\times$ lower than the factor found by Silva et al. (2015), however these two source counts agree within the given uncertainties. In comparison to the environments around HotDOGs these WISE/NVSS selected RWGs have environments that are $\sim 2\times$ more over dense, suggesting that RWGs can be used as signposts for luminous, dusty, active galaxies. Continued study of these populations is important to understand where they fit within the evolution stages of galaxies as both HotDOGs and RWGs appear consistent with an AGN population though the presence of some starburst activity still can not be ruled out. This leads Jones et al. (2015) to hypothesise that luminous WISE selected galaxies could be a transient phase of a merger theory.

Continuing this comparison, Jones et al. (2017) compare the relatively overdensity of SMGs in the environments of RWGs and HotDOGs. Through SCUBA-2 observations of these WISE selected galaxies at respective mean redshifts of $z = 1.7$ and $z = 2.7$, are compared to blank fields from the SCUBA-2 Cosmology Legacy Survey (Geach et al., 2013). They find that the environments around both types of galaxy are over-dense compared with both normal star forming galaxies and SMGs, implying that these luminous, dusty galaxies are signposts for an over-dense environment. Whilst both the RWG and HotDOG selection criteria yield over-dense regions, the Star Formation Rates (SFRs) of the 17 observed companion sources differ, with the SFRs of SMGs around the radio AGN measured as $\sim 18\%$ higher compared to those around Hot DOGS, a difference proportional to their difference in sub mm flux density. The targeted WISE AGN sources exhibit redder colours in comparison to their companion sources, unsurprisingly due to their red selection criteria, implying levels of high dust obscuration and/or higher AGN contribution and dust temperatures compared to their companions (Jones et al., 2017).

Finally Penney et al. (2019b) present Spitzer observations of 33 ultra luminous RWGs at z $>$1.3. Through IRAC imaging on 5.12' $\times$ 5.12' fields and a colour selection criteria of [3.6] - [4.5]

> - 0.1 they find a modest 10% overdensity of IRAC selected galaxies compared to blank fields. However, using a redder colour criteria of [3.6] - [4.5] > 0.4 they find a mean 1.95× overdensity of sources in a 2.5' radius around the targeted RWG in comparison to blank fields. A > 3σ overdensity for 76% of targeted RWGs implies that RWGs inhabit dense regions of redder IRAC galaxies, although Penney et al. measure lower over densities in comparison to Silva et al. (2015) and Jones et al. (2015).

2.7 Summary

AGN are some of the most luminous sources in the universe (Assef et al., 2015; Tsai et al., 2015) and have been detected across the electromagnetic spectrum. Through use of WISE band colour selection criteria, new populations of AGN have been discovered, targeted for their highly luminous and obscured properties. With previous observations providing both a background understanding of these sources and a motivation for further research, there remain open questions around RWGs including their mass, how they are powered, their environments and where they sit in the context of galaxy evolution.

Previous studies of RWGs (Lonsdale et al., 2015; Lonsdale et al., 2016; Jones et al., 2015) have demonstrated the effectiveness in using a WISE colour selection criteria to select an interesting outlier galaxy population. Lonsdale et al. (2015) determined BH masses of $M_{BH} \sim 10^8 - 10^{10}\,\mathrm{M}_\odot$ for their sample of RWGs agreeing with the BH masses measured for HotDOGs and found an expected SED shape for RWGs. In addition Jones et al. (2015) determined that RWGs do lie in overdense regions of SMGs. However there are still many unknowns for RWGs, including their SED shape and the best model fit. This thesis aims to build upon previous work by adding two additional photometry points to aid in SED fitting and help the determination of fitted parameters, including stellar mass, in order to increase our knowledge of these sources. It also provides new BH mass measurements, extinction corrections and investigates the underlying source powering these galaxies. These new parameters will allow us determine which other galaxy populations RWGs most resemble and may be a subset of. This will help to determine what type of galaxies these sources are and whether they are an evolutionary phase of AGN that is previously unknown. If so it will allow us a look into an unknown time into the history of the universe.

Chapter 3

Instrumentation and Data Reduction

3.1 Introduction

This chapter will discuss the different instruments and surveys used throughout the analysis presented in this thesis. The majority of my research is based on observations taken with two instruments at the VLT in Paranal. The NIR imager Infrared Spectrometer And Array Camera (ISAAC) is now since decommissioned but I will present observations of 29 RWGs in the J and K_s bands. X-shooter on the other hand is a multi arm spectograph observing across three wavelength arms providing me with observations of 27 RWGs. This chapter will discuss these instruments used and the data reduction steps taken between the raw data and the final data products used in this work. Please note that the observations were taken by the authors of Lonsdale et al. (2015) with the pipeline data reductions performed at the time of observations.

This chapter will also discuss other instruments and surveys used to produce results that I have also used in my analysis. Firstly I will discuss the WISE satellite, whose observation band fluxes were used create the colour based selection criteria for RWGs and HotDOGs. I will then focus on ALMA, the instrument used mainly by Lonsdale et al. (2015) and whose fluxes I have used for SED fitting. Finally, I will also discuss two surveys - NVSS and FIRST; that I also used to assist in my SED fitting. These surveys were also used as part of the original RWG target selection (Lonsdale et al., 2015) and are therefore important to discuss. The NVSS radio survey (Condon et al., 1998) was the initial survey cross matched with the WISE All-Sky survey (Wright et al., 2010) in order to eliminate non radio powered sources. The FIRST radio survey (Becker et al., 1995) was used to assist with positional information during the initial cross match.

The variety of instruments used throughout my research and discussed in this chapter has provided me with data across the electromagnetic spectrum. From emission line spectra starting at 300 nm to fluxes provided from two different radio surveys, the wide range of instruments used

Figure 3.1: The four unit telescopes of the VLT with the laser guide star adaptive optics on UT4 shown. Credit: ESO

has allowed me ample opportunity to thoroughly investigate this new population of galaxies.

3.2 The Very Large Telescope

The Very Large Telescope or VLT (European Southern Observatory, 1998) [1] is an optical and IR telescope based in Cerro Paranal and situated at an altitude of 2635m. The VLT is comprised of four separate Unit Telescopes (UT); Antu, Kueyen, Melipal and Yepun, each with a primary mirror diameter of 8.20 m and thickness of 17.50 cm. The first of these unit telescopes received first light in May 1998 with the fourth being completed in September 2000, which notably possess a laser guide star (see Figure 3.1). The 4 Laser Guide Star Facility (4LGSF) was finished in 2016 and is a new subsystem of the adaptive optics facility on board the VLT. It consists of four separate laser beams producing an additional four artificial stars in the sky at a height of 90 km.

The VLT unit telescopes use an alt-azimuth mount, allowing a more compact dome to be built around each unit telescope saving on cost. An alt-azimuth mount allows for rotation on two perpendicular axis, vertical and horizontal, in order to change the directional pointing and

[1] www.eso.org/public/unitedkingdom/teles-instr/paranal-observatory/vlt/

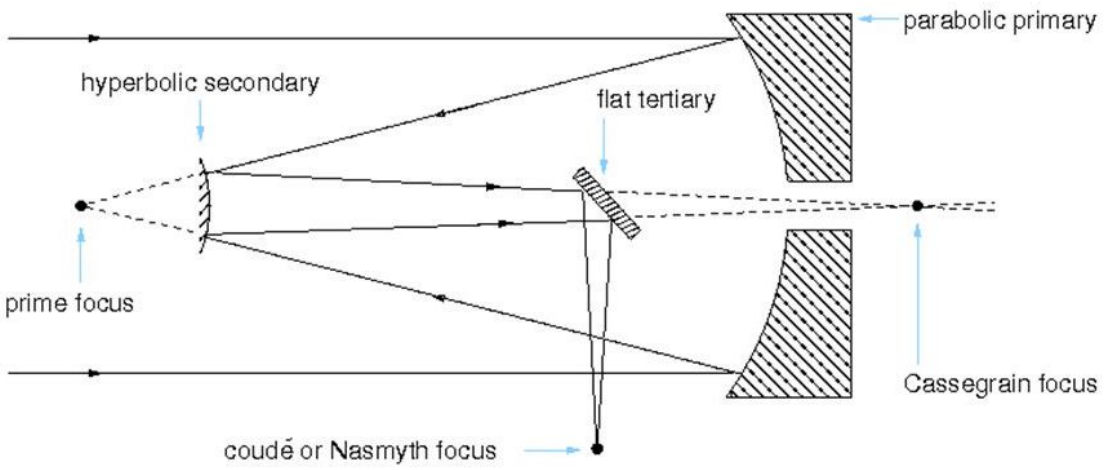

Figure 3.2: The location of Cassegrain, Nasymth and Coudé focuses on an optical telescope. Credit: University of Sheffield

altitude of the observations being made. In addition to the four unit telescopes, the VLT also consists of an additional four movable 1.8m auxiliary telescopes which together form the Very Large Telescope Interferometer (VLTI) with a maximum baseline of 140m. Whilst the four main unit telescopes are fixed, the individual auxiliary telescopes can be moved to 10 separate locations. They can also be used independently to form the VLT Interferometer Small Array (VISA).

The four individual unit telescopes can be used independently where the light is sent to either a Cassegrain focus or one of two Nasymth focuses, depending on which instrument is being used. X-shooter, for example, uses a Cassegrain focus. In the case that all unit telescopes are being used together as the VLTI a Coudé focus station is used. The main differences between these foci is that a Cassegrain focus is located behind the primary mirror where the optical path is folded back on to itself. A Nasymth focus on the other hand, moves with the telescope azimuth axis where a tertiary mirror directs the light along the altitude axis, in a direction perpendicular to a Cassegrain focus. In the case of two Nasymth foci they are located at either end of the altitude axis. For the unit telescopes on the VLT the tertiary mirror can be used to direct light to one of the two Nasymth foci or retracted, allowing light to pass to the Cassegrain focus, and meaning that three instruments can be mounted at once. A Coudé focus also uses a tertiary mirror to direct light along the altitude axis but also requires an aditional fourth mirror to direct light along a fixed axis normally into a separate room. Figure 3.2 shows the positioning if these foci on an optical telescope.

There are currently 13 different instruments installed on the four unit telescopes of the VLT,

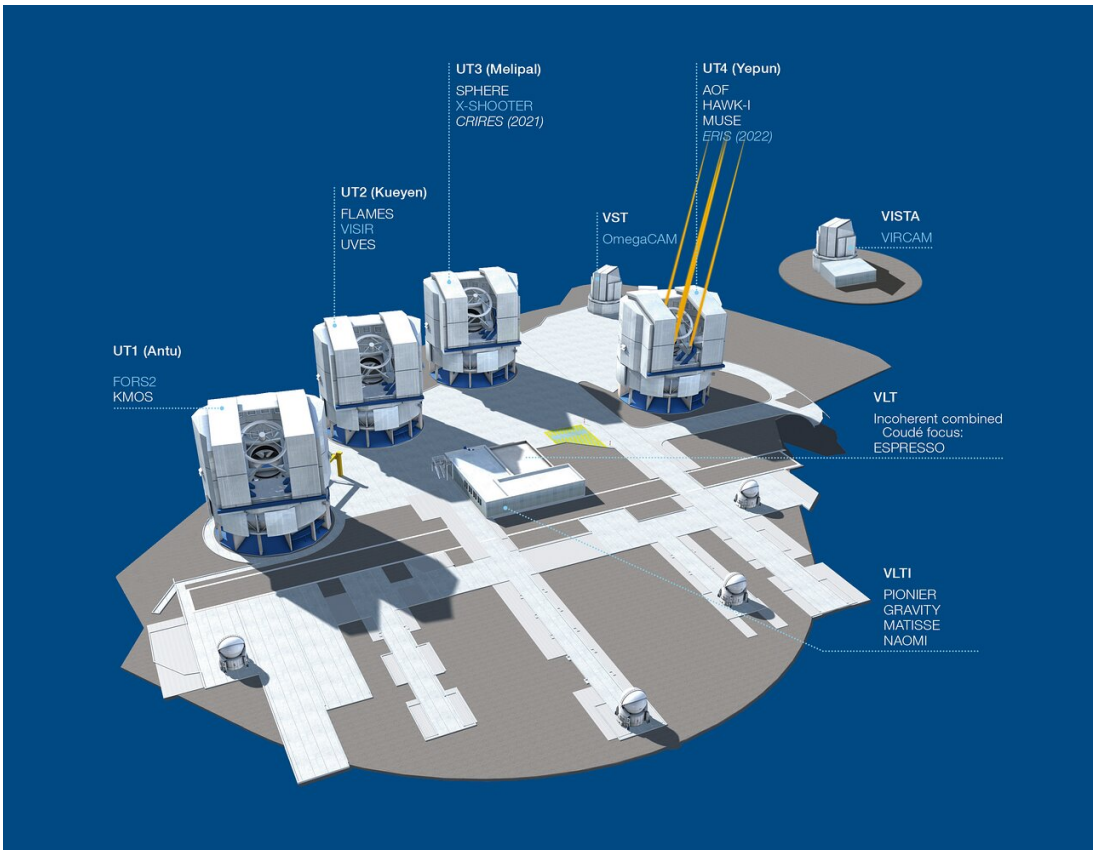

Figure 3.3: The layout of the unit telescopes of the VLT including which instruments are installed where. Credit:ESO

including X-shooter, with a previous eight, including ISAAC, that are now decommissioned. An additional four separate instruments are installed for use with the VLTI with Figure 3.3 showing the layout of the different unit telescopes as well as listing the instruments currently installed on each. Data taken from the VLT may be accessed in raw form from the European Southern Observatory (ESO) Science Archive Facility. The following two sections in this chapter will focus on the two instruments that I have used data from; ISAAC and X-shooter.

3.2.1 ISAAC

The Infrared Spectrometer And Array Camera (Moorwood et al., 1998) shown in Figure 3.4, is a now decommissioned instrument that was situated on UT3 of the VLT. It received its first light in November 1998 to be decommissioned 15 years later to make room for the Spectro-Polarimetric High-contrast Exoplanet REsearch instrument (SPHERE) (Maire, A.-L. et al., 2016). ISAAC was an IR ($1-5\,\mu m$) imager and spectograph that was placed on the Nasymth A focus of UT3. In its short wavelength imaging mode ISAAC had a 0.148”/pixel scale, a total field of view of 152 square arc seconds and a limiting J band magnitude of 24 mags for a one hour exposure.

ISAAC was composed of two separate arms one equipped with a 1024 x 1024 Hawaii Rockwell

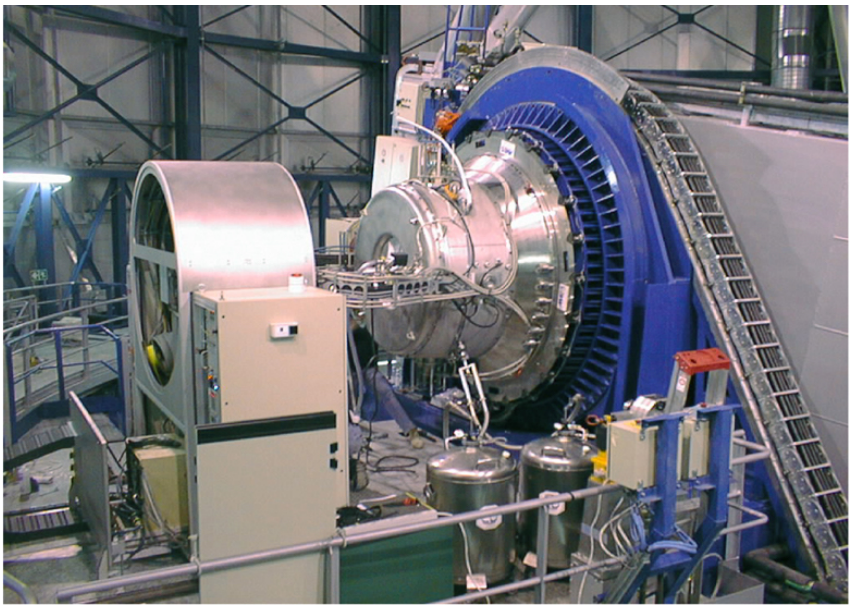

Figure 3.4: The ISAAC instrument when it was initially installed on UT1 of the VLT. Credit:ESO

array and the other equipped with a 1024 × 1024 InSb Aladdin array. The Hawaiian arm was used to observe at short wavelengths ($1-2.5\,\mu m$) and was equipped with a 1024×1024 Hg:Cd:Te pixel array. This array had a pixel size of 18.5 microns, a gain of 4.5 e^-/ADU and a quantum efficiency of 0.65.

The second Aladdin array was also formatted as an 1024 × 1024 array with a pixel size of 27 microns and a quantum efficiency of 0.80. This second arm was also used for J, H and K band imaging later in its operation. In total ISAAC was capable of three different functions at two different wavelength ranges. At the shorter wavelength range of $1-2.5\,\mu m$ ISAAC could provide imaging of a 2.5 × 2.5 arcmin field, imaging polarimetry over a 2.5 × 2.5 arcmin field and medium resolution spectroscopy. At the longer wavelength range of $2.5-5\,\mu m$, ISAAC was capable of imaging over a 1.25 × 1.25 arcmin field and medium resolution spectroscopy.

Observations

Across a nine night observation period 11/04/2013 - 03/06/13 photometric observations of RWGs were acquired with the ISAAC imager under ESO programme 091.A-0545(A). Out of the 30 RWGs discussed throughout this work 29 targets in total were observed under observation ID 200270799.

Data Reduction

ISAAC imaging observations were simultaneously read out in four separate quadrants, which made up a 1024 × 1024 pixel array. As these observations were taken only six months before the

decommissioning of ISAAC, the top left quadrant was broken and failed to read out correctly. The targeted source was therefore aligned in the centre of the working 'L' shaped region rather than the centre of the array, as shown later in Figure 4.2. Data reduction of the 43 observations was performed in situ using the ISAAC `jitter` recipe. The `jitter` technique is required due to the high sky brightness in the IR and its rapid variability. It involves taking ~ 5 sky frames before and after the object frames are taken, which are then shifted, aligned and stacked to form a final sky image. These frames should be located 5 - 10 arcmin either side of the targeted source.

The ISAAC pipeline provided `jitter` recipe supports sky subtraction, but also flat fielding and dark subtraction as well. Dark frames are exposures taken without any detector illumination with three frames taken for each targeted source that are then stacked and subtracted. Flat fielding for ISAAC is performed at twilight with ~ 25 exposures per filter taken allowing the correct flat field to be subtracted for each filter used. The `jitter` recipe can also support the correction of vignetted and bad pixels by replacing them with the mean value of their neighbours, though it is unable to trim whole regions of the image. The reduced exposures are then stacked, a process in which the pipeline removes the highest and lowest exposure values before taking an average for the final frame. The 200 highest and lowest pixels are also removed in case of any bias residuals left over from the dark subtractions. Finally standard stars are observed every night to assist with zero pointing the final science images, though no extinction corrections are made.

This `jitter` pipeline recipe was used to reduce all 43 observations of RWGs taken across two different filters, for use in NIR photometry and SED fitting.

3.2.2 X-shooter

X-shooter (Vernet et al., 2011) is a multi wavelength, medium resolution spectograph that sits at the Cassegrain focus of UT2. It received first light in March 2009 with the science aims of providing broad-range high-resolution spectroscopy of brown dwarfs, type Ia supernovae and gamma-ray bursts. X-shooter observes across a total wavelength range of 300 - 2500 nm and is made up of three separate spectroscopic arms; UVB, VIS and NIR each with optimised optics, dispersive elements and detectors.

X-shooter consists of a separate structure which supports three prism cross dispersed spectrographs as shown in Figure 3.5. Each individual X-shooter arm is an echelle spectrograph using a grating to disperse the received light in to a spectrum. The calibration unit is used for flat fielding and contains wavelength calibration lamps selected to cover the entire wavelength range observed. The acquisition and guiding camera is used for visual detection and centring of

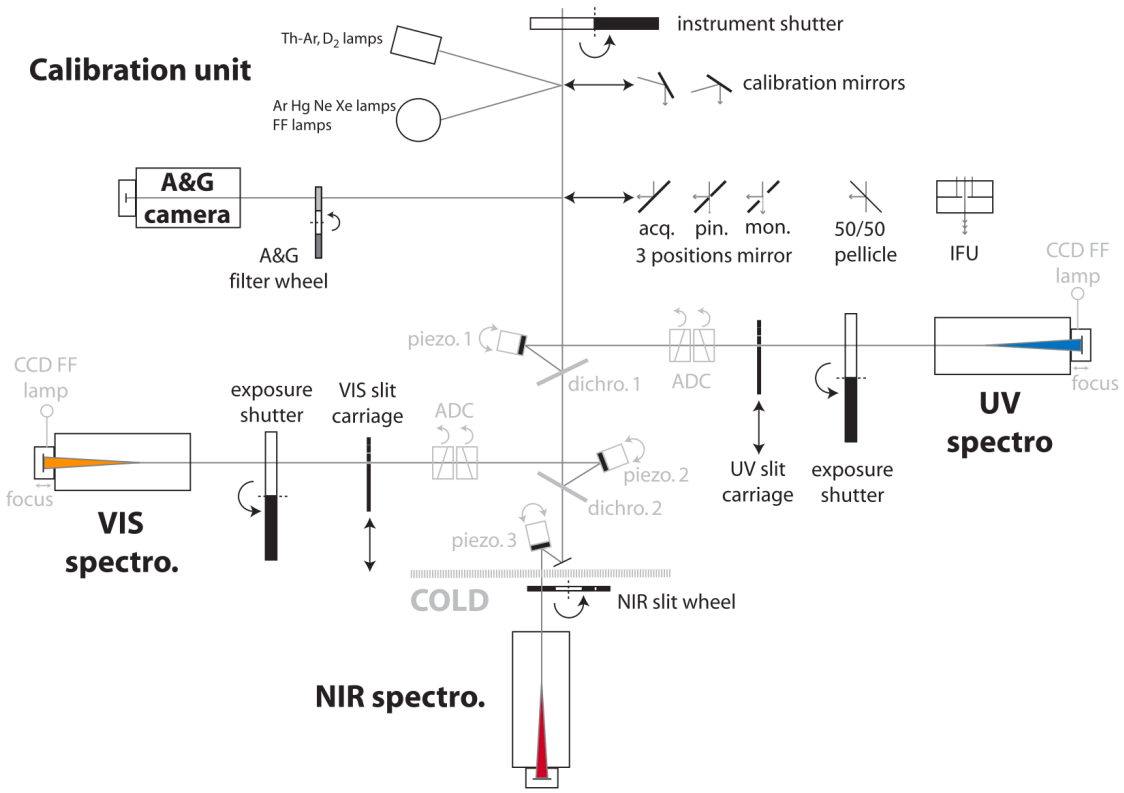

Figure 3.5: A functional diagram of X-shooter, where the light path runs from the top to the bottom of the image. Credit: Figure 2 of Vernet et al. (2011)

objects using a SDSS filter set from the u to the z band.

All of the arm characteristics are summarised in Table 3.1 for easy comparison, giving the number of spectral orders, resolution, gain and readout time for the three wavelength ranges x-shooter observes at. The NIR spectrograph differs from the other two in the fact that it is fully cryogenic with a liquid nitrogen bath cryostat that allows the detector to operate at only 81 K. The detector also uses a different sized array which is 2000 × 2000 pixels large but with only 1000 × 2000 pixels used.

X-shooter operates at a limiting AB magnitude of ∼ 21 mag in one hour across its three spectroscopic arms allowing it to observe both the brightest and faintest of objects. This work

Table 3.1: The three X-shooter arm characteristics.

Arm	Wavelength Range	Spectral Orders	Pixel Scale	Resolution	Gain	Readout Time
	nm	n	”/pixel	$R = \lambda/\Delta\lambda$	e^-/ADU	s
UVB	300 - 560	12	0.161	3200	1.83	8
VIS	550 - 1020	15	0.158	5000	1.64	6
NIR	1020 - 2480	16	0.248	4300	2.29	1.46

focused on observations made with the NIR arm, though unfortunately telluric absorption lines and regions of atmospheric absorption limit the regions that are useful.

Observations

Spectroscopic observations of 27 RWGs were performed with X-shooter under ESO programme 290.A-5042(A) and observation ID 200271118. Observations were performed in the nodding mode with a ABBA sequence providing both one and two dimensional spectra.

Data Reduction

Reduction of the observed X-shooter spectra was performed using the X-shooter `reflex` pipeline[2], which is a combination of 20 different pipeline recipes, including dark subtraction, bias correction and wavelength calibration.

My X-shooter observations were performed in nodding mode with an ABBA nod sequence and a maximum distance of 5" between nod positions. Due to this use of nodding observation mode a flat field correction was not needed. When needed, flat field exposures are taken with a continuum lamp, and provide information on the response of the detector and variations in efficiency at a pixel-to-pixel scale. For the UVB arm two separate flat fields are required; one taken with a halogen lamp and the other with a deuterium lamp.

Bias frames are taken to monitor the readout noise of the Charge Coupled Device (CCD) and for the NIR arm this subtraction is performed automatically. This correction is however not performed for the UVB and VIS arms as there is no detectable readout pattern to subtract. Dark frames are also automatically subtracted for NIR detections and are used to subtract the dark current from the detector. For the UVB/VIS arms this dark current is usually negligible though dark frames are taken on occasion.

Wavelength calibration is performed by comparison of Th-Ar arc lamp pinhole images with an image order table. For my observations a mean 1716 lines were used to find a wavelength solution with a mean error of $\sigma_{RMS} = 0.09$Å. Flux calibration is performed correcting for the instrument response curve and the overall efficiency of the telescope/instrument combination. A standard star exposure is taken between each science frame with two standard stars, LTT3218 and Feige 110, used throughout my observations. Equation 3.1 shows how the resultant flux density is corrected for the instrument response function, atmospheric extinction, exposure time and detector gain.

[2]http://www.eso.org/sci/software/esoreflex/

Table 3.2: The properties of the four separate WISE bands.

Instrument	Central Wavelength	Bandwidth	Angular Resolution	5σ point source sensitivity
	μm	μm	”	mJy
W1	3.35	0.66	6.1	0.08
W2	4.60	1.64	6.5	0.11
W3	11.56	5.61	6.6	1.0
W4	22.09	4.01	12.0	6.0

$$\mathrm{I}\,(\mathrm{erg\,s^{-1}\,cm^{-2}\,\AA^{-1}}) = \frac{\mathrm{I}\,(\mathrm{ADU/pixel}\,(\AA)) \times \mathrm{Response}\,(\mathrm{erg/e^{-}\,cm^{-2}}) \times 10^{(0.4\times\mathrm{airmass}\times\mathrm{ext})}}{\mathrm{Gain}\,(\mathrm{ADU/e^{-}}) \times \mathrm{Exposure\,time}\,(\mathrm{s}) \times \mathrm{Binsize}} \quad (3.1)$$

The final reduced science products of the X-shooter observed spectra include both flux and non flux calibrated 2D and 1D spectra. This is split into each of the three wavelengths arms spanning a total wavelength range of 300 - 2480 nm, with the 2D spectra spanning 15.75” in the spatial direction.

3.3 WISE

The Wide field Infrared Survey Explorer[3] (Wright et al., 2010) is a NASA mission that launched in December 2009 into a sun synchronous orbit and completed entire sky coverage seven months later in July 2010. In February 2011 the WISE satellite had successfully completed scanning the entire sky twice over, observing $> 7.5 \times 10^8$ individual objects. After successfully completing its mission surveys in 2011, and depleting its entire coolant supply, the WISE satellite was put into hibernation until September 2013 when it became the Near Earth Object WISE (NEOWISE) mission. This new mission has the aim of finding near Earth objects and orbits the Earth 15 times a day.

The WISE satellite (Figure 3.6) observes across four IR bands, W1, W2, W3 and W4, at central wavelengths of 3.6, 4.2, 12 and 22 μm. The satellite is composed of a 40 cm telescope encased in a solid hydrogen cooled cyrostat. This cyrostat contains two solid tanks of hydrogen, a larger tank that cools the telescope to 12 K and a smaller tank with the sole purpose of cooling the larger wavelength bands SiAs array to 7.5K. The entire flight system is 2.85 m tall, 2.00 m wide with a depth of 1.73 m. The entire satellite weighs 661 kg, 347 kg of which is the camera and the cryostat (Wright et al., 2010). Attached solar panels provide over 500W of power, with the satellite requiring 301W for full operation.

[3] www.nasa.gov/missionpages/WISE/mission’

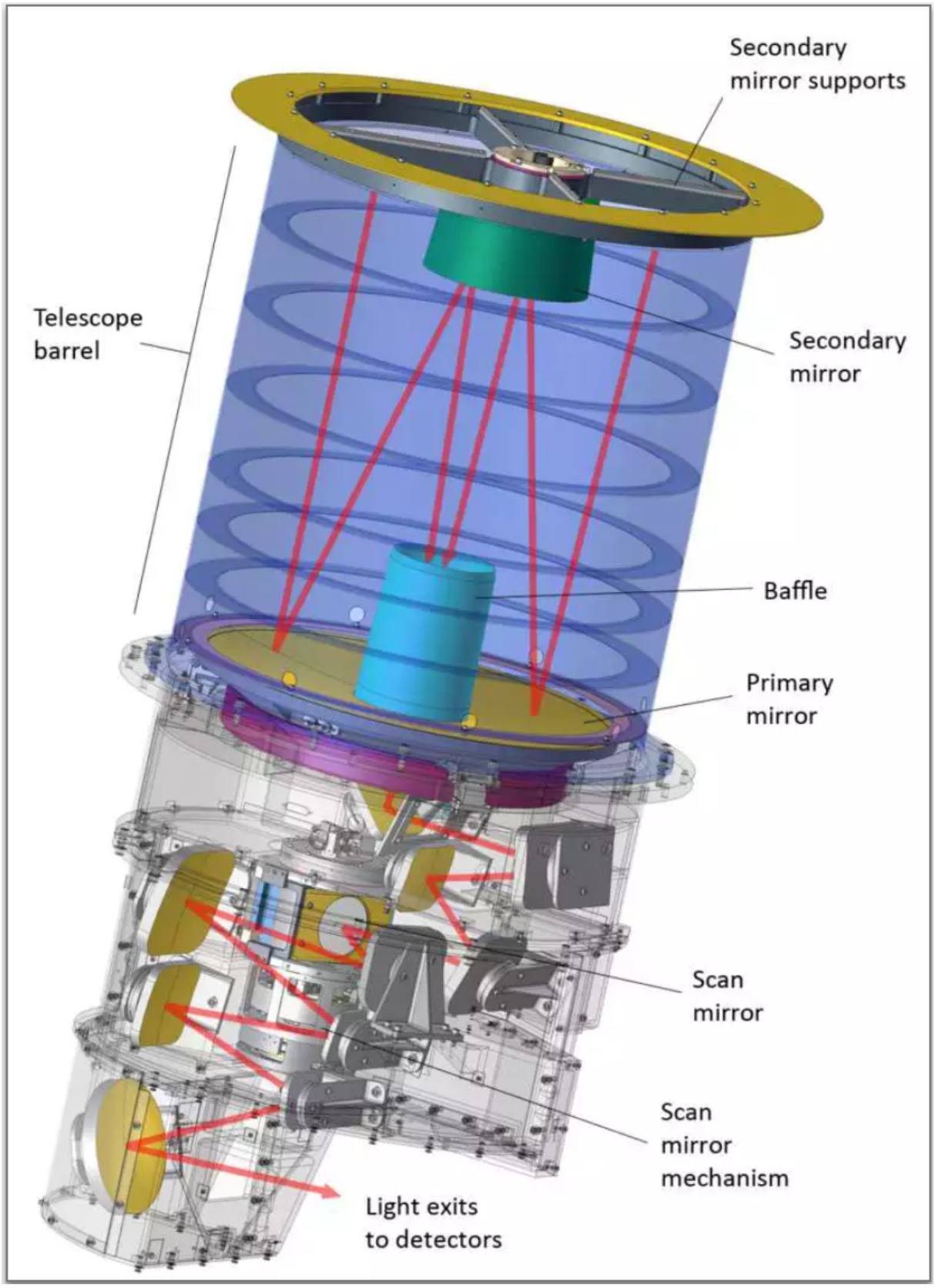

Figure 3.6: A labelled schematic of the main WISE telescope components. Credit: Planetary.org

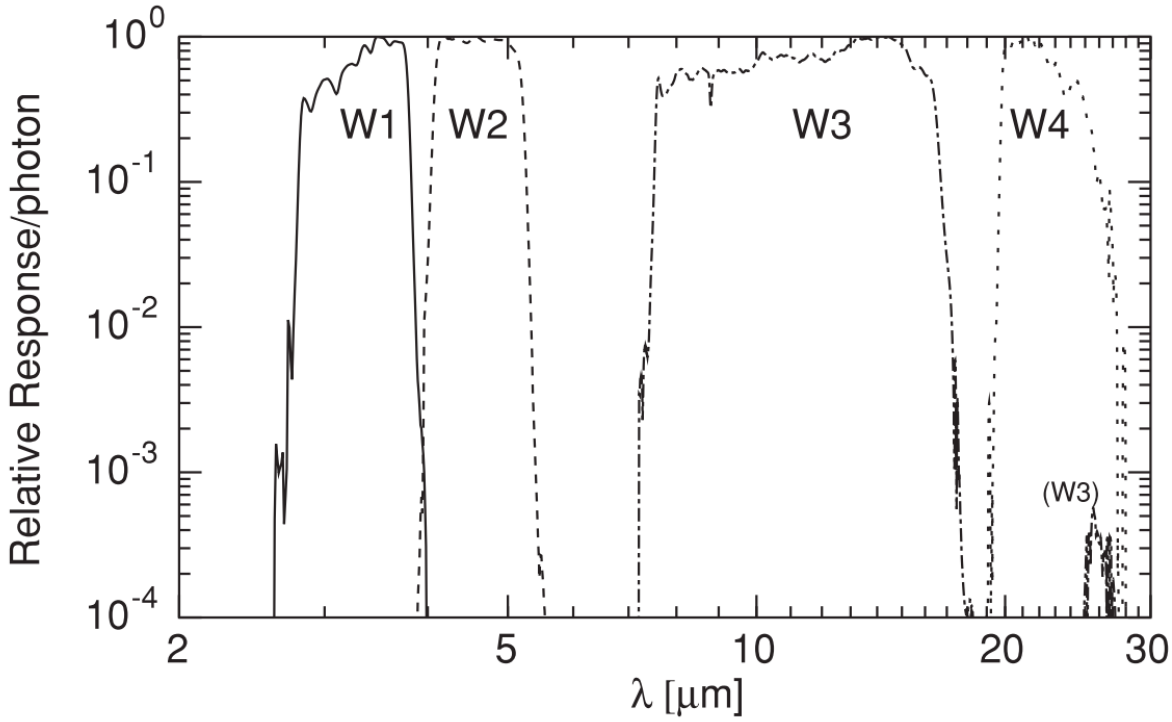

Figure 3.7: Weighted mean WISE relative spectral response functions after normalising to a peak value of unity on a logarithmic scale. Credit: Figure 7 from Wright et al. (2010).

The properties of the four different WISE instruments observing in four different wavelength bands are summarised in Table 3.2. The angular resolution of the four instruments, W1, W2, W3 and W4 is 6.6", 6.6", 6.6" and 12" respectively. Figure 3.7 shows the four WISE instrument band passes and their spectral response function when the peak values are normalised to one.

The WISE instrument is comprised of four wavelength channels for each of each of the four wavelength bands. The channels for the shortest wavelengths bands are comprised of HgCdTe 1024 × 1024 pixel arrays in an 18 μm square, whilst the longer two channels are SiAs arrays also arranged in a 1024 × 1024 pixel square. All four arrays simultaneously image the the same field of view using three diochroic beam splitters. The spectral response of the system is determined in three separate ways; the whole system response is measured using a fourier transform spectrograph, the system response is estimated using the product of component data, and the results are computed from component design calculations (Wright et al., 2010).

The original WISE mission aimed to map the entire sky at a higher precision than its nearest comparable mission the Infra Red Astronomical Satellite (IRAS, Neugebauer et al., 1984). The most fundamental objective of the WISE mission was to provide a sensitive mid IR all sky survey, with the aim of classifying red extra galactic objects and nearby red brown dwarfs. With the aim of using the WISE band colour to classify and discover new sources, Figure 3.8 shows the

expected locations of interesting classes of objects in WISE - WISE colour space.

In the years since the WISE All-sky survey was completed WISE band fluxes have been used in aiding the discovery of the most luminous galaxy in the universe (Tsai et al., 2015; Assef et al., 2015), the discovery of ELIRGs across different redshifts (Laor & Stern, 2012; Eisenhardt et al., 2012; Wu et al., 2012) and cataloguing over 100 new brown dwarfs (Davy Kirkpatrick et al., 2011). WISE band colours were also used as one of the main selection criteria in the discovery of the new population of RWGs (Lonsdale et al., 2015), and the similarly selected population of HotDOGs (Wu et al., 2012).

3.4 ALMA

The Atacama Large Millimeter/submillimeter Array (Wootten & Thompson, 2009) is an interferometer located on the Chajnator plateau in the Chilean Andes at an altitude of 5,059 m. It observes at wavelengths of 0.32 - 8.5 mm (1000 - 35 GHz) and achieved first light in early 2011. ALMA consists of a main array, containing 50 antennae each measuring 12 m in diameter. There is an additional compact array of four 12 m antennae and 12 7 m antennae. The total 66 different antennae can be arranged into different configurations with the distance between antenna baselines ranging from 150 m to a maximum of 16 km. This large baseline and number of antennae allows ALMA to achieve a high level of sensitivity, measuring a spatial resolution of 4.8" at 110 GHz in its most compact form, and a resolution of 43 mas, again at 110 GHz, in its most extended form.

The main science goals of ALMA were to observe molecular gas and dust, with the aim of investigating the building blocks of the universe in the form of star formation and molecular clouds. Key science results from ALMA include imaging the protoplanetary disk HL Tau (Picogna, Giovanni & Kley, Wilhelm, 2015) and observing Einstein rings (Vlahakis et al., 2015). In the context of RWGs, ALMA was used by Lonsdale et al. (2015) to observe 23 RWGs with the resulting data used to assist in SED fitting.

3.5 Surveys

The final two subjects of interest to be discussed in this chapter are not instruments themselves, but instead surveys. Both the NVSS and FIRST radio survey were used as part of the selection criteria used to aid in the discovery of RWGs (Lonsdale et al., 2015).

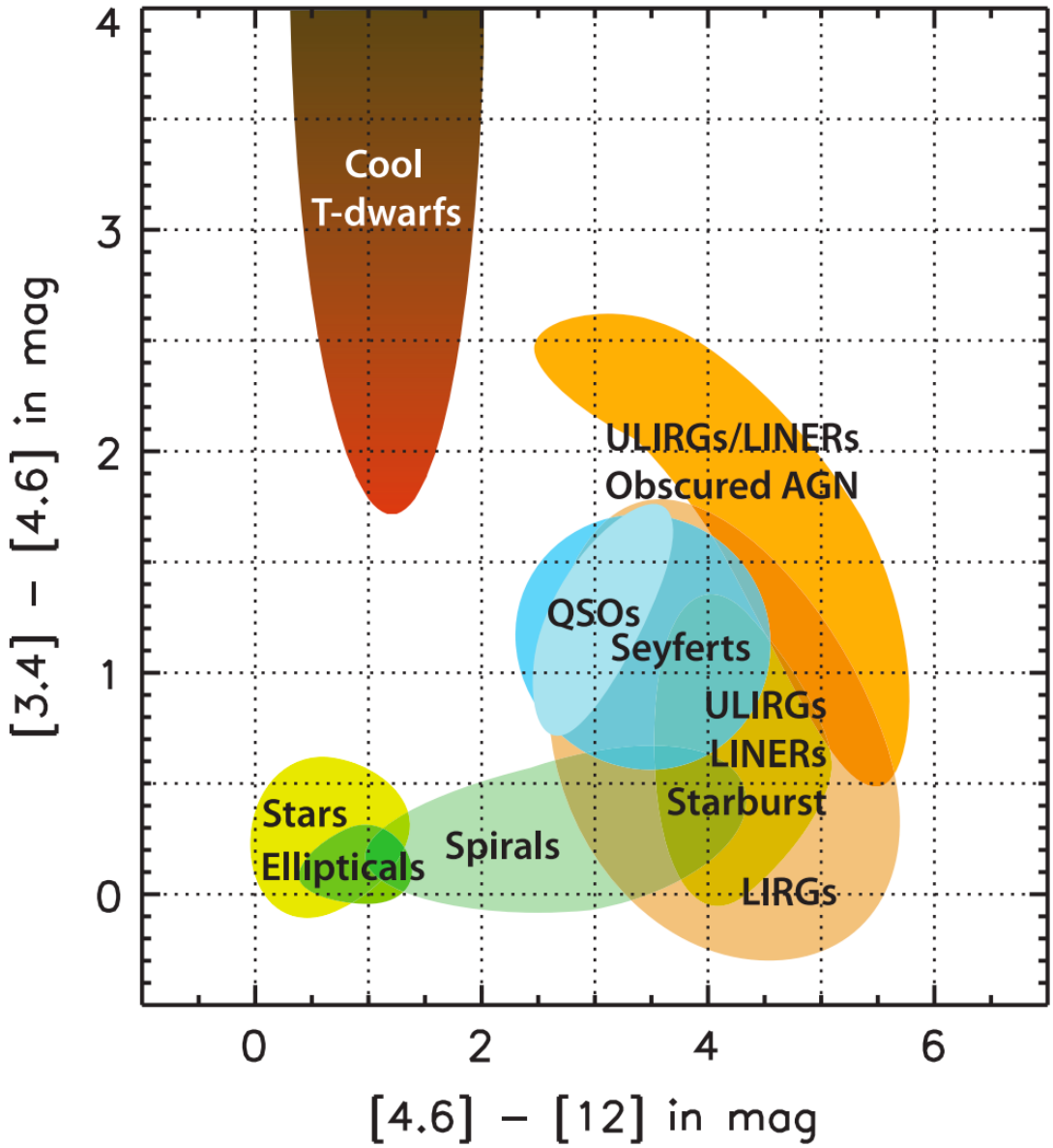

Figure 3.8: Colour–colour diagram showing the locations of interesting classes of objects. Stars and early-type galaxies have colours near zero, whilst brown dwarfs are very red in W1–W2, spiral galaxies are red in W2–W3, and ULIRGS tend to be red in both colours. Credit: Figure 12 from Wright et al. (2010).

3.5.1 NVSS

The NRAO VLA Sky Survey (Condon et al., 1998) was completed between September 1993 to October 1996 using the VLA, and covers all of the sky north of $\delta = -40°$ at 1.4 GHz. The full survey is made up of 217,446 overlapping observations each of which was weighted and combined to yield the primary data products of 2326 $4° \times 4°$ image cubes with the three axes spanning the I, Q and U stokes polarisation parameters. All of the released images had a FWHM resolution of $\theta > 45''$, which was significantly greater than the angular size ($\phi \sim 10''$) of the faint extra galactic sources targeted. The secondary data product was a complete catalogue containing $\sim 2 \times 10^6$ objects, including radio galaxies, quasars and low luminosity AGN, all with flux densities $>$ 2.5 mJy. All of the data products from NVSS, and the related software, were released online[4] as soon as the data was verified, making this survey an excellent tool for the astronomical community.

3.5.2 The FIRST radio survey

The Faint Images of the Radio Sky at Twenty centimetres radio survey (Becker et al., 1995) started in April 1993 and used the VLA to image 10,000 square degrees of the northern sky at a wavelength of 20 cm. The resulting survey images had a flux density limit of 1.0 mJy with an angular resolution $>$ 5.0". The primary data product of this survey was a sky map containing $> 4 \times 10^{10}$ pixels with a noise of $\sigma_{RMS} < 0.15$ mJy. Also released was a 20 cm source catalogue containing measured flux densities, exact positions and morphological information of $> 10^6$ individual sources. All of the data products from the FIRST radio survey were also released online[5], with the raw UV images being available online the day after the observations took place.

3.6 Summary

Many different instruments and surveys have been utilised in the creation of the science products presented in this thesis. In the next chapters I will present analysis of RWG observations taken with ISAAC and X-shooter, at the VLT, with additional observational science results used to assist my work.

[4] www.cv.nrao.edu/nvss/
[5] http://sundog.stsci.edu/

Chapter 4

Using the NIR to determine the Black Hole & Host Galaxy Masses of Radio WISE Galaxies

4.1 Introduction

Please note that the contents of this chapter has been published in Ferris et al. (2021), and all the analysis presented below was undertaken by me.

NASA's WISE (Wright et al., 2010) mission discovered ~ 1000, extremely luminous and rare IR galaxies, though the use of a mid-IR colour selection criteria. Alongside the discovery of Hot-DOGs (Wu et al., 2012; Eisenhardt et al., 2012; Wu et al., 2014; Tsai et al., 2018; Díaz-Santos et al., 2018), were the similarly luminous population of RWGs (Lonsdale et al., 2015; Silva et al., 2015; Jones et al., 2015). Previous follow up campaigns (Lonsdale et al., 2015; Silva et al., 2015; Tsai et al., 2015; Díaz-Santos et al., 2016, 2018) of both RWGs and HotDOGs with ALMA revealed a large range of spectral AGN diagnostics, with many similarities between both populations. However, with past work focused on the HotDOGs, there is now a unique opportunity to investigate the properties of RWGs and work out where they fit among these new type of WISE selected galaxy populations.

It is thought that these new galaxies are likely to be sites of intense AGN fuelling and feedback, allowing for a rare opportunity to investigate extreme AGN phenomena. With similarly selected WISE sources being classified as ELIRGs (Tsai et al., 2015, 2018), it is likely that these RWGs are at the peak of their AGN activity. With RWGs now expected to be extreme cases of AGN, it becomes vital to investigate their BH and host galaxy masses in order to test how current

scaling relations hold up in these dramatic cases. Especially as the evolution of BHs and their hosts appear closely linked and crucially joined by AGN feedback.

This chapter builds upon previous large scale IR spectroscopy (Kim et al., 2013) of RWGs, now with a substantial increase in depth, in order to determine the BH and host galaxy masses of a selection of RWGs. High resolution spectroscopy can now be used in various ways in order to determine supermassive BH masses ($\geq 10^5\,\mathrm{M}_\odot$), and in this chapter I will present three different approaches, all utilising the emission lines from X-Shooter NIR spectroscopy. I use an assumed Eddington ratio and detections of the [OIII]λ5007 emission to calculate the BH mass based on a sources bolometric luminosity. I then follow the work by Greene & Ho (2005) to produce a virial BH mass estimate that relies on a tight correlation between the $L_{5100\,\text{Å}}$ continuum luminosity and the emission line properties of two different Balmer lines, Hα and Hβ. Finally I provide additional mass estimates using the CIV emission line FWHM and bolometric luminosity as derived from the [OIII]λ5007 emission line flux.

In this chapter I present NIR imaging of 30 selected RWGs, taken in good seeing ($\sim 0.8''$), and attempt to fit an SED to my measured fluxes. I then used high-resolution NIR spectra of 27 RWGs to determine their BH and host galaxy masses. Additional spectroscopic information provided by the three wavelength arms of X-shooter will be utilised to provide CIV based masses but returned to later in Chapter 6. First I present my results gained from using three NIR emission lines (and CIV) to measure the BH and host galaxy masses of my sampled RWGs.

4.2 Target Selection

This work discusses a population of 30 selected RWGs, with the data presented collected from observations at the European Southern Observatory under ESO programmes 091.A-0545(A) and 290.A-5042(A). This section will discuss the criteria used to select these 30 RWGs.

The 30 RWGs I discuss throughout this thesis were initially selected from galaxies in the WISE All-Sky catalogue (Wright et al., 2010). The selection criteria for my sources is based on that originally outlined in Lonsdale et al. (2015), and aimed to target compact radio sources that are likely to be highly obscured. The selection process for RWGs starts with the 563,921,584 sources available in the WISE All-Sky catalogue, where the `ext` catalogue flag was first used to reject extended sources.

The initial selection criterion was to cross match point sources in the WISE All-Sky catalogue (Wright et al., 2010) with the NVSS radio catalogue (Condon et al., 1998) in order to eliminate those none radio powered sources. The NVSS catalogue covers everything north of $\delta = -40°$, meaning that those sources to the south of this were automatically eliminated by this cross

match. Where available, positional information from the FIRST radio survey (Becker et al., 1995) was used in order to assist in this cross match between WISE and NVSS with additional position information. All sources $\pm 10°$ of the galactic plane were also eliminated in order to avoid excessive crowding. A total coverage of 28,443 square degrees is shared between the WISE All-Sky and NVSS catalogues, with a total of 54,457 sources having point source detections of S/N > 7 in the W3 and/or W4 WISE bands within this region.

In contrast to previous works (HotDOG selection; Eisenhardt et al., 2012), and in order to remove any potential bias that might be caused by one, a MIR colour cut has not been applied in order to select RWGs. This bias stems from the fact that the observed MIR spectral shapes are complex and strongly redshift dependent. Instead included in this RWG selection are all sources that significantly lie red of the main of WISE galaxy population, defined by the WISE W1 ($3.4\,\mu$m), W2 ($4.6\,\mu$m) and W3 ($12\,\mu$m) bands: $(W2 - W3) + 1.25(W1 - W2) > 7$. These reddest sources are likely to be highly obscured and still in their peak fuelling phases, whilst the most luminous sources in the IR are likely to be radiatively efficient systems. Favouring compact radio sources still confined their hosts, a radio selection criteria is used based on the q $22\,\mu$m loudness parameter. For the rejection of radio quiet sources a criterion of $\log \mathrm{f}_{22\mu\mathrm{m}}/\mathrm{f}_{20\mathrm{cm}} < 0$ is needed, however the criteria $-1 < \log \mathrm{f}_{22\mu\mathrm{m}}/\mathrm{f}_{20\mathrm{cm}} < 0$ is applied leaving this sample to be classified as radio intermediate galaxies. This rejection of extended radio-loud systems ensured the targeting of young radio jets still confined to their hosts which was confirmed by VLA follow-up snapshots (Lonsdale et al., 2016).

Visual inspections of the selected sources in WISE and SDSS images was used to reject any artefacts, sources of a low redshift and any other mistaken sources placed in the sample. All of these selection criteria leave a total of 156 NVSS selected WISE galaxies after their application. In this chapter, and further throughout this work I will present analysis based on observations of 30 selected RWGs. These 30 sources were selected from the final subset of 156 RWGs as they were most suitably situated for southern hemisphere observations in the summer months of 2013.

Figure 4.1 demonstrates the location of my sample in WISE colour - colour space compared to a selection of 10,000 random sources taken from the WISE All-Sky catalogue. The dashed red line represents the mid-IR colour criterion ($(W2 - W3) + 1.25(W1 - W2) > 7$) used and demonstrates the ability of this criteria to select everything significantly redward of the main WISE population. In addition these sources are extremely bright in the W2 as detailed by the colour bar on the right. The criteria successfully target the reddest AGN in the mid/near IR and therefore highly obscured systems that are likely within their peak fuelling phases. The selected sources have a VLT derived redshift distribution of $z \approx 1 - 3$, as shown by the histogram in

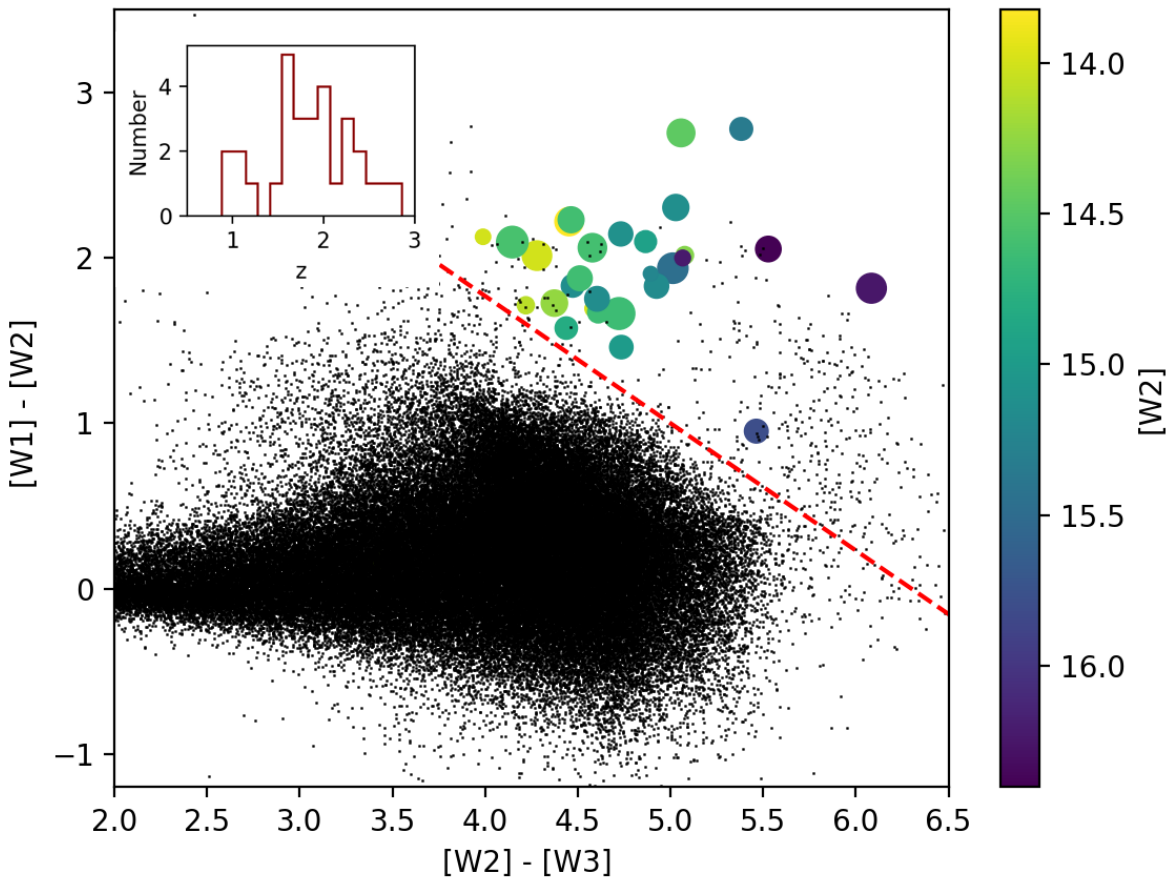

Figure 4.1: WISE W1-W2-W3 colour-colour plot (in Vega magnitudes) showing the colours of the galaxies in our sample (crosses) compared to a random selection of 10,000 galaxies taken from the WISE All-sky data release. The dashed red line demonstrates the colour selection criterion: $(W2 - W3) + 1.25(W1 - W2) > 7$. Marker size is used to represent radio loudness with increased size correlating to increased radio loudness. The marker shading represents W2 magnitude (Vega) as detailed in the colour bar on the right. The inserted histogram and the coloured markers show the redshift distribution of the final 30 galaxies discussed in this thesis.

Figure 4.1, meaning that these selected AGNs span the peak epoch of BH and galaxy formation (Zakamska et al., 2015).

Due to using an identical selection criteria, all 30 selected RWG sources are included in the larger RWG population presented in Lonsdale et al. (2015), providing redshifts and ALMA observations for these galaxies.

4.3 NIR Photometry

All 30 of the selected RWGs were observed in at least one of the J and K_s bands, by the now decommissioned ISAAC instrument. In this section I present the measured NIR flux densities in these bands alongside the results of attempting to fit SEDs to these sources.

4.3.1 Measuring J and K_s band Magnitudes

Over the nine night observation period of 11/04/2013 - 03/06/2013 the sample of 30 RWGs underwent NIR imaging in the J and K_s bands. Situated on UT3 of the VLT, ISAAC (Moorwood et al., 1998) observed 29 RWG sources in the K_s band and an additional 14 sources in the J band. Time constraints prevented imaging of all sources in both bands, however each source was observed in at least one band. The observations were taken under clear sky conditions with a mean seeing of 0.89" and a low airmass of ≤ 1.4 across all exposures. For each source a total of 6×15 s exposures were taken for each observation band. The images were read out simultaneously in four quadrants, however, as this observation period was close to the decommissioning of ISAAC on 10/12/2013, the upper left hand quadrant of the 1024×1024 pixel array failed to read out, resulting in only three quarters of a final science image. This issue was however known about at the time of observation and therefore the targeted sources were centred on the apex of the L - shaped working region of the chip, rather than centred as usual. This failed quadrant and unusual source centring can clearly be seen in Figure 4.2 with the targeted source, W1400, circled in green. The ISAAC data reduction pipelines `jitter` recipe was used in situ to reduce these images, covering dark and sky subtraction, flat fielding, the flagging of bad pixels, stacking of images and the removal of bias variations. Section 3.2.1 provides full details of this data reduction process.

Method

The aperture photometry tool provided by the Source Extractor (Bertin & Arnouts, 1996) analysis program was used to measure the J and K_s band magnitudes for all 30 of the observations

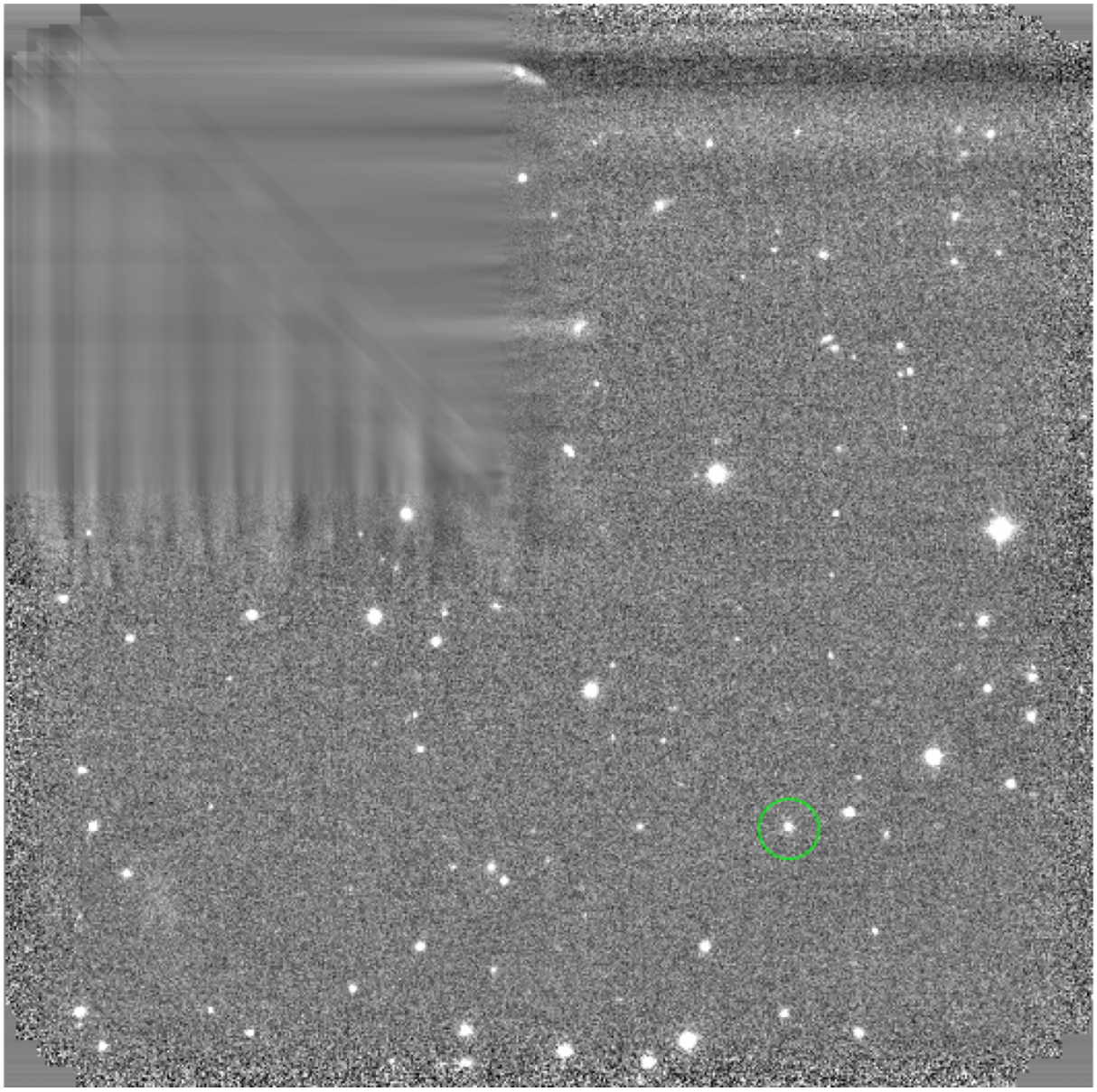

Figure 4.2: The full ISAAC J band observation of W1400 (green circled source), showing the broken quadrant and the area on which the sources were centred.

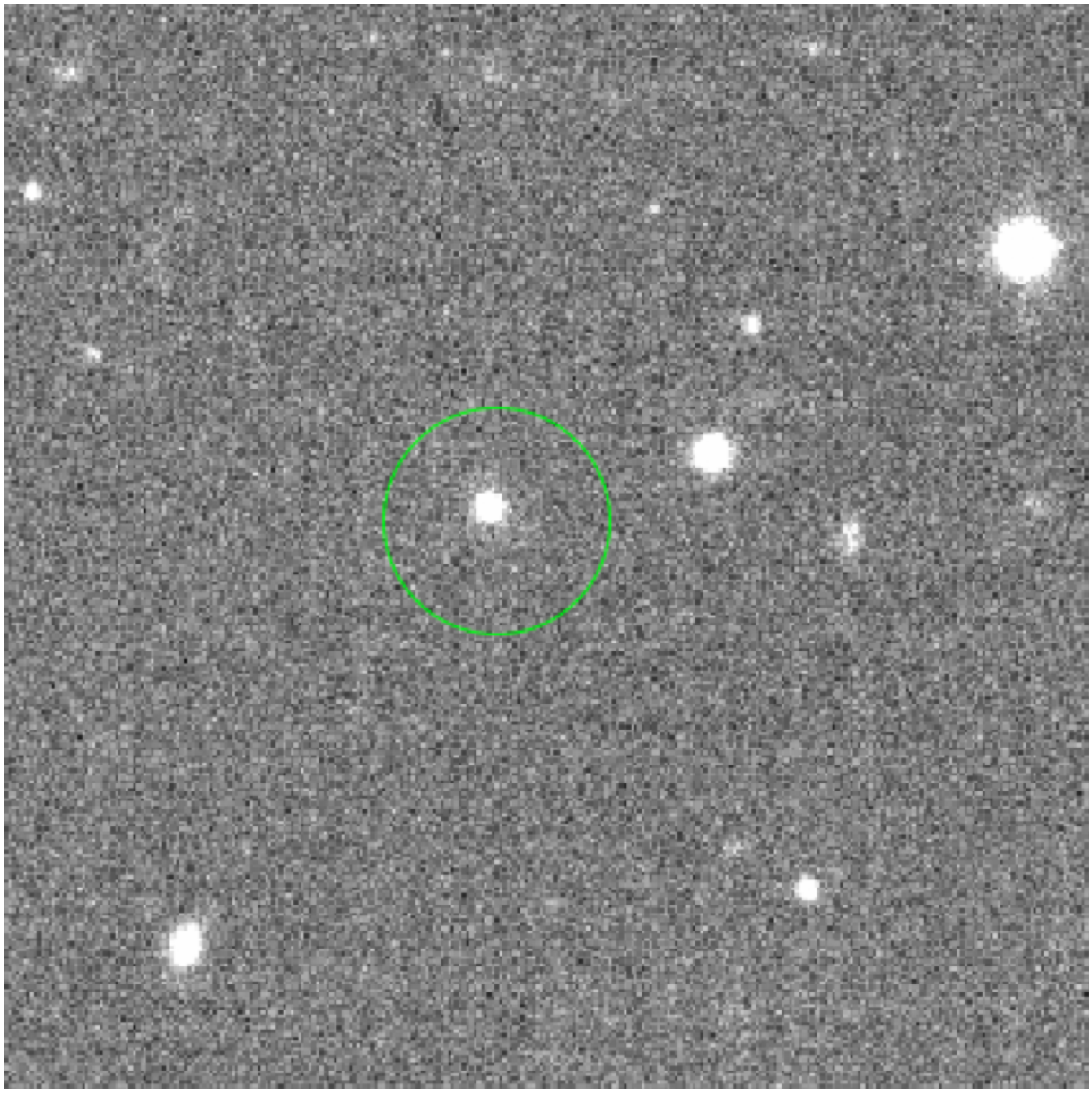

Figure 4.3: A zoomed in 300 × 300 pixel image of W1400 (circled) in the J band, showing near by sources and source morphology.

taken with ISAAC. The ISOCOR aperture was used to perform this aperture photometry process which assumes a smooth Gaussian profile in order to estimate the source flux, including that which may lie beyond the boundaries of a purely circular aperture. A comparison of the extracted source positions with the SIMBAD astronomical database (Wenger et al., 2000) allowed the individual source magnitudes to be distinguished for each of the target galaxies with a WCS correction applied for correct alignment of the field. A zero-point correction was applied to the measured fluxes by comparing a measured magnitude, to that listed for the corresponding waveband in the 2MASS catalogue (Skrutskie et al., 2006), for 10 sources in each field which were randomly selected from those with a 2MASS detection. I obtained a median zero-point value across all nine observation nights to use as the final zero-point correction for my measured magnitudes. This process was performed separately for the J and K_s bands. Figure 4.3 shows an example of J band imaging with several close by sources. In order for easy comparison with the published WISE band flux densities (Wright et al., 2010), a conversion between the measured AB magnitude and flux density of; $S_\nu(\mu\mathrm{Jy}) = 10^{\frac{23.9-\mathrm{AB}}{2.5}}$ was used.

4.3.2 SED Fitting

After computing the measured J and K_s band flux densities for each source, I compiled this data into a RWG source catalogue including measured WISE band flux densities (Wright et al., 2010) and those measured by ALMA (Lonsdale et al., 2015) and the NVSS (Condon et al., 1998). I used the Multi-wavelength Analysis of Galaxy Physical Properties code (`MAGPHYS`) (da Cunha et al., 2008) to fit SEDs for my RWGs. `MAGPHYS` is a self-contained model package used to interpret observed spectral energy distributions of galaxies in terms of galaxy-wide physical parameters including specific star formation rate, galaxy mass and dust temperature. The package outputs a model SED and its best fit parameters, providing me with an easy way to compare SED shapes as well as determining upper limits to stellar masses.

The `MAGPHYS` (da Cunha et al., 2008) works in two stages. Firstly it creates a library of SEDs at the inputted source redshift and observed filters or wavebands. These models are a combination of optical and IR spectra from 25000 stellar population and 50000 dust emission spectra and remain consistent with each other through the assumption that all the energy absorbed by dust is reradiated. Individual SED models are compiled through random selection of adjustable parameters (eg. metallicity) in order to recreate a comprehensive library of 52 SEDs.

Secondly, `MAGPHYS` compares the model flux density to those observed in the given wavebands computing the χ^2_ν value of each fit. These are then used to build likelihood distributions of SED model parameters including stellar mass, dust temperature and specific star formation rate.

Finally the best fitting (lowest χ^2_ν) SED parameters are outputted with their corresponding probability distributions.

I used the `MAGPHYS` code in this case due due the large library of IR spectra available within this model, the large range of outputted parameters, including dust temperature and gas mass, and the separate treatment of dust. Due to the selection criteria of RWGs as highly obscured sources, the inclusion of dust templates was an important factor with the aim of fitting accurate SEDs and determining stellar masses. Previous attempts by Lonsdale et al. (2015) to fit the SEDs of RWGs have been relatively unsuccessful, with the templates by Polletta et al. (2006) being the best fit. The SEDs of HotDOGs have been more successfully fitted (Wu et al., 2012) using the templates from both Polletta et al. (2006) and Polletta et al. (2007), however there are clear differences between the SED shapes of these two galaxy populations, with RWGs having a more defined MIR peak. The templates by `MAGPHYS` were therefore preferred and used in this case, in an attempt to improve upon previous works, rather than repeat.

Previous attempts of fitting SEDs to RWGs (Jones et al., 2014; Lonsdale et al., 2015) have been mixed, with the Polletta et al. (2007) template currently being the best fit. I expected the use of additional data points to help fit a consistent SED shape of a steep red IR power law, mid-IR peak and flatter mid-IR to sub mm that has previously shown to be the typical SED shape of RWGs (Lonsdale et al., 2015). However, an attempt to model the SEDs of RWGs by fitting a suite of various SED templates from the `MAGPHYS` library produced mixed results with some data sets fitted more successfully than others. As expected the SEDs for all targets display a similar shape but are on the whole poorly fitted by the available suite of models and do not necessarily show that expected RWG SED shape, with additional AGN templates needed in the future. This fact is however unsurprising given that previous focused works have also struggled.

Given the library of models used produced these poor SED fits, any parameter values obtained through these fits should be taken with caution. When using a catalogue containing just the measured ISAAC and WISE W1, 2, 3 and 4 band fluxes, the fitted stellar mass parameters for these galaxies range from $10^{11} - 10^{15} M_\odot$. Inclusion of the measured Lonsdale et al. (2015) ALMA 870μm flux densities produced a narrower range of stellar masses ($10^{11} - 10^{13} M_\odot$) with improved SED fitting based on χ^2_ν values. However, including the NVSS 1.4-GHz flux densities made the fits significantly worse (again based on χ^2_ν value) due to forcing enhanced radio emission.

One of the better fitting SEDs is shown in Figure 4.4. With a $\chi^2_\nu = 1.062$, this is the best fitting SED of all 30 sources, with only four SEDs possessing a fit with a value of $\chi^2_\nu < 2$. With only the K_s band ISAAC flux density to fit, in this case fewer data points and parameters may have led to a more acceptably fitting template, especially since including the NVSS fluxes

significantly worsened my fits. This however can not be proven, as out of the four sources measuring SED fits of $\chi^2_\nu < 2$, two sources have only K_s band fluxes, whilst the other two have J band fluxes also. Comparing the 17 sources only observed in one waveband, they have a mean SED fit χ^2_ν value of $\chi^2_\nu \sim 6.52$ in comparison to a mean $\chi^2_\nu \sim 6.17$ for those sources with both.

Whilst Figure 4.4 shows the best of the SED fits, the vast majority are poorly fit. This poor SED fitting, due to the limited range of available SED templates, is exacerbated for those sources that are dominated by AGN emission and exhibit broad line emission as there is a lack of suitable components in the `MAGPHYS` SED templates suite. With the model SED templates dominated by star formation there is a lack of AGN contribution at $\sim 3 - 10\,\mu$m with the most notable difference in Figure 4.4 in the W2 waveband. This difference is emphasised for the other sources, with the observed J, K_s, W1 and W2 wavebands lying above the fitted model, with the observed data points lying in a continuous AGN dominated curve. This lack of AGN emission has therefore added increased uncertainty to my stellar mass estimates for these specific sources, with the resulting stellar masses calculated for all sources taken as upper limits only due to their uncertainties.

4.3.3 NIR Photometry Results

Table 4.1 gives the zero-point corrected ISAAC band flux densities measured in the J and K_s bands. Also included in this table are the WISE W1, 2, 3 and 4 and ALMA flux densities (Lonsdale et al., 2015) used to assist in my SED fitting. Due to the lack of well-fitting IR SED templates for the sources in my RWG sample, χ^2_ν values are provided in the final column as a guide to the uncertainties in the stellar mass estimates also presented in Table 4.1. The AGN sources with detected broad lines have their stellar mass values asterisked in order to distinguish them, as in these cases the stellar masses calculated are likely overestimates of the true values. They are however still a useful indicator of what I can expect the true values of the stellar masses to be.

Comparing my measured ISAAC flux densities to the WISE band flux densities shows agreement with the expected RWG SED shape across the IR, however whilst this provides confidence that my measured flux densities values are correct, it does not do the same for my SED fits and their resulting stellar masses. With a mean $\chi^2_\nu = 2.40 - 10.34$ all stellar mass values should be taken as upper limit indicators rather than exact measurements.

Whilst there are only currently poor fitting SED templates for RWGs, the measured ISAAC J and K_s band fluxes for 14 and 29 sources respectively will greatly help to improve any future attempts at SED fitting by providing extra data points in the NIR. This will help to determine

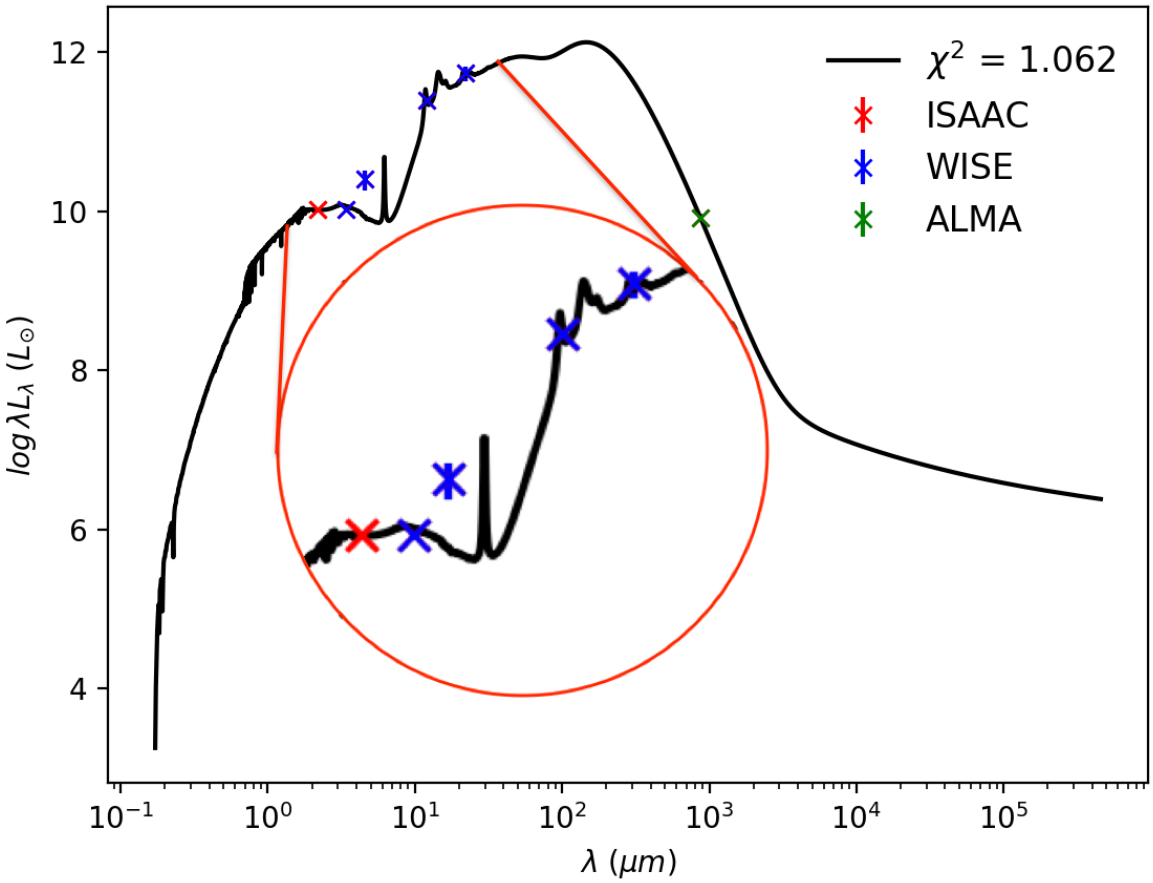

Figure 4.4: The resulting best fit SED from MAGPHYS, fitting the K_s, W1, W2, W3, W4 and ALMA flux densities of W0714.

whether the expected SED shape of steep red IR power law, mid-IR peak and flatter mid-IR to sub mm, is true for a larger sample of RWGs.

4.3.4 Summary of NIR Photometry

Using the NIR photometry from the ISAAC imager on the VLT, I measured the J and K_S band magnitudes for 14 and 29 sources respectively and find that they align with the previously measured WISE band fluxes; W1, W2, W3 and W4. I used these six different waveband magnitudes, in addition to the ALMA fluxes measured by (Lonsdale et al., 2015) to measure the stellar mass of my sources through SED parameter fitting. I measure $\log\left(\frac{\mathrm{M}_*}{\mathrm{M}_\odot}\right) = 9.97$ - 11.99, but due to the lack of well fitting SED templates for RWGs these masses should be only taken as an upper limits with χ^2_ν values provided as a guide to the reliability of my stellar masses. These upper limits may additionally be generous due to the fitted AGN emission assumed to be starlight, therefore causing greater overestimates of the stellar masses.

Table 4.1: The VLT determined redshift of each source along with calculated ISAAC J and K_s band flux densities. Also included are the W1 (3.4 μm), W2 (4.6 μm), W3 (12 μm) and W4 (22 μm) WISE bands and ALMA (870 μm) flux densities (Lonsdale et al., 2015). Stellar masses are determined by `MAGPHYS` SED fitting (see above for details) with χ^2_ν values from the SED fitting provided as a guide to the uncertainties in the stellar masses. Note: Asterisked source names were only observed by ISAAC and not by X-shooter. Asterisked redshifts of 2.00 are the redshifts assumed where no spectroscopic redshift was available. Asterisked stellar mass values are likely overestimates of the true masses due these sources exhibiting broad line emission which is not suitably covered in the SED templates used.

WISE designation	z	$f_{\rm J}$ (μJy)	$f_{\rm Ks}$ (μJy)	$f_{\rm W1}$ (mJy)	$f_{\rm W2}$ (mJy)	$f_{\rm W3}$ (mJy)	$f_{\rm W4}$ (mJy)	$f_{\rm ALMA\,870\,\mu m}$ (mJy)	log M$_*$ (M$_\odot$)	χ^2_ν
J071433.54−363552*	0.88	-	7.64 ± 0.44	< 0.012	0.039 ± 0.011	0.99 ± 0.12	4.01 ± 0.84	2.4 ± 0.3	9.97	1.06
J071912.58−334944	1.63	-	12.0 ± 0.67	< 0.011	0.081 ± 0.012	1.93 ± 0.12	4.06 ± 0.88	5.2 ± 0.6	10.83	4.28
J081131.61−222522	1.11	-	24.4 ± 1.42	0.132 ± 0.0086	0.611 ± 0.023	5.62 ± 0.17	7.61 ± 1.17	< 1.8	10.90*	9.71
J082311.24−062408	1.75	-	13.9 ± 0.49	0.118 ± 0.0078	0.441 ± 0.019	4.08 ± 0.15	10.42 ± 0.97	< 1.8	11.07*	16.8
J130817.00−344754	1.65	19.1 ± 0.19	20.1 ± 0.37	0.086 ± 0.0056	0.248 ± 0.013	3.36 ± 0.12	9.12 ± 0.73	1.38 ± 0.34	10.66*	10.0
J134331.37−113609	2.49	-	21.1 ± 2.03	0.024 ± 0.0057	0.136 ± 0.013	1.61 ± 0.12	3.81 ± 0.79	2.34 ± 0.31	11.24*	4.09
J140050.13−291924	1.67	36.5 ± 0.19	57.4 ± 0.45	0.110 ± 0.0063	0.501 ± 0.018	5.58 ± 0.14	11.85 ± 0.77	< 0.90	11.02*	9.50
J141243.15−202011	1.82	11.2 ± 0.17	34.5 ± 0.41	0.092 ± 0.0063	0.333 ± 0.015	3.39 ± 0.13	7.41 ± 0.78	2.55 ± 0.63	11.57*	9.30
J143419.59−023543	1.92	-	18.2 ± 0.39	0.058 ± 0.0056	0.257 ± 0.014	2.13 ± 0.11	5.04 ± 0.71	< 0.9	11.21*	10.7
J143931.76−372523	1.19	-	34.3 ± 0.42	0.027 ± 0.0071	0.115 ± 0.013	2.34 ± 0.12	3.92 ± 0.83	< 0.6	10.24*	2.77
J150048.73−064939	1.50	11.1 ± 0.16	22.6 ± 0.49	0.068 ± 0.0065	0.293 ± 0.016	6.26 ± 0.17	15.77 ± 0.94	6.11 ± 0.28	11.12*	5.91
J151003.71−220311	0.95	11.7 ± 0.16	37.1 ± 1.57	0.143 ± 0.0095	0.411 ± 0.020	5.34 ± 0.18	14.87 ± 1.09	< 0.9	10.54*	7.09
J151310.42−221004	2.20	9.03 ± 0.13	27.8 ± 0.46	0.037 ± 0.0082	0.214 ± 0.018	2.64 ± 0.16	9.71 ± 1.10	4.86 ± 0.27	11.74*	4.97
J151424.12−341100	1.09	12.2 ± 0.15	26.6 ± 0.43	0.076 ± 0.0091	0.184 ± 0.019	3.21 ± 0.16	7.01 ± 1.03	< 0.9	10.53	1.51
J152116.59+001755	2.63	-	18.8 ± 0.43	0.039 ± 0.0046	0.274 ± 0.014	5.51 ± 0.15	9.51 ± 0.70	1.19 ± 0.28	11.64	12.4
J154141.64−114409	1.58	-	12.4 ± 0.41	0.032 ± 0.0077	0.155 ± 0.017	2.91 ± 0.16	10.74 ± 1.14	1.2 ± 0.3	10.89*	2.68

J163426.87−172139	2.08	4.26 ± 0.15	-	0.039 ± 0.0094	0.101 ± 0.018	1.70 ± 0.17	3.57 ± 1.15	< 0.84	11.08*	2.17
J164107.22−054827	1.84	-	25.2 ± 0.44	0.086 ± 0.0083	0.423 ± 0.020	3.14 ± 0.15	6.26 ± 0.89	2.3 ± 0.29	11.29	12.7
J165305.40−010230	2.02	-	21.3 ± 0.53	0.083 ± 0.0074	0.191 ± 0.015	2.56 ± 0.14	5.31 ± 0.93	< 0.78	10.92	7.88
J165742.88−174049*	2.00*	-	22.2 ± 0.49	0.073 ± 0.0102	0.186 ± 0.026	2.82 ± 0.24	8.60 ± 1.01	< 0.78	10.86	3.06
J170204.65−081108	2.82	-	8.13 ± 0.37	0.021 ± 0.0690	0.074 ± 0.053	3.05 ± 0.26	12.32 ± 1.40	< 1.02	11.23*	2.84
J170325.05−051742	1.80	3.61 ± 0.15	8.94 ± 0.45	0.021 ± 0.0082	0.199 ± 0.018	2.35 ± 0.24	11.66 ± 1.42	1.02 ± 0.27	10.76	3.14
J170746.08−093916*	2.00*	11.4 ± 0.18	52.4 ± 0.53	0.119 ± 0.0073	0.342 ± 0.020	3.46 ± 0.28	3.27 ± 1.26	< 1.02	11.99	5.45
J193622.58−335420	2.24	7.93 ± 0.17	14.7 ± 0.45	0.031 ± 0.0069	0.127 ± 0.016	2.34 ± 0.14	5.27 ± 0.96	1.86 ± 0.36	10.95	5.11
J195141.22−042024	1.58	-	24.1 ± 0.58	0.030 ± 0.0178	0.065 ± 0.036	2.55 ± 0.15	8.56 ± 1.02	< 1.03	11.42*	1.60
J195801.72−074609	1.80	5.66 ± 0.17	16.1 ± 0.44	0.056 ± 0.0086	0.203 ± 0.018	3.29 ± 0.16	7.44 ± 1.06	< 0.93	11.01*	7.82
J200048.58−280251	2.28	-	12.9 ± 0.45	0.027 ± 0.0169	0.113 ± 0.017	3.21 ± 0.17	7.19 ± 1.20	< 0.96	10.81	7.14
J202148.06−261159	2.44	1.09 ± 0.12	6.89 ± 0.50	<0.015	<0.065	10.3 ± 0.15	6.27 ± 1.01	4.4 ± 0.38	11.52	1.35
J204049.51−390400	2.00*	1.84 ± 0.16	9.56 ± 0.57	0.070 ± 0.0077	0.254 ± 0.017	2.75 ± 0.15	4.02 ± 0.91	5.1 ± 0.43	12.14	8.95
J205946.93−354134	2.38	-	18.8 ± 0.55	0.052 ± 0.0069	0.182 ± 0.0015	2.94 ± 0.014	4.74 ± 0.99	< 0.99	11.04	8.98

4.4 NIR Spectroscopy

The previous section focused on the NIR ISAAC imaging of all 30 selected RWGs and the information that could be learnt from them. The rest of this Chapter however, will solely focus on the 27 sources that were observed with X-Shooter, with the following section discussing the results from three NIR emission lines observed with X-shooter spectroscopy. In comparison to the two data points provided for each source by the ISAAC imaging, X-Shooter spectroscopy provides information across a full wavelength range of 300 - 2480 nm.

Across a consecutive three night period from 13/08/13, 27 of the selected RWGs were observed with the X-shooter instrument (Vernet et al., 2011), situated on UT2 of the VLT. Observations were simultaneously performed across its three wavelength arms; UVB, VIS, NIR, at slit widths $1.6''$, $1.5''$ and $1.2''$ respectively, covering a full wavelength range of 300 - 2400 nm. In cases of clear ISAAC imaging, this was used to additionally assist in correct slit placement and which was later confirmed by test guider observations. Nodding mode with an ABBA nod sequence was used to observe my sources with a maximum distance of $5''$ between nodding positions. Despite simultaneous observations the total integration time of each arm slightly varied from 2×600 s for the NIR arm, to 2×400 s for UVB and 2×520 s for the VIS arm. All observations were performed across excellent seeing ranging between $0.67'' - 1.5''$ across the three nights, and at a low air mass value (≤ 1.16). For telluric and relative flux calibration, a standard star (either LTT3218 or Feige110) was observed after each science observation.

This data was again reduced in situ using the X-shooter reflex pipeline, (see section 3.2.2 for more details) providing 1 + 2D spectra for each of the 27 sources observed for the three separate wavelength arms. The UVB, VIS and NIR arms span the wavelength ranges of 300 - 559.5 nm, 559.5 - 1024 nm and 1024 - 2480 nm respectively with the 2D spectra spanning $15''$ in the spatial direction.

The aim of the rest of this chapter is to use the 1D NIR X-shooter spectra to determine four estimates of the BH and host galaxy masses of my selected RWGs. With 27 targets observed with X-shooter I use 1D spectroscopy from the NIR arm to calculate the black hole and host galaxy masses of these sources using either the Balmer line luminosities and widths, or through using the [OIII]λ5007 line as a proxy for the bolometric luminosity and the luminosity at 1350 Å. This chapter therefore mainly makes use of the NIR spectral arm (with the addition of the CIV emission line FWHM), but with 1920.5 nm of spectral information left, I return to the other two spectral arms Chapter 6.

4.4.1 Spectral Properties

As this chapter purely focuses on determining the BH and host galaxy masses of the RWGs, here I discuss the spectral properties of the NIR emission lines that I have used to determine these masses. Using three independent methods to derive the BH masses requires the measurement of the spectral properties of the [OIII]λ5007, Hα, Hβ and CIV emission lines. With my selected RWGs lying in a redshift range of $z \sim 1 - 3$, the observed wavelengths of the for [OIII]λ5007, Hα and Hβ emission lines are situated in the NIR arm of X-shooter with the CIV emission line present in the VIS arm. The sections below detail the fitting procedures of my three detected NIR emission lines, with the properties of the CIV emission lines discussed in Section 4.6.

Detection of NIR Emission Lines

Out of the 30 RWGs in the source sample 27 were observed with the three spectroscopic arms of X-shooter, but only 18 of these sources had detections of at least one emission line with of 15 [OIII]λ5007, 13 Hα and six Hβ emission line detections. There are several possible reasons for the nine sources with no detections including a misplaced slit leading to a missed target or the targeted emission lines falling in regions of strong sky absorption. It is however extremely unlikely that the sources were not correctly observed due to use of the ISAAC imaging to confirm the position. Additionally as there were no overlapping sky lines at the missing wavelength it is more likely that the emission lines were present but heavily extinguished by dust and therefore became indistinguishable from the underlying continuum in the spectrum.

Of these nine sources with no observed [OIII]λ5007 or Balmer lines (Hα and Hβ), five had no IR continuum that could be observed in the NIR spectra. In comparison to all other sources, these were only observed by ISAAC in the K_s band which may have affected the amount and/or quality of the positional information available for targeting. There was however measurable continuum in the remaining four sources with none of these emission lines detected, implying that in this case it is highly unlikely that the slit was misplaced and that the targets were successfully observed. For two of these four sources the detected continuum appeared to be relatively weak in comparison to those sources with successful detections. The remaining two of these four sources had equally strong continuum to those sources with detections, with continuum fluxes that agreed within error to the measured fluxes in the ISAAC photometry. For these four sources it therefore seems more likely that the emission lines were too faint to be distinguished from the underlying continuum as they did not lie in regions of strong sky absorption.

Whilst it is not entirely certain why nine of the sources had no detected [OIII]λ5007, Hα, Hβ emission lines, I will revisit these sources with non-detections in Chapter 6 in the search for

additional emission lines. Below I will present 18 measurements of BH and host galaxy masses which are vital in the understanding of this unique population of RWGs.

Spectral Fitting Method

The 18 sources discussed in the remainder of this chapter have a minimum of one detection of the Hα, Hβ or [OIII]λ5007 emission lines present in the NIR 1D spectra and a possible detection of CIV in the VIS spectra (see Section 4.6). This section will detail the fitting process used to measure the fluxes and FWHM of these NIR emission lines. Firstly, before any spectral fitting was performed, the Image Reduction and Analysis Facility (IRAF, Tody, 1986) `dopcor` package was used to convert the spectra from observed to rest wavelength, in order to make make it easier to search for the same emission lines in sources at different redshifts.

In addition to the Doppler correction, an additional continuum subtraction was applied across the wavelength range of each fitted emission line. Whilst an initial continuum subtraction was applied by the X-shooter pipeline, there was still a noticeable continuum across the wavelength range of some of my detected emission lines. A simple correction was applied by fitting a straight line to the continuum across the emission line profile and then subtracting this continuum fit from the data. The straight line was fitted between two data points either side of the emission, taken as the mean of the first and last ten data points in the fitted emission lines wavelength range, with the `astropy` linear least squares fitter used (The Astropy Collaboration et al., 2018). This range was chosen in order to make sure that no part of the detected emission line profile was subtracted as the continuum fit. The raw data for each emission line was also binned, reducing each ten data points to their median value, in order to reduce the noise present in the spectra and improve the SNR. Whilst this could introduce some bias in the flux determinations, the emission lines were broad, and taking the median allowed the elimination of any extreme noise. Figure 4.5 gives an example of this correction being applied, showing a straight line fitted to my binned data.

In addition to the 1D spectra, X-shooter produces 2D spectra. Figure 4.6 shows an example of this for W1400 in the wavelength range of Hα. Therefore as well as performing a continuum subtraction, the 2D spectra was checked for features before model fitting was undertaken. Using the 2D spectra to assist in fitting, allowed me to confirm the presence of the emission lines in the cases that they appeared blended in the 1D spectra. It also allowed for confidence in the emission lines detected in the 1D spectra with the high levels of noise.

In addition to binning the spectra, in order to reduce the noise present, a σ noise clip was applied to the data. This masked out any data point that was more then 3σ away from a central

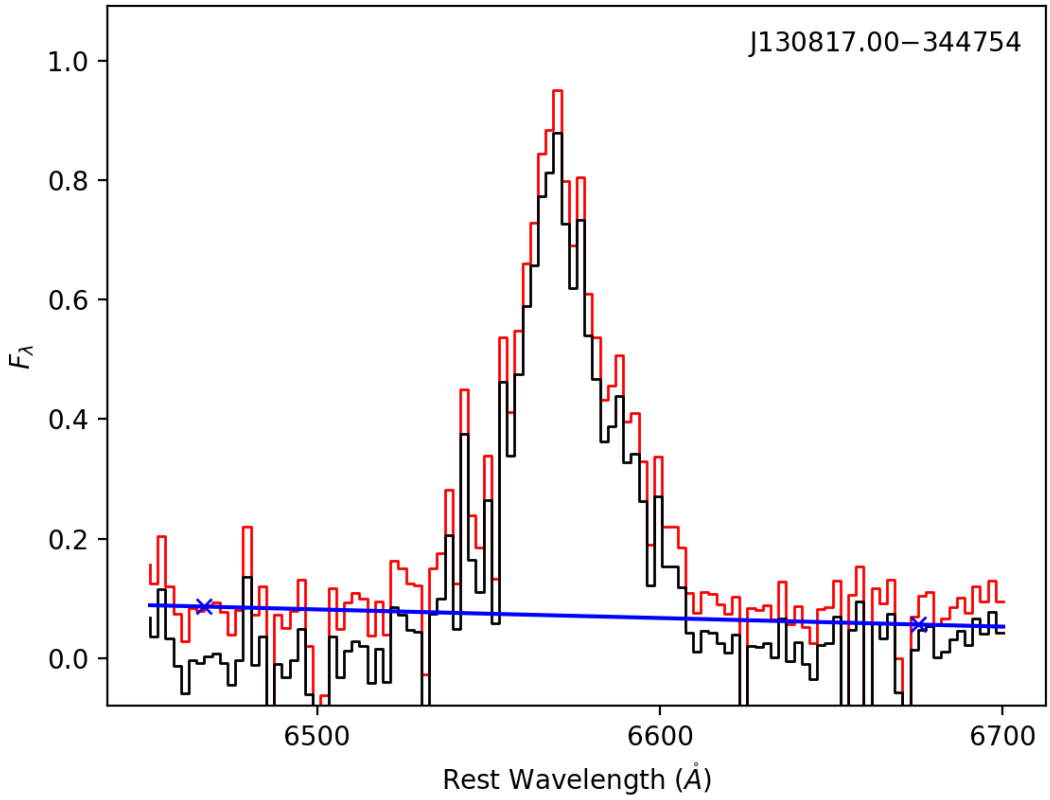

Figure 4.5: The continuum correction applied to the Hα profile of W0823. The blue line shows the continuum model subtracted with the two X's showing the data points the model was fitted to. The red profile is before subtraction and the black profile shows after subtraction.

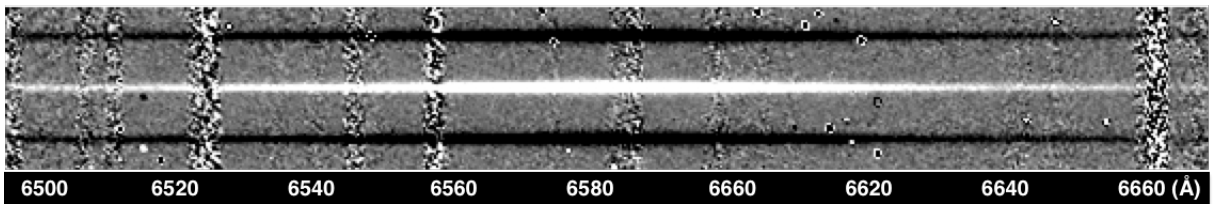

Figure 4.6: The 2D spectra of W1400 in the wavelength region surrounding the Hα emission line.

value, defined as the mean of nearby data points. This was preformed using *astropy.sigma$_c$lip* (The Astropy Collaboration et al., 2018), such that any data points dominated by noise and substantially offset from those nearby would be ignored when attempting to fit the emission lines.These clipped data points have also been masked in Figure 4.9 appearing as gap in the spectra.

To obtain the basic properties of the individual emission lines I followed the procedures outlined in Greene & Ho (2005) in order to fit multi-Gaussian models to the emission line spectra again using `astropy` (The Astropy Collaboration et al., 2018). A multi-Gaussian approach for these lines was required due to their asymmetric nature, allowing both the broad and narrow components to be individually fitted. This asymmetry is most noticeable for the Hα emission lines of J130817.00−344754, J150048.73−064839 and J195141.22−042024. As the focus here is to determine the BH and host galaxy masses, a full investigation into the asymmetric nature of these detected emission lines is given in Section 6.6.

An independent multi Gaussian model was fitted to the Hα emission line, whilst the Hβ line was fitted as a compound model with the [OIII]$\lambda\lambda 4959, 5007$ doublet due to their wavelength proximity. At a wavelength of $\lambda = 6562$ Å, and the resolution of X-shooter, a broad Hα profile encompasses the [NII]$\lambda\lambda 6548, 6563$ doublet completely hiding the [NII]$\lambda\lambda 6548, 6563$ peaks. Whilst other works (Kim et al., 2013) have used a correction factor of [NII]/H$\alpha = 0.83 \pm 0.42$ derived from SDSS selected quasars, I assume the Hα line to be the dominant profile in both the fluxes and FWHMs measured. As a test on this assumption an attempt to fit the [NII]$\lambda\lambda 6548, 6563$ for several sources was undertaken. However, due to the broadness of Hα profile, subtracting the fitted [NII]$\lambda\lambda 6548, 6563$ doublet increased uncertainty yet made a negligible correction to the Hα flux. I was therefore confident in assuming Hα is the dominant profile. As each detection of the Hα emission was modelled by multiple Gaussians these were co-added together to create the final model fit.

To create the compound model for the Hβ and [OIII]$\lambda\lambda 4959, 5007$ emission lines, I used multiple Gaussians to model each individual profile and then added them, fixing the wavelength spacing between each model fit to the known wavelength different between the lines. In addition to fixing the wavelength difference between the doublet models, the FWHMs of both the doublet peaks were fixed to be equal with the peak ratio of [OIII]$\lambda 5007$ to [OIII]$\lambda 4959$ constrained to 2.88 (Kim et al., 2013). The addition of the [OIII]$\lambda 4959$ emission line to my compound model was both helpful in applying a systematic check to the fit of the [OIII]$\lambda 5007$ model, but also helped to distinguish the emission line from underlying noise in some cases. Whilst the Hβ and [OIII]$\lambda\lambda 4959, 5007$ models were combined as a compound model, the measured spectral properties

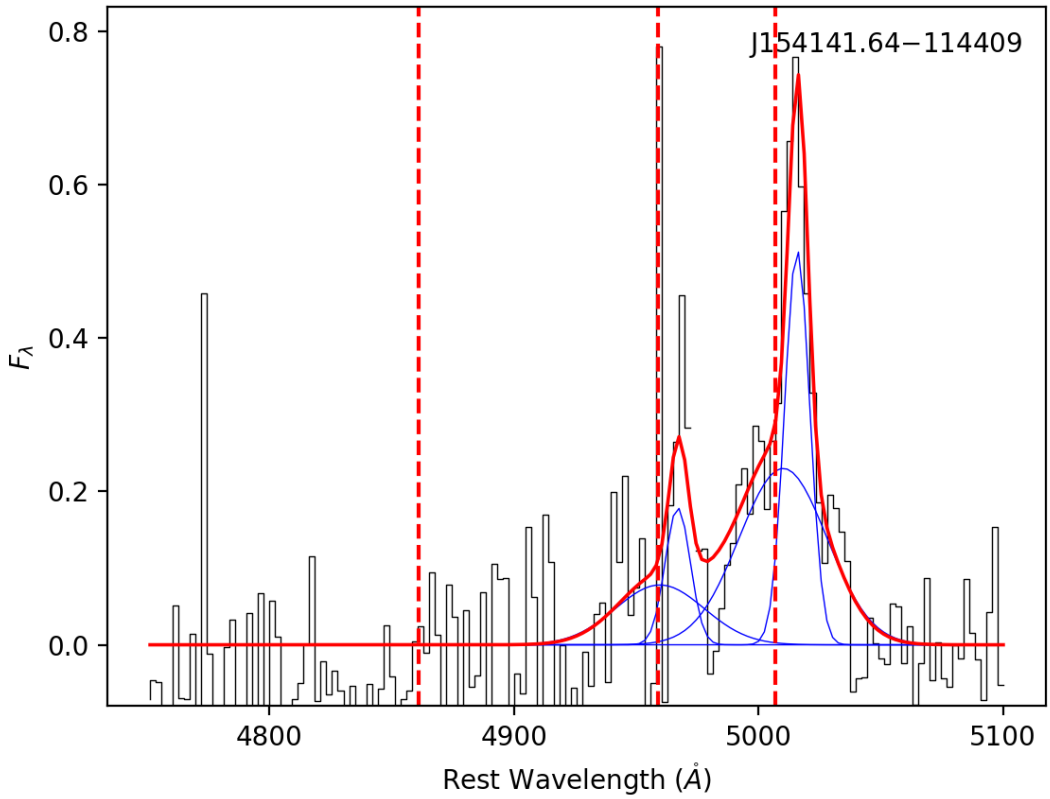

Figure 4.7: The multiple Gaussians (blue) used to create the compound model fit (red) of W1541 in the region surrounding Hβ and [OIII]$\lambda\lambda$4959, 5007. Dashed red lines show the rest wavelengths of the Hβ and [OIII]$\lambda\lambda$4959, 5007 emission lines.

of each line were taken from the individual fits.

Again following previous work (eg. Greene & Ho, 2005; Assef et al., 2011; Jun et al., 2017; Wu et al., 2018; Jun et al., 2020), a minimum number of Gaussians were used to create the final emission line models, with each Gaussian allowed to vary under the constraints outlined above. This multiple Gaussian fitting was done by limiting the width and amplitude of each Gaussian used to fit the individual model features, before they were all combined into a final line and then compound model. A χ^2_ν analysis was performed after each additional Gaussian component was added, with more Gaussians added until the best and optimal fit was achieved. In this case an optimal fit is defined by a low χ^2_ν value ($\chi^2_\nu \sim 1$). This ensured the simplest fit possible as I stopped increasing the number of components when a poorer χ^2_ν fit was generated. A mean of ~ 2 components were used to fit the Hα emission lines with ~ 1 component fitted to Hβ and ~ 3 for [OIII]λ5007. Figure 4.7 demonstrates the multi Gaussian fits used for the compound model of the [OIII]$\lambda\lambda$4959, 5007 lines of W1541.

These multi Gaussian models are used to ensure the most reliable fits possible whilst taking

into account the asymmetric nature of the emission lines. With as many Gaussains as needed used to fit the spectra, the presented fits are the best possible. However not all these fits have values $\chi^2_\nu \sim 1$. With a mean value of $\chi^2_\nu = 1.4$ the [OIII]λ5007 emission line models are the most successfully fitted with the Hβ lines the worst (χ^2_ν ~2.3) due to the larger amounts of noise. However I am confident in the reliability in my model fitting with errors calculated to show the possible range of measurements.

With the multi-Gaussian model fitting dependant on the χ^2_ν values in order to gain the most reliable fit it was important to make sure that the noise was well modelled. Initial steps were taken to increase the SNR of the spectra including binning the 1D data to reduce the scatter. The sigma clip was then applied to remove any remaining outliers, likely due to a cosmic ray hitting the detector that were not cleaned. The remaining noise in the spectra was included in the model fitting, with errors on each flux value provided in an extension to the fits file. However, most noticeable is the increase in spectral noise near the end of an arms wavelength range. Through these data reductions steps and the handling of the spectral errors (described below) 'i am confident that all sources of noise were considered and that the remaining noise in the spectra does not dominate my measured fluxes.

To compute the errors on the flux and line widths measured from my multi Gaussian model fits, I adopted a Monte-Carlo approach (Assef et al., 2011, 2015; Wu et al., 2018). Taking the pipeline given spectral errors from the second extension of the 1D spectra fits file, I simulated 10000 random spectra for each source, allowing the flux at each wavelength point to take a random value within the spectral errors. These simulated spectra where then fitted with the final multi Gaussian models, producing a normal like distribution of measured FWHMs and line fluxes. The standard deviation of the 10000 values were taken as the errors on my measured spectral properties. Figure 4.8 shows the distribution of the measured values for the Hα emission line of W1400. W1400 is shown as an example here as it has a clear line detection but also noticeable asymmetry in the Hα emission line. It therefore should be a good representation of the possible flux and FWHM error distribution. The distributions shown in Figure 4.8 are narrow, with the small flux distribution likely due to the clear line detection. This distribution is broader for those sources with higher levels of noise as shown by the errors given in Table 4.2.

Spectral Fitting Results

Covering the wavelength ranges of 4800 - 5500 Å and 6500 - 6750 Å Figure 4.9 shows the fitted models for the 18 sources with at least one of the Hα, Hβ or [OIII]λ5007 emission lines detected. The red multiple Gaussian models are fitted to the black binned spectra with vertical lines

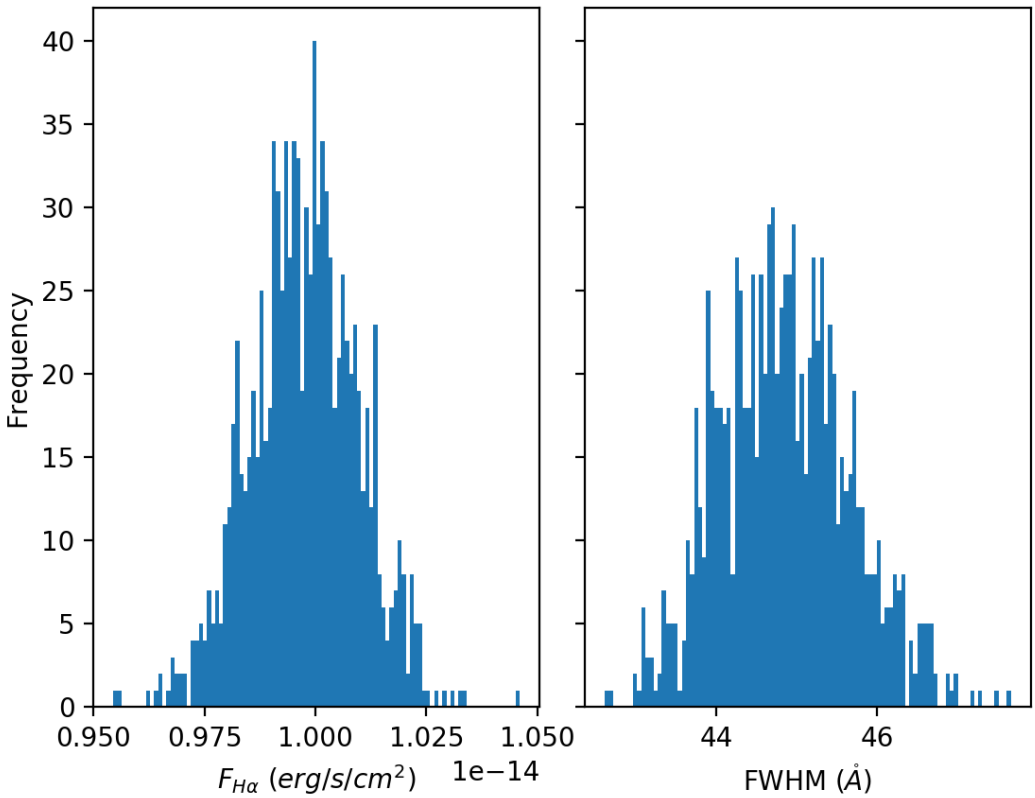

Figure 4.8: The distribution of the measured fluxes and FWHMs for the 10000 stimulated spectra of the Hα profile of W1400.

added at the rest wavelengths of the emission lines I targeted, showing which sources had which emission lines detected. Out of the 18 sources with at least one NIR emission line detected; 13 had detected Hα lines, six had detected Hβ lines and 15 had detected [OIII]λ5007 lines with the exact breakdown provided by Table 4.2. The spectra for the nine sources with none of these emission lines detected are shown in 4.10.

The emission line fluxes and FWHM derived from the multi Gaussian models are given in Table 4.2 and are later used to calculate the BH and host galaxy masses of these 18 sources. Each of these 18 sources has been labelled with a source ID as a shorthand for the source names used in figures presented later in this chapter. A full discussion of detected emission lines is presented in Section 6.2, with additional detections of CIV emission lines discussed later in Section 4.6.

Before moving on to the BH mass calculations, I first discuss the the differences between the number of detections for each emission line, with 15 detections of the [OIII]λ5007 line, 13 detections of the Hα line and only six detections of the Hβ line. The X-shooter arm used is likely to be a factor in the number of lines detected, though in this case all three lines were detected by the NIR arm. There is however a correlation between a higher number of detections for the most luminous emission lines. The mean luminosity of the Hα emission lines is $\sim 3.6\times$ greater than that for Hβ, corresponding to over twice as many detections. With comparable mean luminosities of $\sim 10^{43.60}\,\mathrm{erg\,s^{-1}}$ and $\sim 10^{43.68}\,\mathrm{erg\,s^{-1}}$, there are 15 emission line detections of [OIII]λ5007 and 13 detections of Hα.

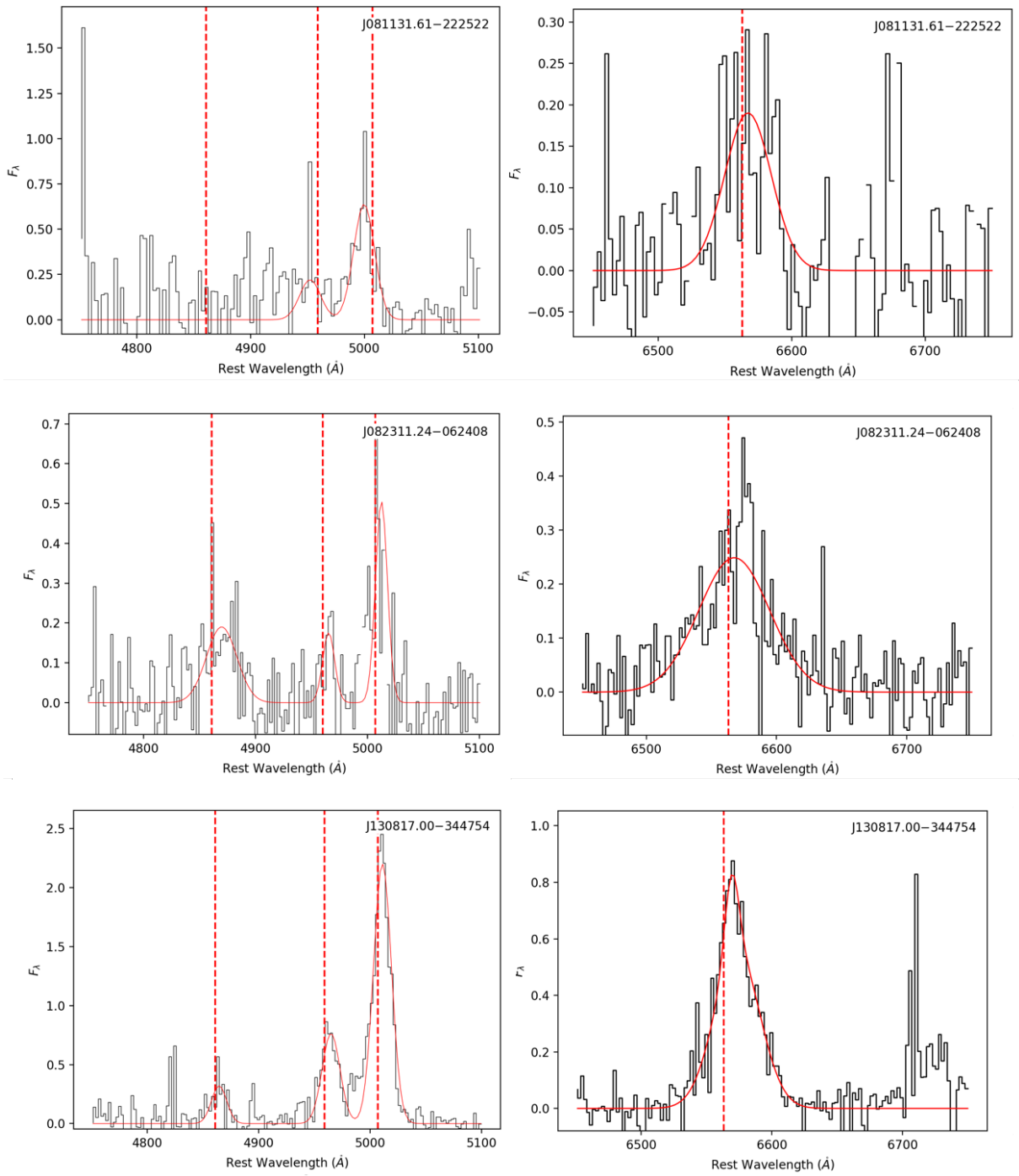

Figure 4.9: Rest frame X-shooter spectra in the region surrounding Hβ, [OIII]$\lambda\lambda$4959, 5007 and Hα. Flux densities are in the units 10^{-16} erg s^{-1}cm^{-2}Å^{-1}. Reduced spectra and fitted model are represented by black histogram and red lines respectively. For Hβ and [OIII]$\lambda\lambda$4959, 5007 spectra the red line represents a combined model of the multi-Gaussian model fitted to each individual peak. For the Hα spectra the red line also represents a multi-Gaussian model fitted to the blended Hα and [NII]$\lambda\lambda$6548, 6563 profile. Vertical dashed red lines indicate the rest frame wavelengths of the Hβ, [OIII]$\lambda\lambda$4959, 5007 and Hα emission lines based on the redshifts from Lonsdale et al. (2015). Note that the redshift of W1702 was too high for the Hα line to be observed.

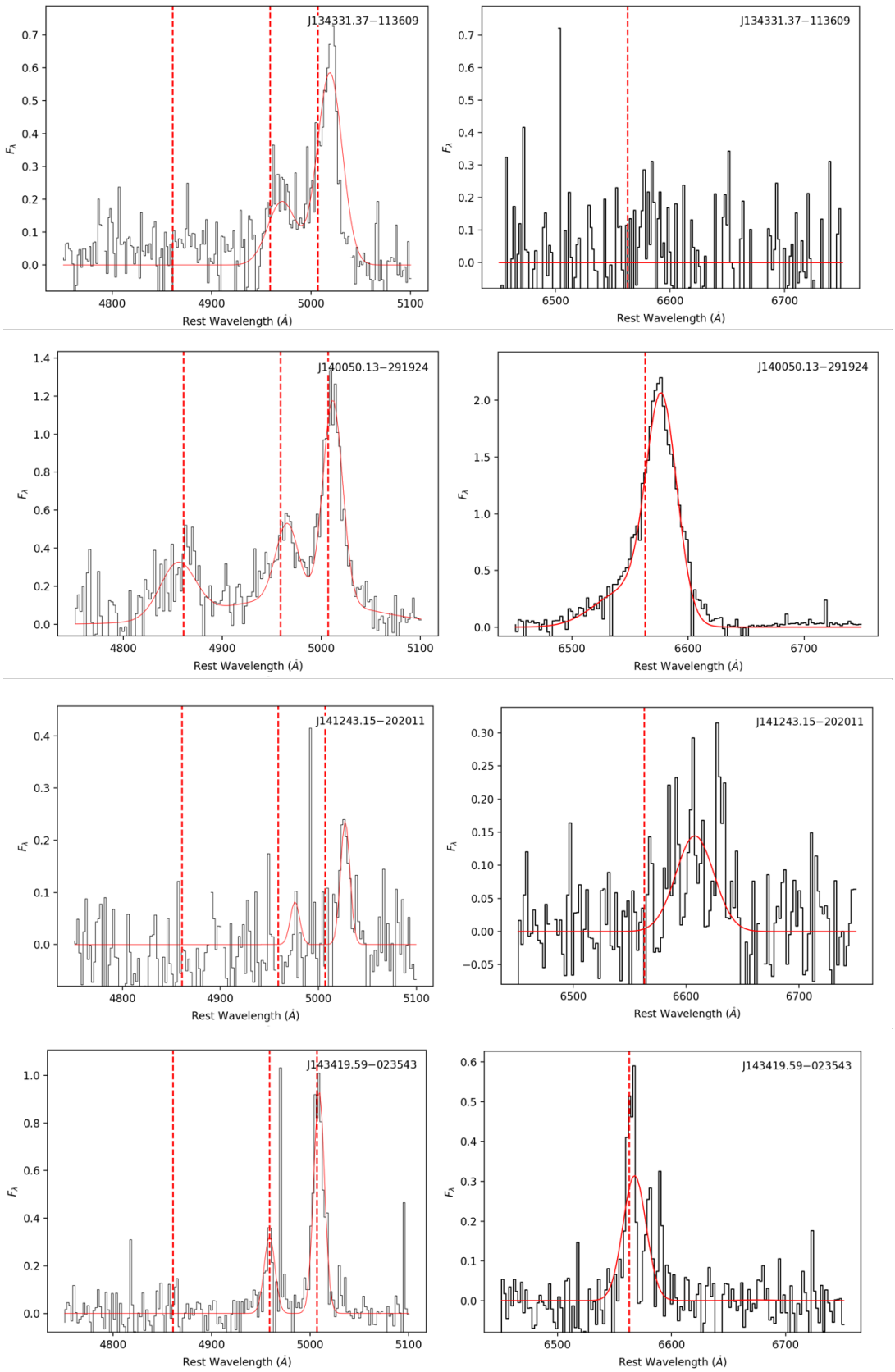

Figure 4.9: Continued

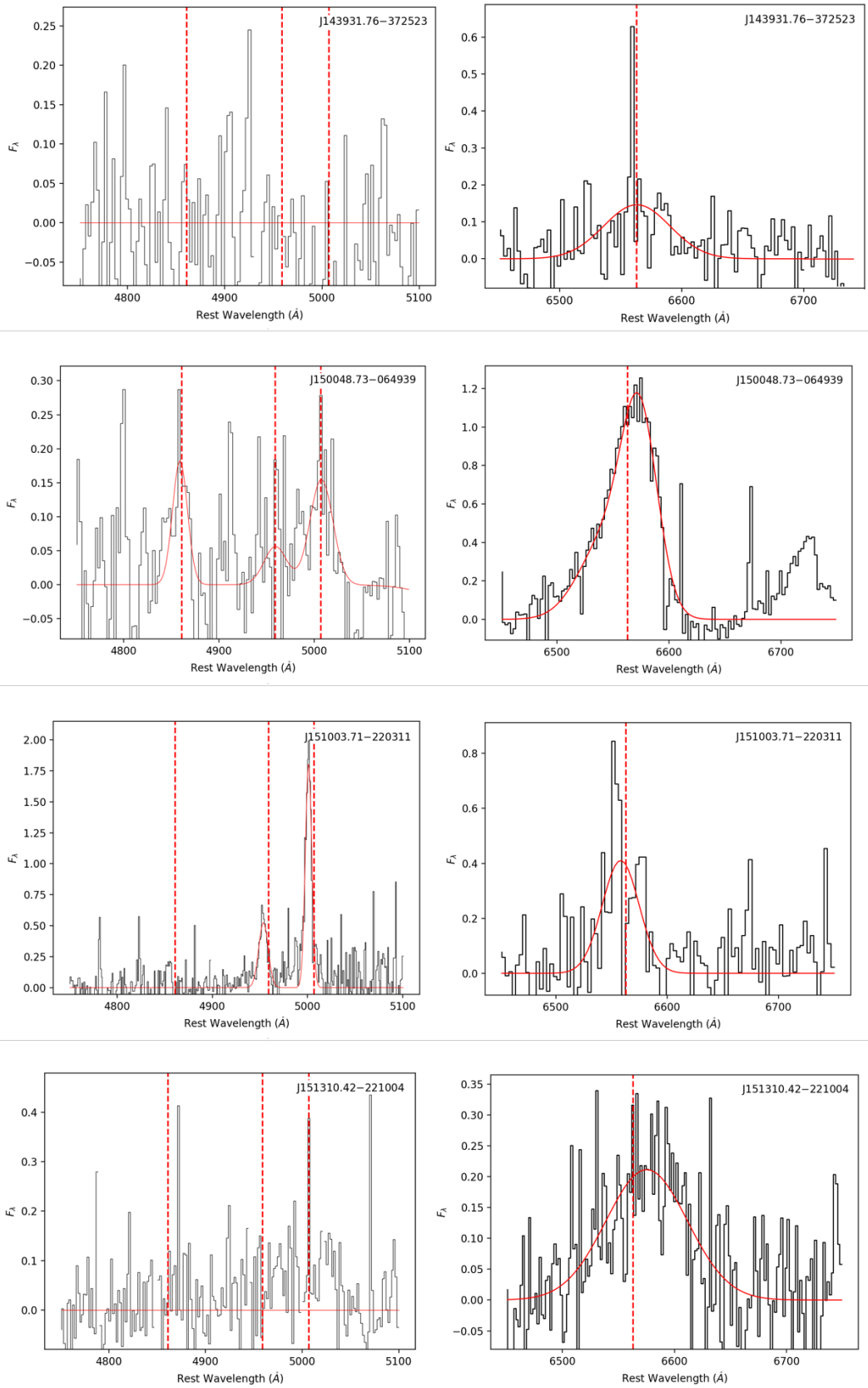

Figure 4.9: Continued

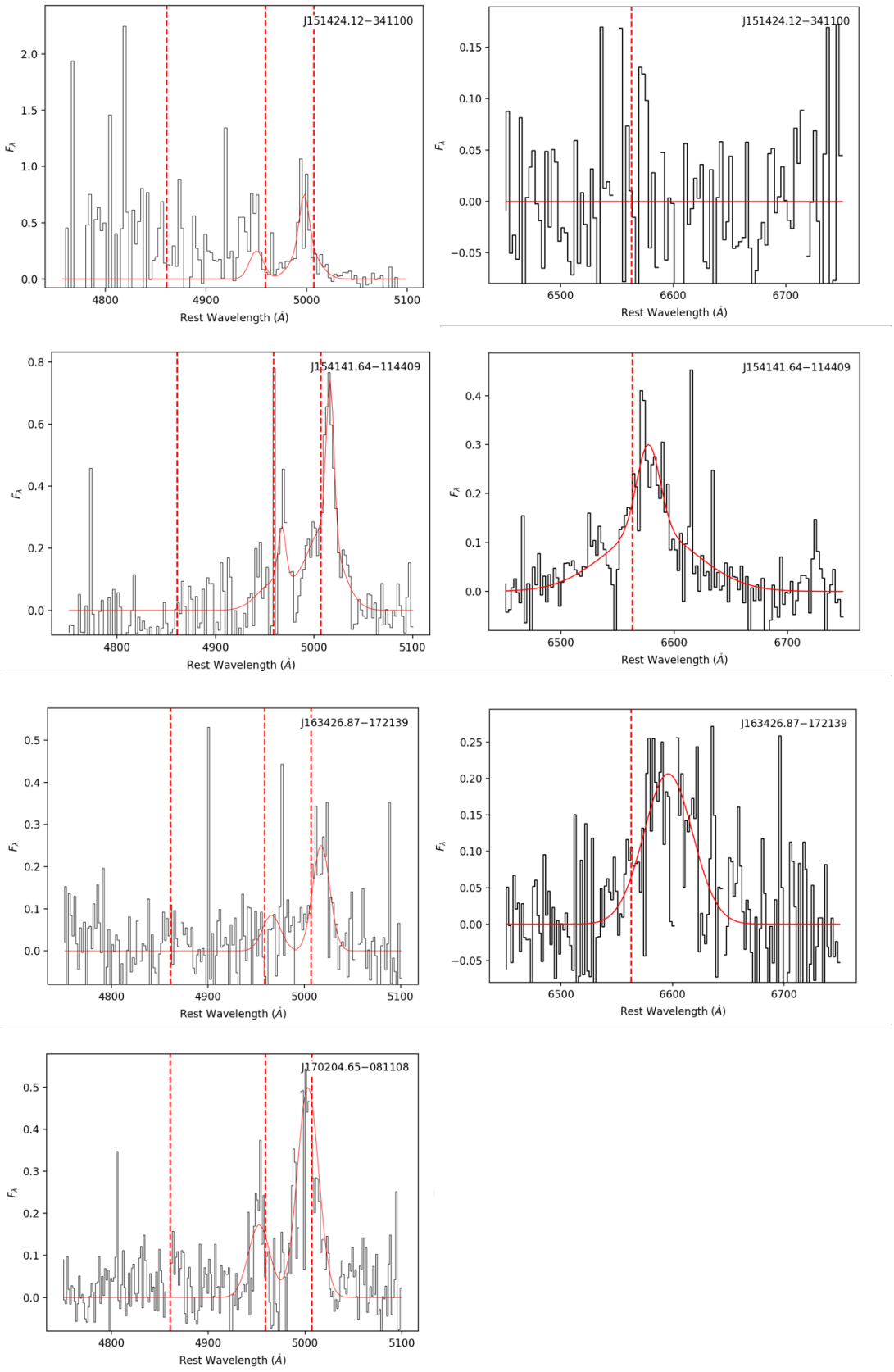

Figure 4.9: Continued

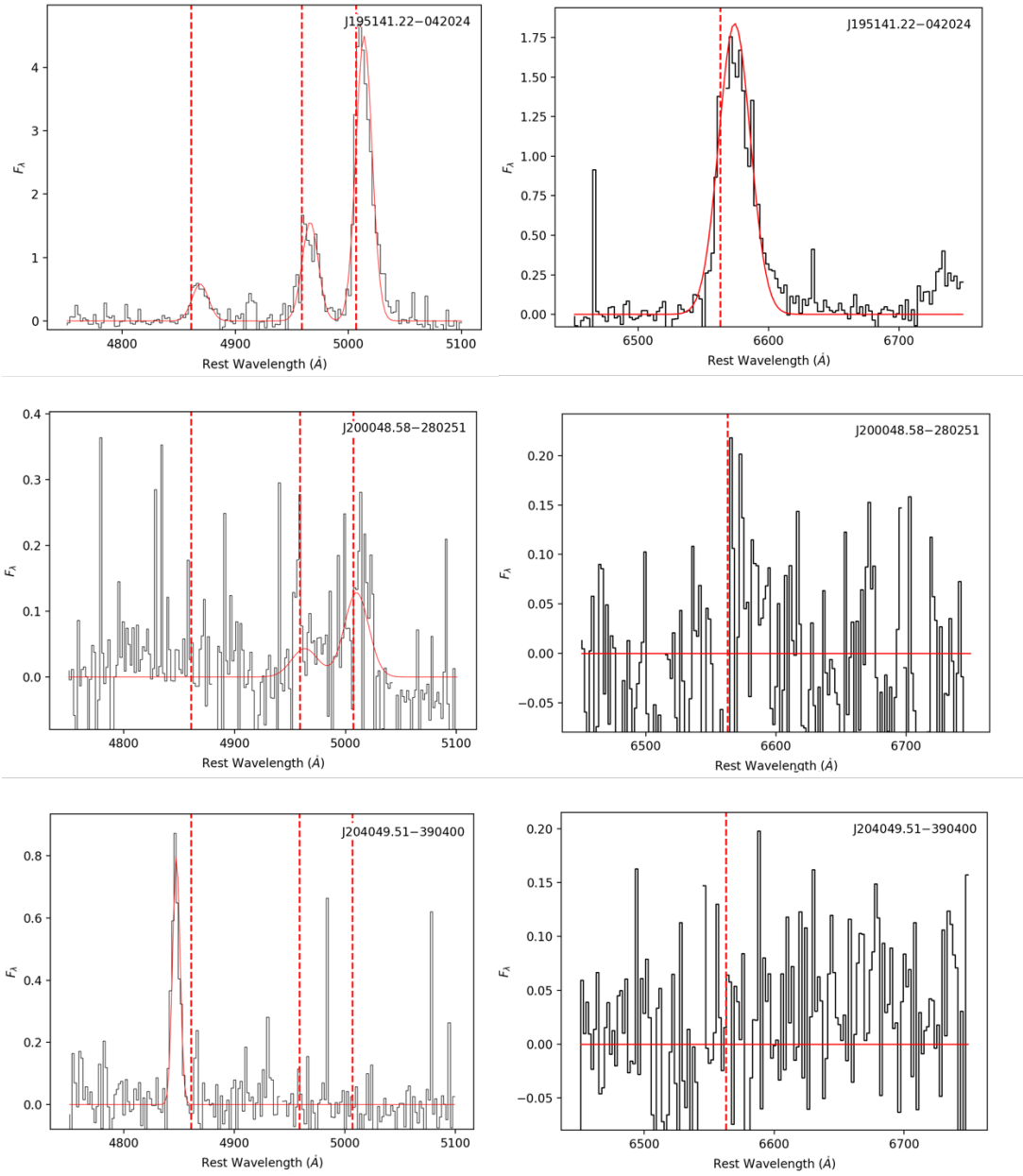

Figure 4.9: Continued

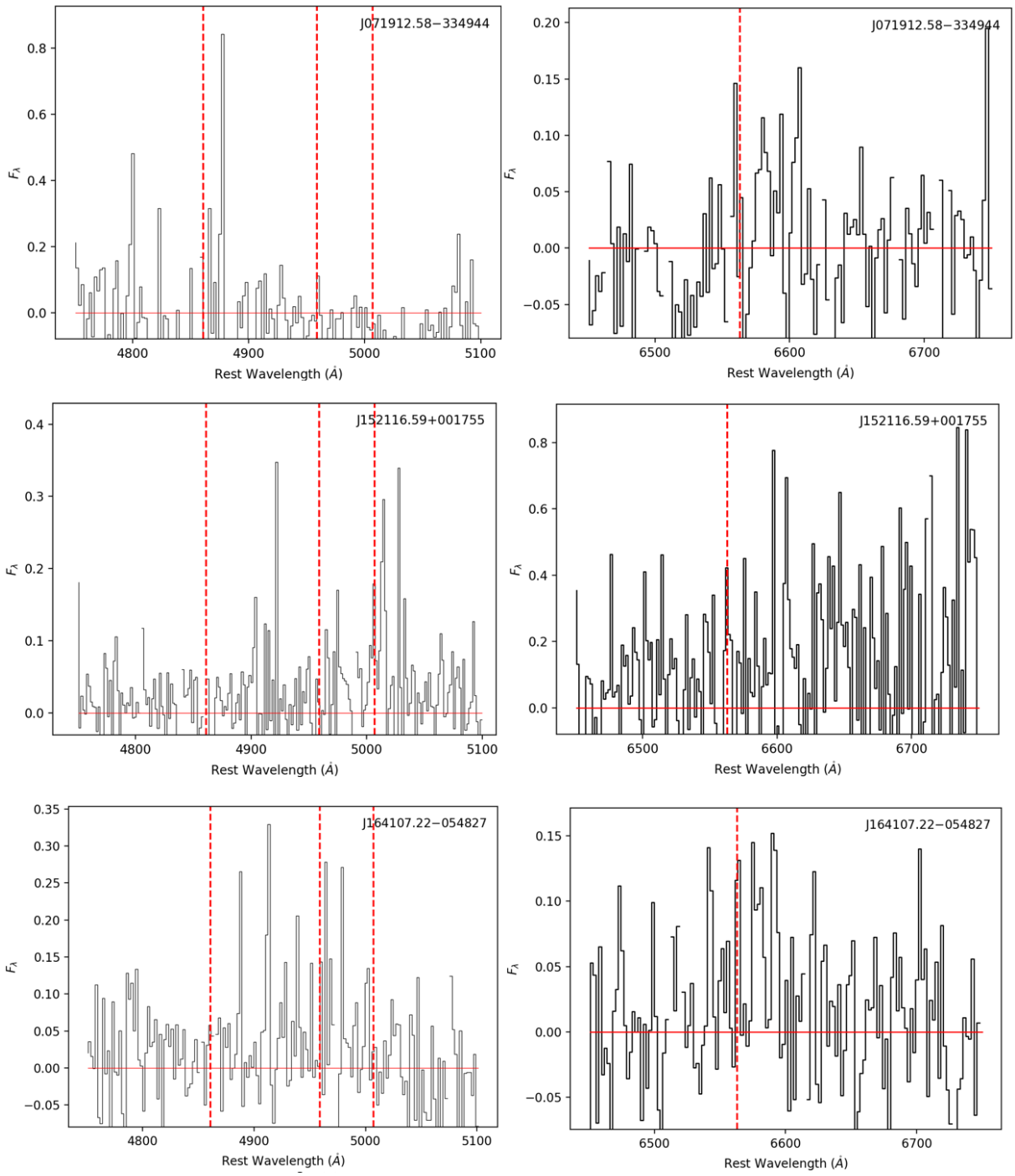

Figure 4.10: Rest frame X-shooter spectra in the region surrounding Hβ, [OIII]$\lambda\lambda$4959, 5007 and Hα for those sources with no line detections. Flux densities are in the units 10^{-16} erg s^{-1}cm^{-2}Å^{-1}. Reduced spectra is shown by a black histogram.

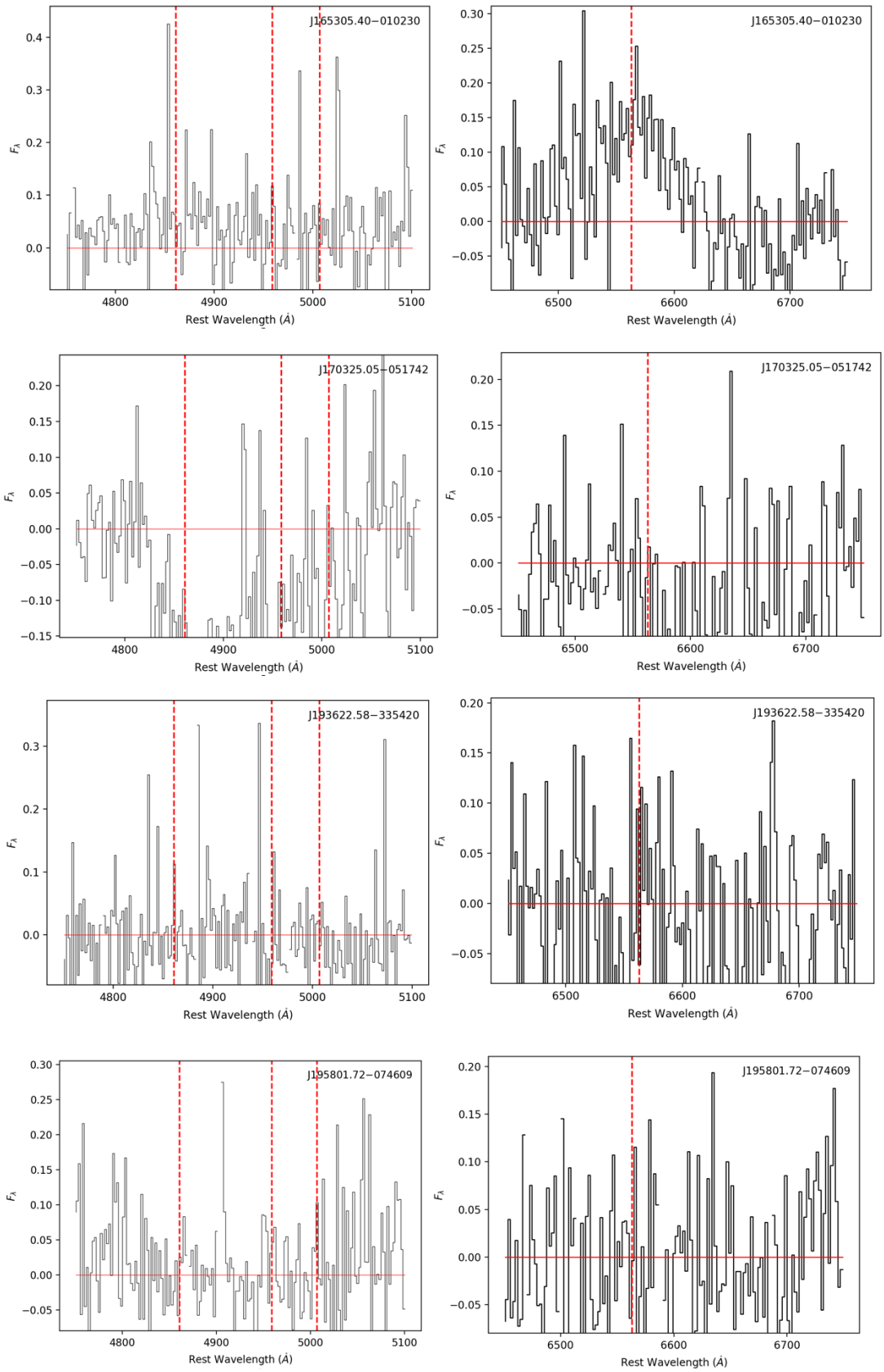

Figure 4.10: Continued

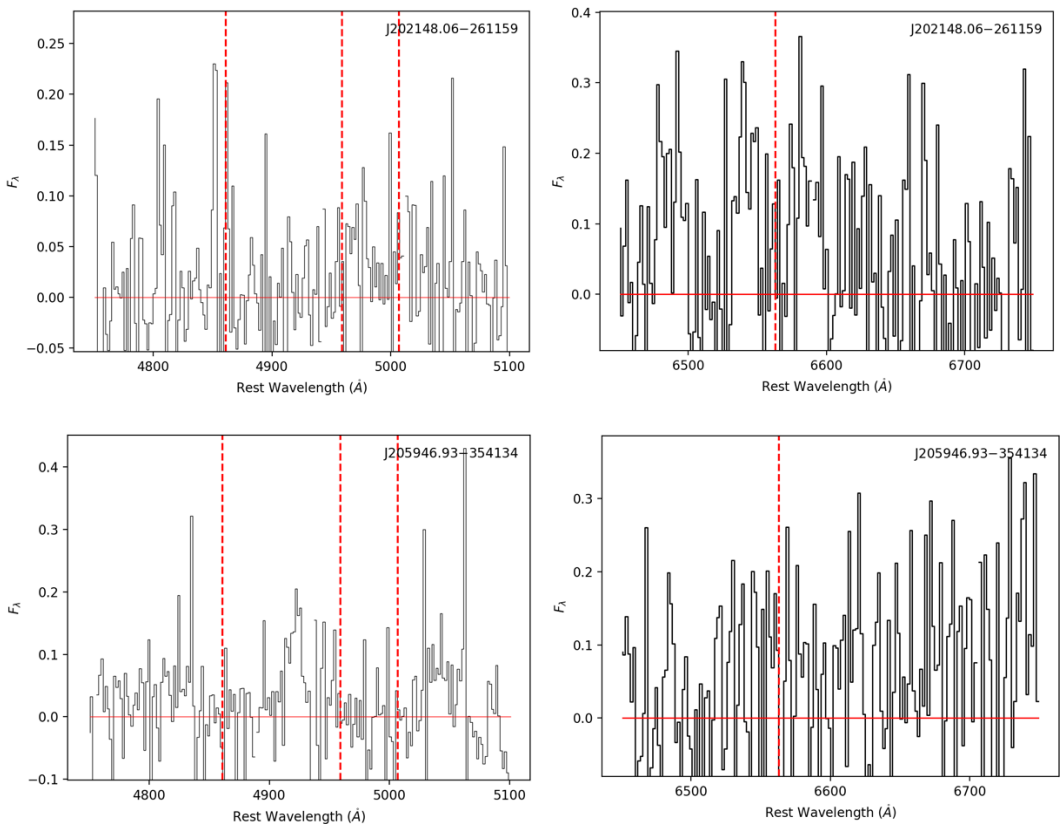

Figure 4.10: Continued

Table 4.2: The line flux and widths measured for the 18 sources with detected emission lines.

Source ID	WISE designation	Flux (10^{-16} erg s^{-1}cm^{-2})			FWHM (kms^{-1})		
		f_{H_α}	f_{H_β}	$f_{[\mathrm{OIII}]\lambda5007}$	Hα	Hβ	[OIII]λ5007
1	J081131.61−222522	8.49 ± 0.46	-	14.76 ± 0.54	1440 ± 150	-	1260 ± 140
2	J082311.24−062408	16.70 ± 3.05	6.04 ± 0.21	8.58 ± 0.30	2890 ± 800	1880 ± 210	1090 ± 510
3	J130817.00−344754	28.07 ± 3.70	5.42 ± 0.12	48.00 ± 3.55	1640 ± 80	1030 ± 110	1140 ± 130
4	J134331.37−113609	-	-	18.72 ± 7.01	-	-	2020 ± 560
5	J140050.13−291924	86.07 ± 4.13	8.59 ± 0.26	32.13 ± 9.32	2130 ± 30	1200 ± 260	1620 ± 50
6	J141243.15−202011	6.74 ± 0.34	-	2.83 ± 0.30	2180 ± 880	-	670 ± 270
7	J143419.59−023543	6.86 ± 0.10	-	14.32 ± 2.07	2220 ± 340	-	780 ± 80
8	J143931.76−372523	9.48 ± 0.15	-	-	2680 ± 280	-	-
9	J150048.73−064939	64.49 ± 2.12	3.66 ± 0.15	2.35 ± 0.22	2350 ± 90	2230 ± 150	1680 ± 520
10	J151003.71−220311	12.65 ± 6.97	-	21.11 ± 1.23	1460 ± 220	-	480 ± 30
11	J151310.42−221004	17.51 ± 1.53	-	-	3690 ± 390	-	-
12	J151424.12−341100	-	-	13.86 ± 5.22	-	-	1040 ± 320
13	J154141.64−114409	23.35 ± 3.92	-	14.77 ± 1.86	2430 ± 470	-	1390 ± 280
14	J163426.87−172139	15.00 ± 3.91	-	5.69 ± 0.14	2680 ± 260	-	1350 ± 200
15	J170204.65−081108	-	-	13.86 ± 7.21	-	-	1570 ± 500
16	J195141.22−042024	55.86 ± 6.52	10.27 ± 3.96	76.85 ± 0.16	1430 ± 390	1060 ± 120	1190 ± 30
17	J200048.58−280251	-	-	5.56 ± 0.14	-	-	1690 ± 270
18	J204049.51−390400	-	3.30 ± 0.82	-	-	490 ± 70	-

4.4.2 Summary of NIR Spectroscopy

Using 1D NIR spectroscopy from X-shooter 18/27 sources have detected NIR emission lines with 15 [OIII]λ5007, 13 Hα and six Hβ emission line detections. I used a multi Gaussian approach to fit these emission lines, applying as many Gaussians as necessary to achieve an optimal fit, and used two models to fit the three emission lines. The Hα line was modelled independently whilst the Hβ and [OIII]$\lambda\lambda 4959, 5007$ doublet was joined as a compound model fixing the [OIII]λ4959:[OIII]λ5007 ratio and the separation between the peaks. A Monte Carlo like approach was used to measure the errors on my line fluxes and widths by simulating and refitting 10,000 spectra in which each data point was allowed to randomly vary between the spectral errors.

4.5 Calculating BH and Host Galaxy Masses using NIR Emission Lines

The NIR spectra presented in the previous section have provided the line fluxes and FWHMs for three different emission lines detected in 18 of my sample of RWGs. This information will now allow me to independently derive the BH and host galaxy masses of these sources using two different methodologies. With this being a new and unique population of galaxies, this information will prove vital in understanding whether this galaxy type follows the expected relations as well as a potential clue as to where these sources fit in terms of galaxy evolution.

First I will use an assumed Eddington ratio and the luminosity of the [OIII]λ5007 line to determine a BH mass based on an estimate of the bolometric luminosity. Afterwards, I will use the two Balmer line widths and luminosties to derive an additional two measurements of the BH mass of each source, where the lines are available. I will present these along with a comparison to Lonsdale et al. (2015) SED derived masses and the masses presented in Kim et al. (2013).

These mass measurements are subject to some assumptions made, including an assumed Eddington ratio and no extinction corrections. For high luminosity sources, selected to be obscure, these assumptions are unlikely to be the real case and therefore corrections to their measured mass values will be the focus of Chapter 5. Throughout this work I also assume, that as is true in most quasars, my detected emission lines are broadened by the gravity of the SMBH and my FWHM values are correct. However Jun et al. (2020) recently suggested that for the similar galaxy population of HotDOGs, outflow contamination is responsible for the broadening of the Balmer emission lines, as well as the [OIII]λ5007 emission lines of a selection obscured AGN (Zakamska et al., 2015), meaning their measured FWHM values were overestimates. Whilst the populations are similar, there are also substantial differences between HotDOGs and these

RWGs, though the assumptions I have made may have an effect on my measured widths and derived masses and therefore is all discussed in Chapter 5.

4.5.1 Using the OIII Emission Lines

The first method used to calculate the BH mass of a RWG, is based on the [OIII]λ5007 emission line luminosity. Under the assumption that the Eddington luminosity should not be exceeded by the bolometric luminosity for any selected BH mass, I calculated a lower limit for the BH masses of my sources with [OIII]λ5007 detections, by using this line luminosity as a proxy for the bolometric luminosity of the source. For 15 of the sources shown in Table 4.2, I could calculate the BH mass using this method for $\sim$ half of my original source sample.

A conversion factor of $\mathrm{L_{Bol}} = 3200\,\mathrm{L_{[OIII]}}$ was derived by Shen et al. (2011) by comparing the spectral properties of broad line quasars from SDSS DR7 (York et al., 2000). This means that I could use the measured luminosity of the [OIII]λ5007 emission line as a proxy for the bolometric luminosity of each source and therefore derive BH masses with a single measured emission line property. Using a conversion between [OIII]λ5007 line luminosity (in $\mathrm{L_\odot}$) and bolometric luminosity and a value for the Eddington ratio λ_{Edd} chosen, Equation 4.1 (Kim et al., 2013) could be used to calculate the BH hole masses of the 15 RWGs with detected [OIII]λ5007 lines.

$$\frac{\mathrm{M_{BH}}}{\mathrm{M_\odot}} = \frac{3200 \times \mathrm{L_{[OIII]}}}{\lambda_{\mathrm{Edd}} \times 3.28 \times 10^4} \tag{4.1}$$

The masses of the host galaxies of theses sources could then be derived from these measured BH masses, assuming the evolution of the M_{BH} - L_{Host} relation with source redshift, as presented in Labita et al. (2010). Equation 4.2 gives this relation which is dependent on the source redshift and yields the parameter Γ defined as $\Gamma = \frac{\mathrm{M_{BH}}}{\mathrm{M_{Host}}}$. Labita et al. derive the redshift dependant Equation 4.2 though fitting a linear correlation between Γ and redshift for a sample of HST quasars at z = 0-3. They found a tight correlation, with no difference found when additional radio AGN are included in their fit. This equation could therefore confidently be used to determine the host masses of RWGs from measurements of their BH masses.

$$\log \Gamma = (0.28 \pm 0.06)z - (2.91 \pm 0.06) \tag{4.2}$$

Table 4.3 gives the determined BH and host galaxy masses of 15 RWGs, which have been calculated as a classical lower limit, under the assumption that $\lambda_{\mathrm{Edd}} = 1$. As shown by Equation 4.1, the calculated BH masses are inversely proportional to their assumed Eddington ratios with $\mathrm{M_{BH}} \propto 1/\lambda_{\mathrm{Edd}}$. Under the assumption of hydrostatic equilibrium, a choice of $\lambda_{\mathrm{Edd}} = 1$ should

Table 4.3: The calculated luminosity and range of BH and host galaxy masses within 1σ error, (given in solar masses) for those sources with measured [OIII]λ5007 emission lines. The M_{BH}/M_* relation is given using the M_* from Table 4.1.

Source ID	WISE designation	log $L_{[OIII]\lambda5007}$ (erg s^{-1})	log $\left(\frac{M_{BH}}{M_\odot}\right)$	log $\left(\frac{M_{Host}}{M_\odot}\right)$	M_{BH}/M_* (10^{-3})
1	J081131.61−222522	43.00 ± 1.44	8.39 - 8.42	10.86 - 11.14	3.19 ± 0.12
2	J082311.24−062408	43.25 ± 1.45	8.64 - 8.67	10.90 - 11.26	3.81 ± 0.14
3	J130817.00−344754	43.94 ± 1.13	9.31 - 9.37	11.60 - 11.98	47.73 ± 3.67
4	J134331.37−113609	43.96 ± 0.42	9.16 - 9.51	11.36 - 11.93	12.37 ± 6.07
5	J140050.13−291924	43.77 ± 0.54	9.02 - 9.28	11.31 - 11.89	13.45 ± 4.68
6	J141243.15−202011	43.80 ± 0.97	8.16 - 8.25	10.40 - 10.83	0.43 ± 0.4
7	J143419.59−023543	43.57 ± 0.84	8.91 - 9.04	11.11 - 11.58	5.83 ± 0.91
9	J150048.73−064939	42.53 ± 1.03	7.89 - 7.97	10.23 - 11.61	0.64 ± 0.06
10	J151003.71−220311	42.99 ± 1.24	8.37 - 8.42	10.89 - 11.18	7.02 ± 0.42
12	J151424.12−341100	42.95 ± 0.42	8.15 - 8.50	10.63 - 11.23	0.38 ± 0.18
13	J154141.64−114409	43.38 ± 0.90	8.72 - 8.83	11.04 - 11.46	7.73 ± 1.04
14	J163426.87−172139	43.25 ± 1.60	8.65 - 8.67	10.79 - 11.18	3.80 ± 0.97
15	J170204.65−081108	43.98 ± 0.28	9.06 - 9.56	10.94 - 11.91	11.90 ± 0.93
16	J195141.22−042024	44.09 ± 2.68	9.50 - 9.60	11.81 - 12.12	12.11 ± 0.03
17	J200048.58−280251	43.12 ± 0.61	8.40 - 8.62	10.47 - 11.09	4.98 ± 1.43

give the lower limit of the true value of the BH mass. If, however, a source is acreting at a super Eddington rate ($\lambda_{\rm Edd} > 1$), the BH mass needed for a source to accrete at the same luminosity will be lower. The chosen value of $\lambda_{\rm Edd}$ is therefore a very important factor in the calculated of the BH masses using 4.1. Whilst, for now, I have assumed $\lambda_{\rm Edd} = 1$ as in Kim et al. (2013), other works have assumed differently including Lonsdale et al. (2015) who chose $\lambda_{\rm Edd} = 0.25$ as is typical of quasars at $z \sim 2$ (Kormendy & Ho, 2013), or Assef et al. (2015) who assume a super Eddington rate of $\lambda_{\rm Edd} \geq 1$.

As previously mentioned there are also further assumptions made that can introduce systematic uncertainty into my measurements of the BH and host galaxy masses. In addition to the choice of $\lambda_{\rm Edd} \geq 1$ and the fact that these sources are selected to be highly obscured and have not been extinction corrected, three other factors can introduce uncertainty. The first of these assumptions in the bolometric correction factor, of $\rm L_{Bol} = 3200\,L_{[OIII]}$, that I assumed as derived from SDSS quasars. This correction may be too low for radio AGNs however, as suggested by Laor & Stern (2012), which will have caused overestimates of the BH and host galaxy masses given in Table 4.3. There is also a redshift dependence in calculating both the emission line luminosity and the host galaxy masses, where I have taken the VLT derived redshifts (Lonsdale et al., 2016), but also had to use an assumed value of 2.00 for J204049.51−390400 where no spectroscopic redshift was available. Finally, the assumed BH–host relation used (Labita et al., 2010) may not be accurate for this unique population of RWGs, though they do use a redshift range of z = 0-3 that includes my sources, but this can affect the accuracy of the host galaxy mass measurements.

4.5.2 Using the Hα and Hβ Emission lines

The previous section calculated the BH and host galaxy masses using the [OIII]λ5007 emission line luminosities. This section instead will use the emission line fluxes and widths of the Balmer lines Hα and Hβ.

I followed the work done by Greene & Ho (2005) and used the FWHMs and the line luminosities of the Hα and Hβ for 13 and six RWGs respectively. A virial BH mass estimate can be inferred from the velocity dispersion and the radius of the Broad Line Region (BLR) as shown by Equation 4.3. With an empirical relation between $R_{\rm BLR}$ and the optical continuum luminosity, a measurement of $\rm M_{BH}$ can be made using only a single spectrum rather than repeated reverberation mapping. First derived by Kaspi et al. (2000), and then more recently Bentz et al. (2009), this is the relation given in Equation 4.4 where $L_{5100} = \lambda \rm L_\lambda$ at $\lambda = 5100\AA$.

$$\mathrm{M_{BH}} \propto \frac{\mathrm{v^2 R_{BLR}}}{\mathrm{G}} \tag{4.3}$$

$$\mathrm{R_{BLR}} \propto \mathrm{L_{5100}^{0.5}} \tag{4.4}$$

Using a selection criteria of a high SNR and an Equivalent Width (EW) constraint of EW($\mathrm{Ca_{II}K}$) ≤ 1.5 Å, a primary sample of objects was selected by Greene & Ho (2005) from the third data release of SDSS (York et al., 2000) in order to formulate a new relation for calculating BH masses. Noticing a well defined correlation between Balmer emission line luminosity and L_{5100} allowed Greene & Ho (2005) to derive relations between L_{5100} and $L_{H\alpha}$ or $L_{H\beta}$, along with a conversion factor to convert between $\mathrm{FWHM_{H\alpha}}$ and $\mathrm{FWHM_{H\beta}}$ (Equation 4.5).

$$\mathrm{FWHM_{H\beta}} = (1.07 \pm 0.07) \times 10^3 \left(\frac{\mathrm{FWHM_{H\alpha}}}{10^3 \mathrm{kms^{-1}}}\right)^{1.03\pm0.03} \mathrm{kms^{-1}} \tag{4.5}$$

Taking $v = (\frac{\sqrt{3}}{2})v_{\mathrm{FWHM}}$ and $v_{\mathrm{FWHM}} = \mathrm{FWHM_{H\beta}}$ (Kaspi et al., 2000) allowed for the calculation of as BH mass purely dependent on the properties of the H_β emission line shown in Equation 4.6. Use of equation 4.5 then allowed for the derivation of a similar equation, dependent only on the luminosity and FWHM of the Hα emission line and given in Equation 4.7.

$$\mathrm{M_{BH}} = (3.6 \pm 0.02) \times 10^6 \left(\frac{\mathrm{L_{H_\beta}}}{10^{42}\,\mathrm{erg\,s^{-1}}}\right)^{0.56\pm0.02} \times \left(\frac{\mathrm{FWHM_{H_\beta}}}{10^3\,\mathrm{kms^{-1}}}\right)^2 \mathrm{M_\odot} \tag{4.6}$$

$$\mathrm{M_{BH}} = (2.0^{+0.4}_{-0.3}) \times 10^6 \left(\frac{\mathrm{L_{H_\alpha}}}{10^{42}\,\mathrm{erg\,s^{-1}}}\right)^{0.55\pm0.02} \times \left(\frac{\mathrm{FWHM_{H_\alpha}}}{10^3\,\mathrm{kms^{-1}}}\right)^{2.06\pm0.06} \mathrm{M_\odot} \tag{4.7}$$

Equations 4.7 and 4.6 were derived by Greene & Ho by fitting tight correlations between a sample of 229 observations of spectroscopically identified AGN from SDSS (York et al., 2000) at z $<$ 2.3. Similarly to RWGs Greene & Ho (2005) include radio loud sources in their, in order to include the effects of jet emission, with radio flux densities taken from FIRST. Whilst both their population and RWGs consist of radio AGN, the majority of their sources are of a lower redshift and therefore some caution must be taken when using Equations 4.7 and 4.6. With these equations derived from the relations above, there is large scatter on the final correlations derived. This scatter is included in the errors on the measured masses, however this scatter in addition to differences in galaxy population used add increased uncertainty to the BH masses below derived using these equations.

With 13 detection of the Hα emission line, and six detections of Hβ, I made a further 18 estimates of the BH masses of RWGs, in addition to the 15 made using the [OIII]λ5007 line. These BH masses were calculated through the use of Equations 4.7 and 4.6, with the 18 host masses calculated, as above, using Equation 4.2. Table 4.4 gives these calculated BH and host galaxy masses.

Table 4.4: The BH and host galaxy masses calculated with the detected Balmer emission lines, Hα and Hβ. Also included the measured FWHMs for these sources from Table 4.2 for comparison.

Source ID	WISE designation	FWHM (kms^{-1})		$\log\left(\frac{M_{BH}}{M_\odot}\right)$		$\log\left(\frac{M_{Host}}{M_\odot}\right)$		M_{BH}/M_* (10^{-3})	
		Hα	Hβ	Hα	Hβ	Hα	Hβ	Hα	Hβ
1	J081131.61−222522	1440 ± 150	-	7.14 - 7.43	-	9.62 - 10.16	-	0.24 ± 0.10	-
2	J082311.24−062408	2890 ± 800	1880 ± 210	7.95 - 8.65	7.56 - 7.86	10.21 - 11.24	9.81 - 10.45	1.68 ± 1.02	0.44 ± 0.18
3	J130817.00−344754	1640 ± 80	1030 ± 110	7.81 - 8.07	6.93 - 7.32	10.09 - 10.68	9.22 - 9.93	1.88 ± 0.66	0.29 ± 0.16
5	J140050.13−291924	2130 ± 30	1200 ± 260	8.35 - 8.53	7.12 - 7.46	10.64 - 11.14	9.40 - 10.06	2.60 ± 0.61	0.18 ± 0.09
6	J141243.15−202011	2180 ± 880	-	7.38 - 8.25	-	9.62 - 10.82	-	0.17 ± 0.15	-
7	J143419.59−023543	2220 ± 340	-	7.75 - 8.13	-	9.95 - 10.68	-	0.54 ± 0.29	-
8	J143931.76−372523	2680 ± 280	-	7.30 - 8.29	-	9.74 - 11.00	-	3.54 ± 2.76	-
9	J150048.73−064939	2350 ± 90	2230 ± 150	8.29 - 8.50	6.65 - 7.45	10.63 - 11.14	8.99 - 10.09	1.89 ± 0.50	0.08 ± 0.12
10	J151003.71−220311	1460 ± 220	-	7.01 - 7.53	-	9.53 - 10.29	-	0.53 ± 0.43	-
11	J151310.42−221004	3690 ± 390	-	8.52 - 8.87	-	10.62 - 11.53	-	0.91 ± 0.45	-
13	J154141.64−114409	2430 ± 470	-	7.92 - 8.46	-	10.24 - 11.08	-	1.99 ± 1.68	-
14	J163426.87−172139	2680 ± 260	-	8.16 - 8.52	-	10.31 - 11.04	-	1.84 ± 0.94	-
16	J195141.22−042024	1430 ± 390	1060 ± 120	7.59 - 8.66	7.03 - 7.51	9.91 - 10.88	9.34 - 10.13	0.32 ± 0.37	0.07 ± 0.05
18	J204049.51−390400	-	490 ± 70	-	6.45 - 6.82	-	-	-	0.03 ± 0.02

In comparison to BH masses previously calculated by other works, the [OIII]λ5007 masses are in greater agreement than these Balmer line masses which can be over an order of magnitude lower. This is possibly due to a greater amount of extinction present at the Hβ wavelength in comparison to [OIII]λ5007, high levels of noise surrounding the Hβ emission line or the blending of the Hα and [NII]$\lambda\lambda 6548, 6563$ lines. The difference in their wavelengths (causing different levels of extinction) and the low S/N of the Hβ spectra, likely explains the difference between the Hα and Hβ calculated masses. This comparison is discussed in more detail in the following section.

4.5.3 Comparison of the NIR Derived BH Masses

Following the methods outlined in the previous two sections has led to a current total of 33 different BH and host galaxy mass estimates for the 18 RWGs with at least one detected emission line. The following discussion will compare the different methods used and the NIR based results gained across this work and work done by others. All of this information is presented in Figure 4.11, with the mass ranges given in Tables 4.3 and 4.4 represented as error bars around the true values calculated.

With different methods used, it is difficult to directly compare the BH masses given in Tables 4.3 and 4.4, to those calculated by Lonsdale et al. (2015) and Kim et al. (2013). Figure 4.11 shows the calculated BH masses for the 18 sources with a detected NIR emission lines, and is ordered in terms of increasing BH mass as calculated in Lonsdale et al. (2015).

In comparison with these Lonsdale et al. (2015) masses, most of my [OIII]λ5007 calculated masses are in agreement. Under the same assumptions, there is a mean difference of ~ 0.40 dex between the masses which corresponds to the use of $\lambda_{\rm Edd} \sim 0.8$ rather my choice of $\lambda_{\rm Edd} = 1$. This is not a fair comparison however, as their method is based on SED fitting and an assumed value of $\lambda_{\rm Edd} = 0.25$. As discussed earlier there is still a lack of well fitting SED templates though Polletta et al. (2007) are currently the best, introducing possible uncertainties in their determined BH masses. Their choice of $\lambda_{\rm Edd} = 0.25$ may have also led to them overestimating their BH masses, as it has been suggested that RWGs may accrete at super Eddington rates.

My measured [OIII]λ5007 masses are also mostly in agreement to those presented in Kim et al. (2013), who also use the [OIII]λ5007 luminosity as a proxy for the bolometric luminosity and make an Eddington ratio choice of $\lambda_{\rm Edd} = 1$. There is a mean difference of ~ 0.46 dex between our results, although this is across a much smaller comparison range of seven sources. For the Balmer line calculations, there is a significant difference between those and Lonsdale et al.'s masses, with my Hα derived BH masses being a mean of ~ 0.94 dex lower, and my Hβ

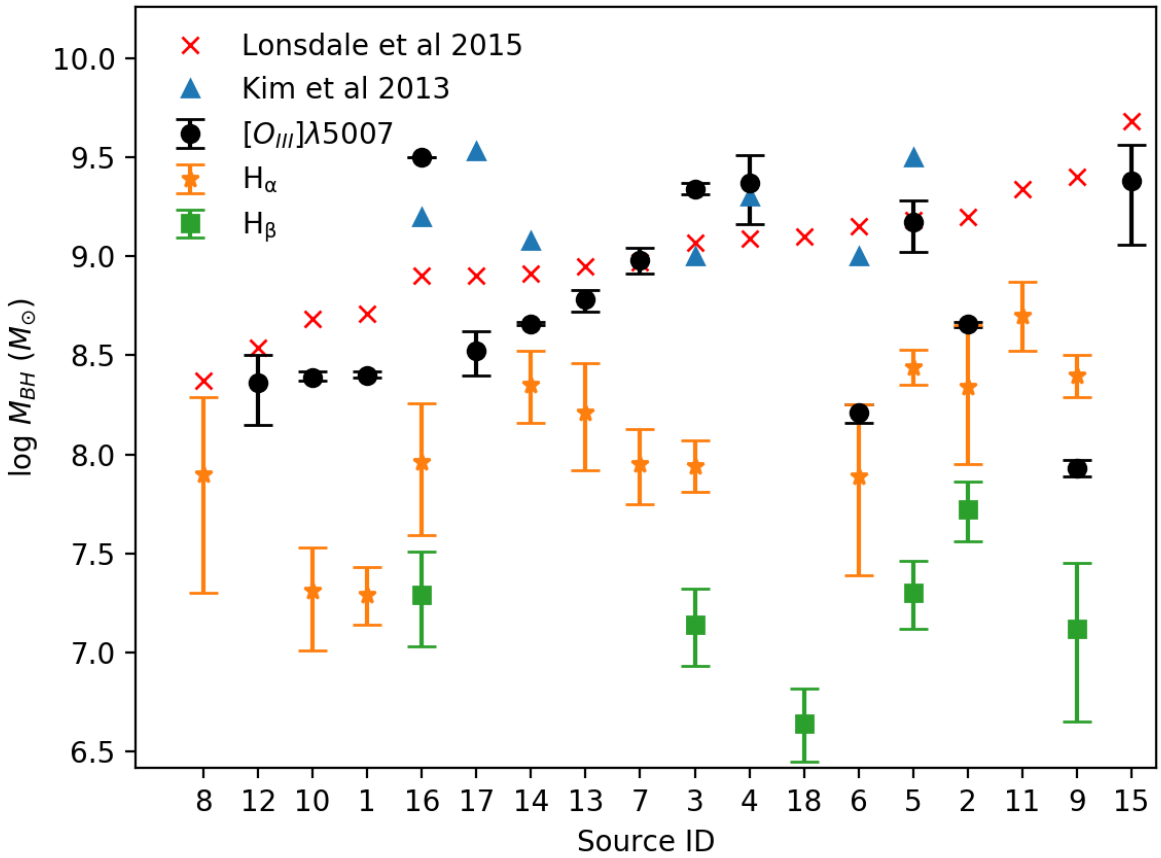

Figure 4.11: The different BH masses calculated; using [OIII]λ5007 (black circles), Hα (orange stars) and Hβ (green squares) emission lines. Also included are results by other works: Kim et al. (2013) (blue triangles) and Lonsdale et al. (2015) (red crosses), where details on those measurements can be found in the original work. Plotted from smallest to largest Lonsdale et al. (2015) mass, source ID corresponds to those used in tables. Note that systematic uncertainties due to the choice of $\lambda_{\rm Edd}$ are not included in the errors shown, the errors instead represent the range of masses given in Tables 4.3 and 4.4.

derived masses a further ~ 0.90 dex smaller.

Across all the masses presented in Figure 4.11, the most noticeable difference is the between the Hβ BH mass estimates in comparison to all of the others. These values agree within error to no other sources and are ~ 1 order of magnitude lower than the Hα based BH mass estimates. A modification of the scaling factor at the start of Equation 4.6 of $\times$ 7.94 would be required to align the Hβ mass estimates with the Hα measured values. This mass difference is likely not due to the difference in Equations 4.7 and 4.6, but due to the fainter Hβ emission lines. Further inspecting the Hβ detections in Figure 4.9, they are much fainter in comparison to the Hα detections and there are also higher levels of noise in the surrounding spectrum. Whilst the Hβ error bars are not all larger than those for the Hα masses, the χ^2_ν values for the multi Gaussian fit to the Hβ spectrum are significantly larger than for the both the Hα and [OIII]$\lambda\lambda 4959, 5007$ fits.

This excess noise in the spectra is a possible reason for the lack of detections of the Hβ emission line in comparison to the others. The inclusion of the Hβ masses in Figure 4.11 produces a large scatter due to the ~ 1 order of magnitude difference between them and the next lowest mass estimates. Due to this uncertainty in the validity of the Hβ masses, I will only include them for the sake of comparison, and not use them as definitive values. Whilst for the majority of the sources there is a large scatter in masses, the removal of the Hβ results as less reliable will much reduce this scatter and increases the overall confidence of the [OIII]λ5007 and Hα calculated masses in comparison to previous works. The uncertainty of these BH masses will play a large role in the next chapter of my thesis.

One final reason for the difference between Hα and Hβ calculated mass corrections is the lack of correction for extinction. Whilst this will be the primary focus of the next chapter, I briefly discuss it here as well. These RWGs have been specifically selected to be highly obscured and therefore will suffer from being affected by visual extinction. Following the dust laws of Cardelli et al. (1989) A_λ at $\lambda = 4861$ Å is greater than A_λ at $\lambda = 6562$ Å and therefore a greater extinction correction will need to be applied at the wavelength of Hβ in comparison to the rest wavelength of Hα. This would mean a larger correction applied to the calculated BH masses based on Hβ than Hα. Whilst this needed correction is likely to narrow the gap between the two Balmer line calculated masses, it will not narrow the gap between the Hβ and other calculated masses. Due to their similar wavelength there will be negligible difference between the extinction corrections for Hβ and [OIII]λ5007 and therefore the mass gap will remain similar.

Despite, the uncertainty in the calculated Hβ masses, I have determined the black hole and host galaxy masses for 18 RWG, with two independent methods using three different emission lines. For five of these sources, all three emission lines are detected providing three new mass

measurements to be compared. No matter the number of different lines detected, these new mass estimates provide an opportunity to compare to those already published. Using the [OIII]λ5007 emission line I have measured BH masses of $\log\left(\frac{M_{BH}}{M_{\odot}}\right)$ = 7.9 - 9.4 and BH masses of $\log\left(\frac{M_{BH}}{M_{\odot}}\right)$ = 7.3 - 8.7 using the Hα emission lines, leading to measured host masses in the range $\log\left(\frac{M_{Host}}{M_{\odot}}\right)$ = 10.4 - 12.0.

4.5.4 Summary of NIR Derived Masses

I used two independent methods to calculate three measurements the BH and host galaxy masses for the 18 RWGs with detected NIR emission lines. Using the [OIII]λ5007 luminosity as a proxy for bolometric luminosity I assumed a value of $\lambda_{Edd} = 1$ and measured classical lower limits to the BH mass. I then used the Hα emission line luminosity and width to calculate the BH mass whilst following equations derived by Greene & Ho. Finally I used the $M_{BH} - M_{Host}$ evolution outlined in Labita et al. (2010) to measure corresponding host galaxy masses.

4.6 Calculating BH and Host Galaxy Masses using the CIV and [OIII]λ5007 Emission Lines

Previously I have used two independent methods to derive the BH and host galaxy masses of 18 RWGs based on three observed NIR emission lines. This sections now aims to expand on those results by providing a fourth BH and host galaxy mass estimate for those sources with detected CIV emission lines. Following the work done by Assef et al. (2015) and Tsai et al. (2018), I could calculate the BH hole masses of five RWGs based on the FWHM of the CIV emission lines in the UVB/VIS arms and the luminosity of the [OIII]λ5007 emission line measured above.

4.6.1 Detection and Fitting of CIV Emission Lines

Out of the 27 RWGs observed with X-shooter, there are 26 possible detections of the CIV emission line at 1549 Å, as W0719 was not observed at this wavelength range. The CIV rest wavelength falls across the UVB and VIS arms of X-shooter and I detected five CIV emission lines in the UVB arms wavelength range of 300 - 560 nm. These observations were taken with exposure times of 2 $\times$400 s and at a slit width of 1.6". For the 13 sources with NIR detections but without CIV detections, only one source had an obvious continuum at this wavelength, J151003.71–220311. This exception had both a strong continuum and a narrow absorption line at the CIV wavelength (see Chapter 6).

The detected CIV emission lines were fitted with as many multiple Gaussians as needed for an

Table 4.5: The line flux and widths measured for the sources with detected CIV emission lines.

WISE designation	Flux (10^{-16} erg s^{-1}cm^{-2})	log Luminosity (erg s^{-1})	FWHM (kms^{-1})
J082311.24−062408	24.14 ± 0.85	43.70 ± 0.02	2480 ± 130
J130817.00−344754	10.10 ± 0.90	43.26 ± 0.04	4360 ± 560
J134331.37−113609	11.28 ± 0.27	43.74 ± 0.01	2170 ± 60
J140050.13−291924	11.64 ± 0.534	43.33 ± 0.02	2180 ± 160
J154141.64−114409	7.48 ± 1.13	43.08 ± 0.06	2150 ± 610

optimal fit, following the same process as described in detail in Section 4.4.1. The 1D spectra were first Doppler corrected using the `dopcor` package from IRAF (Tody, 1986) with an additional continuum subtraction performed. A Monte Carlo error analysis was again performed with the standard deviation of 10,000 simulated spectral properties taken as the errors on my measured flux and FWHM values. The error on my measured fluxes was then propagated through to determine the error on the calculated luminosities given in Table 4.5.

Table 4.5 gives the measured spectral properties of the five detected CIV emission lines, with the fitted spectra shown in Figure 4.12. I measured a mean flux of 12.9×10^{-16} erg s^{-1}cm^{-2} across the five sources with emission line detections and a mean FWHM of 2668 km s^{-1}. These measured widths can then be used to calculate additional BH and host galaxy masses for these five RWGs.

4.6.2 Using the CIV and [OIII]λ5007 Emission Lines to Calculate BH Masses

My five sources with detected CIV emission lines all have at least one BH mass measurement given by Table 4.11. However with the uncertain measurements from the Hβ spectra, my NIR BH mass measurements span a wide range with the hope that these additional five mass measurements allow me to tighten the constraints on my measured mass values. This should also help understand whether the Hβ determined BH masses are underestimates as expected or whether they are within error of these newly determined masses based on a shorter wavelength value of 1549 Å.

Following the methodology discussed for the universe's most luminous galaxy, the HotDOG W2246 (Tsai et al., 2018; Assef et al., 2015), the BH mass of a galaxy can be determined from the FWHM of a detected CIV emission line and the luminosity at 1350 Å. This is given in Equation 4.8 taken from Coatman et al. (2017). They define $L_{1350\,\text{Å}}$ as a monochromatic continuum luminosity, or the continuum luminosity at that specific wavelength, often determined through SED models. The luminosity at 1350 Å can therefore be approximated from the bolometric luminosity as $L_{1350\,\text{Å}} \sim 0.26 \times L_{\text{Bol}}$, derived from the SED templates of Richards et al. (2006). As before,

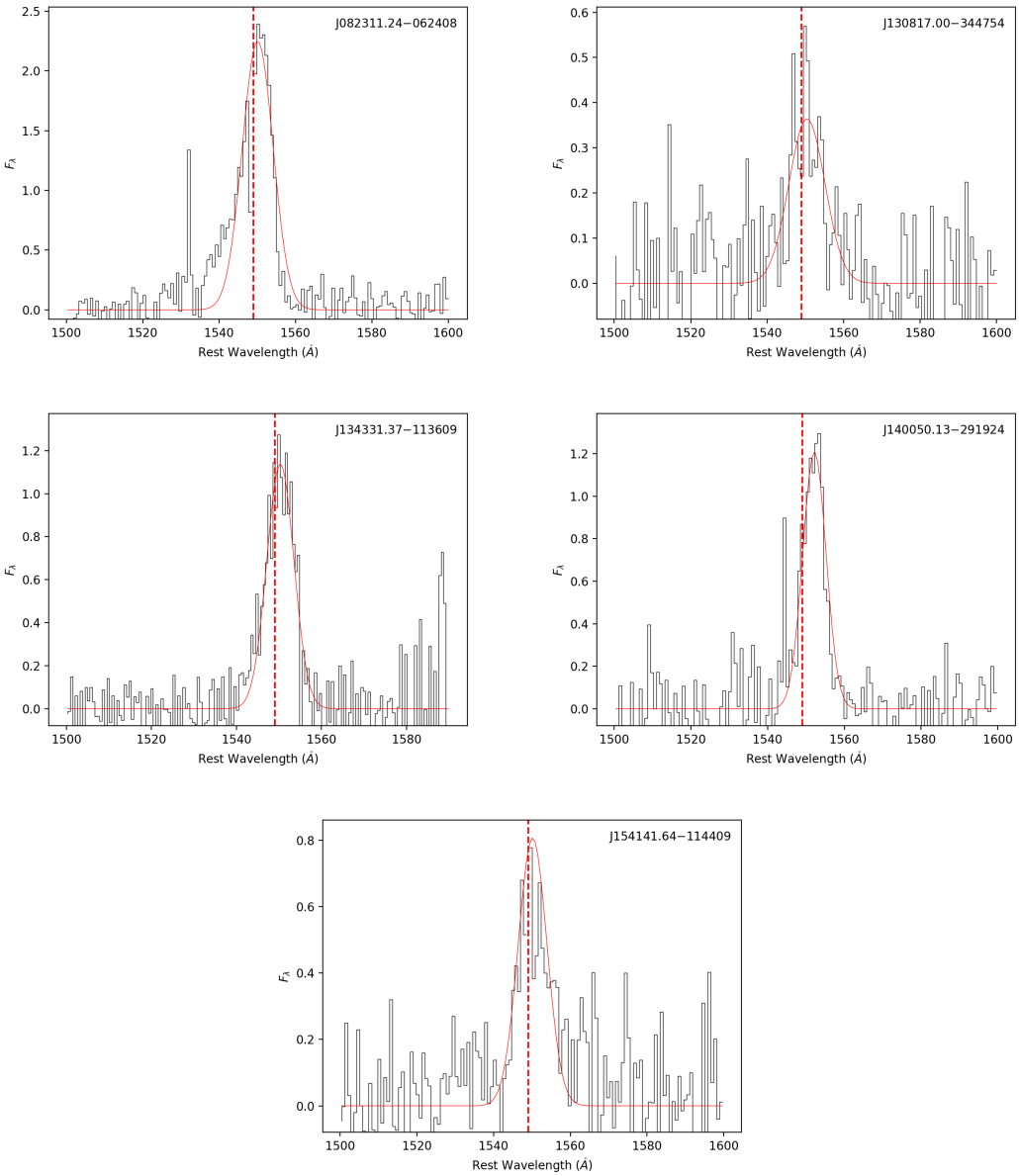

Figure 4.12: The 1D spectra in the region surrounding the CIV emission line. Flux densities are in the units 10^{-16} erg s^{-1}cm^{-2}Å^{-1}. Reduced spectra and fitted model are represented by black histogram and red lines respectively.

I use the luminosity of the [OIII]λ5007 emission line as a proxy for the bolometric luminosity following $L_{Bol} \sim 3200 \times L_{OIII}$ (Kim et al., 2013) or $L_{1350\,\text{Å}} \sim 832 \times L_{OIII}$. The luminosity errors in the measured [OIII]λ5007 emission lines are therefore the propagated to find the error in the $L_{1350\,\text{Å}}$ estimation.

$$\log\left(\frac{M_{BH}}{M_\odot}\right) = 6.71 + 2 \times \log\left(\frac{FWHM_{CIV}}{10^3\,\text{km}\,\text{s}^{-1}}\right) + 0.53 \times \log\left(\frac{L_{1350\,\text{Å}}}{10^{44}\,\text{erg}\,\text{s}^{-1}}\right) \tag{4.8}$$

I note that Tsai et al. (2018) discuss the asymmetry of their CIV emission lines, in addition to the possibility that CIV emission lines may be blue shifted with respect to their system's rest frame, especially in high luminosity systems (Richards et al., 2002; Baskin & Laor, 2005). They state that this significant blue shift can either be attributed to an outflow or the wind component of the broad line (Gaskell, 1982; Murray & Chiang, 1997; Leighly, 2004). Because of this a correction to the FWHM of the CIV line has been suggested (Brotherton et al., 2015; Jun et al., 2017; Coatman et al., 2016, 2017) and is given by equation 4.9 from Coatman et al. (2017).

$$FWHM_{CIV}^{Corrected} = \frac{FWHM_{CIV}^{Measured}}{(0.36 \pm 0.03) \times \left(\frac{CIVBlueshift}{10^3\,\text{km}\,\text{s}^{-1}}\right) + (0.61 \pm 0.04)} \tag{4.9}$$

Tsai et al. (2018) reduce the FWHM of W2246 by a factor of 1.8 through this correction. However I detected no asymmetry nor substantial offset in my measured CIV lines. These factors will be discussed in greater detail later in Section 6.6, but for now I have used my measured CIV widths to calculate the BH masses.

4.6.3 CIV Determined BH Masses and Comparison to NIR Derived Masses

Table 4.6 gives the calculated BH and host galaxy masses based on the FWHM of the CIV emission line. Unlike my previous estimates, this is not an independent measurement based only on the measured properties of one emission line. It depends on both the measured width of the CIV emission line and in my case the luminosity of the [OIII]λ5007 emission line, as I have taken this as a proxy for the bolometric luminosity. This in turn allowed me to calculate the luminosity at 1350 Å, which is also given in Table 4.6. I measured masses in the range of $\log\left(\frac{M_{BH}}{M_\odot}\right) = 8.3$ - 9.6 and $\log\left(\frac{M_{Host}}{M_\odot}\right) = 10.7$ - 12.2. Unlike the purely [OIII]λ5007 derived masses, these values do not depend on an assumed Eddington ratio, but they do depend on the conversion between [OIII]λ5007 luminosity to bolometric luminosity and bolometric luminosity to the luminosity at 1350 Å. The larger error range on these given values is due to the propagation of both the

Table 4.6: The calculated range of BH and host galaxy masses within 1σ error, (given in solar masses) for those sources with measured CIV emission lines.

WISE designation	$\log L_{1350\,\text{Å}}(\text{erg}\,\text{s}^{-1})$	$\log\left(\frac{M_{BH}}{M_\odot}\right)$	$\log\left(\frac{M_{Host}}{M_\odot}\right)$
J082311.24−062408	46.17 ± 0.02	8.59-8.70	10.85-11.28
J130817.00−344754	46.86 ± 0.03	9.38-9.62	11.67-12.23
J134331.37−113609	46.89 ± 0.14	8.80-9.01	10.81-11.43
J140050.13−291924	46.68 ± 0.11	8.69-8.93	10.97-11.53
J154141.64−114409	46.30 ± 0.05	8.34-8.83	10.65-11.46

measured CIV FWHM errors and the error in the determination of the [OIII]λ5007 flux, as the uncertainties from both measurements need to be taken into account, with the errors on both measurements being taken as the standard deviation from 10,000 fits.

Figure 4.13 shows my measured CIV BH masses plotted against both my measured NIR masses and masses calculated from Lonsdale et al. (2015) and Kim et al. (2013). Figure 4.14 shows this same information, but plotted against the Hα BH masses. In comparison to the other mass estimates, the calculated CIV masses do not sit as outliers with four out of five agreeing within error to at least one other estimate. Derived using my [OIII]λ5007 luminosity, my CIV derived BH masses agree within error of the [OIII]λ5007 masses for three sources and are a mean 0.17 dex smaller than my [OIII]λ5007 based estimates, corresponding to a super Eddington rate of $\lambda_{\text{Edd}} = 1.48$.

In comparison to my Hα based BH mass estimates, these CIV masses are a mean ~ 0.68 dex greater, but will be increasingly affected by extinction due to the lower wavelength of the [OIII]λ5007 and CIV emission lines. Compared to the masses calculated by Lonsdale et al. (2015), my CIV masses are ~ 0.21 dex lower, agreeing with my prediction that their masses are overestimates due to their choice of $\lambda_{\text{Edd}} = 0.25$. Finally, with only three sources possessing both measurements, it is hard to compare my CIV derived masses to those presented in Kim et al. (2013). None of these masses agree within error to each other with one CIV mass derived greater than that of Kim et al. (2013) and the other two derived lower. However, lying in agreement within error for four of the five sources allows confidence in my calculated CIV masses and also reinforces the unreliability of my Hβ derived masses as they are still $\sim$ one order of magnitude lower than the next nearest estimate.

4.6.4 Summary of CIV Derived Masses

Whilst I previously calculated BH and host galaxy masses for 18 RWGs based on the NIR emission lines this section adds additional mass measurements for five RWGs based on detected

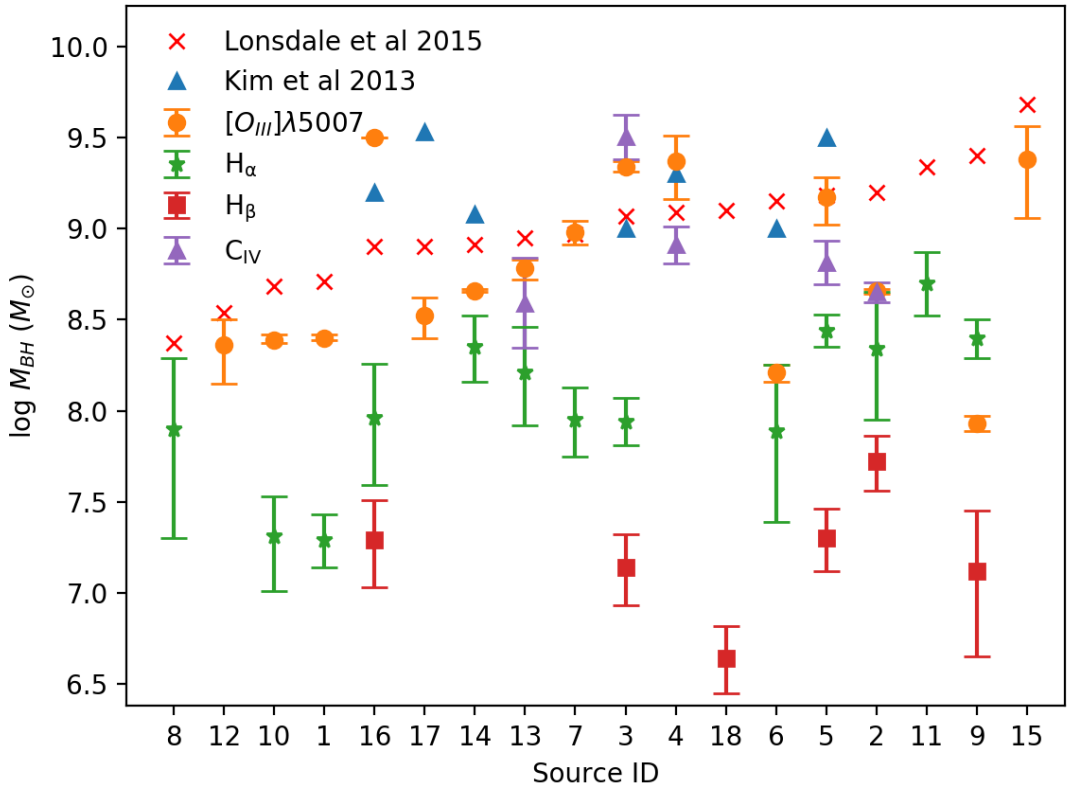

Figure 4.13: The different BH masses calculated; using [OIII]λ5007 (orange circles), Hα (green stars) and Hβ (red squares) NIR emission lines but newly including CIV emission lines (purple triangles). Also included are results by other works: Kim et al. (2013) (blue triangles) and Lonsdale et al. (2015) (red crosses), where details on those measurements can be found in the original work. Plotted from smallest to largest Lonsdale et al. (2015) mass, source ID corresponds to those used in tables. Note that systematic uncertainties due to the choice of $\lambda_{\rm Edd}$ are not included in the errors shown, the errors instead represent the range of masses given in Tables 4.3, 4.4 and 4.6. Exact errors on their values can be found in Lonsdale et al. (2015) and Kim et al. (2013), but a representative mean error would be $\log\left(\frac{\rm M_{BH}}{\rm M_\odot}\right) \pm 0.2$ and $\log\left(\frac{\rm M_{BH}}{\rm M_\odot}\right) \pm 0.46$ respectively.

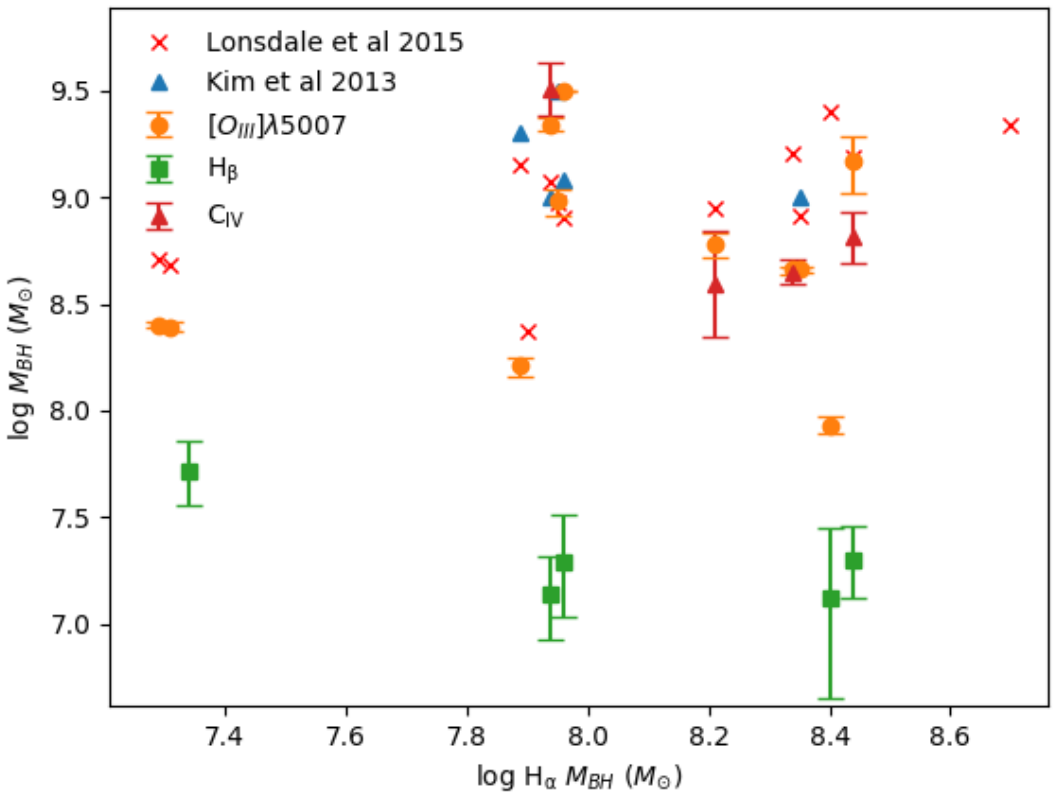

Figure 4.14: The different BH masses calculated; using [OIII]λ5007 (orange) and Hβ (red squares) NIR emission lines but newly including CIV emission lines (purple triangles), plotted against the Hα derived BH mass. Also included are results by other works: Kim et al. (2013) (blue triangles) and Lonsdale et al. (2015) (red crosses), where details on those measurements can be found in the original work.

CIV emission lines. Through use of Equation 4.8 (Coatman et al., 2017), I determined BH mass estimated based on the FWHM of my measured CIV emission lines, with my measured [OIII]λ5007 line luminosities used as a proxy for $L_{1350\,\text{Å}}$. I calculated $\log\left(\frac{\mathrm{M_{BH}}}{\mathrm{M_\odot}}\right)$ = 8.3 - 9.6 which lie in the middle of previous estimates and agree within error for four of the five sources. I additionally measured host masses $\log\left(\frac{\mathrm{M_{Host}}}{\mathrm{M_\odot}}\right)$ = 10.7 - 12.2, also agreeing with those presented earlier in this chapter.

4.7 Conclusions

This chapter has introduced observations of this unique galaxy population of RWGs. Selected similarly to other luminous populations including HotDOGs, RWGs are selected to be W2 bright and to lie redward of the main WISE population. Taken from the WISE All-Sky survey RWGs were selected through a cross matching process with NVSS (Condon et al., 1998), with a additional criterion applied to only select the galaxies defined as radio intermediates. These selection criteria narrowed down the entire WISE All-Sky catalogue to a subset of 156 RWGs. This work has focused on 30 of these sources that were available for observation in summer 2013.

These 30 RWGs were observed at the VLT by the NIR imager ISAAC and the multi wavelength spectograph X-shooter. All of the selected RWGs were observed with ISAAC, with 29 sources observed in the $\mathrm{K_s}$ band and 14 sources observed in the J band. The uneven number of detections was only due to a lack of observation time. The J and $\mathrm{K_s}$ band magnitudes were calculated using `SExtractor` with zero point corrections done by matching to the 2MASS catalogue. Table 4.1 gives these magnitudes and shows that they align with the WISE W1, W2, W3, W4 and ALMA fluxes allowing confidence with the ISAAC measurements.

These ISAAC magnitudes were used along with the WISE band and ALMA fluxes to determine the stellar masses of the RWGs by using the `MAGPHYS` (da Cunha et al., 2008) package to fit an SED to these data points. Due to the lack of well fitting templates, especially for AGN that exhibit broad line behaviour, these masses should only be taken as lower limits. The χ^2_ν values of each SED fit are given along with the calculated stellar masses as a guide to their uncertainty. The difficulty in fitting existing SED templates to RWGs again demonstrates their unique nature and differences in compared to existing AGN populations, indicating their place as a new phase in evolution. These SED fits also indicate additional differences between RWGs and HotDOGs, with different SED shapes and the unsuccessful fitting of HotDOG templates to RWGs, meaning that they likely are different galaxy populations, creating additional questions including the defining difference between these unique populations.

Along with NIR imaging, this chapter also discussed the results of the NIR spectroscopy

performed with X-shooter. With the aim of measuring the BH masses of RWGs, I focused on the detection of the Hα, Hβ and [OIII]$\lambda\lambda 4959, 5007$ emission lines. Out of the 27 sources observed by X-shooter, 18 sources had at least one of these emission lines detected, broken down as; 13 Hα, 6 Hβ and 15 [OIII]λ5007 detections, with the number of detections appearing correlated to the mean luminosity of the emission lines. A multi Gaussian model was used to fit these emission lines, with the minimum number of Gaussians needed for an optimal fit applied. The Hα emission was fitted independently, with the Hβ and [OIII]$\lambda\lambda 4959, 5007$ line fits combined as a compound model, providing the flux and FWHM of each emission lines. Errors on these values were calculated through a Monte Carlo simulation.

Two independent methods were used to determine the BH masses of the 18 RWGs with detected NIR lines. First the [OIII]λ5007 emission line was used as a proxy for the bolometric luminosity, and under the assumption of $\lambda_{\rm Edd} = 1$, a classical limit to the BH mass was derived, with $\log\left(\frac{\rm M_{BH}}{\rm M_{\odot}}\right) = 7.9$ - 9.4 being the range of masses calculated. The second method followed the process of Greene & Ho (2005) who developed a method for calculating the BH mass purely dependent on the line luminosity and width of a single Balmer line. The range of BH masses, $\log\left(\frac{\rm M_{BH}}{\rm M_{\odot}}\right) = 7.3$ - 8.7, was derived using the Hα emission lines, with the Hβ lines providing uncertain masses of up to an order of magnitude lower. These black hole masses led to measured host masses in the range $\log\left(\frac{\rm M_{Host}}{\rm M_{\odot}}\right) = 10.4$ - 12.0.

I additionally measured BH and host galaxy masses for five of these 18 RWGs using detected CIV emission lines. Using the measured FWHM of my CIV lines and the luminosity of my [OIII]λ5007 emission lines as a proxy for the luminosity at 1350 Å I calculated $\log\left(\frac{\rm M_{BH}}{\rm M_{\odot}}\right) = 8.3$ - 9.6. These masses lie in the middle of previous estimates with corresponding host masses of $\log\left(\frac{\rm M_{Host}}{\rm M_{\odot}}\right) = 10.7$ - 12.2.

In comparison to other works the [OIII]λ5007 emission line derived BH masses were the most in agreement, with the Hβ emission lines adding increased statistical scatter to Figures 4.11 and 4.13. These Hβ masses are however likely to be incorrect due to intrinsic line faintness, high levels of spectral noise and the increased affect of extinction at this wavelength. With these Hβ masses discounted, I can remain confident in the BH masses calculated, with the differences being due to the two methods used.

The results of these mass calculations indicate that RWGs are smaller than HotDOGs, with the mass differences between the Hα and [OIII]λ5007 BH masses implying that RWGs are also super Eddington. If RWGs are smaller than HotDOGs it is likely that RWGs are a shorter lived phase of intense AGN feedback as they would not be able to maintain their super Eddington phase for as long. Therefore RWGs are most likely a smaller and rarer population of these

extreme AGN, agreeing with the population sizes selected by the criteria outlined in Chapter 2.

There were however several assumptions made in the calculation of the BH and host galaxy masses, which if incorrect could vastly change the measured masses. With the BH mass being inversely proportional to the Eddington ratio, my choice of $\lambda_{\mathrm{Edd}} = 1$ derived a classical lower limit to the BH mass. It has been suggested that RWGs accrete at super Eddington rates which would lower my BH mass estimates. The emission line spectra were also not corrected for extinction, and as these sources were selected to be highly obscure, it is likely that the measured line fluxes were underestimates of the true values. A correction to the BH masses for this may increase them in line with those published by Lonsdale et al. (2015).

Determining the BH and host galaxy masses of these sources is vital to understand the properties of this unique population and currently shows that they are not the same as HotDOGs but smaller in mass. However, whilst the masses measured in this chapter are mostly in agreement with those published, the assumptions used must be further investigated in order to be confident in the true values of the BH and host galaxy masses of these 18 RWGs and their differences between HotDOGs and other AGN populations. The following chapter will therefore continue this investigation by providing estimates of the true Eddington ratios and correcting these masses for a range of both measured and simulated values of A_V.

Chapter 5

Investigation into the Factors that Affect BH Mass Calculations

5.1 Introduction

Please note that some of the contents of this chapter have been published in Ferris et al. (2021), but all of the analysis was undertaken by me.

The previous chapter introduced how RWGs were selected from the 563,921,584 total galaxies in the WISE All-Sky catalogue (Wright et al., 2010), with a sub sample of 30 RWGs the focus of this work. Using the X-shooter NIR and UVB spectra, I calculated the BH and host masses of 18 RWGs using three independent methods, finding them ~ 1 dex smaller than similarly selected HotDOGs. However, these BH mass measurements were heavily dependent on some assumptions made during the methodology. Therefore making sure that these assumptions are correct and that the calculated masses are accordingly accurate is of extreme importance to understand how RWGs differ from HotDOGs and normal AGN populations. This will then allow determination of the defining characteristics of RWGs, to help with developing further selection criteria and understanding which evolutionary phase they are a part of.

As the assumed Eddington ratio is inversely proportional to BH mass, the assumption of $\lambda_{\rm Edd}$ made is a major factor affecting my final calculated BH masses. My choice of $\lambda_{\rm Edd} = 1$ assumes that the sources remain in hydrostatic equilibrium, and therefore represents the calculation of a classical lower limit to the BH mass. Recent works (Assef et al., 2015; Tsai et al., 2015, 2018; Wu et al., 2018) have however suggested that the similar population of HotDOGs accrete at unsustainable super Eddington rates, which if true for RWGs would mean that my BH mass measurements are overestimates of the true values. An estimation of the correct value of the

Eddington ratio would therefore allow for the calculation of more accurate BH masses.

RWGs are selected to be extremely luminous in the mid-IR (Lonsdale et al., 2015), and thus dominated by hot dust emission, likely indicating the proximity of substantial extinction to the central engine. Due to the expected high levels of dust scattering, the calculated optical luminosities under the assumption of zero extinction above are likely to be underestimates of the true unobscured values. I tested this by measuring the extinction of nuclear emission lines allowing for the original spectra to be corrected and BH masses to be recalculated. As RWGs are selected to be highly obscured systems these are important corrections that need to be made to properly compare RWGs to other AGN populations.

This chapter focuses on correcting these two main assumptions previously used in calculating the BH and host galaxy masses. First, I used both the measured [OIII]λ5007 and Hα BH masses to estimate the true Eddington ratio of each source. Comparing the calculated masses with the new Eddington ratio to those calculated with the choice of $\lambda_{\rm Edd} = 1$ allows for a better idea of how powerfully these sources accrete. Secondly, I used the measured Hα and Hβ emission line fluxes to estimate the extinction parameters of A_V and E(B-V) for each source that has both these lines detected. I also simulate a realistic Hβ line profile to provide extinction estimates for those sources without a Hβ detection.

Correcting both of these assumptions made allowed for a better idea of the true values of the BH and host galaxy masses, whilst comparing these new masses to previous works also allowed me to determine how likely these estimations of the Eddington ratio and dust obscuration are.

5.2 Measuring the Eddington Ratio

This section aimed to calculate the Eddington ratios of the 18 sources with measured NIR emission lines. With previous works (Assef et al., 2015; Tsai et al., 2015, 2018; Wu et al., 2018) investigating the Eddington ratios of the similarly luminous and obscured population of HotDogs and suggesting that they accrete at super Eddington rates, this calculation is important in order to determine the true masses of RWGs.

The Eddington ratio is one of the two free parameters used to describe the accretion mechanism of AGNs (Raimundo & Fabian, 2009), along with relative radiation efficiency η, and has been assumed to be either a function of mass or constant (Shankar et al., 2008). The Eddington ratio, $\lambda_{\rm Edd}$, relates the bolometric luminosity L of a source to the Eddington luminosity L_E through $\mathrm{L} = \lambda_{\rm Edd} L_E$ where $L_E = 4\pi c G M m_H/\sigma_T$, $m_H = 1.673 \times 10^{-27}$ kg and $\sigma_T \approx 6.65 \times 10^{-25}\,\mathrm{cm}^2$. Super Eddington accretion occurs when $\lambda_{\rm Edd} > 1$ and said source is accreting at a luminosity

greater than the Eddington luminosity[1]. This accretion is unsustainable for long periods of time[2], and if RWGs do accrete at super Eddington rates we may be seeing a very specific stage of galaxy evolution. With measured bolometric luminosities calculated from the [OIII]λ5007 emission lines exceeding $\sim 10^{13} L\odot$, super Eddington accretion will require lower BH masses to produce this accretion luminosity than for a classically accreting source.

Previous Evidence for Super Eddington Accretion

A comparison of the emission line widths presented in Table 4.2 showed that in some cases the [OIII]λ5007 are comparably broad, if not broader than the measured Hα and Hβ emission line widths. For the 11 sources with both OIII and Hα line detections the FWHMs agree within error for three sources. Similarly, for the 5 sources with both [OIII]λ5007 and Hβ detections, all source FWHMs agree to within error and the measured widths of the [OIII]$\lambda\lambda 4959, 5007$ lines are wider for three of the sources. This broad nature of the [OIII]$\lambda\lambda 4959, 5007$ emission lines suggests outflows may be broadening the measured line widths, a process which may require super Eddington accretion.

Outflows as a mechanism for broadening emission lines has been recently suggested for the similar population of HotDOGs (Jun et al., 2020), and for RWGs (Kim et al., 2013), providing more evidence for super Eddington accretion, though this possibility will be discussed in further detail in Chapter 6. It is, however, possible that for those sources with comparable widths across the Balmer and [OIII]λ5007 emission lines, the broad line emission of the Balmer lines was obscured and therefore Balmer line emission is dominated by the narrow line region. In this case the Balmer line calculated BH masses and the subsequent Eddington ratios will be inaccurate due to the increased distance to the narrow-line region. If this is the case the [OIII]λ5007 base results may be the most reliable.

The following discussion covers the methodology used to estimate a true value of the Eddington ratio for the 11 sources with both of these Hα and [OIII]λ5007 mass calculations. I then use these new Eddington ratios to recalculate the [OIII]λ5007 BH and host galaxy masses and compare them to the masses discussed in the previous chapter.

[1]The maximum luminosity a source achieves, beyond which radiation pressure will overcome the gravitational force.

[2]For example Tidal Disruption Events only remain in super-Eddington phases for months to years (Levan et al., 2015), but AGN are more liely to be in this pahse for 100's of years.

Table 5.1: The measured Eddington ratios for the 11 sources with both Hα and [OIII]λ5007 line detections.

WISE designation	$\lambda_{\rm Edd}$
J081131.61−222522	12.98 ± 4.83
J082311.24−062408	2.07 ± 0.32
J130817.00−344754	25.24 ± 10.39
J140050.13−291924	5.41 ± 3.24
J141243.15−202011	2.09 ± 0.27
J143419.59−023543	10.66 ± 3.02
J150048.73−064939	0.34 ± 0.18
J151003.71−220311	12.06 ± 2.61
J154141.64−114409	3.74 ± 0.74
J163426.87−172139	2.02 ± 0.61
J195141.22−042024	34.59 ± 5.51

5.2.1 Determination of Eddington Ratios

As the choice of Eddington ratio, $\lambda_{\rm Edd}$, is a determining factor in the calculated value of BH mass when using Equation 4.1, understanding the rate at which these sources accrete is extremely important. In the previous chapter I chose the value $\lambda_{\rm Edd} = 1$ to give a classical lower limit to the mass assuming the sources remain in hydrostatic equilibrium. Here I instead aimed to calculate the true value of the Eddington ratio.

I measured 15 sources with detected [OIII]λ5007 emission lines, 13 sources with detected Hα emission lines and 11 sources with detections of both lines. By equating the Hα and [OIII]λ5007 BH masses I could estimate a value for the Eddington ratio through the reversal of Equation 4.1. Across these 11 sources with both lines detected, I calculated $\lambda_{\rm Edd} = 0.34 - 34.59$ with a mean value of $\lambda_{\rm Edd} = 10.12$. This breaks down into 10 sources with $\lambda_{\rm Edd} \geq 1$ and only the one source, W1500, with $\lambda_{\rm Edd} \leq 1$. Within these 10 sources accreting at super Eddington rates, I measure $1 \leq \lambda_{\rm Edd} \leq 5$ for six sources and $10 \leq \lambda_{\rm Edd} \leq 13$ for two sources. I measure $\lambda_{\rm Edd} > 25$ for W1308 and W1951, but these measurements are consistent within large errors to each other.

The Eddington ratios and their associated errors, calculated for 11 RWGs are presented in Table 5.1. These $\lambda_{\rm Edd}$ ratios imply that RWGs do accrete at super Eddington rates with measurements of $\lambda_{\rm Edd} > 1$ for 10 of the 11 sources, though these values are not all statistically significant. With large uncertainties on the calculated $\lambda_{\rm Edd}$ values, $\lambda_{\rm Edd} = 1$ is within 2σ for two sources and within 3σ for five of the 10 sources with measured super Eddington rates. Whilst it is therefore likely that RWGs do accrete at super Eddington rates I can only show this with

significance for half of my population.

The Hα determined BH mass was used for this calculation as it allowed the derivation of $\lambda_{\rm Edd}$ for 11 sources. Comparatively there were only seven sources with detected [OIII]λ5007 emission lines that overlap with population observed by Kim et al. (2013) and five that overlap with Hβ detections. Additionally Kim et al. used an identical method to calculate their BH masses, also assuming $\lambda_{\rm Edd} = 1$, and the Hβ derived BH masses are likely unreliable due to the higher levels of noise in the spectra. Both the [OIII]λ5007 and Hα emission lines are measured with the same wavelength arm of the same instrument eliminating any additional bias. No assumptions of the value of $\lambda_{\rm Edd}$ were made in my calculation of the Hα BH masses, nor were any extinction corrections used in the determination of either mass.

However, with 6/11 RWGs in Table 5.1 measuring $\lambda_{\rm Edd} > 5$ this may be an indicator that either the Hα BH masses are underestimates or an unaccounted for factor is at play. Though dependent on no external factors these high Eddington ratios are remarkable, which may lead to questioning of the Hα BH masses or the final $\lambda_{\rm Edd}$ results.

With matching mass measurements for all of the [OIII]λ5007 BH masses derived from a completely independent data set, the results published by Lonsdale et al. may have been the more obvious choice to use for this investigation. However, they also used an assumed value for $\lambda_{\rm Edd}$ when deriving their BH masses. Based on SED fitting, they use an assumed value of $\lambda_{\rm Edd} = 0.25$ as is typical of quasars of a similar redshift (Kormendy & Ho, 2013), and if RWGs accrete at super Eddington rates, as the data suggests, this means that their BH masses will be overestimates and should be considered only as upper limits.

For completion, I also present estimates of the Eddington ratio for all 15 of the RWGs with detected [OIII]λ5007 emission lines, through inserting the masses from Lonsdale et al. (2015) into Equation 4.1. These estimated $\lambda_{\rm Edd}$ values are given in Table 5.2. Here I measured a mean $\lambda_{\rm Edd} = 0.95$ with $\lambda_{\rm Edd} > 1$ for 5 sources, predicting super Eddington rates for 1/3rd of my sample. However a value of $\lambda_{\rm Edd} = 1$ is within 1σ for all four of these sources with none of there values statistically significant. With large errors on the measured values of $\lambda_{\rm Edd}$ they are likely unreliable estimates, with only the $\lambda_{\rm Edd}$ measurements for W1400 agreeing within error to those value presented in Table 5.1. However both sets of results calculate the smallest value of $\lambda_{\rm Edd}$ for W1500 and the largest value for W1951. Out of the 15 $\lambda_{\rm Edd}$ values calculated using the BH masses from Lonsdale et al. (2015), 12 of these values agree within error to Lonsdale et al.'s originally assumed value of 0.25, however this is likely due to the large errors on my measurements with the errors being $> 100\,\%$ for 12 of $\lambda_{\rm Edd}$ measurements.

Whilst the second set of calculated Eddington ratios are not in agreement with these based

Table 5.2: The measured Eddington ratios for the 15 sources with both Lonsdale et al. (2015) and [OIII]λ5007 line detections.

WISE designation	$\lambda_{\rm Edd}$
J081131.61−222522	0.49 ± 0.53
J082311.24−062408	0.29 ± 0.51
J130817.00−344754	1.87 ± 2.01
J134331.37−113609	1.89 ± 2.57
J140050.13−291924	1.22 ± 1.12
J141243.15−202011	0.11 ± 0.12
J143419.59−023543	1.02 ± 1.10
J150048.73−064939	0.03 ± 0.02
J151003.71−220311	0.51 ± 1.05
J151424.12−341100	0.66 ± 1.56
J154141.64−114409	0.68 ± 1.12
J163426.87−172139	0.56 ± 0.60
J170204.65−081108	0.50 ± 0.54
J195141.22−042024	3.97 ± 2.07
J200048.58−280251	0.42 ± 0.60

on Hα masses, their large errors and inherently assumed value of $\lambda_{\rm Edd}$ makes these results less reliable than the previous. Assuming the Eddington ratios calculated with the Hα BH masses are most reliable, I predict that RWGs do accrete at super Eddington rates and can significantly show this for five sources.

5.2.2 Mass Corrections and Comparisons

With new values for the Eddington ratios I can recalculate the [OIII]λ5007 BH and host galaxy masses using Equations 4.1 and 4.2. Table 5.3 presents the corrected masses using both sets of Eddington ratios discussed above. Whilst I believed the Eddington ratios calculated from the Lonsdale et al. (2015) masses to be less reliable due to the inherently assumed value of $\lambda_{\rm Edd} = 0.25$, the corrected masses are given here for completeness.

The [OIII]λ5007 masses recalculated using the new Eddington ratio values from Table 5.1 are a mean of ~ 0.68 dex lower than my original masses, and consistent with the Hα masses they were derived from. With the originally calculated [OIII]λ5007 masses the closest in comparison to those calculated by other works, a reduction of the BH masses now however means that they only agree within error for one source.

Figure 5.1 shows the corrected masses from Table 5.3 in comparison to my originally cal-

Table 5.3: The corrected BH and host galaxy masses for using the new values of λ_{Edd} calculated from the Hα and Lonsdale et al. BH masses.

WISE designation	λ_{Edd} from Table 5.1		λ_{Edd} from Table 5.2	
	$\log\left(\frac{M_{BH}}{M_\odot}\right)$	$\log\left(\frac{M_{Host}}{M_\odot}\right)$	$\log\left(\frac{M_{BH}}{M_\odot}\right)$	$\log\left(\frac{M_{Host}}{M_\odot}\right)$
J081131.61−222522	7.27 - 7.31	9.74 - 10.04	8.69 - 8.73	11.16 - 11.46
J082311.24−062408	8.32 - 8.35	10.58 - 10.94	9.18 - 9.22	11.44 - 11.81
J130817.00−344754	7.91 - 7.97	10.2 - 10.58	9.04 - 9.1	11.33 - 11.71
J134331.37−113609	-	-	8.88 - 9.23	10.88 - 11.65
J140050.13−291924	8.29 - 8.55	10.58 - 11.15	9.04 - 9.3	11.33 - 11.90
J141243.15−202011	7.84 - 7.93	10.08 - 10.50	9.10 - 9.19	11.34 - 11.76
J143419.59−023543	7.88 - 8.01	10.08 - 10.56	8.90 - 9.03	11.10 - 11.58
J150048.73−064939	8.35 - 8.44	10.88 - 11.20	9.36 - 9.44	11.70 - 12.08
J151003.71−220311	7.28 - 7.33	9.76 - 10.06	8.66 - 8.71	11.19 - 11.47
J151424.12−341100	-	-	8.33 - 8.68	10.81 - 11.41
J154141.64−114409	8.15 - 8.26	10.3 - 10.77	8.89 - 9.00	11.2 - 11.62
J163426.87−172139	8.34 - 8.36	10.22 - 10.7	8.90 - 8.92	11.05 - 11.43
J170204.65−081108	-	-	9.36 - 9.86	11.24 - 12.20
J195141.22−042024	7.86 - 8.06	10.17 - 10.68	8.90 - 8.90	11.21 - 11.52
J200048.58−280251	-	-	8.78 - 9.00	10.86 - 11.47

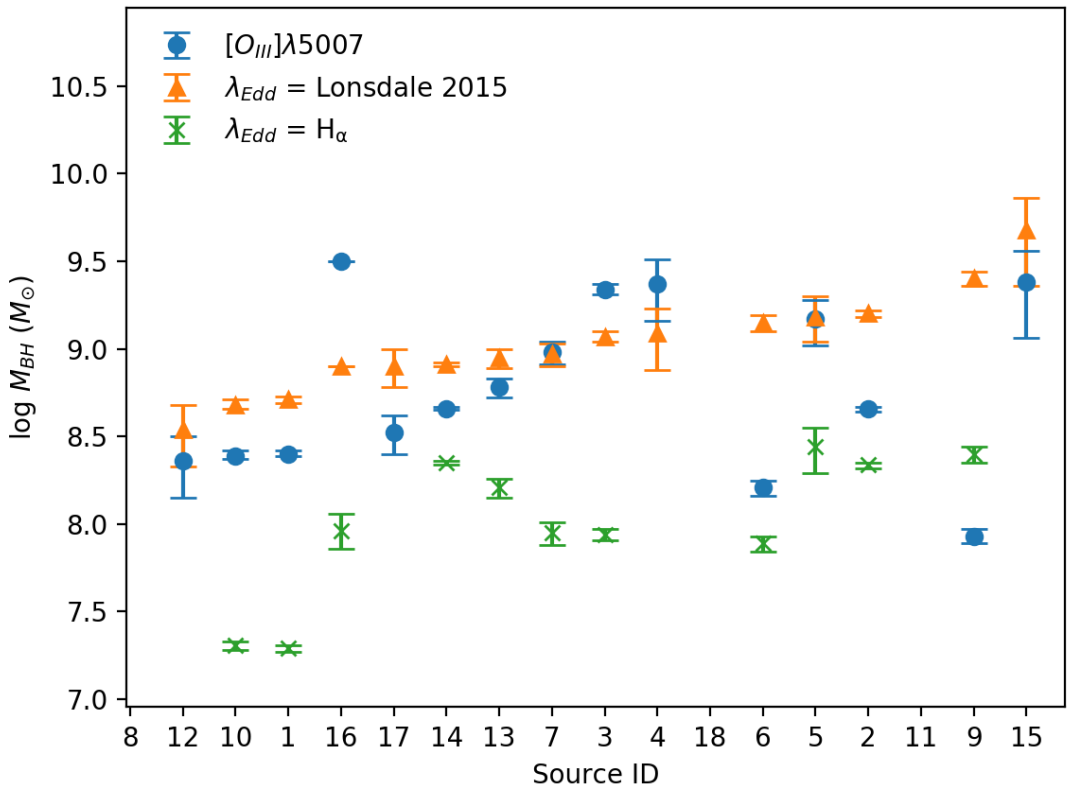

Figure 5.1: The corrected BH masses using the $\lambda_{\rm Edd}$ values from Tables 5.1 and 5.2. Source ID is used as a shorthand for the galaxy ID as in the previous chapter.

culated [OIII]λ5007 BH masses. The masses are ordered based in the BH mass published in Lonsdale et al. (2015) with the source ID shorthand the same as in Chapter 4. There is no agreement within error between the original BH masses and those with $\lambda_{\rm Edd}$ corrections based on the Hα BH mass. For those with $\lambda_{\rm Edd}$ corrections based on Lonsdale et al. (2015) there is agreement within error for 1/3 of the sources, but with the masses derived by Lonsdale et al. likely to be overestimates, the Hα $\lambda_{\rm Edd}$ corrected masses are more reliable, and therefore I do predict that RWGs accrete at super Eddington rates. Whilst the newly corrected BH masses are currently much lower compared to the others, additional corrections for dust obscuration would cause them to increase.

There were several advantages to performing this investigation into the [OIII]λ5007 determined BH masses rather than simply taking the Hα based masses as the most reliable. Firstly, it allowed an estimation of the Eddington ratio and shows that RWGs accrete at higher than normal and likely super-Eddington rates. Keeping the additional mass estimate also allowed for greater comparison between sources and methods. Whilst the [OIII]λ5007 masses are dependant on the Eddington ratio, the Hα masses are measured using a correlation based on another galaxy population. Keeping both mass estimates therefore allowed me to see the differences these assumptions have made. This also allowed for a independent measurement to be corrected for extinction, rather than one from which the extinction is being measured.

5.2.3 Comparison of measured Eddington Ratios

In the previous section, I predicted that 10/11 RWGs accrete at super Eddington rates based on corrections made with the Hα based BH masses. This has also been shown to be true for the similarly luminous population of HotDOGs (Jun et al., 2020), with perhaps the most famous HotDOG, and most luminous galaxy in the universe, W2246−0526 accreting at a measured Eddington ratio of $\lambda_{\rm Edd} = 2.8^{+0.9}_{-0.7}$ (Tsai et al., 2018). Figure 5.2 plots my measured Eddington ratios (given in Table 5.1) against my Hα calculated BH masses. For comparison 20,000 quasars with similar redshifts of $1.5 < z < 5$ (Shen et al., 2011) taken from SDSS DR7, have been plotted in order to investigate how my RWGs compare with typical QSOs. These comparative QSO's were also selected through cross matching with the FIRST radio catalogue and were selected such that each source had at least one emission line broader than 1000 km/s, making them suitable for comparison.

The calculated BH masses were an average 0.14 dex smaller than those catalogued by Shen et al., and lie to the left of the typical SDSS QSO mass region. I calculated a mean Eddington ratio $\sim 40 \times$ greater than Shen et al. (2011), leaving the sources lying to the upper left of this

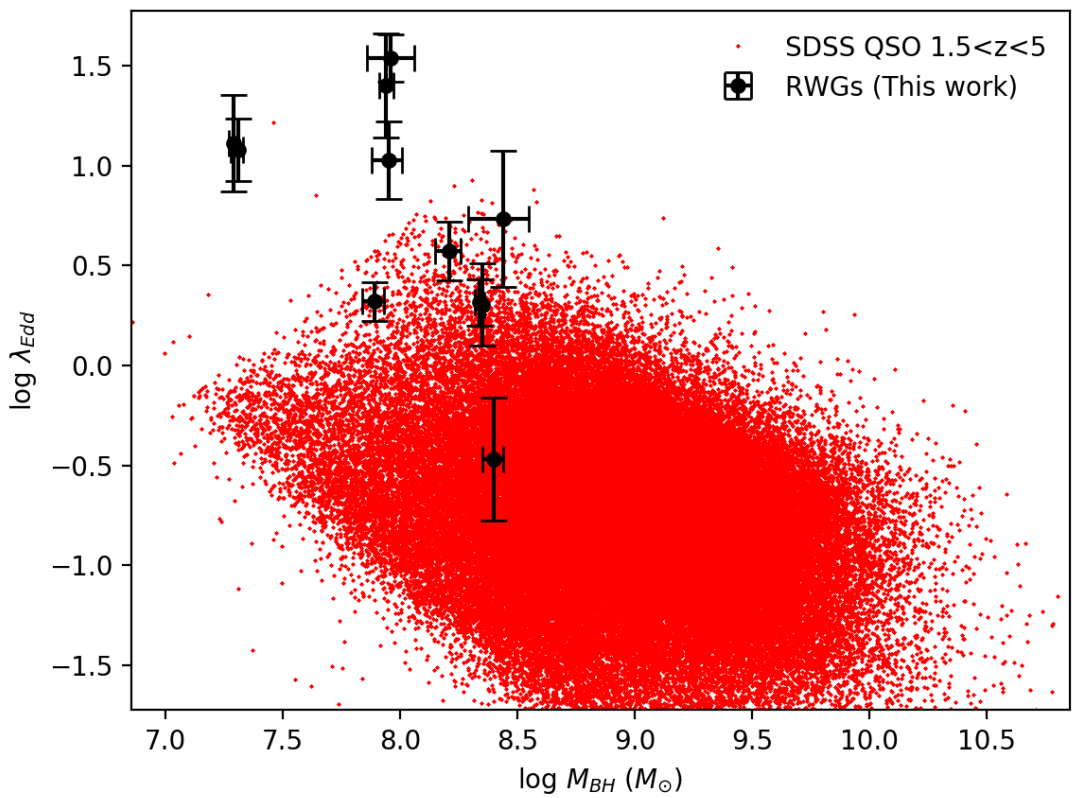

Figure 5.2: The Eddington ratio needed, such that the [OIII]λ5007 emission luminosity equates to the BH mass measured from the Hα emission line. Eddington ratio is plotted against the Hα calculated BH mass. Also included are 20000 typical QSOs from Shen et al. (2011) for comparison.

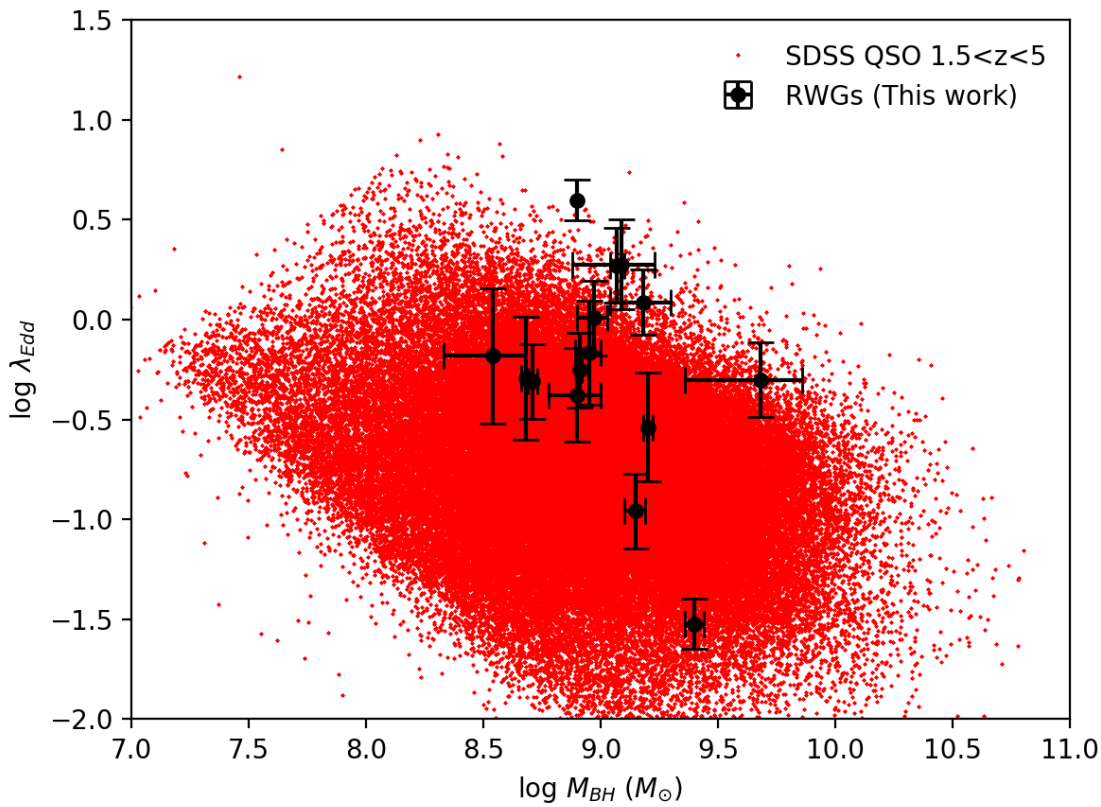

Figure 5.3: The Eddington ratio needed, such that the [OIII]λ5007 emission luminosity equates to the BH mass measured from the Lonsdale et al. emission line. Eddington ratio is plotted against the Lonsdale et al. calculated BH mass. Also included are 20000 typical QSOs from Shen et al. (2011) for comparison.

Eddington ratio - BH mass distribution. Five of the sources lie completely outside this QSO distribution with much greater values of $\lambda_{\rm Edd}$ measured. This shows that in comparison to typical quasars of a similar redshift, RWGs accrete at higher than average Eddington ratios.

Figure 5.3 shows this same comparison with the 20,000 Shen et al. QSOs for the Eddington ratios based on the Lonsdale et al. (2015) BH masses. Using these different BH masses, the data points lie a lot more central in comparison to Figure 5.2. The Lonsdale et al. BH masses are a mean $1.4\times$ greater than the mean SDSS QSO BH masses placing them centrally in the typical QSO distribution. With only one of the Eddington ratio values in Table 5.2 indicating super Eddington accretion, the SDSS QSO $\lambda_{\rm Edd}$ values are only a mean $\sim 3.6\times$ smaller.

The two different Eddington ratio corrections shown in Figures 5.2 and 5.3 lie in noticeably different areas compared to each other and typical SDSS quasars. The Eddington ratio values based on the Hα BH masses have a lower mean BH mass and with a mean $\lambda_{\rm Edd} \sim 40\times$ greater, my RWGs lie almost completely outside the SDSS QSO distribution. Comparatively, with only a slightly larger mean BH mass and Eddington ratio, the RWGs in Figure 5.3 lie centrally within the SDSS QSO distribution, with only one source lying completely outside this range. Despite the different distributions shown in the two figures, and different $\lambda_{\rm Edd}$ values calculated, both Figures show that RWGs accrete at higher than typical Eddington rates for quasars of a similar redshift.

Notable in Figures 5.2 and 5.3 is the large uncertainties in my calculated $\lambda_{\rm Edd}$ values. These large uncertainties mean that I could only significantly show that RWGs accrete at super Eddington rates for five sources in total. The individual errors propagated to these large uncertainties have a variety of origins. Firstly the measured Hα flux can not be distinguished from the [NII]$\lambda\lambda 6548, 6563$ doublet, and such I have assumed that the entirety measured flux come from the Hα emission line. This is likely not the case and whilst it will be a small amount, with some of the measured flux originating from the [NII]$\lambda\lambda 6548, 6563$ doublet the Hα flux may be overestimated by a maximum of 34%. Line blending may have also affected the measured broad line FWHM values Additionally, there is an uncertainty in the conversion factor between bolometric luminosity and the [OIII]$\lambda 5007$ luminosity (Kim et al., 2013; Shen et al., 2011) adding to the measured errors on my [OIII]$\lambda 5007$ mass calculations.

Whilst there are large uncertainties in the measured $\lambda_{\rm Edd}$ values, I could still statically significantly show that five of my RWGs accrete at super Eddington rates and suggest super Eddington rates for a further five sources. Compared to typical SDSS QSOs of $1.5 < z < 5$ with a mean $\lambda_{\rm Edd} = 0.26$, I measured mean values of $\lambda_{\rm Edd} = 10.11$ and $\lambda_{\rm Edd} = 0.98$ respectively for Hα and Lonsdale et al. (2015) estimations. I can therefore say that my RWGs accrete at higher

than typical Eddington rates.

5.2.4 Summary of Calculated Eddington Ratios

As λ_{Edd} is inversely proportional to BH mass, discovering the true Eddington rate of RWGs is an important factor is understanding their true mass. By equating two differently calculated BH masses, I estimated the Eddington ratio for 11 sources and find that 10 of the sources accrete at super Eddington rates as expected. This value is statistically significant for five sources, meaning that their previously measured BH masses are overestimates of their true values. Using these new values of λ_{Edd} I measured $\log\left(\frac{\mathrm{M_{BH}}}{\mathrm{M_{\odot}}}\right)$ = 7.2 - 8.5 with corresponding host masses of $\log\left(\frac{\mathrm{M_{Hst}}}{\mathrm{M_{\odot}}}\right)$ = 9.7 - 11.2 using the [OIII]λ5007 emission line.

5.3 Extinction Corrections of my Measured Masses

With the masses calculated in Chapter 4 dependent on two main assumptions, this chapter aims to investigate them and recalculate the BH and host galaxy masses where necessary. Above I showed that these RWGs accrete at higher than typical Eddington ratios. The other main assumption used throughout the previous analysis is that my measured emission line fluxes are not effected by dust extinction. The selection criteria originally outlined in Lonsdale et al. (2015) and detailed in the Chapter 4, means my selection of RWGs lie redward of the main WISE population based on a WISE W2 - W3, W1 - W2 colour plot. These RWGs are selected to be extremely luminous in the MIR and thus dominated by host dust emission. This likely indicates the proximity of substantial extinction to the central engine and means that I expect to measure high levels of dust scattering. These high levels of extinction means that the optical luminosties I previously measured are underestimates of the true unobscured values. This is an important correction to be made in order to understand how luminous my RWGs truly are and to accurately calculate their BH and host galaxy masses.

Determining the Visual Extinction

Extinction is defined as the absorption and scattering of electromagnetic radiation by dust particles between the source and the observer. This can cause reddening of radiation where the properties observed are different from that originally emitted. The amount of reddening observed can be categorised by a colour excess defined as the difference between a sources observed colour and its intrinsic colour. Colour is the magnitude difference between two wavelength bands with B - V used to classify extinction through $\mathrm{E(B-V)} = \mathrm{(B-V)_{observed}} - \mathrm{(B-V)_{intrinsic}}$. The

total visual extinction, A_V, is related to reddening through Equation 5.1 where an assumed parameter R_V relates to the size of the dust grains causing the obscuration and extinction.

$$A_V = R_V \times E(B - V) \tag{5.1}$$

Dust extinction is wavelength dependent with the amount of extinction present at each wavelength defined by an extinction law. Figure 5.4 demonstrates the different extinction predicted by the extinction models published in Cardelli et al. (1989); O'Donnell (1994); Fitzpatrick (1999); Calzetti et al. (2000); Fitzpatrick & Massa (2007). There is little difference between these extinction models, with the exception of that by Calzetti et al. who ignore the extinction 'bump' at 2175 Å. Following Greene & Ho (2005), as before, I used the extinction model by Cardelli et al. to estimate the visual extinction, A_V, and reddening, E(B-V), as shown by the blue line in Figure 5.4. Unlike others, this model differs for the observed wavelength range required and its development specifically included observation in the NIR, making it most suitable to correct my NIR emission lines. I later repeated this same analysis instead using the extinction law defined by Calzetti et al. (2000), as it differs most from the shown in Figure 5.4. This law is most suitable for star forming galaxies, however as later discussed in Chapter 6, at least one RWG appears of this nature, making this a useful model to compare to. Unlike the model by Cardelli et al., Calzetti et al. (2000) ignore the 'bump' at 2175 Å (see Bohren & Huffman, 1983), a wavelength range that I did not consider in this work. Therefore, whilst the model is not used in the base results of this work, it may be the most suitable model for a least one RWG, and additionally shows how sensitive the extinction corrections made are to the model used.

The Cardelli et al. extinction law is dependent on a chosen value of R_V and throughout the remainder of analysis in this chapter I use the value of $R_V = 3.1$ as is true of the Milky Way, where R_V relates to the size of the dust grains. This is the same choice made for the similarly selected population of HotDOGs, and for the measurements performed in (Kim et al., 2013). Figure 5.5 shows the (Cardelli et al., 1989) extinction law for 5 different values of R_V centred around $R_V = 3.1$ to show how this chosen value effects the amount of extinction measured at my wavelengths of interest. At a value $A_V = 1$ mag, an error of $R_V = 3.1 \pm 1$ produces $A_\lambda = 0.82^{+0.02}_{-0.04}$ at $\lambda = 6562$ Å (Hα), $A_\lambda = 1.12^{-0.03}_{-0.05}$ at $\lambda = 5007$ Å ([OIII]λ5007) and $A_\lambda = 1.16^{-0.04}_{-0.07}$ at $\lambda = 4861$ Å (Hβ). This error corresponds to a $\sim 9\%$ flux difference assuming my mean measured Hα emission line flux. Whilst an important factor, this shows that my choice of $R_V = 3.1$ was unlikely to have had a significant impact on my extinction corrected fluxes and subsequently corrected BH masses. Cardelli et al. (1989) also note that a choice of $R_V < 5$ does not significantly alter the results of their model. I therefore felt confident proceeding with my chosen value of $R_V = 3.1$,

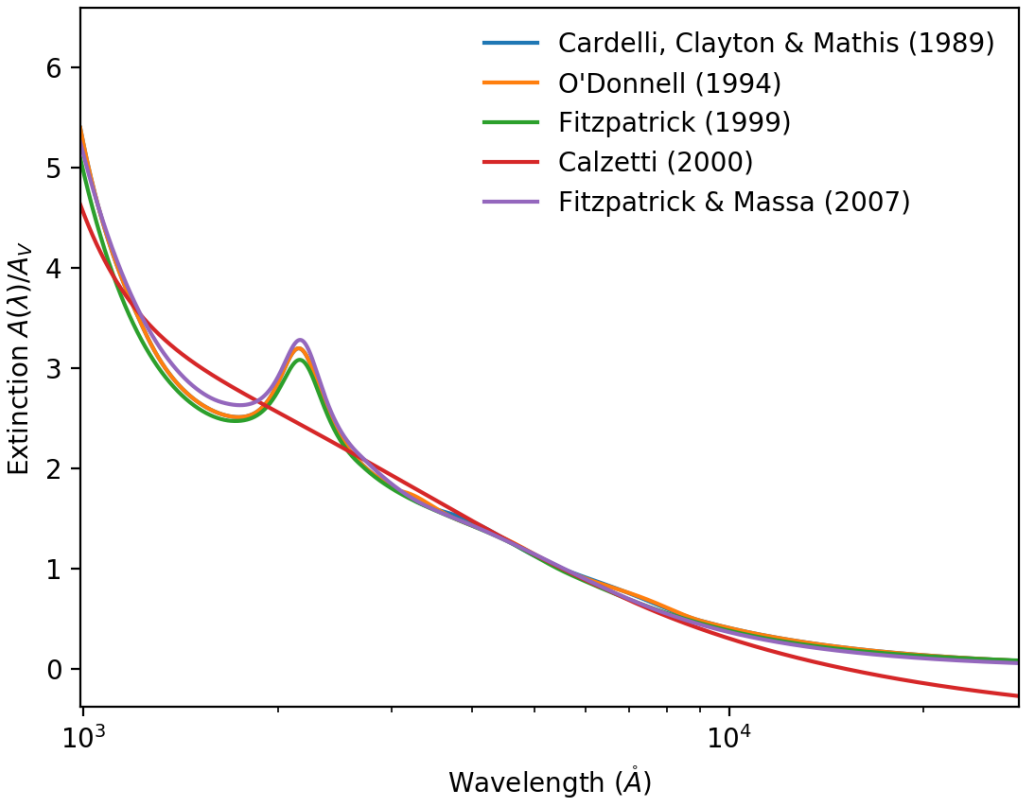

Figure 5.4: The measured value of $\left\langle \frac{A_\lambda}{A_V} \right\rangle$ estimated by five different extinction models assuming $A_V = 1$ and $R_V = 3.1$ as in Milky Way based extinction laws..

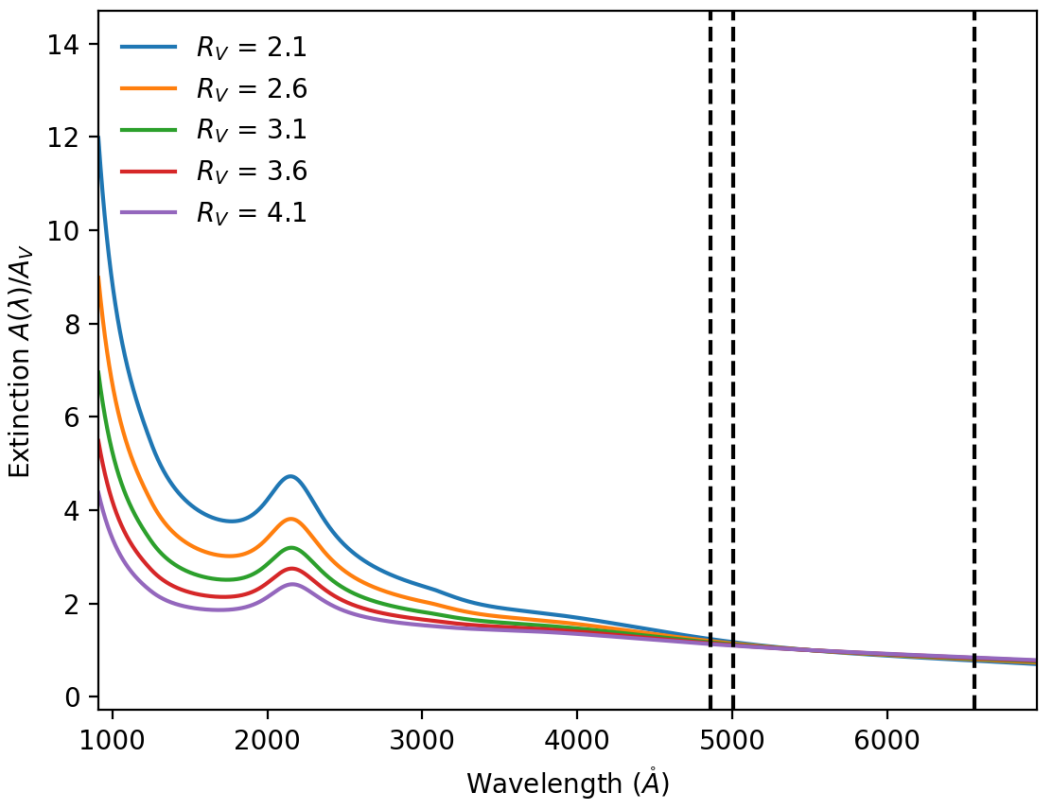

Figure 5.5: The measured value of $\left\langle \frac{A_\lambda}{A_V} \right\rangle$ estimated for five different values of R_V assuming $A_V = 1$ and using the extinction law from Cardelli et al. (1989). The vertical lines represent the rest wavelengths of the Hβ, [OIII]λ5007 and Hα emission lines.

a standard value for the diffuse ISM (Cardelli et al., 1989) and an assumption of a Milky Way based extinction law, for the rest of this chapter.

The R_v dependent (Cardelli et al., 1989) extinction law takes the form given by Equation 5.2. For the optical to NIR region that my emission lines of interest are situated in, ($0.3\,\mu\mathrm{m}^{-1} \leq x \leq 1.1\,\mu\mathrm{m}^{-1}$), $y = x - 1.82$ with the values of $a(x)$ and $b(x)$ are given by equations 5.3 and 5.4.

$$\left\langle \frac{A_\lambda}{A_V} \right\rangle = a(x) + b(x)/R_V \tag{5.2}$$

$$a(x) = 1+0.17699y-0.50447y^2-0.02427y^3+0.72085y^4+0.01979y^5-0.77530y^6+0.32999y^7 \tag{5.3}$$

$$b(x) = 1.41338y+2.28305y^2+1.07233y^3-5.38434y^4-0.62251y^5+5.30260y^6-2.09002y^7 \tag{5.4}$$

Highly wavelength dependent, extinction corrections should be applied per individual wavelength of a spectrum rather than correcting the measured emission line flux for the extinction value at that central wavelength. Using a measured value of the visual extinction A_V, the measured flux at a particular wavelength can be de-reddened using Equation 5.5.

$$\mathrm{f}_\lambda\,(\mathrm{de-reddened}) = \mathrm{f}_\lambda\,(\mathrm{Observed}) \times 10^{0.4\times\left\langle \frac{\mathrm{A}_\lambda}{\mathrm{A}_\mathrm{V}} \right\rangle} \tag{5.5}$$

The easiest way to estimate the extinction in the V band is through using the Balmer decrement (Domínguez et al., 2013; Kim et al., 2013; Greene & Ho, 2005). This relies on the measured ratio of the Hα and Hβ Balmer line fluxes, stating that a flux ratio that differs from the optical depth value expected from case-B recombination, Hα/Hβ = 2.86, is due to dust extinction. Case-B recombination is where photons above 13.6 eV are not reabsorbed during the radiative decay of an electron from an unbound to a bound state of Hydrogen. Using the measured Balmer line fluxes and the extinction model from Cardelli et al. (1989), Equation 5.6 can be used to calculate the visual extinction in magnitudes.

$$A_V = \frac{2.5 \times \log \frac{f_{H\alpha}}{f_{H\beta}} - 2.5 \times \log 2.86}{\left\langle \frac{A_{H\alpha}}{A_V} \right\rangle - \left\langle \frac{A_{H\beta}}{A_V} \right\rangle} \tag{5.6}$$

This section uses the equations described above to estimate the visual extinction and reddening affecting my measured RWG fluxes and correct their measured BH and host galaxy masses for these values. This correction then allowed me to determine just how bright and massive RWG

really are. I did this first for the five sources with both Balmer emission lines detected. Due to the uncertainties in the measured Hβ emission line fluxes and widths I secondly used a simulated Hβ emission line with the aim of predicting the visual extinction for all of my RWGs with detected Hα emission lines.

5.3.1 Using Measured Hβ Emission Lines to Calculate Extinction.

Following work previously done (Domínguez et al., 2013; Kim et al., 2013), the Balmer decrement can be used to estimate the visual extinction of my RWGs. In the sample of 18 RWGs with detected NIR emission lines, I have 13 detections of the Hα emission line and six detections of the Hβ line. With all Hβ detected sources, except W2040, having corresponding Hα detections I can use these measured Balmer line fluxes to estimate the dust extinction for five RWGs.

Following the methods outlined above, I used the measured Hα and Hβ emission line flues, given in Table 4.2, compared to the expected value of 2.86 to measure the amount of visual extinction effecting these 5 RWGs. This was done through use of Equation 5.6 with the `python.extinction` (Barbary, 2016) package used to apply the Cardelli et al. extinction law. Finally, I used Equation 5.2 to also calculate the expected reddening present in these five sources. Whilst this entire analysis assumes a value of $R_V = 3.1$, a different value of R_V is unlikely to have had a large effect on my measured A_V values. As shown above, choosing a different R_V value within $R_V \pm 1$ produces a $\sim 7\%$ difference in the final A_V value measured, and $\sim 9\,\%$ difference in the corrected flux and I was confident proceeding under this assumed R_V value of 3.1.

Results

Table 5.4 gives the measured reddening and extinction measurements at the visual and central wavelengths of my three detected emission lines Hα, Hβ and [OIII]λ5007. I measured Hα/Hβ > 2.86 for four sources listed in Table 5.4, with only W0823 measuring $A_V < 0$[3]. Inspecting the model fits for this source (Figure 4.9), there are high levels of noise across both the Hα and Hβ Gaussian profiles with $\sim 18\%$ error on my measured Hα flux. Unlike for the majority of my sources however, there appears to be a well defined Hβ profile, implying that it had not been obscured despite the large levels of noise surrounding it. Uncertainties from the blending of the [NII]$\lambda\lambda 6548, 6563$ and Hα line profiles are also at play here, but any corrections due to this would lead to a smaller Hα/Hβ ratio measured. It is therefore possible that despite being selected as highly obscured, the observations of W0823 were not affected by dust extinction. However, even

[3] $A_V < 0$ corrections were not applied.

Table 5.4: The calculated reddening and extinction (visual and at the wavelengths of the four observed emission lines) for the five sources with both Balmer lines detected.

WISE designation	E(B-V) (mag)	A_λ (mag)				
		$\lambda = V$	$\lambda = H\alpha$	$\lambda = H\beta$	$\lambda = [OIII]\lambda5007$	$\lambda = CIV$
J082311.24−062408	$-0.03^{+0.21}_{-0.24}$	$-0.11^{+0.64}_{-0.74}$	$-0.09^{+0.52}_{-0.61}$	$-0.12^{+0.74}_{-0.57}$	$-0.12^{+0.74}_{-0.57}$	$-0.03^{+0.55}_{-0.63}$
J130817.00−344754	$0.60^{+0.39}_{-0.35}$	$1.86^{+1.21}_{-1.09}$	$1.52^{+0.99}_{-0.89}$	$2.16^{+1.42}_{-1.54}$	$2.08^{+1.36}_{-1.46}$	$0.6^{+1.02}_{-0.91}$
J140050.13−291924	$1.27^{+0.07}_{-0.08}$	$3.93^{+0.24}_{-0.25}$	$3.21^{+0.20}_{-0.20}$	$4.58^{+0.28}_{-0.29}$	$4.40^{+0.27}_{-0.28}$	$1.27^{+0.18}_{-0.21}$
J150048.73−064939	$1.84^{+0.07}_{-0.07}$	$5.70^{+0.23}_{-0.23}$	$4.66^{+0.19}_{-0.19}$	$6.64^{+0.27}_{-0.28}$	$6.39^{+0.26}_{-0.27}$	$1.84^{+0.18}_{-0.18}$
J195141.22−042024	$0.65^{+0.13}_{-0.14}$	$2.01^{+0.39}_{-0.43}$	$1.64^{+0.32}_{-0.35}$	$2.34^{+0.45}_{-0.49}$	$2.26^{+0.44}_{-0.45}$	$0.65^{+0.34}_{-0.36}$

with $H\alpha/H\beta < 2.86$ measured for this source, positive values of visual extinction and reddening are still within error due to the larger uncertainties in the measured flux values.

I measured $H\alpha/H\beta > 2.86$ and a value of $A_V > 2$ mag for the other four sources based on their Balmer decrement. For three of these sources a value of $A_V = 0$ was more than 3σ away so I could confidently show that these sources have high levels of dust extinction measured. For W1308 a value of $A_V = 0$ is however within 2σ.

With NIR spectroscopy of a subset of the RWGs from FIRE (Simcoe et al., 2013) on the Baade telescope, Kim et al. estimate the visual extinction for three RWGs including W1400 and W1951 based on measured Balmer decrements. For W1400 Kim et al. (2013) measured a much larger value of $\log A_V = 1.3^{+0.8}_{-0.6}$, which does not agree within error to my measured values. They additionally measured a value of $\log A_V = 0.00^{+0.5}_{-0.0}$ for W1951 which does agree within errors to my measured value. Across the large errors in their calculated A_V values and uncertainties in the measurements performed here, it is was to measure the exact value of dust extinction that effects these RWGs. However, I am confident in saying that RWGs have on the whole been successfully selected as highly obscured galaxies.

With high levels of dust extinction measured for four of these five RWGs, their measured emission line fluxes given in Table 4.2 are underestimates of their true and unobscured values. All the BH and host galaxy masses subsequently calculated will also be underestimates meaning that these RWGs were more massive BHs than I originally calculated. Correcting these BH and host galaxy masses is therefore the next step in understanding this population of galaxies.

BH and Host Galaxy Mass Corrections

I calculated the BH masses of 18 RWGs in Chapter 4 using the $H\beta$, [OIII]λ5007 and $H\alpha$ emission line fluxes and widths measured. This was done under the assumption that the measured emission line fluxes were not affected by dust and are therefore underestimates of their real values. Here I

now look to rectify this by correcting the 1D NIR for my extinction values measured above, and recalculate my BH and host galaxy masses.

With the nature of extinction being wavelength dependent, it was more difficult to measure the effect that extinction will have on my calculated masses. Rather than correcting the measured emission line fluxes for extinction and recalculating the corrected masses that way, I have corrected the original spectra. This means that I applied an extinction correction, at a chosen value of A_V, to each wavelength point in the 1D NIR spectra, ie. I corrected the entire spectra for extinction. I then refitted this data, using the methods described in Chapter 4 to remeasure my newly extinction corrected emission line fluxes and FWHMs. A Monte Carlo approach was again taken to calculate the errors on these measured spectral properties, with 10000 spectra simulated and the standard deviation of the measured properties of these simulated lines taken as the measured line flux and width errors. In addition to allowing each data point to randomly vary between its given errors, this time the value of A_V used to de-redden the spectra was allowed to randomly vary between the errors given in Table 5.4. For this a normal distribution was used centred around my measured value of A_V, with an example shown in Figure 5.6 for W1400 with a measured value of $A_V = 3.93$ mag. These newly measured emission line flux and width values were then used to recalculate my BH masses as before.

Figure 5.7 shows an example of this process at the Hα emission line wavelength for W1400 with the original and extinction corrected line profiles shown. If I instead corrected my previously measured fluxes for the single extinction value at the emission lines central wavelength, I measured an extinction corrected flux $\sim 55\%$ greater than when correcting the entire spectrum, an overestimate of the corrected flux value. Using these corrected spectra to refit my Gaussian models allowed me to calculate new BH and host galaxy masses for the four RWGs I have measured $A_V > 0$. Table 5.5 gives the corrected BH and host galaxy mass measurements using my remeasured Hα, Hβ, [OIII]λ5007 and CIV emission lines. Note that the [OIII]λ5007 BH masses were measured assuming $\lambda_{\rm Edd} = 1$, but as I have measured super Eddington accretion rates for these sources, there true masses are likely to be in line with those determined by the Hα emission line.

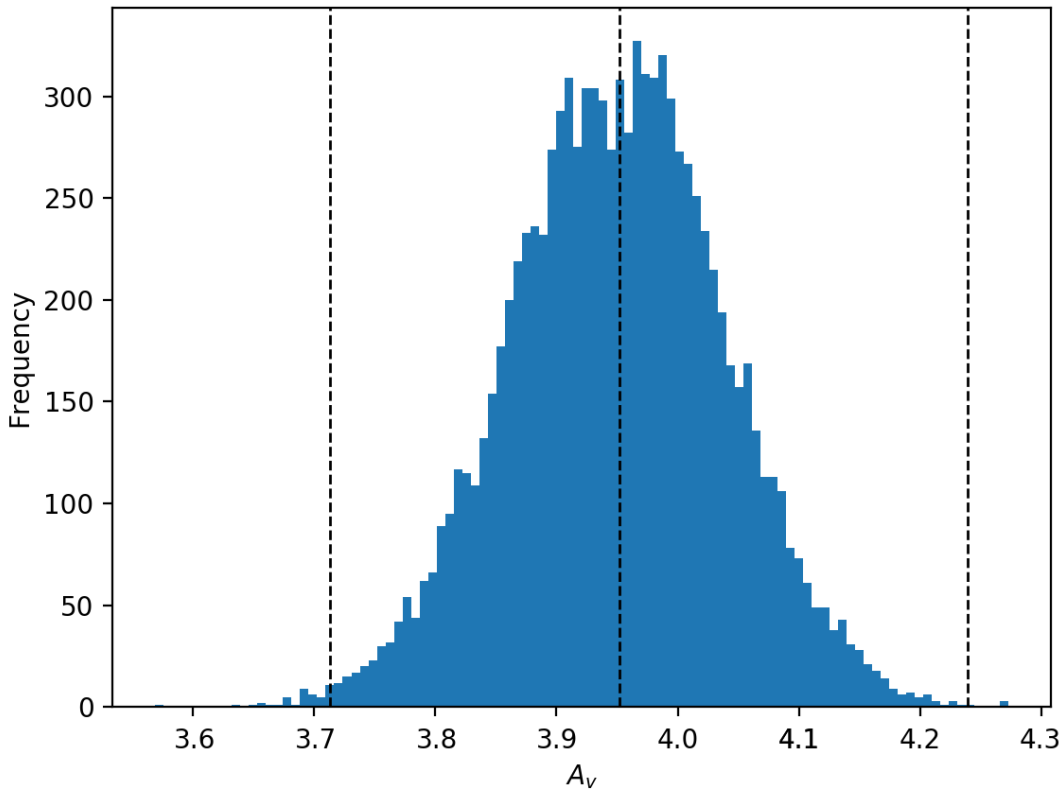

Figure 5.6: The distribution of 10000 A_V values used to de-redden the 1D spectra of W1400. The vertical black lines show the mean and standard deviations of the distribution.

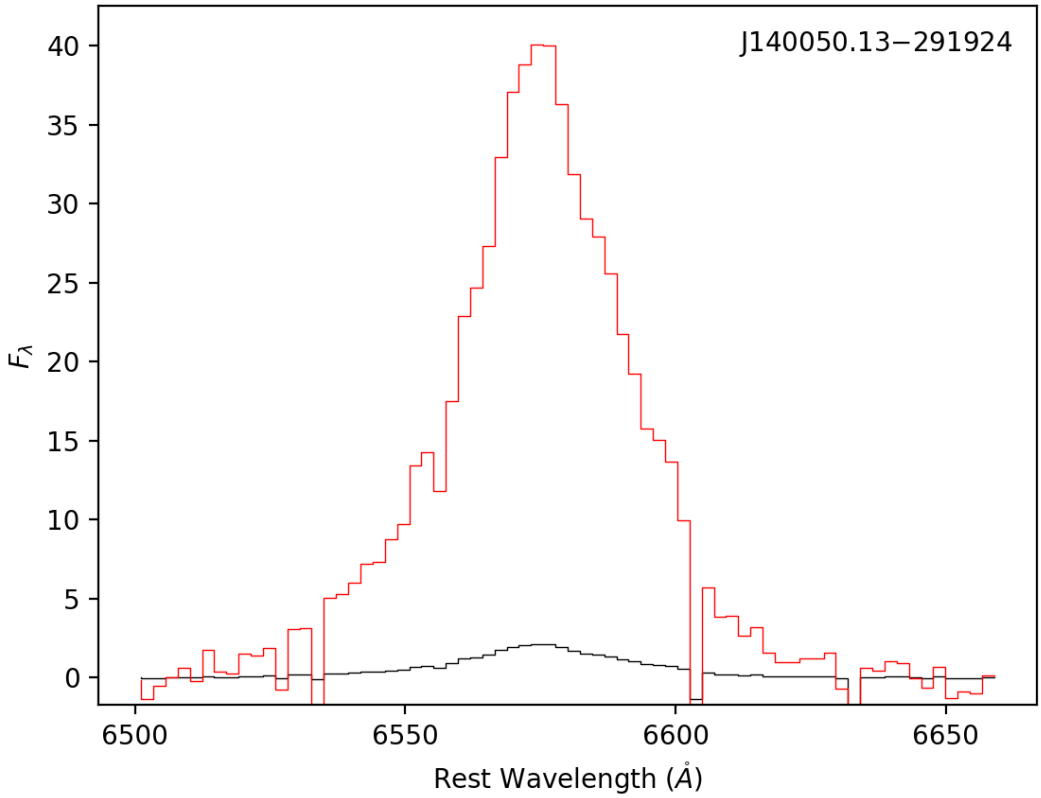

Figure 5.7: The 1D spectra of W1400 around the Hα emission line before (black) and after (red) being corrected for my measured value of extinction $A_V = 3.93\,\mathrm{mag}$. Flux densities are in the units 10^{-16} $\mathrm{erg\,s^{-1}cm^{-2}Å^{-1}}$.

Table 5.5: The BH and host galaxy masses calculated with the detected Balmer emission lines, Hα and Hβ, [OIII]λ5007 ($\lambda_{\rm Edd} = 1$) and CIV emission lines, corrected for the measured A_V values given in Table 5.4. Dashed values are given for the two sources without detected CIV emission lines

WISE designation	$\log\left(\frac{M_{BH}}{M_\odot}\right)$				$\log\left(\frac{M_{Host}}{M_\odot}\right)$			
	Hα	Hβ	[OIII]λ5007	CIV	Hα	Hβ	[OIII]λ5007	CIV
J130817.00−344754	7.85 - 8.69	7.54 - 8.15	9.65 - 10.74	9.82 - 10.07	10.83 - 11.03	9.83 - 10.75	11.94 - 13.35	12.11 - 12.67
J140050.13−291924	8.91 - 9.45	8.01 - 8.58	10.67 - 11.15	9.13 - 9.37	11.19 - 12.06	10.30 - 11.18	12.96 - 13.75	11.42 - 11.98
J150048.73−064939	9.29 - 9.90	7.99 - 9.04	10.33 - 10.62	-	11.64 - 12.54	10.39 - 11.69	12.68 - 13.26	-
J195141.22−042024	7.52 - 8.71	7.61 - 8.15	10.20 - 10.57	-	9.84 - 11.33	9.78 - 10.78	12.51 - 13.19	-

In comparison to the previously measured BH masses, these new extinction corrected masses are increased by ~ 1 order of magnitude compared to the originally calculated masses. Extinction has the weakest effect at the Hα wavelength (see Figure 5.5) with a mean BH mass increase of ~ 0.8 dex compared to ~ 0.9 dex for the Hβ masses and ~ 1.3 dex for the [OIII]λ5007 masses. This mass increase will bring my measured masses in line with those calculated by Lonsdale et al. (2015), however these are not corrected for extinction and are likely to be overestimates due to their $\lambda_{\rm Edd}$ value chosen.

Summary of Extinction Corrections using Measured Emission Lines

Due to the obscured nature of RWGs an extinction correction is an extremely important factor in understanding just how luminous these galaxies are in the NIR. Through use of the Balmer decrement, I used my measured Hα and Hβ emission line fluxes to measure the visual extinction and reddening for five of my sources with both of these emission lines detected. I measured a positive visual extinction for four sources with a mean of $A_V = 3.94$ mag, with a value of $A_V > 0$ within error for the fifth. Using these measured A_V values to correct the original 1D NIR spectra, I refitted the Hα, Hβ and [OIII]λ5007 emission lines to measure BH mass increases of $\sim$one order of magnitude in comparison to the previous masses. I now predict BH masses in the range of $\log\left(\frac{\rm M_{BH}}{\rm M_\odot}\right) = 7.5$ - 9.1 with corresponding host masses of $\log\left(\frac{\rm M_{Host}}{\rm M_\odot}\right) = 9.84$ - 12.94 using the Hα emission line. As a check on these results I repeated this methodology using the extinction law from Calzetti et al. (2000) to no change in results.

5.4 Extinction Corrections of Measured Masses using Simulated Hβ Emission Lines

Above I have used my measured Hα and Hβ emission line fluxes to estimate the visual extinction and reddening of five RWGs through use of the Balmer decrement. These visual extinction measurements led to BH mass increases in the order of one magnitude compared to my previous measurements. However, these extinction measurements rely on my Hβ data, and as previously discussed this does not appear to be most reliable due to the lack of detections and high levels of noise in the spectra. With a low number of detections, high noise in the spectra and BH mass estimates that do not agree with the other emission lines, my measured Hβ emission line width and fluxes should not be accepted without caution.

Looking back at Figure 4.11 the Hβ calculated masses lie considerably lower than others calculated in this work in the absence of extinction. Before extinction corrections were applied

there were no agreements within error for the six Hβ BH mass measurements, and they sat a mean of 0.95 dex lower than the next smallest BH mass estimate. This all implied that the BH masses calculated using Equation 4.6 are unreliable or an unidentified systematic that has not yet been accounted for. Correcting the Hβ masses for my measured value of extinction has increased them by a mean $\sim$ 0.9 dex, narrowing the gap between them and my other BH mass measurements. After correcting for the measured values of extinction, there is now agreement within error for two sources, however its highly likely this is only due to the large errors on these values, caused by propagating the errors from my A_V values and measured line properties.

Therefore, the combination of a low number of line detections and high noise in the 1D spectra leads me to conclude that the Hβ emission lines are unreliable. Discounting these measurements now allowed me to make tighter constraints on my measured BH and host galaxy masses along with making additional extinction estimates for those sources without apparent Hβ emission lines. In order to make extinction estimates for these sources, I used my BH mass measurements to simulate a realistic Hβ emission line profile. This then allowed me to estimate the visual extinction and reddening via the Balmer decrement for the 13 sources with detected Hα emission lines.

5.4.1 Simulating Hβ Emission Lines

With only six detections of the Hβ emission line, in comparison to 13 detections of Hα, I previously measured the visual extinction and reddening for five RWGs using the Balmer decrement. However, in this section I used a simulated Hβ emission line in order to measure the extinction for the other sources with detected Hα lines. My aim of these simulations was to understand just how obscured by sources truly are, with large errors on my measured A_V and E(B-V) dominated by the large uncertainties in the noisy and hard to measure Hβ emission lines.

Under the assumption that all of my emission line measurements should derive the same value of BH mass, I used a BH mass calculated from a different emission line to predict the Hβ emission line flux at a given FWHM by reversing Equation 4.6, see Equation 5.7. This means that I could calculate the expected Hβ line luminosity for a given BH mass at a specific value of FWHM. In order to make this extinction estimate as realistic as possible I could use these calculated Hβ emission line properties to simulate a realistic spectrum at the Hβ, and surrounding, wavelengths. I could then use the line luminosity to simulate a Gaussian profile of the assumed FWHM with the amplitude set such that the luminosity contained under the Gaussian is equal to the luminosity that I would expect to measure. Noise is then inserted into

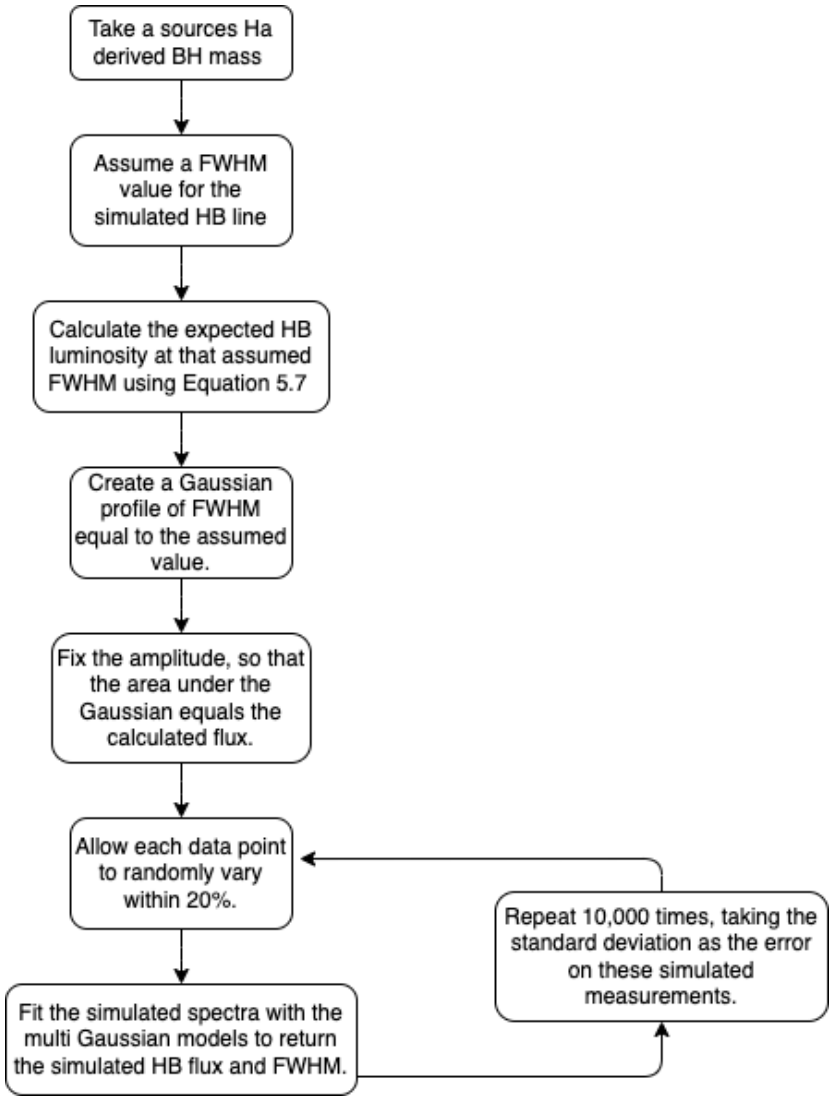

Figure 5.8: Flowchart outlined the steps taken to simulate a Hβ emission line at an assumed FWHM.

the spectra by allowing each flux density value to randomly vary within 20%[4] of its original value. These steps are outlined as a flow diagram in Figure 5.8.

$$\left(\frac{L_{\mathrm{H}_\beta}}{10^{42}\,erg\,s^{-1}}\right) = \left(\frac{\mathrm{M_{BH}}}{3.6\times10^{6}\times\mathrm{FWHM}^2_{\mathrm{H}_\beta}}\right)^{\left(\frac{1}{0.56\pm0.02}\right)} \tag{5.7}$$

These steps allowed me to simulate a Hβ line profile as realistically as possible. Following the same fitting procedure previously outlined then allowed me to measure the emission line flux of my simulated spectra as if it were real data. To account for the different amounts of noise randomly introduced into this spectra, I simulated and fit each emission line 10000 times taking the mean and standard deviation as my measured fluxes and errors respectively.

As a test, of how accurately the missing Hβ emission lines could be measured, I attempted this

[4]A value of 20% is chosen as the mean ratio of error to data point at the surrounding Hβ wavelengths for W1400 is error/data point = 0.22.

simulation for the Hβ emission line of W1400, and set the assumed FWHM to its measured value of 1200 km s^{-1} (see Table 4.2). Using Equation 5.7 and the Hα derived BH mass of W1400, I used the predicted Hβ luminosity to simulate a Gaussian profile of FWHM 1200 km s^{-1} at the needed amplitude, with each data point allowed to randomly vary within 20% to add noise. Fitting this simulated emission line with the multi Gaussian models used in Chapter 4, I measured the flux and FWHM to be within error of those measured from the observed spectra, though with errors $\sim 1.5\times$ as large due to the simulation [5]. This test was repeated for the other four sources with both Hα and Hβ line detections, to no change in findings. I was therefore confident in using these simulated Hβ emission line fluxes, as with the measured values above, to derive limits on the visual extinction using the Balmer decrement.

These simulated and measured typical Hβ line fluxes then allowed me to measure the Balmer decrements, as described above, calculating expected values of A_V and E(B-V). Whilst these measurements were not exact, these simulated line detections should provide suitable extinction measurements and allow me to estimate a lower limit to how obscured my sources are. Again using my test Hβ simulated flux, I measured $A_V = 3.87^{+0.29}_{-0.30}$ mag agreeing within error to my measured result in Table 5.4. Matching these measured results within error, I remained confident that this simulation produced realistic emission lines, however the main source of uncertainty in this process will be the FWHM value assumed.

In order to understand how these simulated values of A_V affect my BH mass measurements, I used these A_V values to de-redden my original 1D spectra. Following the same process outlined above the de-reddened spectra was fitted with my original multi Gaussian models in order to measure the de-reddened emission line fluxes and FWHMs. The standard deviation of the measured line fluxes and FWHMs from 10000 spectra are taken as the errors on these values, with each data point and an A_V value allowed to randomly vary within errors for each run. With extinction corrected emission line fluxes and FWHMs (and their corresponding errors) I was then able to recalculate my BH and host galaxy masses.

These simulations depended on two parameters; the assumed FWHM of the central Gaussian and the inserted BH mass. First I repeated these simulations using four different values for the assumed FWHM; 3000 km s^{-1}, 1480 km s^{-1}, 1315 km s^{-1} and the FWHM of the sources measured Hα FWHM. These values of FWHM are chosen as: 3000 km s^{-1} is a typical width of a very broad emission line, 1480 km s^{-1} is the mean FWHM of all my detected Hβ profiles with an underlying broad component, 1315 km s^{-1} is the mean FWHM of all my detected Hβ emission lines and the corresponding Hα FWHM should be a good indicator of the expected width.

[5] Specifically for W1400 I measured a flux of $(8.81 \pm 0.41) \times 10^{-16}\, erg\, s^{-1} cm^{-2}$ and FWHM of $1200 \pm 310\, kms^{-1}$

As the chosen FWHM is the main determining factor on my calculated A_V values, I also investigated the minimum FWHM required in order to measure a visual extinction of a certain value. I did this to find the minimum width required for A_V values of 0, 3, 5, 10 and 15 magnitudes, allowing for comparison with other extinction estimates in order to see if the widths required would be physically allowed.

The other variable parameter in this simulation is the BH mass that I assumed the simulated Hβ luminosity and width should equate to. Firstly I used the BH mass measured with the Hα emission line. These were derived from the same spectra as my measured Hβ lines, using the same fitting procedure and method to determine the BH mass. Unlike other methods, this does not assume any measured values, except the lack of extinction that I now aimed to measure, and should be the most reliable BH mass to simulate the missing Hβ emission line luminosity.

Whilst the Hα BH mass should be the most comparable I extended this study by using additional BH mass measurements to estimate the extinction present in these RWGs. With BH masses derived from the same spectra and fitted together as a compound model, my [OIII]λ5007 calculated BH mass could also be used. With central wavelengths in the same proximity, the Hβ and [OIII]λ5007 emission lines are almost equally affected by dust extinction. However, the [OIII]λ5007 BH mass estimates are dependent on the value of $\lambda_{\rm Edd}$ chosen with $\lambda_{\rm Edd} \propto 1/{\rm M_{BH}}$. I therefore used both the masses calculated in Table 4.3 with $\lambda_{\rm Edd}$ and the masses in Table 5.5 with my measured Eddington ratios from Table 5.1 in this investigation. I also used the CIV and [OIII]λ5007 derived BH masses for the four RWGs with both lines detected.

Finally I repeated this simulation using the BH masses published by Lonsdale et al. (2015) and Kim et al. (2013). The BH masses derived by Lonsdale et al. (2015) are from SED models, however they are likely overestimates due to their chosen value of $\lambda_{\rm Edd} = 0.25$. In contrast, Kim et al. (2013) derive their BH masses using measured [OIII]λ5007 line luminosities but also with an assumed value of $\lambda_{\rm Edd} = 1$.

These simulation were performed rather than using limits taken from the observed spectra. This is because I wanted to extend this investigation for as many RWGs as possible with the aim of comparing to extinction measurements made for HotDOGs. An attempt to derive limits on the Hβ fluxes was made, however it was unsuccessful due to the high level of noise in the spectra. In the majority of cases there was no indication of a potential emission line with a constant level of high noise across the expected emission line and surrounding wavelengths. Any attempt to use limits would have instead been less reliable with much larger errors. I therefore remained confident with using the simulated emission lines to derive limits, rather than taking them straight from the spectra. These simulations were performed for as many sources as possible

with both a measured Hα emission line flux and chosen BH mass required for each source.

5.4.2 Deriving Extinction Corrections with my Measured Emission Lines

I first used my previously measured Hα, [OIII]λ5007 and CIV based BH masses in order to estimate the Hβ emission lined expected flux for a given FWHM. This will then allow me to use the Balmer decrement to calculate expected levels of extinction and predict true BH mass values based on these. For each case I present the corrected BH masses in a figure, but also detail the corrected BH and host galaxy masses for the source W1400 in a table. W1400 is again chosen as a test case due to its clear line detections and measured A_V value. This allowed for a comparison of both my measured extinction and mass values but also my simulated FWHMs.

Using the Hα BH Mass to Simulate a Hβ Line Profile

I first assumed that the measured Hα and Hβ derived BH masses should be equal which allowed me to estimate the visual extinction and reddening for the 13 sources with measured Hα emission lines.

Table 5.6 gives my measured values of A_V and E(B-V) (in magnitudes) for the 13 sources with detected Hα emission lines at four different assumed FWHM values. I predicted positive extinction for all 13 sources using an assumed FWHM = 3000 km s^{-1} and measured a mean value of $A_V = 11.52 \pm 2.78$ mag. This value of A_V would correspond to a measured FWHM of 2821 km s^{-1} for W1400. Compared to my previously measured extinction values, I now predict that W0823 will be affected by dust extinction, as I would expect, though none of the values agree within error to those I measured. This assumed FWHM is more than 2$\times$ larger than the mean of my measured Hβ FWHM and is likely broader than the Hβ emission lines truly are.

I also measured $A_V > 0$ for all 13 sources assuming the FWHM of the Hβ line is equal to that of the Hα line. With a mean value of $A_V = 7.68 \pm 0.81$, this would be measured by a FWHM of 1999 km s^{-1} for W1400. I again predicted a positive value of extinction for W0823, though none of these values agree within error to my measured values.

Assuming FWHM = 1480 km s^{-1} I measured $A_V > 0$ for 12 sources with a mean value of $A_V = 3.62 \pm 2.78$ corresponding to a FWHM of 1390 km s^{-1} for W1400. The simulated value of A_V agree within error for my measurement of W1400, this is not unexpected with 1480 km s^{-1} being within 5% of my measured Hβ FWHM including the large error on this value.

Finally with the assumption of FWHM = 1315 km s^{-1} I measured a mean $A_V = 2.23 \pm 0.21$ with $A_V > 0$ for 11 sources. In line with my measured A_V values I don't expect W0823 to be affected by dust extinction at this FWHM, nor do I expect W1513 to be affected at this

assumed width. These measured extinction values agree within error for two of the measured values allowing me confidence in my simulations as 1315 $\mathrm{km\,s^{-1}}$ is within error for my measured Hβ FWHM of 1200 ± 260 $\mathrm{km\,s^{-1}}$ for W1400. With these simulations being so dependent on FWHM this is a good sign. As a final check on these simulations I inputted my measured Hβ FWHM for the five sources with measured Balmer lines and find my simulated A_V values to agree within error for all sources except W0823 where I measure larger extinction values.

Table 5.6: The calculated reddening and extinction for my 13 sources with detected Hα emission lines, assuming different FWHMs and that the Hβ and Hα BH masses are the same. Results are given in magnitudes.

WISE Designation	FWHM = 3000 km s^{-1}		FWHM = Hα		FWHM = 1480 km s^{-1}		FWHM = 1315 km s^{-1}	
	A_V	E(B-V)	A_V	E(B-V)	A_V	E(B-V)	A_V	E(B-V)
J081131.61−222522	$15.07^{+3.71}_{-1.80}$	$4.86^{+1.2}_{-0.58}$	$6.83^{+2.79}_{-1.58}$	$2.2^{+0.90}_{-0.51}$	$7.17^{+2.82}_{-1.59}$	$2.31^{+0.91}_{-0.51}$	$5.84^{+2.70}_{-1.56}$	$1.88^{+0.87}_{-0.50}$
J082311.24−062408	$8.64^{+3.36}_{-3.36}$	$2.79^{+1.08}_{-1.08}$	$8.20^{+3.35}_{-3.35}$	$2.65^{+1.08}_{-1.08}$	$0.73^{+3.18}_{-3.18}$	$0.24^{+1.02}_{-1.02}$	$-0.59^{+3.14}_{-3.14}$	$-0.19^{+1.01}_{-1.01}$
J130817.00−344754	$14.43^{+2.71}_{-1.76}$	$4.65^{+0.87}_{-0.57}$	$7.66^{+2.19}_{-1.58}$	$2.47^{+0.71}_{-0.51}$	$6.52^{+2.11}_{-1.55}$	$2.10^{+0.68}_{-0.5}$	$5.20^{+2.02}_{-1.51}$	$1.68^{+0.65}_{-0.49}$
J140050.13−291924	$12.23^{+1.22}_{-0.95}$	$3.94^{+0.39}_{-0.31}$	$8.37^{+1.02}_{-0.83}$	$2.70^{+0.33}_{-0.27}$	$4.32^{+0.82}_{-0.71}$	$1.39^{+0.26}_{-0.23}$	$3.00^{+0.76}_{-0.67}$	$0.97^{+0.24}_{-0.21}$
J141243.15−202011	$11.23^{+3.43}_{-3.43}$	$3.62^{+1.11}_{-1.11}$	$7.64^{+3.34}_{-3.34}$	$2.47^{+1.08}_{-1.08}$	$3.32^{+3.24}_{-3.24}$	$1.07^{+1.04}_{-1.04}$	$2.00^{+3.20}_{-3.20}$	$0.65^{+1.03}_{-1.03}$
J143419.59−023543	$11.06^{+4.51}_{-1.82}$	$3.57^{+1.46}_{-0.59}$	$7.71^{+3.96}_{-1.73}$	$2.49^{+1.28}_{-0.56}$	$3.15^{+3.35}_{-1.62}$	$1.02^{+1.08}_{-0.52}$	$1.83^{+3.2}_{-1.59}$	$0.59^{+1.03}_{-0.51}$
J143931.76−372523	$8.95^{+3.57}_{-3.57}$	$2.89^{+1.15}_{-1.15}$	$5.59^{+3.48}_{-3.48}$	$1.8^{+1.12}_{-1.12}$	$1.04^{+3.37}_{-3.37}$	$0.34^{+1.09}_{-1.09}$	$-0.28^{+3.34}_{-3.34}$	$-0.09^{+1.08}_{-1.08}$
J150048.73−064939	$11.00^{+1.44}_{-1.04}$	$3.55^{+0.47}_{-0.34}$	$8.27^{+1.29}_{-0.96}$	$2.67^{+0.42}_{-0.31}$	$3.09^{+1.02}_{-0.81}$	$1.00^{+0.33}_{-0.26}$	$1.77^{+0.95}_{-0.77}$	$0.57^{+0.31}_{-0.25}$
J151003.71−220311	$14.89^{+4.83}_{-4.83}$	$4.80^{+1.56}_{-1.56}$	$6.81^{+13.49}_{-4.64}$	$2.20^{+4.35}_{-1.50}$	$6.99^{+13.9}_{-4.65}$	$2.25^{+4.48}_{-1.50}$	$5.67^{+11.65}_{-4.62}$	$1.83^{+3.76}_{-1.49}$
J151310.42−221004	$6.41^{+3.05}_{-1.74}$	$2.07^{+0.98}_{-0.56}$	$8.73^{+3.29}_{-1.8}$	$2.82^{+1.06}_{-0.58}$	$-1.50^{+2.36}_{-1.53}$	$-0.48^{+0.76}_{-0.49}$	$-2.82^{+2.26}_{-1.49}$	$-0.91^{+0.73}_{-0.48}$
J154141.64−114409	$10.40^{+2.85}_{-2.85}$	$3.36^{+0.92}_{-0.92}$	$8.02^{+2.79}_{-2.79}$	$2.59^{+0.90}_{-0.90}$	$2.5^{+9.50}_{-2.66}$	$0.81^{+3.07}_{-0.86}$	$1.17^{+8.57}_{-2.63}$	$0.38^{+2.76}_{-0.85}$
J163426.87−172139	$9.48^{+3.78}_{-2.12}$	$3.06^{+1.22}_{-0.68}$	$8.21^{+3.63}_{-2.09}$	$2.65^{+1.17}_{-0.67}$	$1.58^{+2.97}_{-1.92}$	$0.51^{+0.96}_{-0.62}$	$0.25^{+2.85}_{-1.88}$	$0.08^{+0.92}_{-0.61}$
J195141.22−042024	$16.05^{+3.14}_{-3.14}$	$5.18^{+1.01}_{-1.01}$	$7.76^{+2.94}_{-2.94}$	$2.50^{+0.95}_{-0.95}$	$8.14^{+2.95}_{-2.95}$	$2.63^{+0.95}_{-0.95}$	$6.82^{+2.92}_{-2.92}$	$2.20^{+0.94}_{-0.94}$

These simulated and measured A_V values were used to de-redden my X-shooter spectra and remeasure my BH and host galaxy masses. With the $\lambda_{\rm Edd}$ dependency of my [OIII]λ5007 BH masses, I have focused on correcting my Hα derived BH masses and the ranges of masses calculated at each assumed FWHM is shown in Figure 5.9. However, for completeness the Hα and [OIII]λ5007 corrected BH masses for W1400 are given in Table 5.12.

In comparison to my previous BH mass measurements, these extinction corrections can cause increases of $\sim$ 2 dex leading to nonphysically large BH and host galaxy masses at a FWHM of 3000 km s^{-1}. The masses measured using my mean FWHM of 1480 km s^{-1} are much more reasonable with an increase of $\sim$ 0.5 dex for my BH and host galaxy masses. This $\sim$ 0.5 dex increase means I measured corrected BH masses in the range of $\log\left(\frac{\rm M_{BH}}{\rm M_\odot}\right) = 8.66$ - 9.14, matching Hα calculated masses of radio quiet QSOs at z = 2 (Orellana, G. et al., 2011), and SDSS z = 6 QSOs (Kurk et al., 2008). These masses may be scaled with chosen $\lambda_{\rm Edd}$ values, but it is clear more investigation in this area is needed, likely with additional measured Hβ profiles required to know the true extent of extinction corrections in RWGs.

Whilst the Hα derived BH mass is used to help scale the simulated Hβ emission line in order to estimate the extinction, it is dependent on the both the source redshift and FWHM as well as the flux. These different factors have caused large errors on my final calculated BH mass values due to the host of errors propagated through to this final calculation. These error sources were included throughout the simulation of the Hβ emission lines, where measured flux and FWHM values were allowed to randomly vary within their measured errors. Spectral noise was also randomly varied. Including the measured flux uncertainties, spectral noise and line blending, the corrected masses presented here are large ranges but should provide a good estimate for the true values of the masses of these 13 RWGs.

As these A_V values are so dependent on the assumed FWHM, I also investigated the minimum FWHM required to predict a certain extinction level. Table 5.7 shows these for values of A_V = 0, 3, 5, 10 and 15 magnitudes, with the relation between measured A_V, E(B-V) and minimum FWHM required shown for W1400 in Figure 5.10. This shows the minimum values required for a certain A_V value to be derived with the corresponding error region plotted as a shaded region.

As expected the minimum FWHM required increases with measured A_V value. These minimum A_V values showed that I would require a mean measured Hβ FWHM of 1100 ± 270 km s^{-1} in order to measure a value of $A_V > 0$. The two sources that require the largest FWHM's measured are W0823 and W1513 (which has the lowest calculated Hα BH mass), whilst W1951 requires the narrowest simulated line of 716 km s^{-1} in order to measure $A_V > 0$.

These simulations have shown that these RWGs have successfully been selected as highly

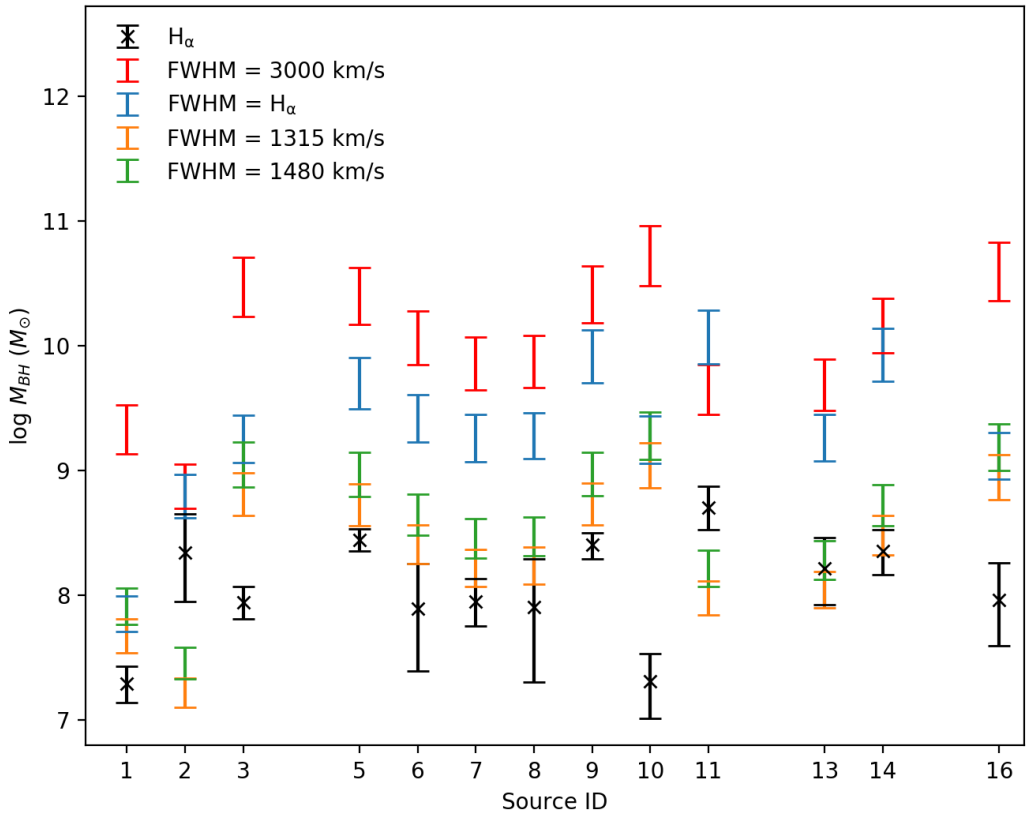

Figure 5.9: The corrected Hα derived BH masses when I use the Hα BH mass to predict the expected measures of extinction. Source ID corresponds to the source labelling system given in Table 4.2.

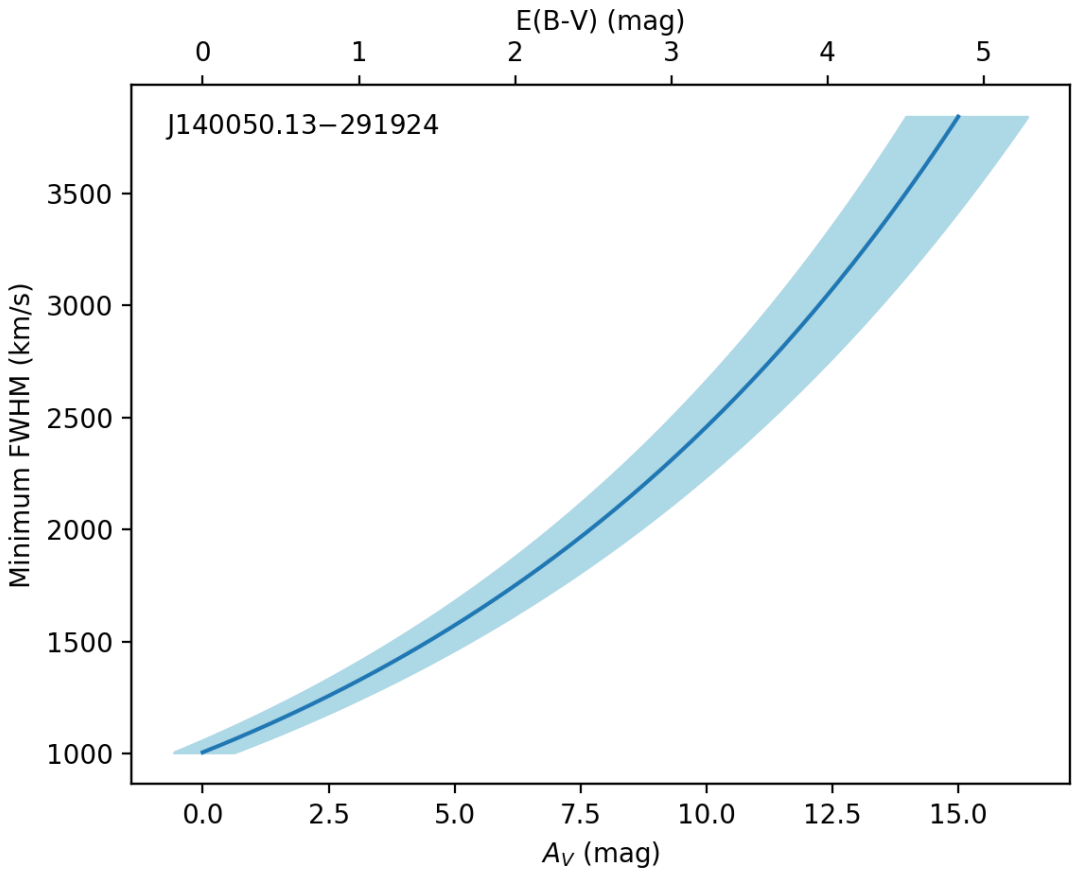

Figure 5.10: The FWHM of a simulated Hβ emission line required to measure an A_V of a certain value. This is shown for W1400 available when assuming that the Hβ emission line calculated mass is the same as that from Hα. The shaded blue area represents the error region.

Table 5.7: The minimum FWHMs required for different values of visual extinction, based on the Hα calculated BH masses

WISE Designation	Minimum FWHM ($\mathrm{km\,s^{-1}}$) required				
	$A_V = 0$ mag	$A_V = 3$ mag	$A_V = 5$ mag	$A_V = 10$ mag	$A_V = 15$ mag
J081131.61−222522	781	1021	1222	1915	2984
J082311.24−062408	1338	1814	2171	3402	5302
J130817.00−344754	827	1081	1294	2028	3160
J140050.13−291924	1007	1317	1576	2469	3849
J141243.15−202011	1110	1438	1719	2686	4196
J143419.59−023543	1118	1461	1749	2740	4271
J143931.76−372523	1349	1763	2108	3293	5146
J150048.73−064939	1124	1469	1759	2756	4295
J151003.71−220311	794	1037	1241	1945	3032
J151310.42−221004	1694	2215	2650	4153	6473
J154141.64−114409	1186	1550	1855	2907	4530
J163426.87−172139	1287	1682	2013	3155	4917
J195141.22−042024	716	935	1119	1754	2734

obscured sources, with a minimum FWHM of ~ 1000 km s^{-1} required to have measured values of $A_V > 0$. With BH and host galaxy masses increasing by ~ 2 dex at the extremes, the assumed FWHM values of 1480 km s^{-1} and 1315 km s^{-1} produce the most reasonable results with physical BH and host galaxy mass corrections. Whilst large mass ranges, due to the various propagated errors, are presented they should provide a good estimate of the masses I could expect to measure if I had detected these Hβ emission lines.

Using the OIII ($\lambda_{\rm Edd} = 1$) BH Mass to Simulate a Hβ Line Profile

Unlike the BH masses calculated using the Hα emission lines, the [OIII]λ5007 based emission lines depend heavily on the value of $\lambda_{\rm Edd}$ chosen with $\lambda_{\rm Edd} \propto 1/{\rm M_{BH}}$. However the H$\beta$ and [OIII]λ5007 should be almost identically affected by extinction and are measured together as a compound model where both are present.

This section uses simulated emission lines to measure A_V and E(B-V), assuming that the Hβ and [OIII]λ5007 ($\lambda_{\rm Edd} = 1$) BH masses are the same. This was done for the 10 sources with both the Hα and [OIII]λ5007 emission lines detected in order to use the Balmer decrement with my measured Hα and simulated Hβ emission line fluxes. Following the exact same procedure as for the Hα BH masses, I estimated the visual extinction at four assumed widths; FWHM = 3000 km s^{-1}, the measured Hα FWHM, 1480 km s^{-1} and 1315 km s^{-1}. I also investigated the minimum FWHM required to measure A_V values of 0, 3, 5, 10 and 15 magnitudes.

Table 5.8 gives the measured A_V and E(B-V) values for the 11 sources with measured Hα and [OIII]λ5007 emission lines. With my measured [OIII]λ5007 BH masses ~ 0.4 dex larger than my Hα BH masses, the luminosity required to measure a BH mass will be much greater per specific assumed FWHM than as measured above. This means that the simulated Hβ fluxes measured here will be much larger and I am less likely to measure Hα/H$\beta > 2.86$, possibly leading to negative extinction corrections.

For an assumed FWHM of 3000 km s^{-1} I measured $A_V > 0$ for nine sources with mean $A_V = 2.38$ mag. Only the measured A_V for W1500 agrees within error to my measured extinction values with the rest of the previously measured values being larger than simulated here. With these being the broadest assumed widths and hence the smallest Hβ fluxes that I will measure here (${\rm M_{BH}} \propto$ flux $\times$ FWHM), the rest of my simulated A_V values do not agree with my measured ones. Assuming the FWHM is equal to the measured Hα FWHM I measure $A_V > 0$ for four sources with mean $A_V = -2.27$ mag. I measured $A_V > 0$ for zero sources with a mean $A_V = -5.72$ mag assuming a FWHM of 1480 km s^{-1} and $A_V > 0$ for zero sources again with a mean $A_V = -7.05$ mag assuming the FWHM = 1315 km s^{-1}. As expected zero of these simulated values agree

within error to those presented in Table 5.4.

Table 5.8: The calculated reddening and extinction for my 13 sources with detected Hα emission lines, assuming different FWHMs and that the Hβ and [OIII]λ5007 BH masses are the same. Results are given in magnitudes and errors are calculated using the standard deviation on the 10000 simulated Hβ profiles.

WISE Designation	FWHM = 3000 km s^{-1}		FWHM = Hα		FWHM = 1480 km s^{-1}		FWHM = 1315 km s^{-1}	
	A_V	E(B-V)	A_V	E(B-V)	A_V	E(B-V)	A_V	E(B-V)
J081131.61−222522	$1.15^{+0.75}_{-0.63}$	$0.37^{+0.24}_{-0.2}$	$-7.10^{+0.39}_{-0.36}$	$-2.29^{+0.12}_{-0.11}$	$-6.76^{+0.4}_{-0.37}$	$-2.18^{+0.13}_{-0.12}$	$-8.08^{+0.35}_{-0.32}$	$-2.61^{+0.11}_{-0.10}$
J082311.24−062408	$4.35^{+0.02}_{-0.02}$	$1.4^{+0.01}_{-0.01}$	$3.91^{+0.04}_{-0.04}$	$1.26^{+0.01}_{-0.01}$	$-3.56^{+0.3}_{-0.35}$	$-1.15^{+0.10}_{-0.11}$	$-4.88^{+0.34}_{-0.41}$	$-1.57^{+0.11}_{-0.13}$
J130817.00−344754	$0.42^{+1.04}_{-0.87}$	$0.14^{+0.34}_{-0.28}$	$-6.35^{+0.72}_{-0.66}$	$-2.05^{+0.23}_{-0.21}$	$-7.49^{+0.67}_{-0.62}$	$-2.42^{+0.22}_{-0.2}$	$-8.81^{+0.62}_{-0.57}$	$-2.84^{+0.20}_{-0.19}$
J140050.13−291924	$1.95^{+0.42}_{-0.5}$	$0.63^{+0.14}_{-0.16}$	$-1.90^{+0.55}_{-0.68}$	$-0.61^{+0.18}_{-0.22}$	$-5.96^{+0.68}_{-0.89}$	$-1.92^{+0.22}_{-0.29}$	$-7.28^{+0.72}_{-0.96}$	$-2.35^{+0.23}_{-0.31}$
J141243.15−202011	$4.41^{+0.09}_{-0.08}$	$1.42^{+0.03}_{-0.03}$	$0.82^{+0.05}_{-0.05}$	$0.27^{+0.02}_{-0.02}$	$-3.49^{+0.2}_{-0.22}$	$-1.13^{+0.07}_{-0.07}$	$-4.82^{+0.25}_{-0.28}$	$-1.55^{+0.08}_{-0.09}$
J143419.59−023543	$-0.66^{+0.04}_{-0.05}$	$-0.21^{+0.01}_{-0.02}$	$-4.01^{+0.16}_{-0.2}$	$-1.29^{+0.05}_{-0.06}$	$-8.56^{+0.31}_{-0.42}$	$-2.76^{+0.10}_{-0.13}$	$-9.89^{+0.35}_{-0.48}$	$-3.19^{+0.11}_{-0.16}$
J150048.73−064939	$7.20^{+2.95}_{-1.55}$	$2.32^{+0.95}_{-0.50}$	$4.47^{+2.68}_{-1.48}$	$1.44^{+0.86}_{-0.48}$	$-0.70^{+2.23}_{-1.34}$	$-0.23^{+0.72}_{-0.43}$	$-2.03^{+2.12}_{-1.31}$	$-0.65^{+0.69}_{-0.42}$
J151003.71−220311	$3.84^{+0.09}_{-0.09}$	$1.24^{+0.03}_{-0.03}$	$-4.24^{+0.2}_{-0.22}$	$-1.37^{+0.07}_{-0.07}$	$-4.07^{+0.20}_{-0.21}$	$-1.31^{+0.06}_{-0.07}$	$-5.39^{+0.24}_{-0.27}$	$-1.74^{+0.08}_{-0.09}$
J154141.64−114409	$1.07^{+0.45}_{-0.39}$	$0.35^{+0.14}_{-0.13}$	$-1.31^{+0.35}_{-0.31}$	$-0.42^{+0.11}_{-0.1}$	$-6.84^{+0.12}_{-0.12}$	$-2.21^{+0.04}_{-0.04}$	$-8.16^{+0.07}_{-0.07}$	$-2.63^{+0.02}_{-0.02}$
J163426.87−172139	$3.58^{+0.05}_{-0.05}$	$1.16^{+0.02}_{-0.02}$	$2.31^{+0.09}_{-0.10}$	$0.75^{+0.03}_{-0.03}$	$-4.32^{+0.32}_{-0.38}$	$-1.39^{+0.1}_{-0.12}$	$-5.65^{+0.37}_{-0.44}$	$-1.82^{+0.12}_{-0.14}$
J195141.22−042024	$-3.34^{+0.55}_{-0.68}$	$-1.08^{+0.18}_{-0.22}$	$-11.65^{+0.81}_{-1.13}$	$-3.76^{+0.26}_{-0.36}$	$-11.25^{+0.8}_{-1.10}$	$-3.63^{+0.26}_{-0.36}$	$-12.57^{+0.84}_{-1.18}$	$-4.05^{+0.27}_{-0.38}$

With only 15/44 simulations measuring $A_V > 0$, this simulation is unrealistic with the larger [OIII]λ5007 forcing larger Hβ fluxes, reducing the majority of my measured mass values in comparison with those originally calculated. These [OIII]λ5007 calculated BH masses are however overestimates as above I showed that RWGs accrete at super Eddington rates, and will use these Eddington corrected BH masses in the following section. Through de-reddening and refitting the original spectra, I have recalculated my BH masses assuming the values of A_V from Table 5.8.

Figure 5.11 gives the corrected BH masses at the four assumed values of FWHM. These figures clearly show the sources for which I measure $A_V < 0$ and the effect this would have on my BH mass values compared to those with no extinction corrections. They would reduce the measured Hα BH masses by ~ 2 orders of magnitude, corrections that should not be applied, indicating that these masses are much smaller than expected for this population of galaxies based on previous estimates (Lonsdale et al., 2015; Kim et al., 2013).

These masses again show the effect that a negative visual extinction measurements would have on my results. With larger values of FWHM required to predict sources with $A_V > 0$, the [OIII]λ5007 masses have allowed me to simulate Hβ emission lines of higher flux, now comparable to that measured for the Hα emission line. Table 5.9 gives the minimum FWHM required to measure an extinct source. In order to measure a value of $A_V > 0$ I required a mean FWHM = 2468 km s^{-1}, a width greater than all of my measured Hβ FWHMs. As these sources are selected to be highly obscured, this high minimum FWHM required to measure a value of $A_V > 0$ would require unreasonably broad emission lines to measure levels of obscuration in agreement with that predicted by Kim et al. (2013).

Through the assumption that the Hβ and [OIII]λ5007 BH masses should be identical, I measured $A_V > 0$ a total of 15/44 times using four different assumed FWHMs, causing a mean decrease in my calculated BH mass values by a mean ~ 2 dex. With the [OIII]λ5007 BH masses simulating larger measurements of Hβ fluxes, a mean FWHM of ~ 2450 km s^{-1} is required to measure values of A_V and E(B-V) > 0.

Using the CIV BH Mass to Simulate a Hβ Line Profile

The final extinction estimations done in this section will assume the the Hβ and CIV determined BH masses should be the same. Derived in Section 4.6, these masses are determined from the FWHM of detected CIV emission lines, whilst using the luminosity of the [OIII]λ5007 emission line as a proxy for the luminosity at 1350 Å. Unlike the [OIII]λ5007 derived BH mass used above this does not rely on an assumed Eddington ratio, but two assumed correction factors; one between the measured [OIII]λ5007 luminosity and the bolometric luminosity and from the

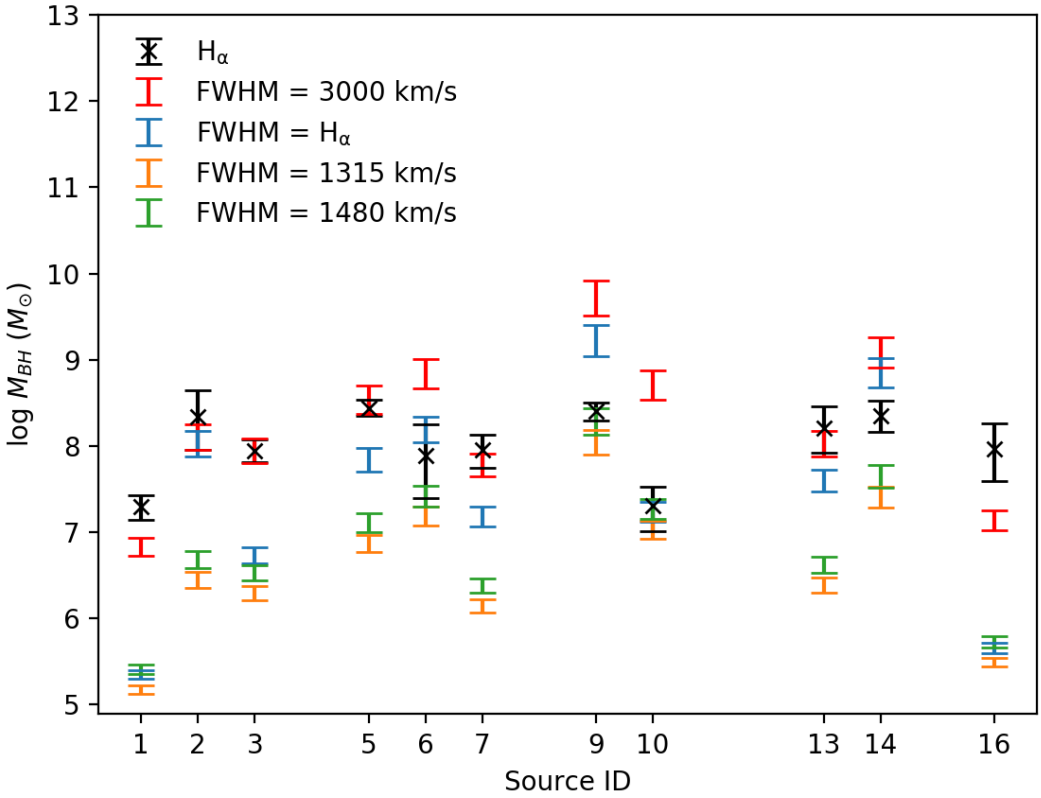

Figure 5.11: The corrected Hα derived BH masses when we use the [OIII]λ5007 BH mass to predict the expected measures of extinction. Source ID corresponds to the source labelling system given in Table 4.2.

Table 5.9: The minimum FWHMs required for different values of visual extinction based on the BH hole masses calculated using [OIII]λ5007 and assuming $\lambda_{Edd} = 1$

WISE Designation	Minimum FWHM (km s^{-1}) required				
	$A_v = 0$ mag	$A_v = 3$ mag	$A_v = 5$ mag	$A_v = 10$ mag	$A_v = 15$ mag
J081131.61−222522	2710	3541	4235	6624	10333
J082311.24−062408	2035	2660	3181	4975	7777
J130817.00−344754	3993	5218	6241	9761	15227
J140050.13−291924	2522	3296	3941	6165	9636
J141243.15−202011	2024	2644	3162	4946	7731
J143419.59−023543	3183	4160	4972	7781	12138
J150048.73−064939	1577	2061	2465	3855	6026
J151003.71−220311	2131	2784	3330	5208	8140
J154141.64−114409	2728	3565	4263	6668	10403
J163426.87−172139	2179	2848	3406	5327	8326
J195141.22−042024	4046	5287	6323	9889	15427

bolometric to the luminosity at 1350 Å. Due to their close rest wavelengths, the luminosity of the Hβ and [OIII]λ5007 emission lines should be equally affected by extinction, but at a much shorter wavelength of 1549 Å the extinction effects are $\sim 2.24\times$ greater for the CIV line.

With five detections of the CIV emission line, and 15 detections of [OIII]λ5007, I previously determined five BH masses using these properties. Four of these sources have measured Hα fluxes so their measured A_V and E(B-V) values are given below in Table 5.10. Under an assumed Hβ FWHM of 3000 km s^{-1}, I measured $A_V > 0$ for three out of four sources with mean $A_V = 0.99$ mag. I additionally measure $A_V > 0$ for three out of four sources assuming my measured Hα FWHM but measured a mean $A_V = -0.11$ mag across the four sources as it is dominated by the result for W1308. Under the assumption that my simulated Hβ emission lines have narrower FWHMs of 1480 or 1315 km s^{-1}, I predict $A_V < 0$ for all sources with mean values of $A_V = -1.57$ mag and $A_V = -1.99$ mag respectively.

Compared to the dust extinction I predict from my measured Hα and Hβ emission lines (given in Table 5.4 for five RWGs), none of my predicted A_V values agree within error for W0823, no matter the FWHM assumed, with an assumed FWHM of 1889 km s^{-1} required to match my previously measured A_V value. This value is not unlikely, but not covered by my chosen simulation range. For W1308, I previously measured $A_V > 0$ meaning that these simulated values do not agree with my measured ones, and I would require an unreasonably broad FWHM of 4760 km s^{-1}. My measured value of $A_V = 1.27$ mag for W1400 is however in agreement within error assuming a simulated Hβ emission line of FWHM 2126 km s^{-1} equal to that of my measured Hα line. Unfortunately, with no detected Hβ emission line I can't compare my simulated W1541 emission lines with my measured extinction. Compared to my measured A_V values, the simulated values for W0823 and W1400 agree within error and with similar A_V values predicted for W1541 these are therefore reasonable values to assume in order to predict the effect extinction has on the calculated BH masses.

Table 5.10: The calculated reddening and extinction for my 13 sources with detected Hα emission lines, assuming different FWHMs and that the Hβ and [OIII]λ5007 BH masses are the same. Results are given in magnitudes.

WISE Designation	FWHM = 3000 km s^{-1}		FWHM = Hα		FWHM = 1480 km s^{-1}		FWHM = 1315 km s^{-1}	
	A_V	E(B-V)	A_V	E(B-V)	A_V	E(B-V)	A_V	E(B-V)
J082311.24−062408	$1.66^{+0.15}_{-0.14}$	$5.14^{+0.47}_{-0.44}$	$1.52^{+0.15}_{-0.14}$	$4.7^{+0.46}_{-0.42}$	$-0.89^{+0.05}_{-0.05}$	$-2.77^{+0.15}_{-0.16}$	$-1.32^{+0.03}_{-0.03}$	$-4.09^{+0.1}_{-0.11}$
J130817.00−344754	$-1.47^{+0.5}_{-1.27}$	$-4.57^{+1.54}_{-3.95}$	$-3.66^{+0.56}_{-1.78}$	$-11.34^{+1.73}_{-5.53}$	$-4.02^{+0.57}_{-1.9}$	$-12.48^{+1.76}_{-5.9}$	$-4.45^{+0.58}_{-2.07}$	$-13.8^{+1.79}_{-6.41}$
J140050.13−291924	$2.22^{+0.63}_{-0.39}$	$6.89^{+1.96}_{-1.22}$	$0.98^{+0.55}_{-0.36}$	$3.04^{+1.72}_{-1.13}$	$-0.33^{+0.48}_{-0.33}$	$-1.01^{+1.49}_{-1.03}$	$-0.75^{+0.46}_{-0.32}$	$-2.33^{+1.42}_{-0.99}$
J154141.64−114409	$1.53^{+3.42}_{-0.69}$	$4.73^{+10.59}_{-2.13}$	$0.76^{+2.68}_{-0.67}$	$2.35^{+8.29}_{-2.07}$	$-1.02^{+1.89}_{-0.62}$	$-3.17^{+5.86}_{-1.93}$	$-1.45^{+1.77}_{-0.61}$	$-4.5^{+5.49}_{-1.9}$

Table 5.11: The minimum FWHMs required for different values of visual extinction based on the BH hole masses calculated using [OIII]λ5007 and assuming $\lambda_{Edd} = 1$

WISE Designation	Minimum FWHM ($\mathrm{km\,s^{-1}}$) required				
	$A_v = 0$ mag	$A_v = 3$ mag	$A_v = 5$ mag	$A_v = 10$ mag	$A_v = 15$ mag
J082311.24−062408	1896	2479	2965	4635	7234
J130817.00−344754	4517	5896	7050	11021	17229
J140050.13−291924	1621	2120	2534	3963	6185
J154141.64−114409	1966	2571	3074	4807	7502

By reddening the original spectra for the A_V values given in Table 5.10 I recalculated my Hα derived BH masses with the results given in Figure 5.12. Whilst exact masses will be given later in Table 5.12, this Figure can be used to see how the different assumed FWHM values affect the final BH mass values, with a maximum increase of $\sim$ 1 order of magnitude. At the larger assumed FWHM's these increased BH masses align more with those measured by Lonsdale et al. (2015).

With unreasonably large values required to measured positive extinction for W1308, it is interesting to investigate the minimum simulated Hβ FWHM required in order to measure a specific value of A_V. Table 5.11 gives the minimum simulated Hβ FWHM required to measure a visual extinction of 0, 3, 5, 10 or 15 magnitudes. I required a mean FWHM Hβ values of 2500, 3267, 3906, 6107 and 9538 $\mathrm{km\,s^{-1}}$ to be simulated in order to predict visual extinction of 0, 3 5, 10 and 15 magnitudes and these required widths to measure $A_V > 0$ are not unrealistic. For example, I measured the FWHM of W0823 to be 1880 $\mathrm{km\,s^{-1}}$ compared to the width of 1896 $\mathrm{km\,s^{-1}}$ which I predicted is needed to measure $A_V > 0$, whilst the predicted width for W1400 is within 2 σ of the measured value. However, I predicted an Hβ FWHM $\sim 4.4\times$ greater than measured is required for positive extinction and an unphysically broad width would be required to match the extinction measured by Kim et al. (2013).

These three previous sections have shown how different assumed Hβ BH mass values and FWHMs affect the predicted amount of extinction present. Below provides a brief comparison of the results to see which is more realistic.

Comparison of Derived Extinction Corrections

Above I have shown how assuming that the Hβ BH mass equates to other calculated BH mass values changes the predicted level of visual extinction. Now I look to compare the use of the Hα, [OIII]λ5007 and CIV determined BH masses in order to predict which set of simulations is most realistic. I did this by comparing their corrected emission line spectra at the Hα rest wavelength

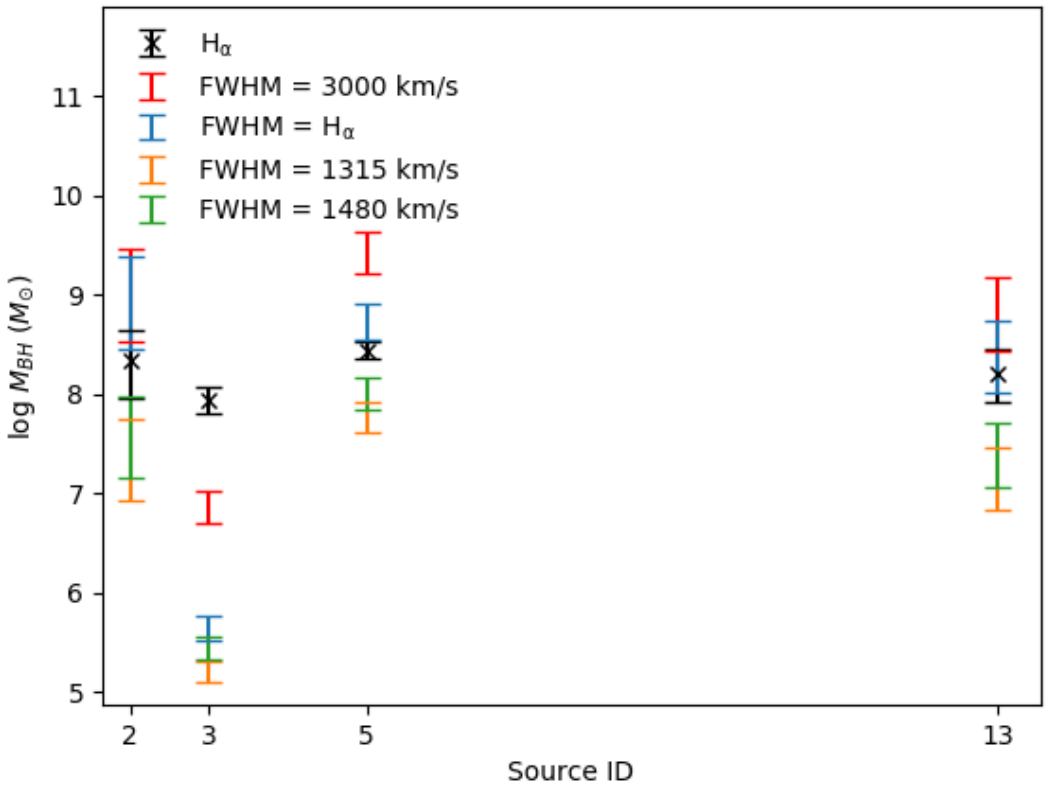

Figure 5.12: The corrected Hα derived BH masses when I use the CIV BH mass to predict the expected measures of extinction. Source ID corresponds to the source labelling system given in Table 4.2.

and by correcting the Hα, [OIII]λ5007 and CIV derived BH masses for a typical source W1400. Figure 5.13 shows the effect of the FWHM chosen on the extinction corrected spectra for W1400 at the rest wavelength of the Hα emission line. This makes it easy to compare how the assumed FWHM affects the emission line spectra, compared to the original (black) with no corrections. It also allowed for comparison between the assumed BH masses. For example no matter the assumed FWHM, under the assumption that the Hβ BH mass equals that derived from the Hα emission line, all extinction corrections will increase the measured flux of the Hα emission line and the subsequently derived BH and host galaxy masses. In comparison only a very broad assumed FWHM of $3000\,\mathrm{km\,s^{-1}}$ would cause a BH mass increase assuming the [OIII]λ5007 BH mass, whereas both assumed widths of 3000 and $2126\,\mathrm{km\,s^{-1}}$ would cause an increase in the BH mass of W1400 assuming the Hβ BH mass equates to that derived from the CIV FWHM.

Table 5.12 gives the corrected BH and host galaxy mass measurements using the Hα, [OIII]λ5007 and CIV emission lines for an example source of W1400. Here I have assumed $\lambda_{\mathrm{Edd}} = 1$ for simplicity, but the Hα derived masses are more realistic as above I proved that RWGs are likely to accrete at super Eddington rates. With the highest predicted levels of visual extinction, assuming the Hβ BH mass should equate to that calculated from the Hα emission lines provides the largest BH and host galaxy mass measurements. At the largest assumed mass there is a 2.25 dex difference between the smallest and largest Hα corrected BH masses with a mean difference of 2.21 dex across the assumed masses. This table therefore again shows how the BH mass assumed affects the final corrected BH and host galaxy masses in addition to the chosen width. At the largest assumed FWHM the Hα predicted BH mass of $\sim 2.5 \times 10^4\,\mathrm{M_\odot}$ is unrealistically huge, however at the mean FWHM, a value of $\sim 10^9\,\mathrm{M_\odot}$ is in agreement to that measured by Kim et al. (2013) for this source and to the mean BH mass predicted for HotDOGs (Jun et al., 2020).

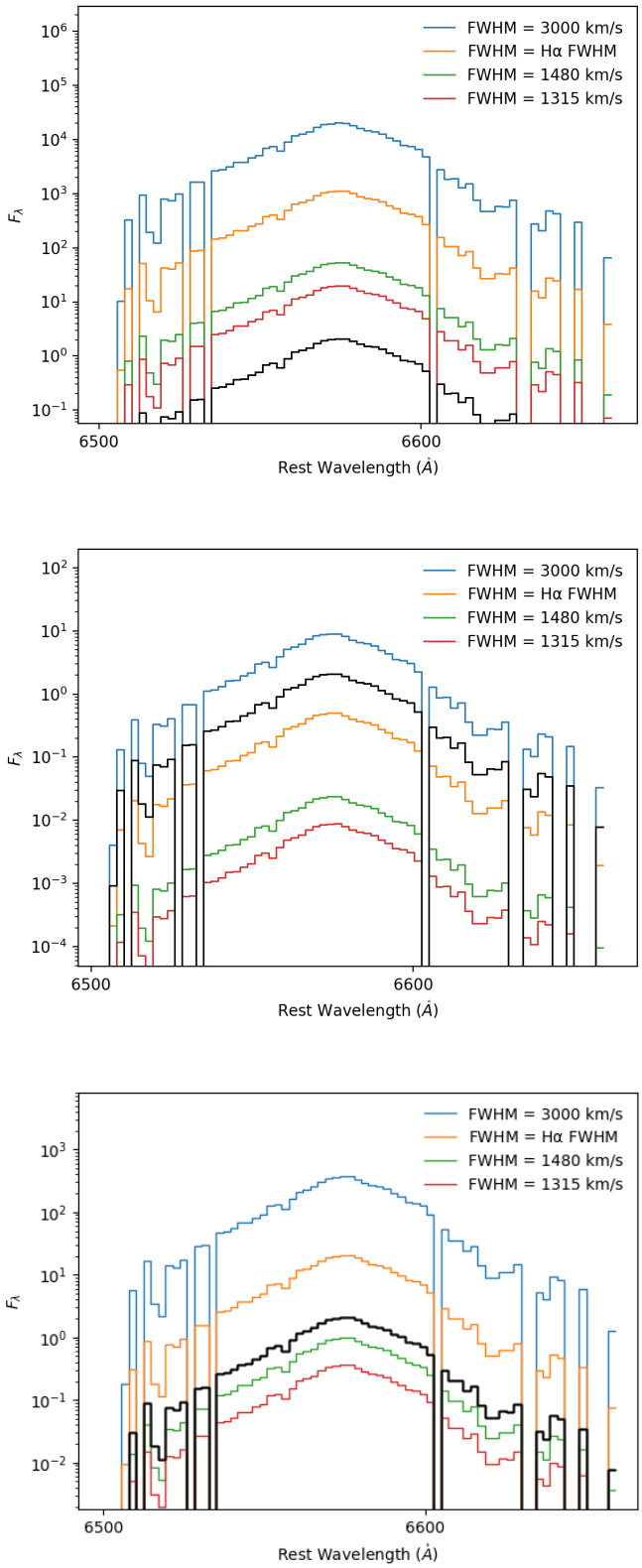

Figure 5.13: The 1D spectra in the region surrounding the Hα emission line corrected for extinction with assuming the Hβ BH mass is equivalent to the Hα, [OIII]λ5007 and CIV BH masses (from top to bottom) at different assumed FWHMs. The uncorrected spectra is shown in black with flux densities in units 10^{-16} erg s^{-1}cm^{-2}Å^{-1}.

Table 5.12: My corrected BH masses, host masses and Eddington ratio for W1400. These are calculated when my spectra are corrected for different FWHM values assuming the Hβ BH mass equals that of the Hα, Hβ and CIV masses. Note the [OIII]λ5007 BH masses assume $\lambda_{\rm Edd} = 1$.

Assumed BH mass	Assumed FWHM ($\rm km\,s^{-1}$)	A_V (mag)	Correcting the Hα BH mass $\log\left(\frac{M_{BH}}{M_\odot}\right)$	Correcting the Hα BH mass $\log\left(\frac{M_{Host}}{M_\odot}\right)$	Correcting the [OIII]λ5007 BH mass $\log\left(\frac{M_{BH}}{M_\odot}\right)$	Correcting the [OIII]λ5007 BH mass $\log\left(\frac{M_{Host}}{M_\odot}\right)$	Correcting the CIV BH mass $\log\left(\frac{M_{BH}}{M_\odot}\right)$	Correcting the CIV BH mass $\log\left(\frac{M_{Host}}{M_\odot}\right)$	$\lambda_{\rm Edd}$
Hα	3000	12.23	10.17 - 10.62	12.45 -13.23	14.72 - 14.81	17.01-17.42	11.6 - 11.84	13.88 - 14.44	24000 ± 11000
	2130[6]	8.37	9.49 - 9.90	11.78 - 12.51	10.68 - 10.92	12.97 - 13.52	13.00 - 13.09	15.28 - 15.69	2250 ± 1100
	1480	4.32	8.79 - 9.14	11.07 - 11.75	11.18 - 11.27	13.47 - 13.88	9.72 - 9.96	12.00 - 12.56	190 ± 110
	1315	3.00	8.56 - 8.89	10.84 - 11.50	10.60 - 10.67	12.89 - 13.28	9.40 - 9.64	11.69 - 12.25	80 ± 50
[OIII]λ5007	3000	1.95	8.37 - 8.70	10.66 - 11.30	10.13 - 10.21	12.40 - 12.81	9.15 - 9.39	11.44 - 12.00	40 ± 30
	2130	-1.90	7.70 - 7.98	9.99 - 10.58	8.40 - 8.49	10.69 - 11.09	8.24 - 8.48	10.53 - 11.08	4.09 ± 3.10
	1480	-5.96	7.00 - 7.22	9.28 - 9.82	6.58 - 6.67	8.87 - 9.28	7.28 - 7.52	9.56 - 10.12	0.34 ± 0.33
	1315	-7.28	6.76 - 6.97	9.05 - 9.58	5.99 - 6.08	8.28 - 8.69	6.96 - 7.2	9.25 - 9.81	0.15 ± 0.14
CIV	3000	6.89	9.22 - 9.63	11.50 - 12.23	12.11 - 12.37	14.39 - 14.97	10.33 - 10.57	12.61 - 13.17	2680 ± 1625
	2130	3.04	8.55 - 8.91	10.82 - 11.51	10.38 - 10.64	12.66 - 13.24	9.41 - 9.65	11.7 - 12.26	$50 \pm 30.$
	1480	-1.01	7.85 - 8.16	10.13 - 10.76	8.57 - 8.83	10.85 - 11.43	8.45 - 8.69	10.74 - 11.30	0.77 ± 0.47
	1315	-2.33	7.62 - 7.91	9.90 - 10.51	7.97 -8.237	10.25 - 10.84.	8.14 - 8.38	10.42 - 10.98	0.19 ± 0.1

In the sections above I measured the minimum FWHM required in order to measure a specific visual extinction for each of the masses assumed. Figure 5.14 shows how my measured A_V values change with assumed FWHM for all sources at the three assumed masses. For clarity the errors on these calculated values of A_V are not shown but an example of a typical error is given in Figure 5.10. This should again allow for easy comparison on what assumptions and simulations result in realistic results or whether unrealistically broad widths are required to measure reddened sources as predicted, or to match the high extinction levels predicted for RWGs by Kim et al. (2013).

Whilst these sections have predicted the extinction levels though assumptions of my three measured BH masses, next I again use the [OIII]λ5007 masses calculated with the Eddington ratios derived in Section 5.2.

5.4.3 Deriving Extinction Corrections with my Measured and Corrected Emission Lines

The following utilises the first results of this chapter from Section 5.2 and the Eddington rate corrected [OIII]λ5007 BH masses to derive expected extinction corrections.

Using the Eddington Corrected [OIII]λ5007 BH Mass to Simulate a Hβ Line Profile

As shown in Section 5.2, RWGs accrete at super Eddington rates with measured values of $\lambda_{\rm Edd} > 1$ for 10 of the 11 sources investigated. With super Eddington accretion rates present, the previous BH mass measurements using the [OIII]λ5007 emission line and assumed $\lambda_{\rm Edd} = 1$, will be overestimates of their true mass measurements. This may explain why the simulated emission line widths above are predicted to be unreasonably broad in order to measure the high levels of obscuration that these sources were selected for. Now, I instead use the Eddington ratio corrected BH masses (see column 2 of Table 5.3) to estimate values for A_V and E(B-V) at my four assumed FWHM values for the 11 sources with measured Eddington ratios.

I have used the exact same methodology as described above to calculate A_V and E(B-V) at four assumed FWHM values (3000, 1480, 1315 km s^{-1} and at the measured Hα FWHM) with the results given in Table 5.13. At an assumed value of FWHM = 3000 km s^{-1}, I measured values of $A_V > 0$ for all 11 sources with a mean value of $AV = 11.8$ mag. At this broad width, unsurprisingly none of these values agree within error to my measured values (Table 5.4), however all of the values agree within error to those assuming Hβ BH mass = Hα BH mass (Table 5.6). This is unsurprising as the Eddington corrected $\lambda_{\rm Edd}$ values are derived from the BH mass, but is a reassuring check that this simulation works.

I measured a mean $A_V = 7.4$ mag assuming the Hβ FWHM is equivalent to the Hα FWHM,

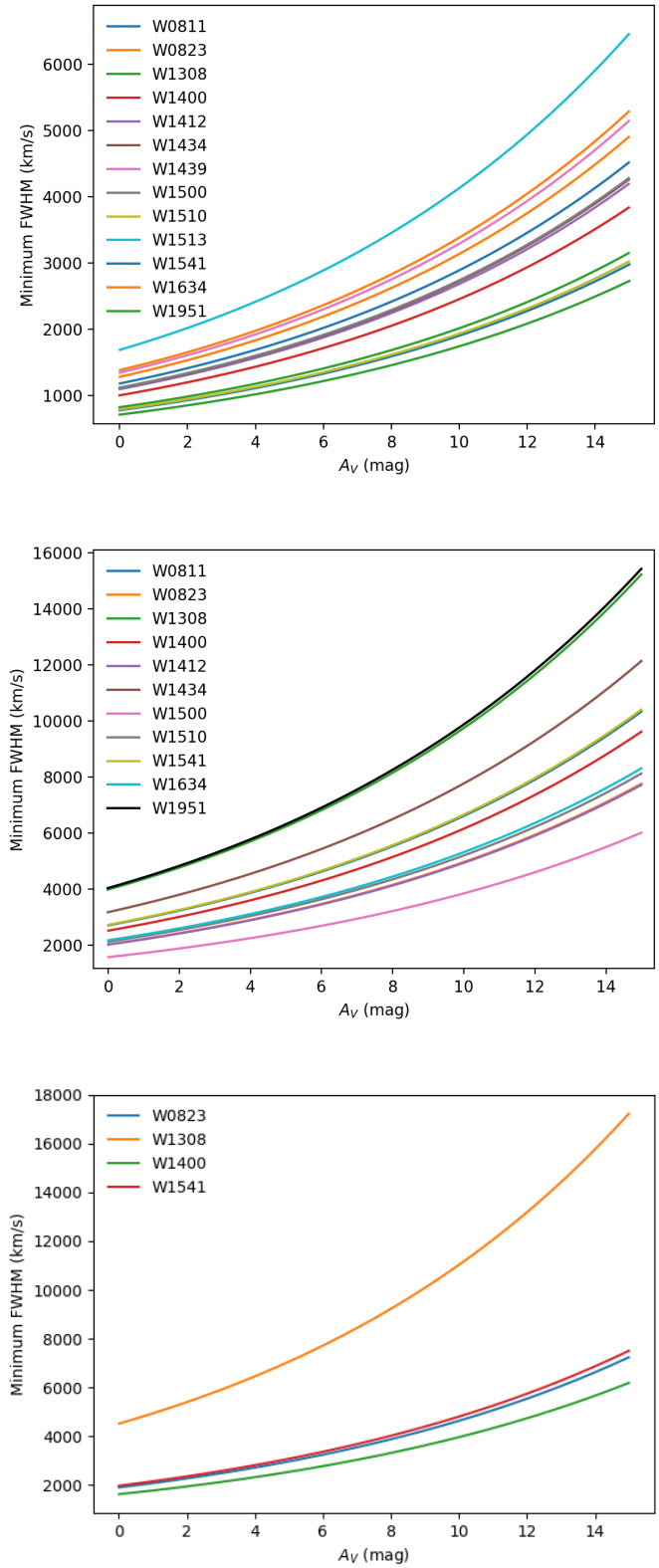

Figure 5.14: The FWHM of a simulated Hβ emission line required to measure an A_V of a certain value. This is shown for all sources available when assuming that the Hβ emission line calculated mass is the same as that from Hα (top), [OIII]λ5007 (middle) and CIV (bottom).

again with $A_V > 0$ for all 11 sources. With an assumed FWHM = 1480 km s^{-1} I again measured $A_V > 0$ for all 11 sources with a mean value of $A_V = 3.9$ mag, and a mean $A_V = 2.6$ mag for an assumed FWHM = 1315 km s^{-1}. However, at this width I only measured $A_V > 0$ for eight sources. Only my measured value of $A_V = 3.26$ mag for W1400, at 1480 km s^{-1}, agrees within error to my measured masses, and in this case 1480 km s^{-1} is within error of the originally measured FWHM of the detected Hβ emission line for this source.

Again following the procedure describe above, these A_V values were used to de-redden my 1D spectra (see Figure 5.15 for a specific example), and by applying my multiple Gaussian model fits I use the remeasured emission line fluxes and widths to calculate my extinction corrected BH and host galaxy masses which are shown in Figure 5.16 for this scenario. Table 5.14 gives the exact mass corrections for W1400 including both the corrected Hα and [OIII]λ5007 BH masses. At my mean broad line Hβ FWHM of 1480 km s^{-1} I measured a $\log\left(\frac{\mathrm{M_{BH}}}{\mathrm{M_\odot}}\right) = 8.6$ - 8.9 with a corresponding host masses of $\log\left(\frac{\mathrm{M_{BH}}}{\mathrm{M_\odot}}\right) = 10.9$ - 11.6. After correcting the measured BH masses for these simulated extinction values, the BH masses of W1400 now agrees within error to that published in Lonsdale et al. (2015) and my original classical lower limit ($\lambda_{\mathrm{Edd}} = 1$) BH mass estimate from the [OIII]λ5007 line luminosity.

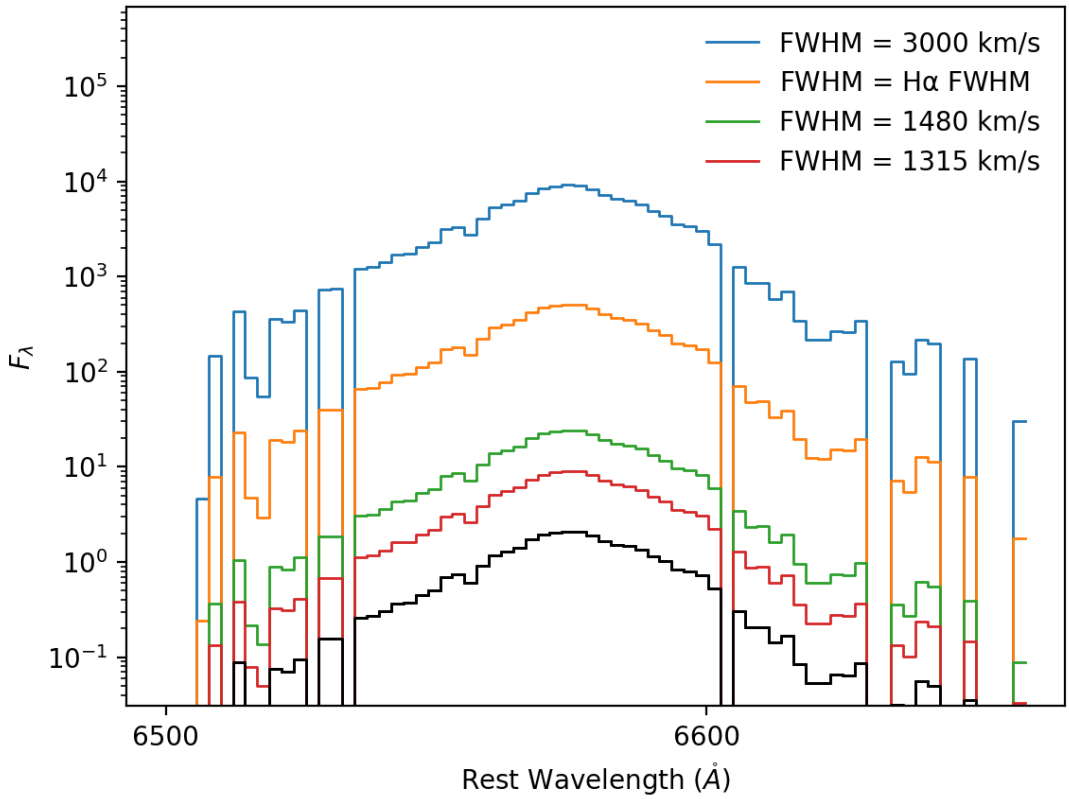

Figure 5.15: The 1D spectra in the region surrounding the Hα emission line corrected for extinction with assuming the Hβ BH mass is equivalent to the Eddington corrected [OIII]λ5007 mass, at different assumed FWHMs. Uncorrected spectra are shown in black with flux densities are in the units 10^{-16} erg s^{-1}cm^{-2}Å^{-1}.

Table 5.13: The calculated reddening and extinction for my 11 sources with detected Hα emission lines, assuming different FWHMs and that the Hβ and Eddington corrected [OIII]λ5007 BH masses are the same. Results are given in magnitudes.

WISE Designation	FWHM = 3000 km s^{-1}		FWHM = Hα		FWHM = 1480 km s^{-1}		FWHM = 1315 km s^{-1}	
	A_V	E(B-V)	A_V	E(B-V)	A_V	E(B-V)	A_V	E(B-V)
J081131.61−222522	$14.79^{+0.67}_{-0.57}$	$4.77^{+0.22}_{-0.18}$	$6.54^{+0.31}_{-0.29}$	$2.11^{+0.1}_{-0.1}$	$6.88^{+0.33}_{-0.31}$	$2.22^{+0.11}_{-0.1}$	$5.56^{+0.27}_{-0.26}$	$1.79^{+0.09}_{-0.08}$
J082311.24−062408	$8.71^{+0.14}_{-0.14}$	$2.81^{+0.05}_{-0.05}$	$8.27^{+0.12}_{-0.13}$	$2.67^{+0.04}_{-0.04}$	$0.8^{+0.14}_{-0.16}$	$0.26^{+0.05}_{-0.05}$	$-0.52^{+0.19}_{-0.21}$	$-0.17^{+0.06}_{-0.07}$
J130817.00−344754	$13.42^{+0.6}_{-0.56}$	$4.33^{+0.19}_{-0.18}$	$6.65^{+0.32}_{-0.33}$	$2.14^{+0.1}_{-0.11}$	$5.51^{+0.28}_{-0.29}$	$1.78^{+0.09}_{-0.09}$	$4.19^{+0.23}_{-0.24}$	$1.35^{+0.07}_{-0.08}$
J140050.13−291924	$11.16^{+1.75}_{-1.14}$	$3.6^{+0.56}_{-0.37}$	$7.31^{+1.51}_{-1.04}$	$2.36^{+0.49}_{-0.33}$	$3.26^{+1.29}_{-0.93}$	$1.05^{+0.42}_{-0.3}$	$1.94^{+1.22}_{-0.89}$	$0.62^{+0.39}_{-0.29}$
J141243.15−202011	$10.93^{+0.68}_{-0.57}$	$3.52^{+0.22}_{-0.18}$	$7.34^{+0.52}_{-0.45}$	$2.37^{+0.17}_{-0.15}$	$3.02^{+0.34}_{-0.31}$	$0.97^{+0.11}_{-0.1}$	$1.7^{+0.28}_{-0.26}$	$0.55^{+0.09}_{-0.09}$
J143419.59−023543	$11.86^{+1.21}_{-1.03}$	$3.83^{+0.39}_{-0.33}$	$8.51^{+1.05}_{-0.93}$	$2.74^{+0.34}_{-0.3}$	$3.95^{+0.84}_{-0.78}$	$1.28^{+0.27}_{-0.25}$	$2.63^{+0.78}_{-0.74}$	$0.85^{+0.25}_{-0.24}$
J150048.73−064939	$9.96^{+0.47}_{-0.43}$	$3.21^{+0.15}_{-0.14}$	$7.23^{+0.36}_{-0.34}$	$2.33^{+0.12}_{-0.11}$	$2.05^{+0.16}_{-0.16}$	$0.66^{+0.05}_{-0.05}$	$0.73^{+0.11}_{-0.11}$	$0.24^{+0.03}_{-0.04}$
J151003.71−220311	$17.01^{+0.69}_{-0.58}$	$5.49^{+0.22}_{-0.19}$	$8.93^{+0.34}_{-0.31}$	$2.88^{+0.11}_{-0.1}$	$9.11^{+0.35}_{-0.32}$	$2.94^{+0.11}_{-0.1}$	$7.78^{+0.3}_{-0.27}$	$2.51^{+0.1}_{-0.09}$
J154141.64−114409	$9.12^{+0.64}_{-0.54}$	$2.94^{+0.21}_{-0.17}$	$6.73^{+0.54}_{-0.46}$	$2.17^{+0.17}_{-0.15}$	$1.21^{+0.3}_{-0.28}$	$0.39^{+0.1}_{-0.09}$	$-0.11^{+0.25}_{-0.23}$	$-0.04^{+0.08}_{-0.08}$
J163426.87−172139	$8.27^{+0.07}_{-0.07}$	$2.67^{+0.02}_{-0.02}$	$7.00^{+0.02}_{-0.02}$	$2.26^{+0.01}_{-0.01}$	$0.36^{+0.21}_{-0.24}$	$0.12^{+0.07}_{-0.08}$	$-0.96^{+0.26}_{-0.30}$	$-0.31^{+0.08}_{-0.1}$
J195141.22−042024	$14.83^{+1.62}_{-1.08}$	$4.78^{+0.52}_{-0.35}$	$6.52^{+1.13}_{-0.85}$	$2.10^{+0.36}_{-0.27}$	$6.92^{+1.15}_{-0.86}$	$2.23^{+0.37}_{-0.28}$	$5.6^{+1.08}_{-0.82}$	$1.81^{+0.35}_{-0.26}$

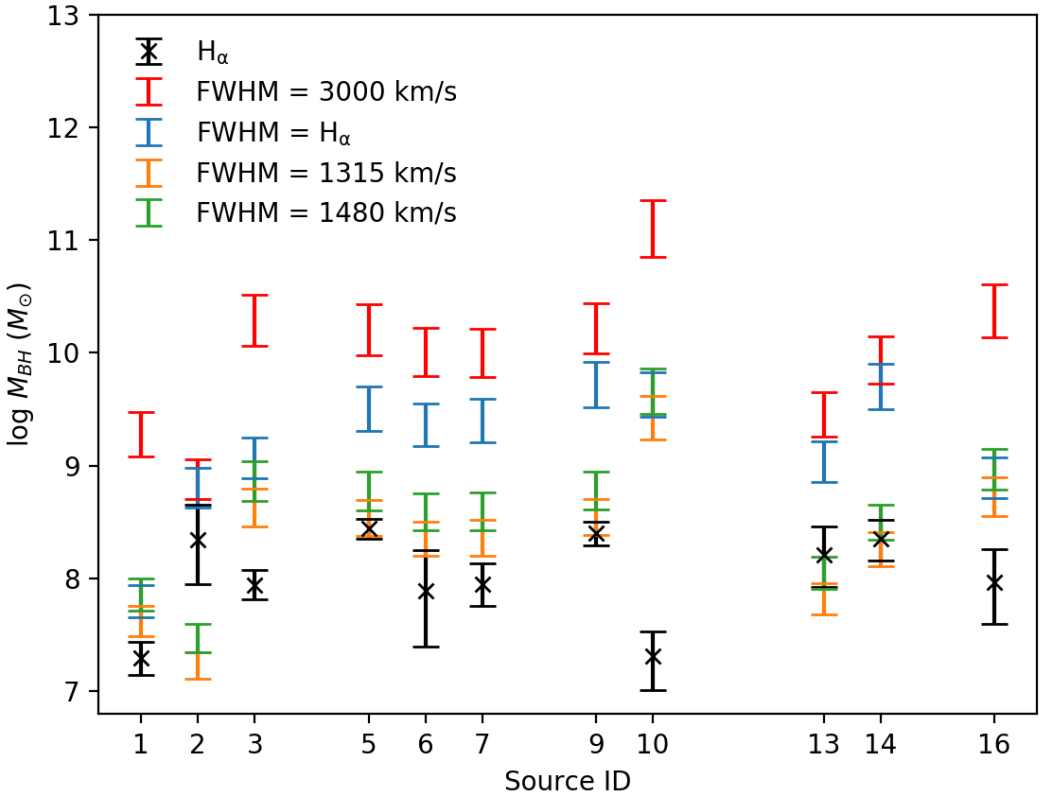

Figure 5.16: The corrected Hα derived BH masses when I use the Eddington corrected [OIII]λ5007 BH mass to predict the expected measures of extinction. Source ID corresponds to the source labelling system given in Table 4.2.

Table 5.14: My corrected BH masses and host masses for W1400. These are calculated when my spectra are corrected for different FWHM values assuming the Hβ and Eddington corrected [OIII]λ5007 BH masses are the same. Note the [OIII]λ5007 BH masses assume $\lambda_{\rm Edd} = 1$.

Assumed FWHM	A_V	Correcting the Hα BH mass		Correcting the [OIII]λ5007 BH mass		Correcting the CIV BH mass	
(km s^{-1})	(mag)	$\log\left(\frac{M_{BH}}{M_\odot}\right)$	$\log\left(\frac{M_{Host}}{M_\odot}\right)$	$\log\left(\frac{M_{BH}}{M_\odot}\right)$	$\log\left(\frac{M_{Host}}{M_\odot}\right)$	$\log\left(\frac{M_{BH}}{M_\odot}\right)$	$\log\left(\frac{M_{Host}}{M_\odot}\right)$
3000	11.16	9.98 - 10.43	12.26 - 13.03	14.25 - 14.34	16.53 - 16.94	11.34 - 11.58	13.63 - 14.19
2130	7.31	9.31 - 9.70	11.59 - 12.31	12.53 - 12.61	14.81 - 15.22	10.43 - 10.67	12.71 - 13.27
1480	3.26	8.60 - 8.94	10.89 - 11.55	10.71 - 10.79	13.00 - 13.40	9.47 - 9.70	11.75 - 12.31
1315	1.94	8.37 - 8.69	10.66 - 11.30	10.11 - 10.21	12.40 - 12.81	9.15 - 9.39	11.44 - 12.00

Table 5.15: The minimum FWHMs required for different values of visual extinction, based on the Eddington corrected [OIII]λ5007 calculated BH masses

WISE Designation	Minimum FWHM ($\mathrm{km\,s^{-1}}$) required				
	$A_v = 0$ mag	$A_v = 3$ mag	$A_v = 5$ mag	$A_v = 10$ mag	$A_v = 15$ mag
J081131.61−222522	801	1046	1251	1957	3054
J082311.24−062408	1378	1805	2158	3381	5270
J130817.00−344754	905	1185	1417	2220	3460
J140050.13−291924	1107	1450	1733	2715	4231
J141243.15−202011	1130	1481	1770	2773	4322
J143419.59−023543	1040	1362	1628	2551	3976
J150048.73−064939	1232	1614	1929	3023	4712
J151003.71−220311	656	859,	1027	1610	2509
J154141.64−114409	1329	1741	2081	3261	5082
J163426.87−172139	1434	1878	2245	3518	5483
J195141.22−042024	798	1045	1249	1957	3050

I measured $A_V > 0$ for all sources at the FWHM of 3000, 1480 $\mathrm{km\,s^{-1}}$ and at the Hα width with $A_V > 0$ for eight out of 11 sources at an assumed FWHM of 1315 $\mathrm{km\,s^{-1}}$. A mean FWHM of 1074 $\mathrm{km\,s^{-1}}$ is required for me to measure $A_V > 0$ for these simulated Hβ lines, with a mean FWHM of $\sim$ 4100 $\mathrm{km\,s^{-1}}$ required to measure an extremely obscured visual extinction of 15 magnitudes. Whilst this would require a very broad line, this is not an unphysically large measurement requirement. With Kim et al. (2013) measuring a highly obscured value of $A_V = 10^{1.3}$ magnitudes for W1400, I would require a FWHM of $\sim$ 7250 $\mathrm{km\,s^{-1}}$ to match this value, $\sim 6\times$ greater and $\sim 30\,\sigma$ away from my measured width. Whilst this is unlikely, a FWHM $\sim$ 1400 $\mathrm{km\,s^{-1}}$ would be required to match this A_V using the non Eddington corrected BH mass. Table 5.15 gives the minimum FWHM required to measure visual extinction values of A_V = 0, 3, 5, 10 and 15 magnitudes, with the exact relation between visual extinction and minimum FWHM required shown by Figure 5.17.

Through using my Eddington rate corrected [OIII]λ5007 BH masses, my simulated Hβ lines require a mean FWHM of 1074 $\mathrm{km\,s^{-1}}$ in order to measure A_V and E(B-V) > 0. Compared to the FWHM required if a value of $\lambda_{\mathrm{Edd}} = 1$ was used, these widths are far more realistic, and narrower than I measured assuming $\lambda_{\mathrm{Edd}} = 1$, providing evidence that RWGs do accrete at super Eddington rates.

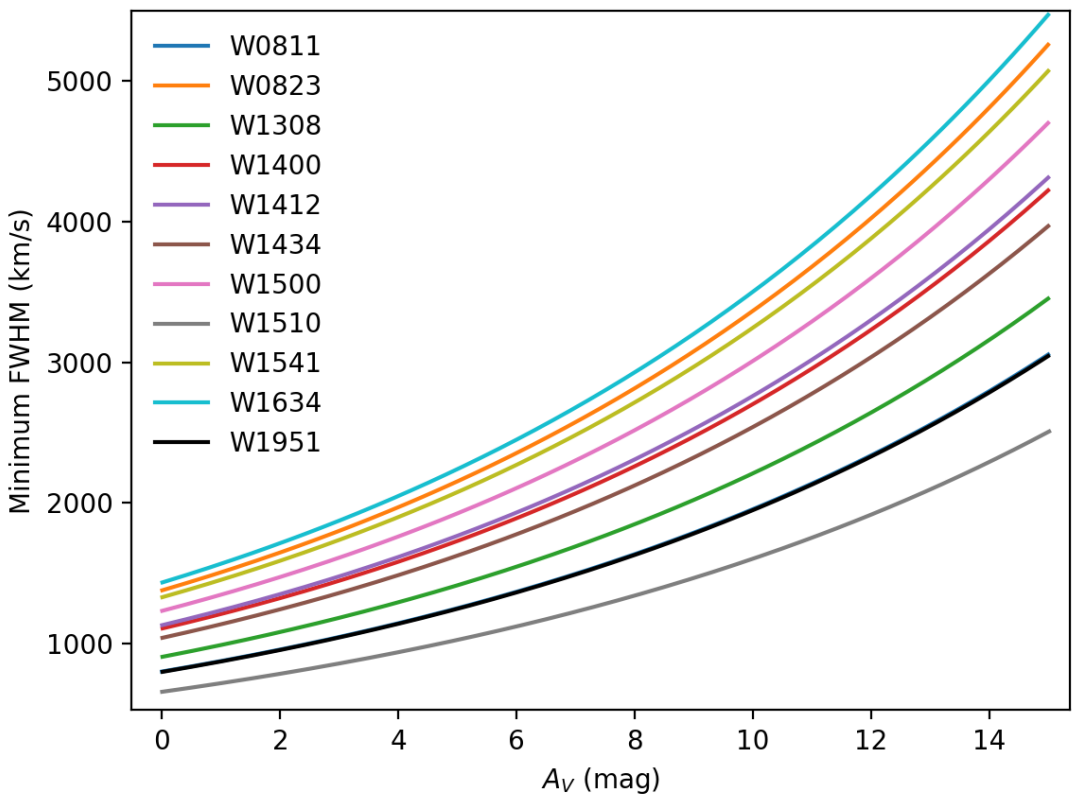

Figure 5.17: The FWHM of a simulated Hβ emission line required to measure an A_V of a certain value when assuming that the Hβ emission line calculated mass is the same as Eddington corrected [OIII]λ5007 BH mass.

5.4.4 Deriving Extinction Corrections with Previously Determined BH Masses

The final two investigations to be made use previously published BH mass estimates derived independently from my spectroscopic measurements. These BH mass estimates were derived independently from my own, with different photometric and spectroscopic data used and different assumptions made, including the $\lambda_{\rm Edd}$ value used. These analytic methods used are again identical to those reiterated above so below I only present the final results for these final two discussions. Section A goes through these results in further detail.

Using the Lonsdale et al. (2015) BH Mass to Simulate a Hβ Line Profile

The Lonsdale et al. (2015) BH masses are $\sim$ 0.9 dex greater than my Hα based BH mass results and I require a mean extinction correction of A_V = 6.13 magnitudes for my Hα BH masses to align with them. Lonsdale et al. use an assumed value of $\lambda_{\rm Edd}$ = 0.25 increasing their mass measurements through this choice. Across my four assumed FWHMs of 3000, Hα FWHM, 1480 and 1315 km s^{-1} I measured eight, two, zero, and zero visual extinction values greater than zero and mean values of A_V of 0.48, -3.1, -7.4 and -8.7 magnitudes respectively.

The minimum FWHM required to measure a positive value for visual extinction was 2955 km s^{-1}. This required width is $> 2\times$ as broad as the mean of the measured broad Hβ FWHMs, and I would require a value of FWHM = 12,984 km s^{-1} in order to measure an A_V value in agreement with Kim et al. (2013) for W1400. As RWGs are selected to be highly obscured sources, these broad FWHM required to measure $A_V > 0$ mean that the BH masses calculated in Lonsdale et al. (2015) are highly likely be overestimates of the true values.

Using the Kim et al. (2013) BH Mass to Simulate a Hβ Line Profile

Kim et al. (2013) and I used identical methods to determine BH mass, assuming that the [OIII]λ5007 emission line luminosity can be used as a proxy for the bolometric luminosity and that $\lambda_{\rm Edd}$ = 1. However, despite our identical methods Kim et al. measure BH masses $\sim$ 0.46 dex greater than my own. Therefore the FWHM of my simulated Hβ emission lines have to be broader in order to measure the same Hβ luminosity. This means that FWHMs $\sim 2.3\times$ broader than I originally measured are required to measure the Hα fluxes 2.86 $\times$ greater than those measured from my simulated Hβ emission lines.

A mean minimum FWHM of 3144 km s^{-1} is required to measure a simulated Hβ flux $<$ Hα flux / 2.86, which is greater than all of my measured Hβ FWHMs and $> 2\times$ my mean measured FWHM. This very broad FWHM requirement is again likely due to their assumed value of $\lambda_{\rm Edd}$ = 1, whilst both my above work and that by Kim et al. (2013) show that some RWGs accrete

at super Eddington rates.

Comparison of Derived Extinction Corrections

Above (and in Section A) I have discussed how assuming that the Hβ BH mass equates to other calculated BH mass values changes the predicted level of visual extinction. Now I look to compare the use of measured RWG BH masses by previous works Lonsdale et al. (2015) and Kim et al. (2013) in order to predict which set of simulations is most realistic, and to compare them to my measured masses. I did this by comparing their corrected emission line spectra at the Hα rest wavelength and again by correcting the Hα, [OIII]λ5007 and CIV derived BH masses for W1400.

Figure 5.18 shows the effect of the FWHM chosen on the extinction corrected spectra for W1400 at the rest wavelength of the Hα emission line. This is shown assuming previously derived BH masses by Lonsdale et al. (2015) and Kim et al. (2013). This can be used to compare which assumed FWHMs measure positive visual extinctions as expected. Under the assumption that the Hβ BH mass equals that measured by Lonsdale et al. (2015), only the broadest FWHM results in a value of $A_V > 0$. Similarly assuming the Hβ BH mass equals that from Kim et al. (2013), none of the assumed widths leading to positive visual extinction values. These results are in contrast to those measured previously where no matter the assumed FWHM, under the assumption that the Hβ BH mass equals that derived from the Hα emission line, all extinction corrections will increase the measured flux of the Hα emission line.

For completeness the Hα, [OIII]λ5007 and CIV corrected BH and host galaxy masses for W1400 are given in Table 5.16. As discussed above only the broadest assumed FWHM (if Hβ = Lonsdale et al. (2015)) predicts a positive visual extinction and increases my measured BH masses. This resulted in a mean BH mass of $\log\left(\frac{\mathrm{M_{BH}}}{\mathrm{M_\odot}}\right) = 9.5$, which does agree to my previously corrected masses. However the rest of the results in this table are likely unrealistic due to the assumed masses. I have previously shown that RWGs are likely accreting at super Eddington rates, making these two previously calculated BH masses overestimates of the true values. Reducing the Eddington ratio would equate to a smaller simulated Hβ flux and therefore a larger predicted value for extinction. The negative visual extinction predicted here therefore implies that the FWHM required are likely broadened or these assumed BH masses are too big.

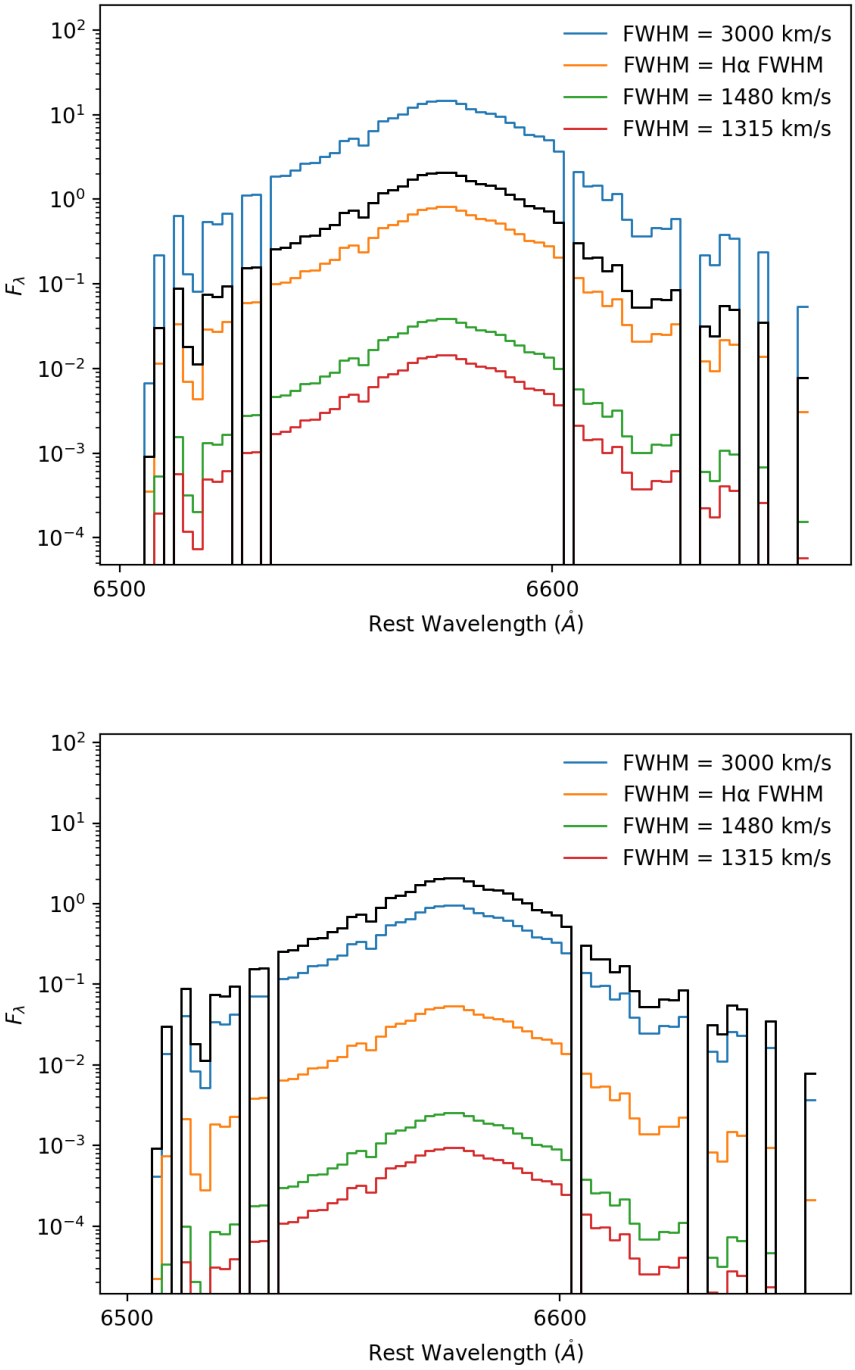

Figure 5.18: The 1D spectra in the region surrounding the Hα emission line corrected for extinction assuming the Hβ BH mass is equivalent to the Lonsdale et al. (2015) (top) and Kim et al. (2013) (bottom) measured BH masses at different assumed FWHMs. The uncorrected spectra is shown in black with flux densities in units 10^{-16} erg s^{-1}cm^{-2}Å^{-1}.

Table 5.16: My corrected BH masses, host masses and Eddington ratio for W1400. These are calculated when my spectra are corrected for different FWHM values assuming the Hβ BH mass equals that of the Lonsdale et al. (2015) and Kim et al. (2013) masses. Note the [OIII]λ5007 BH masses assume $\lambda_{\rm Edd} = 1$.

Assumed BH mass	Assumed FWHM ($\rm km\,s^{-1}$)	A_V (mag)	Correcting the Hα BH mass		Correcting the [OIII]λ5007 BH mass		Correcting the CIV BH mass		$\lambda_{\rm Edd}$
			$\log\left(\frac{M_{BH}}{M_\odot}\right)$	$\log\left(\frac{M_{Host}}{M_\odot}\right)$	$\log\left(\frac{M_{BH}}{M_\odot}\right)$	$\log\left(\frac{M_{Host}}{M_\odot}\right)$	$\log\left(\frac{M_{BH}}{M_\odot}\right)$	$\log\left(\frac{M_{Host}}{M_\odot}\right)$	
Lonsdale et al. (2015)	3000	2.60	8.48 - 8.82	10.77 - 11.42	10.41 - 10.50	12.70 - 13.10	9.31 - 9.55	11.59 - 12.15	60 ± 40
	2130	-1.26	7.81 - 8.10	10.10 - 10.70	8.69 - 8.78	10.97 - 11.38	8.39 - 8.63	10.68 - 11.24	6.10 ± 4.60
	1480	-5.31	7.11 - 7.34	9.39 - 9.94	6.87 - 6.89	9.16 - 9.57	7.43 - 7.67	9.72 - 10.27	0.50 ± 0.47
	1315	-6.63	6.88 - 7.09	9.16 - 9.69	6.29 - 6.37	8.57 - 8.97	7.12 - 7.36	9.40 - 9.96	0.22 ± 0.17
Kim et al. (2013)	3000	-1.03	7.85 - 8.14	10.14 - 10.74	8.79 - 8.99	11.07 - 11.49	8.45 - 8.69	10.73 - 11.29	7.01 ± 5.20
	2130	-4.88	7.18 - 7.42	9.47 - 10.02	7.06 - 7.16	9.35 - 9.77	7.53 - 7.77	9.82 - 10.38	0.66 ± 0.59
	1480	-8.93	6.48 - 6.66	8.76 - 9.26	5.25 - 5.34	7.54 - 7.95	6.57 - 6.81	8.86 - 9.41	0.05 ± 0.07
	1315	-10.26	6.25 - 6.41	8.53 - 9.02	4.67 - 4.74	6.96 - 7.35	6.26 - 6.49	8.54 - 9.10	0.02 ± 0.03

Shown in Table 5.16 is how both the assumed BH mass and FWHM change the final corrected BH and host galaxy masses. With 7/8 simulations predicted negative visual extinction and mass reductions I will now compare how the FWHM assumed effects the predicted A_V for the previously determined BH masses. Figure 5.19 shows how my measured A_V values change with assumed FWHM for all sources at the three assumed masses. In order to predict $A_V > 0$ I required a minimum FWHM of $2100\,\mathrm{km\,s^{-1}}$, with a maximum FWHM of $4126\,\mathrm{km\,s^{-1}}$ required across all sources. For larger values of $A_V = 3$ and $A_V = 5$, I required a minimum FWHM values of $\sim 3000\,\mathrm{km\,s^{-1}}$ and $\sim 3700\,\mathrm{km\,s^{-1}}$ respectively. Whilst these minimum widths are not unphysical these simulations have produced unrealistic results compared to those based on the measured masses and the results should be used only for comparison purposes.

5.4.5 Summary of Extinction Corrections using Simulated Emission Lines

With RWGs selected to be highly obscured, measurements of the visual extinction are crucial in order to know the true luminosities of these sources. With only five sources having both Hα and Hβ line detections, I could not use the Balmer decrement to estimate extinction for the rest of my sources. However, through use of a simulated Hβ emission line, I calculated the visual extinction for the 13 RWGs with an Hα emission line detection. Using the assumption that all BH masses calculated should be equal, I used a given BH mass to calculate the Hβ emission line luminosity required to measure this BH mass at a given FWHM. I additionally measured the minimum FWHM required such that I derive $A_V > 0$, in order to determine both if the width required is realistic and whether the assumed mass allows for highly obscured extinction measurements. I also re-applied all these extinction corrections using the Calzetti et al. (2000) extinction law, as a further test, with no difference to my final results as all A_V values derived were within error of the results presented here. However, it may be that none of these extinction curves represent this unique population, as with current SED templates or the extinction may be greyer than the extinction curves used (e.g. Roebuck et al., 2019) due to radiative transfer effects.

5.5 Comparison of Measured Extinction Values

I used the Balmer decrement to measure the reddening and visual extinction of the five RWGs (Table 5.4) where I successfully detected both the Hα and Hβ emission lines. I measured $A_V > 0$ for four galaxies with this value being within error for the fifth. The selection criteria originally outlined in Lonsdale et al. (2015) (see Figure 4.1) aimed to select galaxies that lie redward of the main WISE population through using the colour selection criterion of $(W2 - W3) + 1.25(W1 -$

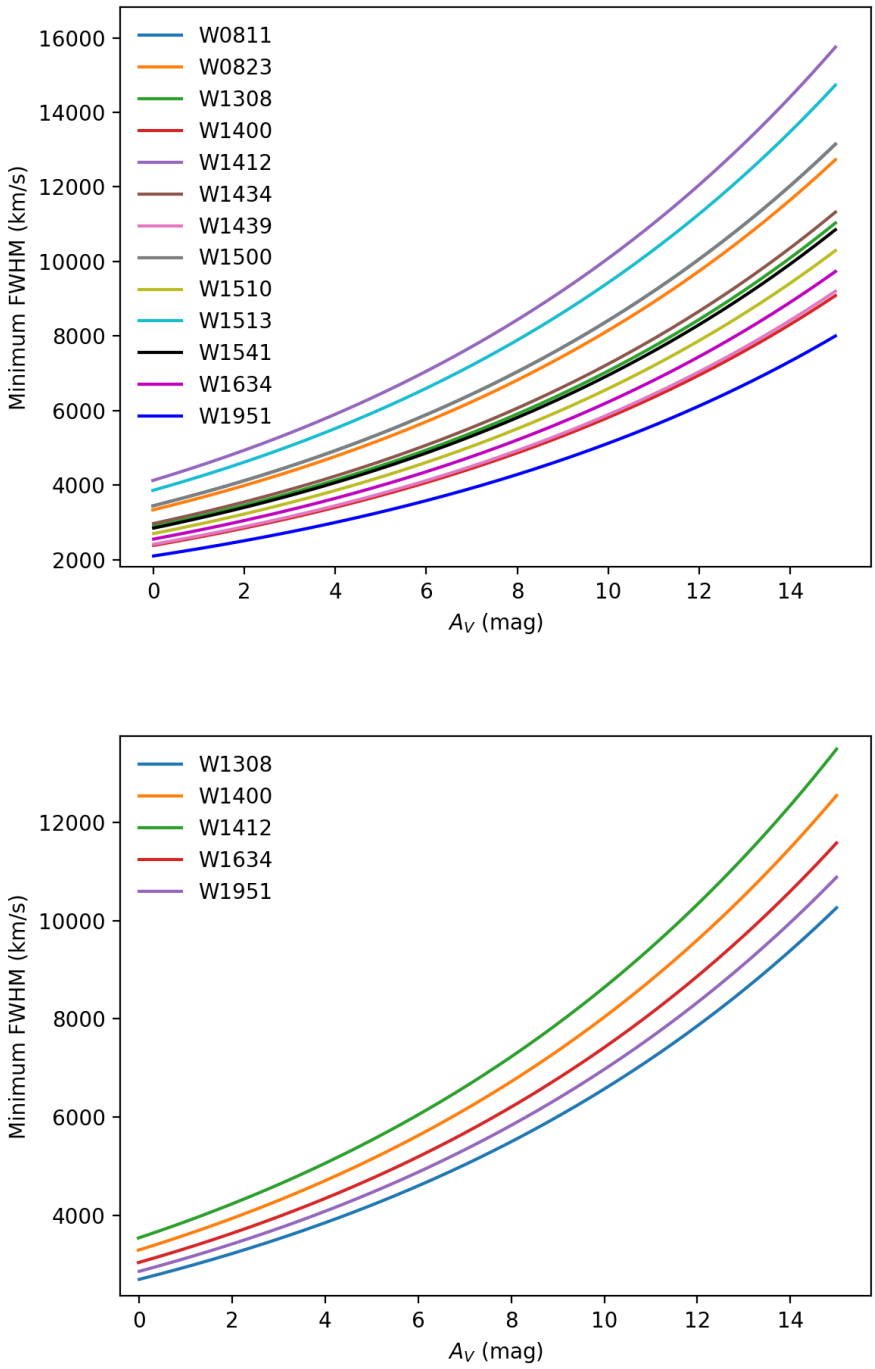

Figure 5.19: The FWHM of a simulated Hβ emission line required to measure an A_V of a certain value. This is shown for all sources available when assuming that the Hβ emission line calculated mass is the same as that from Lonsdale et al. (2015) (top) and Kim et al. (2013) (bottom).

$W2) > 7$, with my measured visual extinction values showing that this criterion was successful.

Kim et al. (2013) used this same selection criteria to observe an analyse a subset of RWGs overlapping with the sources discussed in this thesis. They used the Balmer decrement to measure the visual extinction of three sources W1400, W1951 and W2000 as $\log A_V = 1.3^{+0.8}_{-0.6}$, $0^{+0.5}_{0.0}$ and > 0.2 mag respectively. They measured the visual extinction of W1400 $\sim 5\times$ greater than I do, with my results being within an order of magnitude of theirs when taking into account their large error range. Comparing our Balmer line fluxes, they measured emission line fluxes $\sim 6\times$ greater than I do, though with similar Hα/Hβ ratios. We both however, measured A_V values for W1951 that agree within error of each other. Whilst the measured levels of reddening do not agree within error, we both show that these RWGs are affected by dust extinction and therefore require mass corrections for extinction.

HotDOGs are a similarly selected WISE population of galaxies with a red selection of sources which lie in the same area of WISE - WISE colour space as RWGs. With only a small subset of RWG observations available, this is a similar population suitable for comparison. Published in Jun et al. (2020) are their E(B-V) measurements for seven HotDOGs, with an additional three HotDOG E(B-V) measurements published in Stern et al. (2014). Jun et al. measure E(B-V) > 0 for six sources with this value being within error for the seventh source. They measured a mean E(B-V) = 0.59 mag, 32% lower than my measured mean of E(B-V) = 0.87 mag but not inconsistent.

Comparatively, Stern et al. (2014) measured a mean E(B-V) = 12.7 mag across the three HotDOGs that they observed. This is $\sim 15\times$ greater than my mean measured E(B-V) value and $\sim 22\times$ greater than the reddening measured by Jun et al.. Both Stern et al. (2014) and Jun et al. (2020) used a similar selection criteria and similar source redshifts, so the difference between their values is unclear. However Jun et al. (2020) had a large source sample. Whilst the levels of extinction are shown to vary across the different sources, both Jun et al. and Stern et al. find that HotDOGs are affected by dust extinction in agreement with the findings for RWGs. With similar selection criteria used to determine these two different galaxy populations, these findings are both reassuring and unexpected as both populations are selected to have highly obscured natures.

5.6 Conclusions

This chapter has discussed two different assumptions used in the calculation of my BH and host galaxy masses with the effects they have had on my final calculated mass values. These corrections were motivated through the aim of comparing how different the populations of RWGs

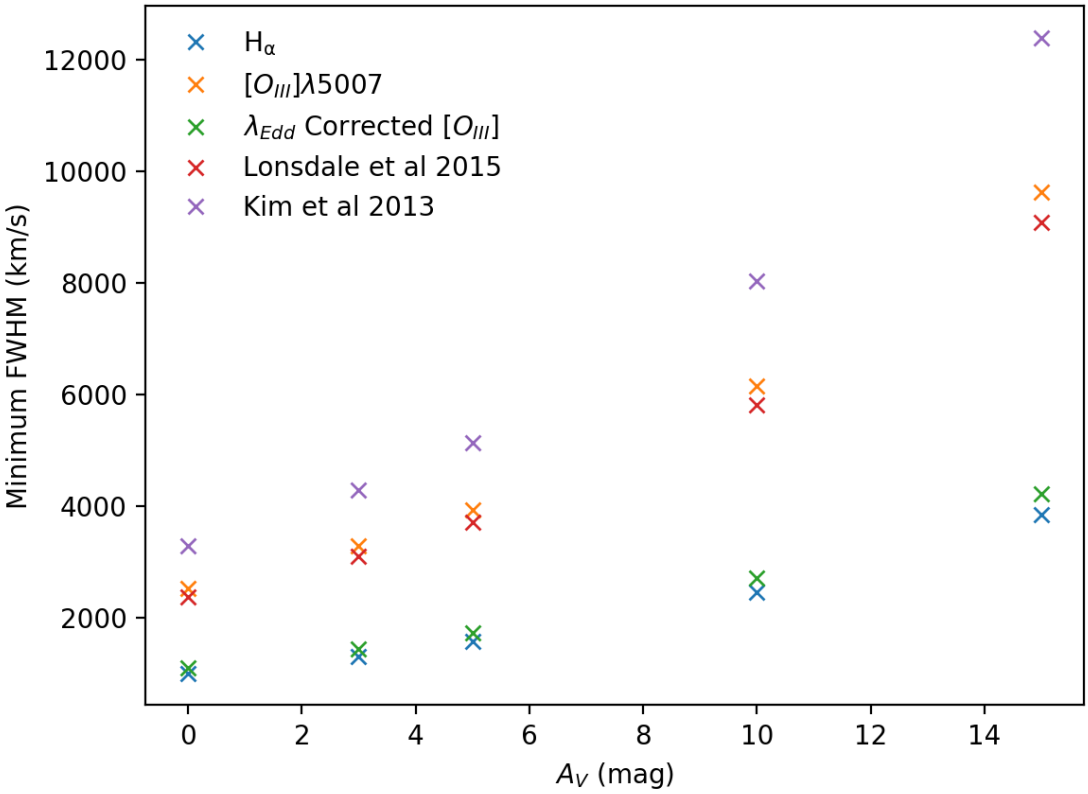

Figure 5.20: The minimum FWHM required to measure a certain A_V magnitude for W1400 assuming that the Hβ BH mass is equal to another BH mass estimate.

.

and HotDOGs are. With previous measurements showing that HotDOGs can accrete at super-Eddington rates, I expected the same to be true of RWGs. BH mass corrections will also allow determination of whether RWGs are ~ 1 dex smaller than HotDOGs and therefore likely undergo an extremely active phase that is shorter than for HotDOGs.

Firstly discussed was the value of $\lambda_{\rm Edd} = 1$ assumed when using the [OIII]λ5007 emission line luminosity to calculate the BH masses of 15 sources. Through equalising the calculated Hα and [OIII]λ5007 BH masses I measured a mean value of $\lambda_{\rm Edd} = 10.12$ across the 11 sources with both lines detected. This is an extremely large Eddington ratio, though similar and greater ratios have previously been measured in type 2 quasars at a similar redshift (Kong & Ho, 2018), and are the same order of magnitude to those measured by Jun et al. (2020). This shows that despite their smaller size RWGs are as active as HotDOGs, but also that a higher super-Eddington ratio (~ 10) may be an additional indicator of a RWG and could be used to distinguish RWGs from other active QSO's. In total I measured Eddington rates in the range $\lambda_{\rm Edd} = 0.34 - 34.59$, with 10/11 sources showing super Eddington accretion with this being statistically significant for five sources. These newly measured Eddington rates reduced my measured BH masses by ~ 0.68 dex aligning them, within error, to the Hα based BH mass estimates. This again shows that RWGs are physically smaller than HotDOGs, and remain distinct from other QSO's at a similar redshift.

Repeating my methodology but assuming the [OIII]λ5007 and BH masses calculated in Lonsdale et al. (2015) are equal, I measured a mean $\lambda_{\rm Edd} = 0.95$ across all 15 sources with [OIII]λ5007 detections. Under this assumption I measured super Eddington rates for 1/3 of my sample, however a value of $\lambda_{\rm Edd} = 1$ is within error for all five of these sources.

Compared to SDSS QSOs (Shen et al., 2011) of a similar redshift, these RWGs lie mainly outside the QSO population with the measured $\lambda_{\rm Edd}$ values in Table 5.1 being on average 40$\times$ greater than measured for these SDSS QSOs. With the $\lambda_{\rm Edd}$ values from Table 5.2 additionally being $\sim 40\times$ greater, it is clear that RWGs accrete at higher that average and most likely super Eddington rates. Whilst these super Eddington rates agree with those found for other sources at z$\sim$ 2, they will be unsustainable for long periods of time. This again demonstrates that these extreme sources are being observed at an extremely active and short lived phase of their evolution, and therefore observing these sources will give us a snapshot of the conditions in the early universe.

Secondly, I aimed to estimate the amount of visual dust extinction and reddening that affected my measured emission line fluxes. Quantifying this dust will provide indicators of the surrounding environment during this very active phase as well as assisting with future SED fitting attempts.

All of my presented results were calculated using the extinction law from Cardelli et al. (1989), but I also repeated all calculations using the extinction law from Calzetti et al. (2000) to no change. With five sources having detections of both the Hα and Hβ emission lines, I used the Balmer decrement and a value of $R_V = 3.1$ to measure a mean $A_V = 2.68$ mag and E(B-V) = 0.86 magnitudes. Measurements of $A_V > 0$ for four of these sources led to a ~ 0.8 dex increase in my Hα BH and host galaxy mass measurements. Despite these corrections RWGs are found to be smaller than HotDOGs, meaning their size could be used as a distinguishing factor between the two populations.

However with only five sources having detections of both Balmer lines and with larger uncertainties in my measured Hβ line properties, I used a simulated Hβ emission line to estimate the amount of dust extinction present in all 13 sources with an Hα line detection. Using an assumed BH mass value and four different assumed FWHMs (3000, 1480, 1315 $\mathrm{km\,s^{-1}}$ and the FWHM of the corresponding Hα profile) I predicted the visual extinction and reddening of my sources under the assumption that all BH mass calculations should give the same result.

Assuming that the Hα and Hβ BH mass calculations should give the same result, I measured $A_V > 0$ for 12/13 sources at my mean Hβ FWHM of 1480 $\mathrm{km\,s^{-1}}$ with a mean value of A_V = 3.62 magnitudes. This calculation was repeated using all BH mass measurements for each source with a Hα detection to different results. I also calculated the minimum FWHM required to measure A_V values of 0, 3, 5 10 and 15 magnitudes with a summary of these values given for W1400 in Figure 5.20. Using different BH masses to equate the Hβ luminosity to in this investigation led to a variety of measured extinction and reddening values however it is clear that RWGs are affected by dust extinction with my measured BH and host galaxy masses being increased by ~ 2 dex in the most obscured cases.

Understanding the exact properties of these sources is of the upmost importance. If, as suggested, they are an extremely active phase of galaxy evolution, we now have the opportunity to observe sources at their most active and during an evolutionary phase which all galaxies may go through. With such higher Eddington ratios measured, and the smaller masses, it is likely that for RWGs this phase is short lived. This suggests that RWGs will be a smaller population than HotDOGs and therefore these sources provide us with a unique look at the universe's history and will allow greater insight into galactic evolution.

Chapter 6

Classifying RWGs through Newly Measured Emission Lines

6.1 Introduction

Please note that part of this chapter has been published in Ferris et al. (2021), but all of the analysis was undertaken by me.

RWGs are a unique population of galaxies selected to be radio intermediates, W2 bright and be redder in colour than the rest of the WISE galaxy population. It has been suggested that they may be a new stage in galaxy evolution (Lonsdale et al., 2015; Lonsdale et al., 2016), though not much was known about them, nor whether they fit the standard assumptions and methodologies applied to similarly luminous galaxies. It is therefore of the utmost importance to investigate their various properties, find how they compare to similar galaxy populations and see how they fit known relation standards. With their smaller mass and high Eddington rate, is likely that these extreme and rare galaxies are being observed in a short lived and very active phase of their evolution, which all galaxies may go though. Understanding their properties therefore provides an insight into the surrounding environment and wider universe at this extreme time period - allowing us to observe the universe in its most active state, along with allowing the classification of other galaxies as RWGs through similar parameters. This will allow us to expand our population size and place tighter constraints on the parameters we have previously observed.

In chapter 4 I used the NIR ISAAC J and K_S band imaging to fit SEDs to 30 RWGs using the `MAGPHYS` (da Cunha et al., 2008) AGN SED templates. I also used NIR spectroscopy from X-shooter to measure the BH and host galaxy masses of 18 RWGs using the [OIII]λ5007 and Balmer emission lines, with additional mass estimates derived from CIV emission lines detected in the UVB arm. In Chapter 5, I aimed to address the assumptions made in measuring my BH

masses. I measured less extinction compared to other work (Kim et al., 2013) and applied the extinction using the standard methods, though my outcome was still uncertain. With extinction constrained by the total power of their SEDs and possible time variations, new and more complicated methodology may be needed for accurate extinction estimates. The findings in these previous two chapters have led to additional open questions including whether the standard methodology is valid for these uniquely selected galaxies.

This chapter aimed to investigate the remaining X-shooter spectroscopy and determine the different properties of RWGs in order to see how they compare to other similar galaxy populations, aiming to uncover additional similarities that may be used to select future RWGs. The X-shooter spectograph observes simultaneously across the three spectral arms of UVB, VIS and NIR at a total wavelength range of 300 - 2480 nm. I previously only measured four emission lines (CIV, Hβ, [OIII]$\lambda\lambda$4959, 5007 and Hα) across the NIR and UVB arms, focusing on those emission lines needed for BH mass calculations. However, I now look for emission lines across all three spectral arms, as well as investigating whether any absorption lines are present, which will provide information on the surrounding environment.

I use these newly detected emission lines to place the RWGs on Baldwin, Phillips & Terlevich (BPT) diagrams (Baldwin et al., 1981) in an aim to classify the galaxies types and investigate how extinction corrections change the placement of individual RWGs. I also aim to see how well the calculated BH masses fit the $M_{BH} - M_{sph}$ relation (Bennert et al., 2011) in comparison to previously observed HotDOGs (Assef et al., 2015; Wu et al., 2018), to uncover more differences between these populations. Finally, I investigate the profiles of the spectral emission lines themselves, measuring their asymmetric nature and determining the sources whose measured FWHM may be broadened through the presence of outflows.

With 27 RWGs observed across the three spectral arms, I have previously detected emission lines for only 18 sources and it is therefore interesting to see how many other emission lines can be detected across the remaining wavelengths and the remaining nine galaxies.

6.2 Detecting Additional Emission Lines

Across a consecutive three night period 27 RWGs were observed with the X-shooter instrument (Vernet et al., 2011) on UT2 of the VLT. As described in section 3.2.2, X-shooter simultaneously observed across three wavelength arms; NIR, VIS and UVB over a total wavelength range of 300 - 2480 nm. These arms are split individual wavelength ranges of 300 - 560 nm, 550 - 1020 nm and 1020 - 2480 nm across the UVB, VIS and NIR arms respectively at slit widths of 1.6”, 1.5” and 1.2”. These observations were done at excellent seeing (0.67” - 1.5”) and low air mass ≤ 1.16.

Previously I fitted multi Gaussian models to the CIV, Hβ, [OIII]λ5007 and Hα emission lines at rest wavelengths of 1549 Å, 4861 Å, 5007 Å, and 6563 Å detecting five, six, 15 and 13 emission lines. With a total of 18 sources with detected emission lines, there are still nine sources with no detections and two other spectral arms that have hardly been investigated. This section therefore aimed to exploit the rest of this data and search for other common spectral lines generally present in AGN. This will allow me to classify these RWGs by placing them on BPT diagrams as well as having a larger data set for each individual source. This was be especially useful for those sources with zero detections to see whether they were missed targets or the expected NIR emission lines were not present. Additional line detections also aid in the comparison to other populations through matching how well they fit known relations.

Following the previously described methodology I used the 1D Gaussian model package from `astropy.fitting` (The Astropy Collaboration et al., 2018) to fit multiple Gaussians (Greene & Ho, 2005; Assef et al., 2011; Jun et al., 2017; Wu et al., 2018; Jun et al., 2020) to each detected emission line in order to measure their flux and FWHM. The spectra were first Doppler corrected using the IRAF (Tody, 1986) `dopcor` package to convert from the observed to rest wavelength frame. An additional continuum subtraction was applied across the width of the emission line, as shown in Figure 4.5, due to uncertainties in the continuum subtraction applied by the reduction pipeline. I fitted as many Gaussians as necessary in order to create an acceptable fit, as defined by a low χ^2_ν value, with additional Gaussians added as long as the measured χ^2_ν value was reducing, and each component allowed its own velocity offset. For the majority of these fits only a single Gaussian was needed to produce an acceptable fit, compared to the two or three Gaussians required to fit the Hβ, [OIII]λ5007 and Hα emission lines. This is most likely due to the obvious asymmetry present in some detected Hα emission lines.

Each of the single emission lines was modelled as an independent line, with the OI emission line doublet modelled together as a compound model. In the case of line doublets the separation between the models was fixed to the known wavelength difference and their FWHMs were constrained to be equal. A Monte Carlo approach was again used to estimate the errors on my measured line fluxes and widths. The errors were estimated by simulating 10,000 spectra with each data point allowed to randomly vary within the given spectral errors. These simulated spectra were fitted with the models described above with the standard deviations on the measured flux and FWHMs taken as the error on my measured values.

I searched for nine new emission lines across the three spectral arms along with four common absorption lines[1], looking across the rest wavelength range of 1034Å - 8500 Å. Detections were

[1]All line widths are taken from SDSS: http://classic.sdss.org/dr6/algorithms/linestable.html

initially searched for at the rest wavelengths of new emission lines with confirmation visually in the 2D spectra. The following subsections discuss the different lines detected across each arm giving their measured fluxes and FWHMs. With the observed wavelengths of each detected emission line redshift dependent, the same emission line may be observed by different arms for different sources depending on the wavelength range covered by each arm.

Across the 27 RWGs observed with X-shooter I have a redshift range of z = 0.88 - 2.85 with a mean redshift of z $\sim$ 1.84. The following sections are divided based on the which wavelength arm the emission lines of W1702 fall in. Whilst previously discussed under the NIR detections, emission lines up to the wavelength of 5007Å are also detected in the VIS arm's wavelength range for those sources of lower redshifts. Similarly, the HeII emission lines are found in the UVB arms wavelength range for a subset of sources, and the rest wavelength of the previously measured CIV lines fall in the UVB arms wavelength range for some sources including W1702.

6.2.1 Additional Line Detections in the NIR

The NIR arm of X-shooter observes across the wavelength range of 1020-2480 nm. It has a slit width of 1.2" and my observations were taken with an exposure time of 2$\times$600 s. I have previously detected three emission lines Hβ, [OIII]λ5007 and Hα measuring six, 15 and 13 detections respectively across a total of 18 sources. These lines were initially searched for in order to derive the BH masses of these RWGs with all the results given in Chapter 4. In this section I now searched for five new emission lines; OII, Hδ, Hγ, OI and SII at rest wavelengths of 3727 Å, 4103 Å, 4340 Å, 6302+6365 Å and 6732 Å respectively.

OII Detections

I detected 13 OII emission lines with a mean flux of 8.01×10^{-16} erg s^{-1}cm^{-2}. Compared to the original 18 sources with detected NIR emission lines, I now detect an emission line in the NIR arm for W2059 which previously had no detections of the [OIII]λ5007 or Balmer emission lines. Whilst there is excess noise in the previously looked at spectra of W2059, the detection proves that no previous detections were not due to an incorrect redshift. The fitted models for the 13 sources with OII detections are shown in Figure 6.1 with the measured fluxes, FWHMs and emission line luminosities given in Table 6.1.

Hδ Detections

I detected Hδ emission lines in six sources, including two sources that had no emission lines previously detected, with a mean measured flux of 8.73×10^{-16} erg s^{-1}cm^{-2}Å^{-1}. Figure 6.2

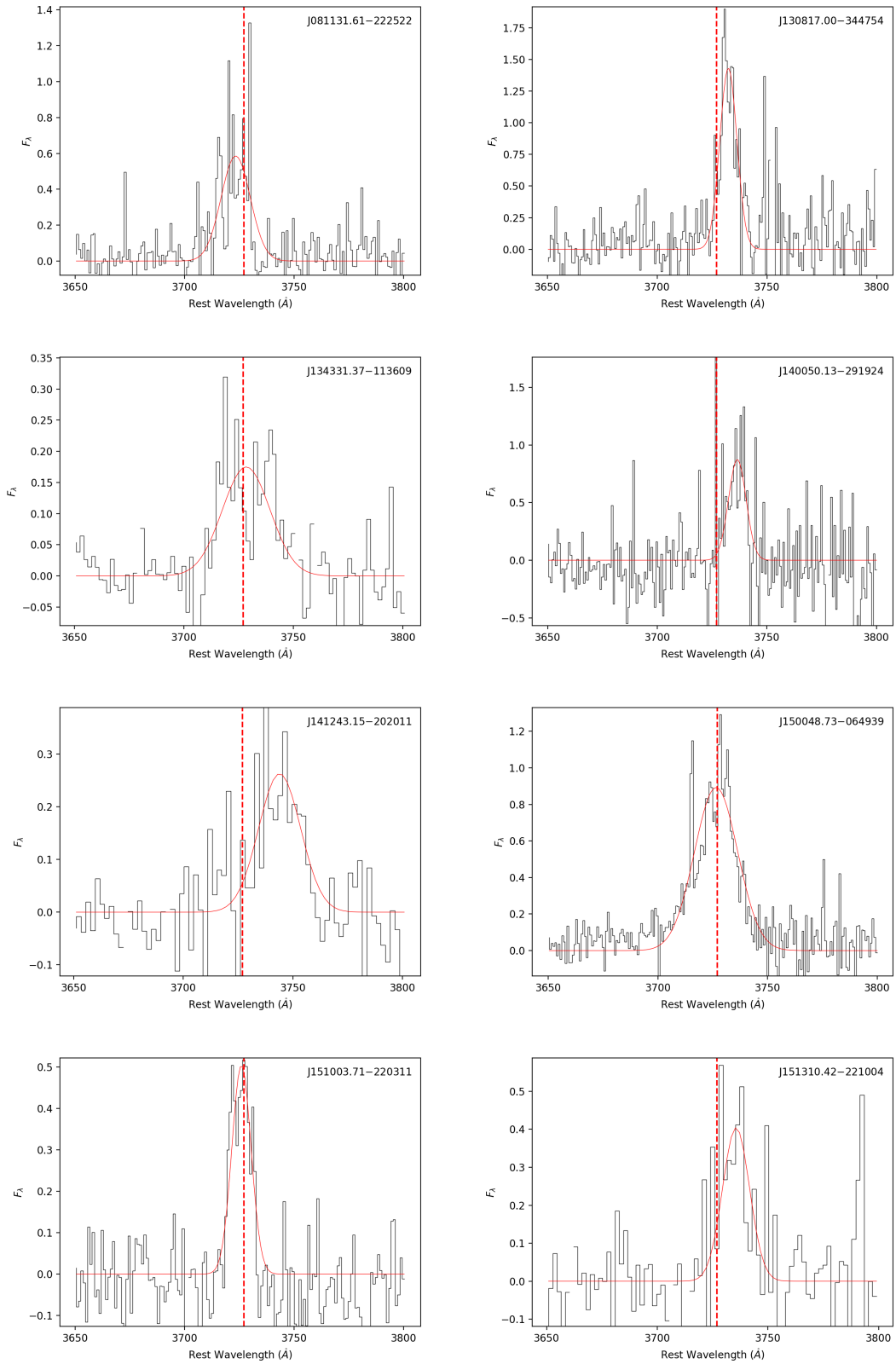

Figure 6.1: The 1D spectra in the region surrounding the OII emission line. Flux densities are in the units 10^{-16} erg s^{-1}cm^{-2}Å^{-1}. Reduced spectra and fitted model are represented by black histogram and red lines respectively.

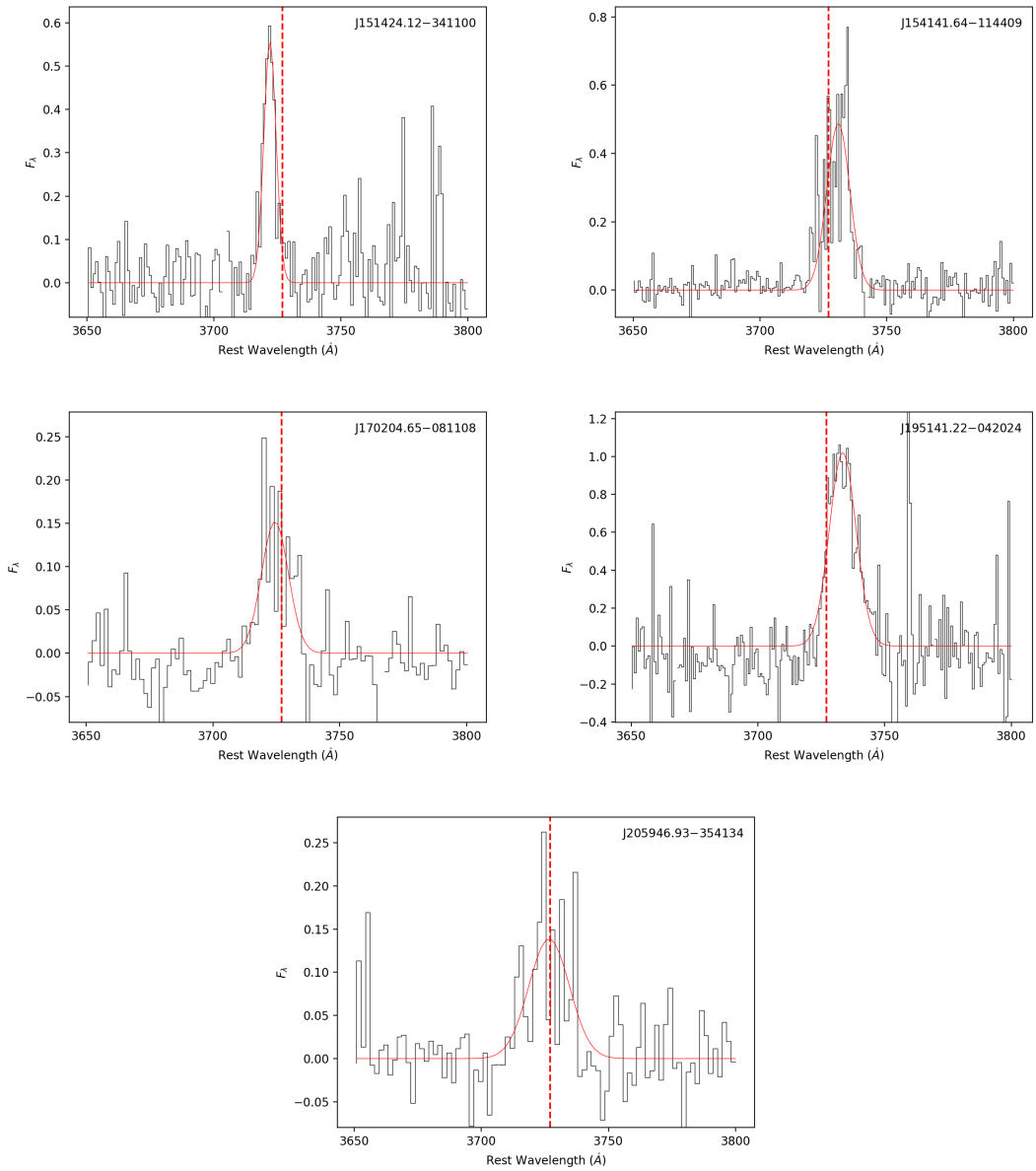

Figure 6.1: Continued

Table 6.1: The line flux and widths measured for the sources with detected O_{II} emission lines.

WISE designation	Flux (10^{-16} erg s^{-1}cm^{-2})	log Luminosity (erg s^{-1})	FWHM (kms^{-1})
J081131.61−222522	9.19 ± 0.49	42.79 ± 0.02	1430 ± 100
J130817.00−344754	14.04 ± 0.75	43.40 ± 0.02	740 ± 60
J134331.37−113609	4.78 ± 2.86	43.37 ± 0.20	1920 ± 740
J140050.13−291924	8.79 ± 0.75	43.21 ± 0.04	780 ± 90
J141243.15−202011	6.31 ± 1.86	43.15 ± 0.11	1820 ± 740
J150048.73−064939	22.07 ± 0.57	43.50 ± 0.01	1840 ± 120
J151003.71−220311	5.53 ± 0.27	42.40 ± 0.02	840 ± 40
J151310.42−221004	6.18 ± 1.74	43.35 ± 0.11	1010 ± 100
J151424.12−341100	3.38 ± 0.29	42.34 ± 0.04	460 ± 60
J154141.64−114409	5.56 ± 0.66	42.95 ± 0.05	860 ± 30
J170204.65−081108	2.02 ± 0.51	43.14 ± 0.10	1010 ± 310
J195141.22−042024	13.50 ± 0.51	43.34 ± 0.02	1260 ± 120
J205946.93−354134	2.78 ± 1.66	43.09 ± 0.20	2040 ± 1200

Table 6.2: The line flux and widths measured for the sources with detected Hδ emission lines.

WISE designation	Flux (10^{-16} erg s^{-1}cm^{-2})	log Luminosity (erg s^{-1})	FWHM (kms^{-1})
J130817.00−344754	8.67 ± 2.66	43.19 ± 0.12	1630 ± 930
J143419.59−023543	6.31 ± 1.30	43.22 ± 0.08	1830 ± 560
J150048.73−064939	20.70 ± 2.40	43.47 ± 0.05	1520 ± 190
J170325.05−051742	5.75 ± 0.84	43.10 ± 0.06	1260 ± 260
J193622.58−335420	1.45 ± 0.72	42.74 ± 0.18	1470 ± 660
J195141.22−042024	9.49 ± 1.32	43.19 ± 0.06	2650 ± 420

shows the fitted models for these six sources with their measured spectral properties given in Table 6.2.

Hγ Detections

I additionally detected six Hγ emission lines with a mean flux of 5.60×10^{-16} erg s^{-1}cm^{-2}Å^{-1} with the measured properties given in Table 6.3 and shown in Figure 6.3.

O$_{\text{I}}$ Detections

I detected the O$_{\text{I}}$ doublet in eight sources and measured a mean flux of 4.33×10^{-16} erg s^{-1}cm^{-2}Å^{-1}, detecting an emission line in W1958, which has no previous emission line detections.

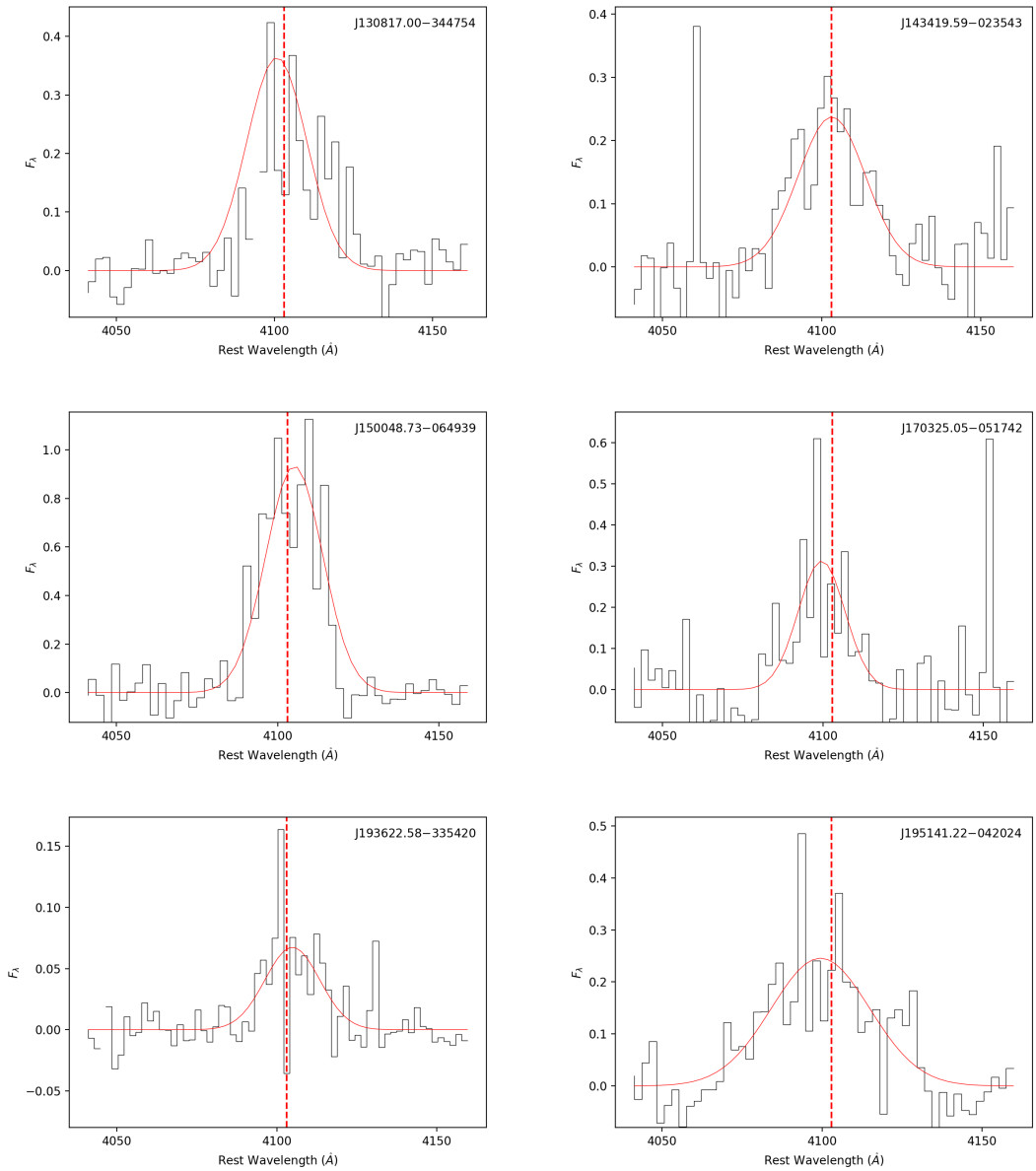

Figure 6.2: The 1D spectra in the region surrounding the Hδ emission line. Flux densities are in the units 10^{-16} erg s^{-1}cm^{-2}Å^{-1}. Reduced spectra and fitted model are represented by black histogram and red lines respectively.

Table 6.3: The line flux and widths measured for the sources with detected Hγ emission lines.

WISE designation	Flux (10^{-16} erg s^{-1}cm^{-2})	log Luminosity (erg s^{-1})	FWHM (kms^{-1})
J082311.24−062408	3.45 ± 2.83	42.85 ± 0.26	840 ± 90
J140050.13−291924	6.55 ± 1.25	43.08 ± 0.08	1170 ± 280
J151424.12−341100	2.23 ± 0.48	42.16 ± 0.08	880 ± 180
J170325.05−051742	13.85 ± 3.40	43.48 ± 0.10	1280 ± 1100
J195141.22−042024	4.05 ± 1.01	42.82 ± 0.10	970 ± 380
J200048.58−280251	3.42 ± 0.57	43.13 ± 0.07	1110 ± 260

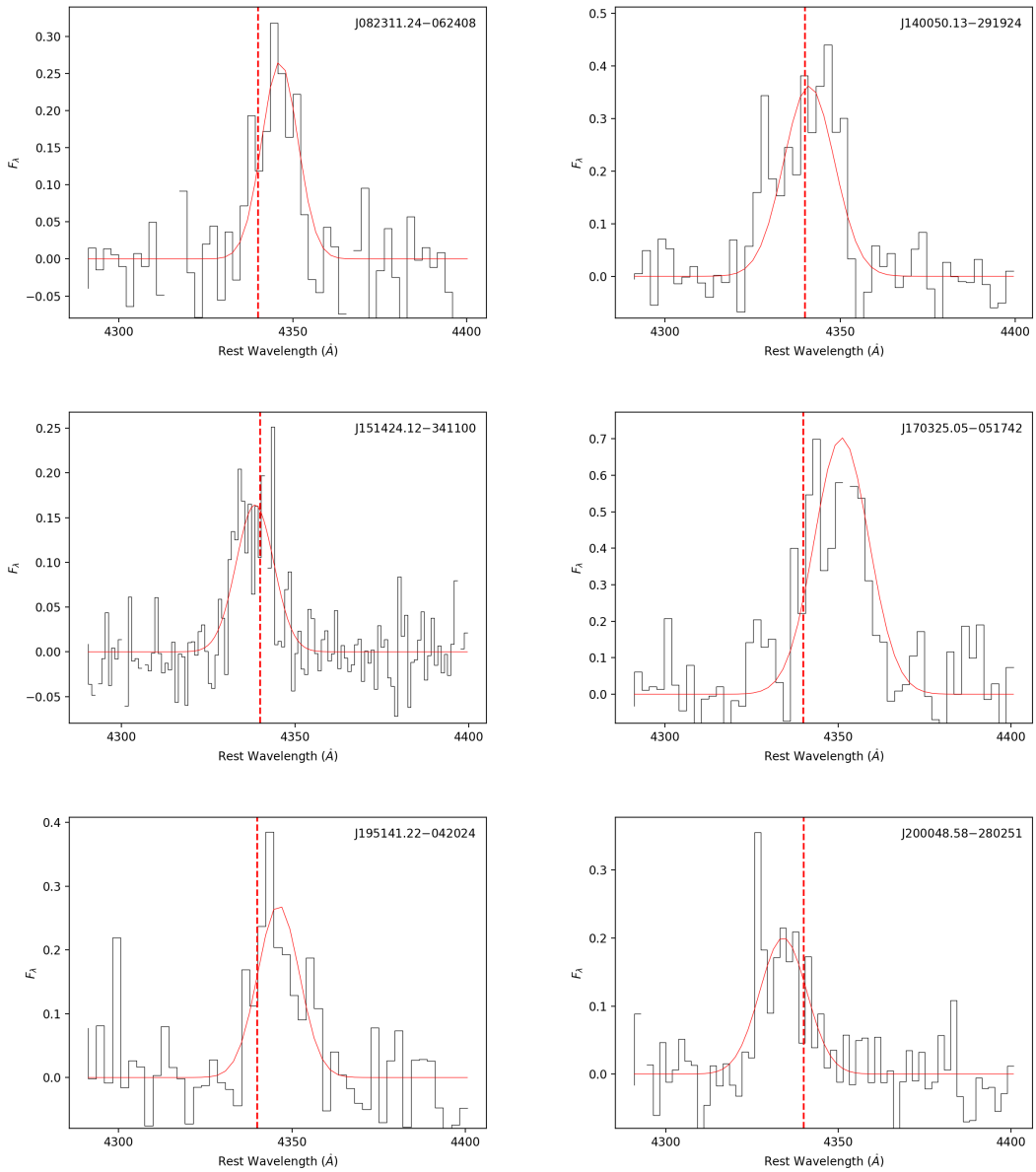

Figure 6.3: The 1D spectra in the region surrounding the Hγ emission line. Flux densities are in the units 10^{-16} erg s^{-1}cm^{-2}Å^{-1}. Reduced spectra and fitted model are represented by black histogram and red lines respectively.

Table 6.4: The line flux and widths measured for the sources with detected O_I emission lines.

WISE designation	Flux (10^{-16} erg s^{-1}cm^{-2})		log Luminosity (erg s^{-1})		FWHM (kms^{-1})	
	$\lambda = 6302$	$\lambda = 6365$	$\lambda = 6302$	$\lambda = 6365$	$\lambda = 6302$	$\lambda = 6365$
J071912.58−334944	0.53 ± 0.37	2.33 ± 0.73	41.97 ± 0.23	42.61 ± 0.12	590 ± 450	580 ± 450
J130817.00−344754	13.88 ± 1.95	4.27 ± 1.58	43.4 ± 0.06	42.89 ± 0.14	320 ± 40	310 ± 40
J140050.13−291924	5.49 ± 0.46	4.01 ± 1.79	43.0 ± 0.04	42.86 ± 0.16	1180 ± 90	1170 ± 90
J143419.59−023543	3.39 ± 0.5	3.32 ± 0.36	42.95 ± 0.06	42.94 ± 0.05	810 ± 340	800 ± 330
J150048.73−064939	5.89 ± 0.02	1.47 ± 0.36	42.92 ± 0.0	42.32 ± 0.1	1080 ± 110	1070 ± 110
J154141.64−114409	1.43 ± 0.47	0.49 ± 1.28	42.36 ± 0.12	41.9 ± 0.56	710 ± 350	700 ± 340
J195141.22−042024	1.98 ± 0.67	1.09 ± 0.63	42.5 ± 0.13	42.24 ± 0.2	740 ± 530	730 ± 520
J195801.72−074609	2.01 ± 0.79	1.66 ± 1.74	42.65 ± 0.14	42.57 ± 0.31	2970 ± 230	2950 ± 230

Table 6.5: The line flux and widths measured for the sources with detected S_{II} emission lines.

WISE designation	Flux (10^{-16} erg s^{-1}cm^{-2})	log Luminosity (erg s^{-1})	FWHM (kms^{-1})
J130817.00−344754	6.69 ± 2.29	43.08 ± 0.13	1380 ± 520
J140050.13−291924	2.82 ± 1.45	42.71 ± 0.18	620 ± 180
J143931.76−372523	5.18 ± 0.96	42.62 ± 0.07	1290 ± 210
J150048.73−064939	12.25 ± 3.86	43.24 ± 0.12	1530 ± 820
J154141.64−114409	6.39 ± 0.97	43.01 ± 0.06	1500 ± 430
J193622.58−335420	1.57 ± 0.59	42.77 ± 0.14	470 ± 240
J195141.22−042024	7.23 ± 3.02	43.07 ± 0.15	1240 ± 510
J195801.72−074609	3.47 ± 0.69	42.89 ± 0.08	1050 ± 290

SII Detections

Finally, I measured a mean flux of 5.69×10^{-16} erg s^{-1}cm^{-2}Å^{-1} across 8 detected SII emission lines, with the measured fluxes and fitted models for these two emission lines given by Figures 6.4 and 6.5 and Tables 6.4 and 6.5.

Total NIR Line Detections

In total I now detect NIR emission lines in 23/27 sources observed, measuring emission lines in an additional five sources compared to the 18 measured previously. Unlike previously there appears to be no correlation between the emission line luminosity and the number of detections.

6.2.2 Emission Line Detections in the VIS

The VIS arm of X-shooter observes across the wavelength range of $550 - 1020$ nm at a slit width of 1.5" with my observations taken with an exposure time of 2×520 s. I so far have detections of

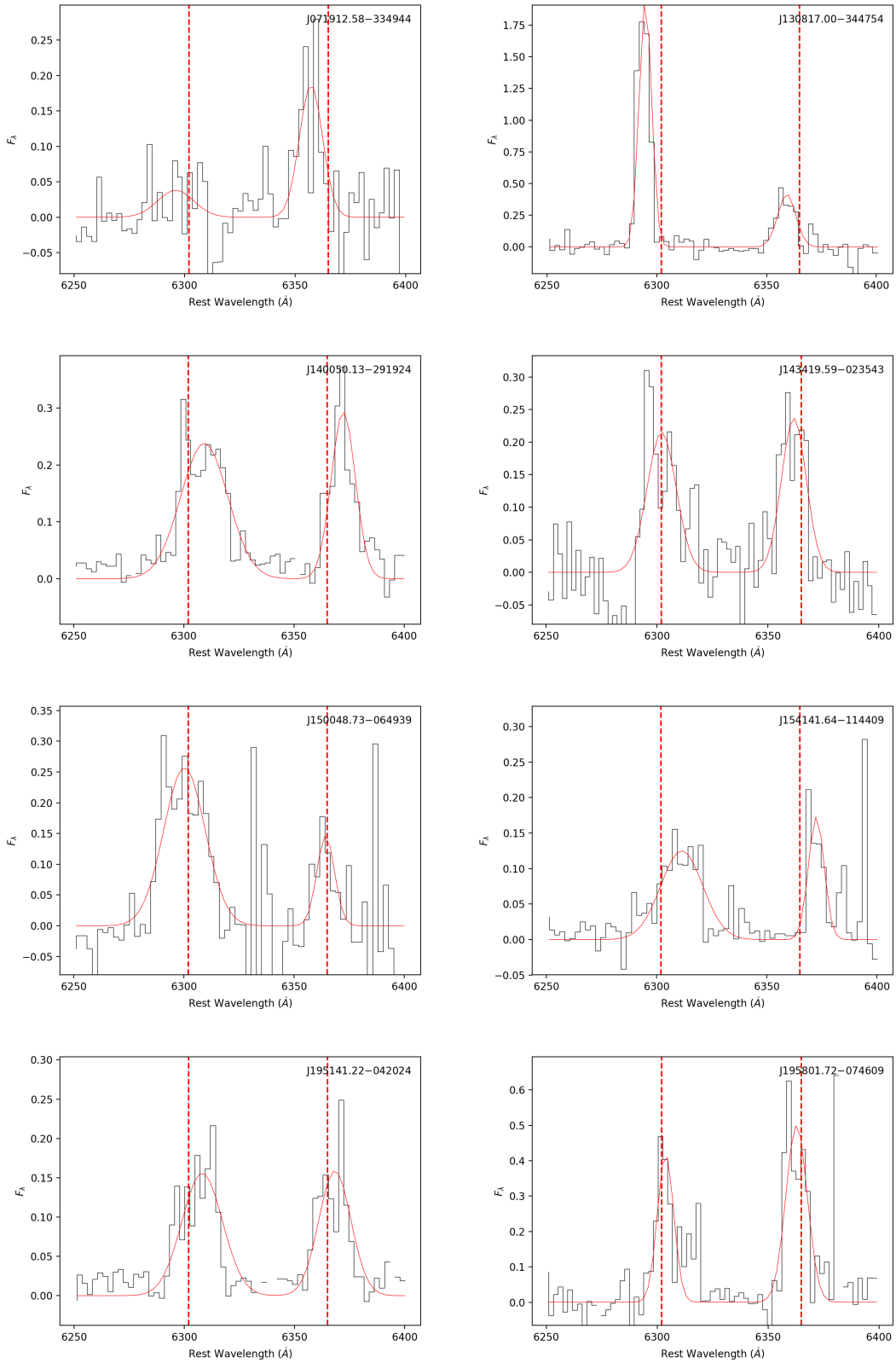

Figure 6.4: The 1D spectra in the region surrounding the OI emission line doublet. Flux densities are in the units 10^{-16} erg s^{-1}cm^{-2}Å^{-1}. Reduced spectra and fitted model are represented by black histogram and red lines respectively.

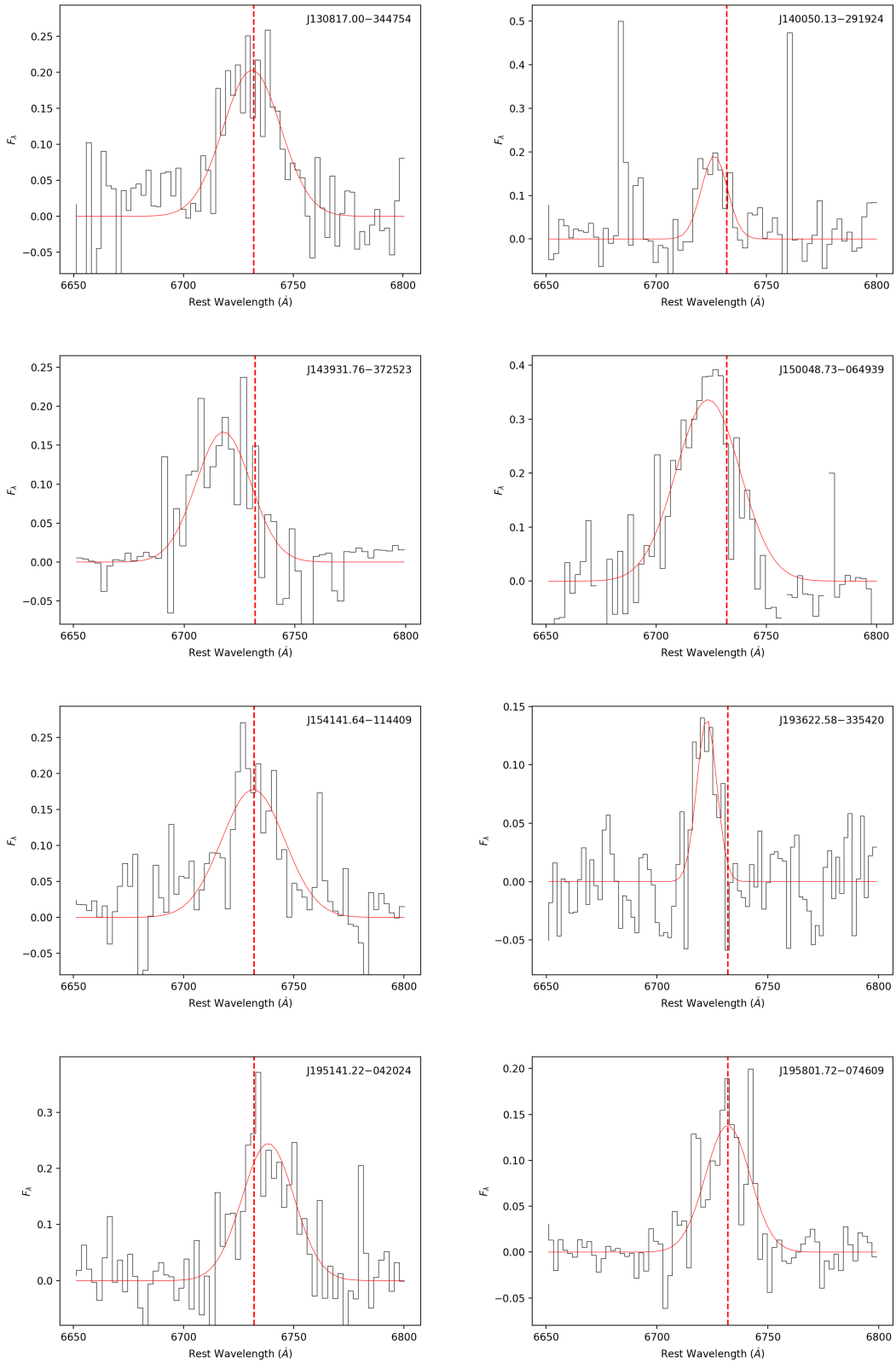

Figure 6.5: The 1D spectra in the region surrounding the SII emission line. Flux densities are in the units 10^{-16} erg s^{-1}cm^{-2}Å^{-1}. Reduced spectra and fitted model are represented by black histogram and red lines respectively.

Table 6.6: The line flux and widths measured for the sources with detected He_{II} emission lines.

WISE designation	Flux (10^{-16} erg s^{-1}cm^{-2})	log Luminosity (erg s^{-1})	FWHM (kms^{-1})
J130817.00−344754	6.25 ± 0.44	43.05 ± 0.03	3000 ± 320
J140050.13−291924	6.21 ± 2.43	43.05 ± 0.14	3720 ± 2600
J205946.93−354134	19.12 ± 1.31	43.93 ± 0.03	3930 ± 450

emission lines in 23 of the 27 galaxies observed with X-shooter, based on only the NIR and CIV emission line observations. In this section I searched for an additional emission line present in the wavelength range of the VIS arm, HeII at a wavelength of 1640 Å.

HeII Detections

Figure 6.6 shows the spectra in the region surrounding the HeII emission line for the three sources with detections of this emission line. These three sources have had previous detections in the NIR arm meaning that after investigating the emission lines present in both the NIR and VIS X-shooter arms there are still four sources with no detected lines, nor no discernible continuum. I measured a mean flux of 10.5×10^{-16} erg s^{-1}cm^{-2} across the three sources with all fluxes, luminosities and widths given in Table 6.6.

Total VIS Line Detections

Across the emission lines detected by the VIS X-shooter arm, I detected five and three sources with the CIV (see Section 4.6) and HeII emission lines respectively. There is a larger number of detections of the CIV emission line (×1.67), which has a higher mean flux (×1.23), however with only two emission lines to compare, no correlations can be drawn between the number of detections and emission line luminosity.

6.2.3 Emission Line Detections in the UVB

The final and shortest wavelength arm of X-shooter is the UVB arm observing at wavelengths of 300 - 560 nm. My observations were taken with exposures of 2 × 400 s and a slit width of 1.6". In the previous sections I searched for seven different emission lines across the NIR and VIS arms of X-shooter, and detected at least one of those emission lines in 23 of the 27 galaxies observed. Now I will search for an additional two emission lines; OVI and Lyα at respective central wavelengths of 1034 Å and 1216 Å. Despite the large redshift range of my RWGs all of the detected OVI and Lyα emission lines are present in the wavelength range of the UVB arm.

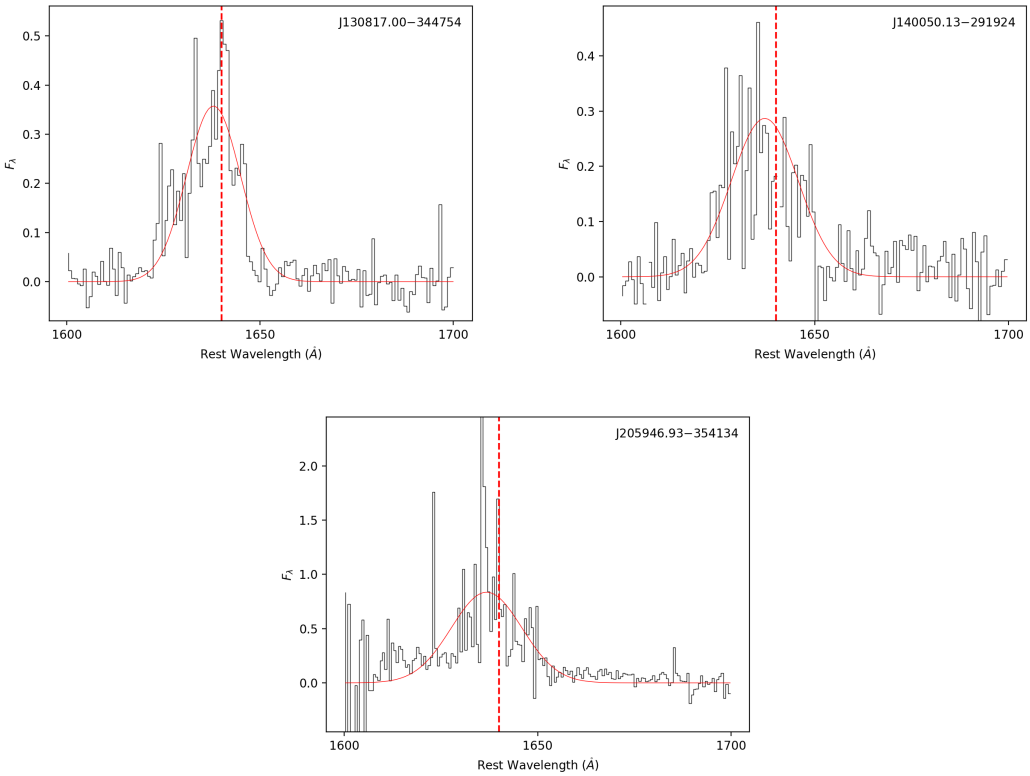

Figure 6.6: The 1D spectra in the region surrounding the HeII emission line. Flux densities are in the units 10^{-16} erg s^{-1}cm^{-2}Å^{-1}. Reduced spectra and fitted model are represented by black histogram and red lines respectively.

OVI Detections

Table 6.7 gives the measured emission line fluxes, widths and luminosities of the two detected OVI emission lines I measure. This is currently the lowest number of detections I measured for a searched line however the emission line wavelength of 1034 Å was not visible by UVB arm for those sources at the lowest redshift ($z < 1.3$). This was the case for 15 RWGs such that I detected two out of 12 possible detections, a detection percentage of 16.67% similar to the CIV emission lines. I measured a mean flux of 6.64×10^{-16} erg s^{-1}cm^{-2} with the two multi Gaussian fitted models used to derive this shown in Figure 6.7.

Lyα Detections

Figure 6.8 shows the fitted spectral models for the 10 detections of the Lyα emission line that I measure. Only one source was not within the visible wavelength range of any of X-shooters arm, so I detect ten out of 26 emission lines with my measured Lyα fluxes and widths given in Table 6.8. I measured a mean flux of 4.87×10^{-15} erg s^{-1}cm^{-2}, the largest mean flux I measured across all 12 detected emission lines in this chapter. However this mean value is dominated by the emission line luminosity of W1500 where I measured a Lyα flux of $2.46 \pm 0.24 \times 10^{-14}$ erg s^{-1}cm^{-2}.

One thing particularly notable about the Lyα emission spectra is the asymmetric nature of W1308 (see Figure 6.8), with the majority of the measured flux (> 60%) lying to of my the central wavelength of my fitted Gaussian. Through stacking all of my detected Lyα emission lines I found evidence of an underlying broad red component. The only other measurable asymmetry in my detected emission lines is for a subset of my Hα detections, which will be investigated fully in Section 6.5. However this noticeable red component differentiates the Lyα spectra from the others detected in this chapter.

Total UVB Detections

With the UVB arm of X-shooter I detected two OVI emission lines and 10 Lyα emission lines. The Lyα emission lines are the brightest found in this chapter and are $\sim 8\times$ more luminous than those from OVI. However, all of these UVB detected emission lines are present in sources that have previously had other emission line detections, leaving four sources with none. Whilst it it highly unlikely that these were unsuccessful observations, these sources did not coincide with atmospheric lines and it is therefore unclear way these sources had no observed emission lines.

Table 6.7: The line flux and widths measured for the sources with detected O_{IV} emission lines.

WISE designation	Flux (10^{-16} erg s^{-1}cm^{-2})	log Luminosity (erg s^{-1})	FWHM (kms^{-1})
J134331.37−113609	8.50 ± 0.705	43.62 ± 0.04	3460 ± 370
J205946.93−354134	4.78 ± 0.77	43.32 ± 0.07	3390 ± 1350

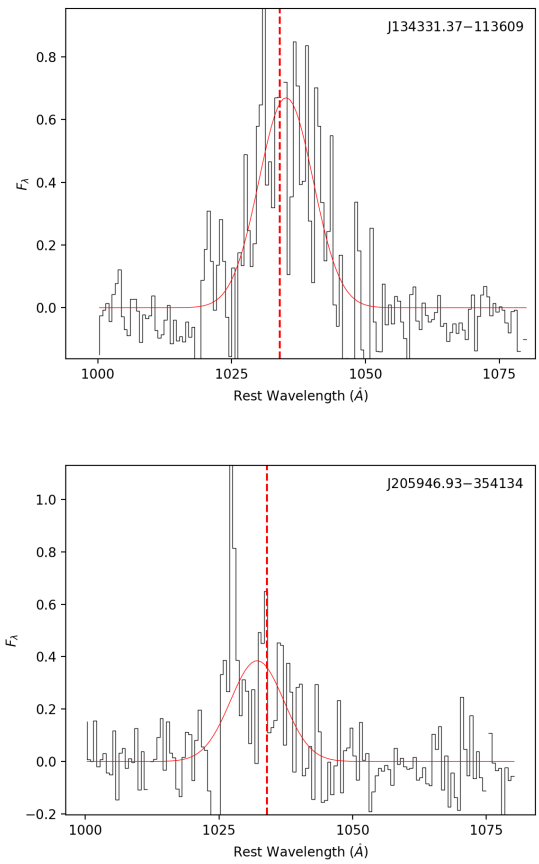

Figure 6.7: The 1D spectra in the region surrounding the OVI emission line. Flux densities are in the units 10^{-16} erg s^{-1}cm^{-2}Å^{-1}. Reduced spectra and fitted model are represented by black histogram and red lines respectively.

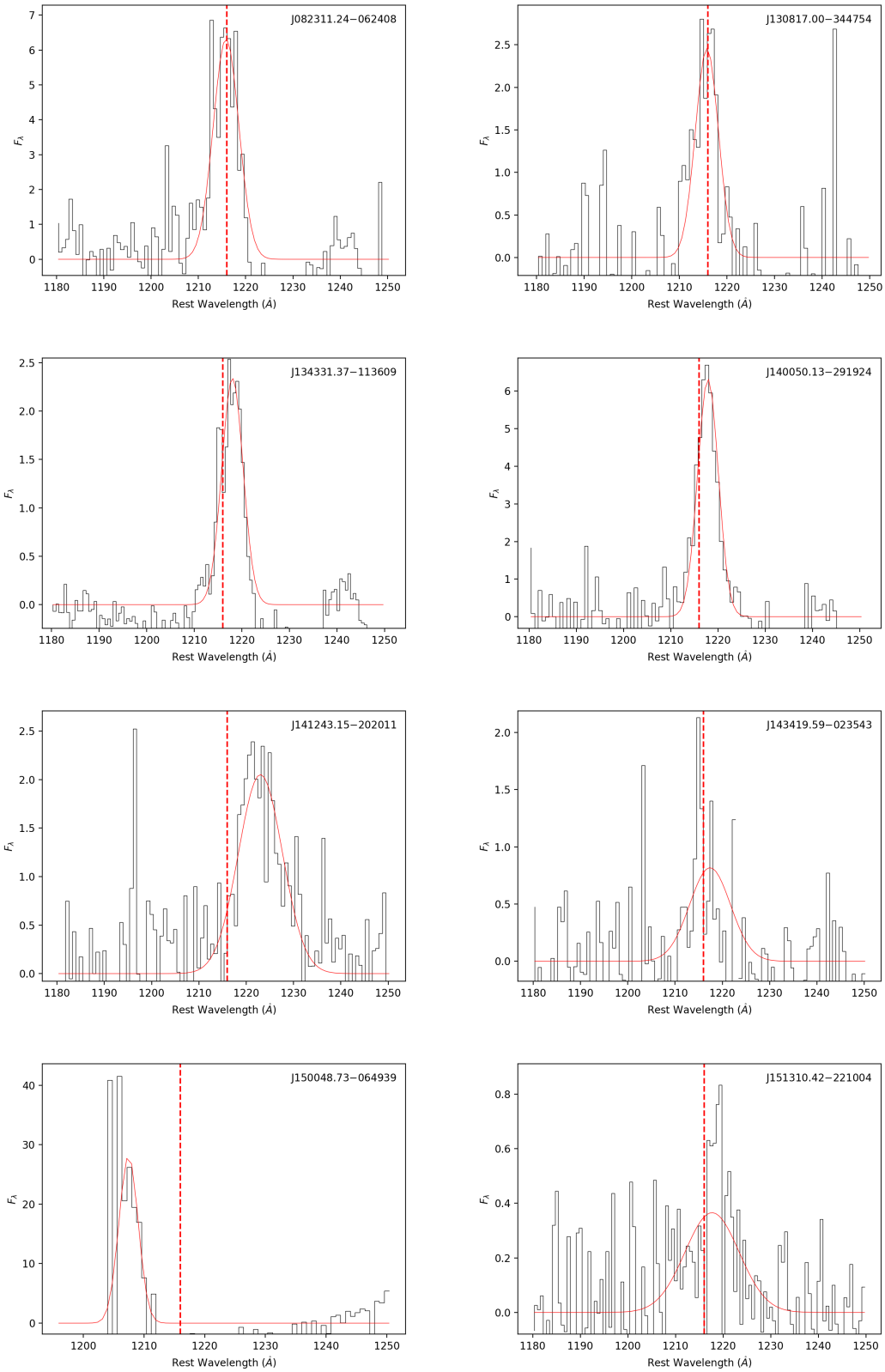

Figure 6.8: The 1D spectra in the region surrounding the Lyα emission line. Flux densities are in the units 10^{-16} erg s^{-1}cm^{-2}Å^{-1}. Reduced spectra and fitted model are represented by black histogram and red lines respectively.

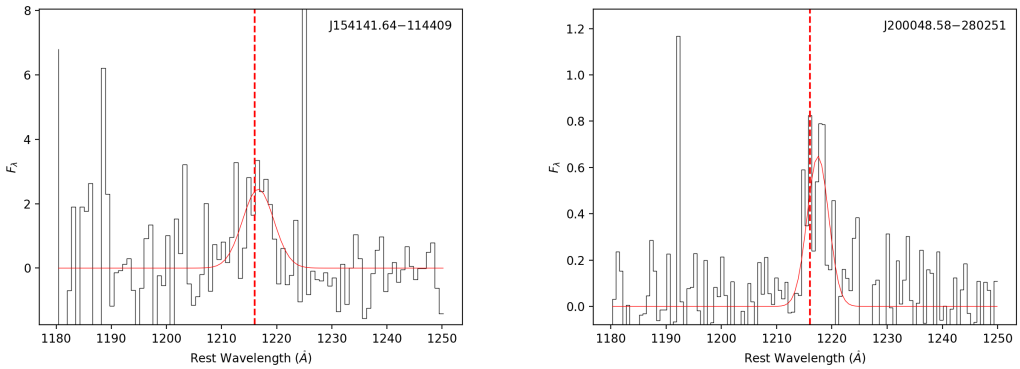

Figure 6.8: Continued

Table 6.8: The line flux and widths measured for the sources with detected Lyα emission lines.

WISE designation	Flux (10^{-16} erg s^{-1}cm^{-2})	log Luminosity (erg s^{-1})	FWHM (kms^{-1})
J082311.24−062408	62.00 ± 3.02	44.12 ± 0.02	2030 ± 150
J130817.00−344754	26.16 ± 2.83	43.67 ± 0.05	2080 ± 350
J134331.37−113609	20.87 ± 4.82	44.01 ± 0.01	1750 ± 50
J140050.13−291924	41.18 ± 2.19	43.87 ± 0.02	1460 ± 110
J141243.15−202011	36.99 ± 2.60	43.92 ± 0.03	3330 ± 310
J143419.59−023543	16.45 ± 1.31	43.63 ± 0.03	3560 ± 350
J150048.73−064839	246.41 ± 24.11	44.54 ± 0.04	1380 ± 50
J151310.42−221004	5.09 ± 1.68	43.7 ± 0.12	2350 ± 790
J154141.64−114409	29.18 ± 1.55	43.62 ± 0.03	2250 ± 310
J200048.58−280251	3.59 ± 0.39	43.14 ± 0.05	1180 ± 150

Table 6.9: The line flux and widths measured for the sources with detected Ca(K) emission lines.

WISE designation	Flux (10^{-16} erg s^{-1}cm^{-2})	log Luminosity (erg s^{-1})	FWHM (kms^{-1})
J170325.05−051742	17.93 ± 2.75	43.6 ± 0.06	2670 ± 410

6.2.4 Absorption Line Detections

Looking across all three arms of the X-shooter spectra I have detected 12 different emission lines across 23/27 RWGs. Fitting multi Gaussian models to the spectra in the region surrounding the targeted emission lines, I measure the widths, fluxes and luminosities allowing for further investigation, including galaxy classification (see section 6.3) and calculation of BH and host galaxy masses. Now, in this section I searched for six common absorption lines that fall in the NIR and VIS arms wavelength range. I aimed to specifically detect the Ca(K), Ca(H), Ca(G), Mg, Na and Ca_{II} absorption lines at respective wavelengths of 3933 Å, 3968 Å, 4305 Å, 5175 Å, 5894 Å and 8500 Å.

I detected zero absorption lines at the wavelengths of Ca(H), Ca(G) and Na so will not discuss them any further in this work. However, these non detections were not due to the rest wavelengths of the lines redshift as they were observed by 26, 26 and 27 RWGs respectively.

I detected one peak at the central wavelength of the Ca(K) line, measuring an emission not absorption line, with a positive amplitude as shown by the results in Table 6.9 and Figure 6.9. I additionally detect three lines with a positive amplitude at the central wavelength of the Mg absorption line with a mean flux of 5.93×10^{-16} erg s^{-1}cm^{-2}, again with the fitted models and measured spectral properties given in Table 6.10 and Figure 6.10.

I did however detect one absorption line at the Ca_{II} 8500 Å rest wavelength of this emission line triplet. Figure 6.11 shows this absorption line detected in W1400 with the measured flux and width and Table 6.11. At a measured FWHM of 2670 km s^{-1} this is broader than my other previously detected absorption line at the rest wavelength of CIV (Chapter 4), and the broadest of all detected emission line FWHMs for W1400.

All of these additional absorption/emission lines are present in sources with previously detected emission lines such that I measured emission and/or absorption lines in 23/27 RWGs observed with X-shooter.

6.2.5 Summary of all Lines Detected

In this section I have detected an additional eight emission lines, across the the three observed arms of X-shooter. These detected emission lines have been well modelled by again fitting multiple Gaussians to the corrected spectra spectra, with a Monte Carlo approach used to determine

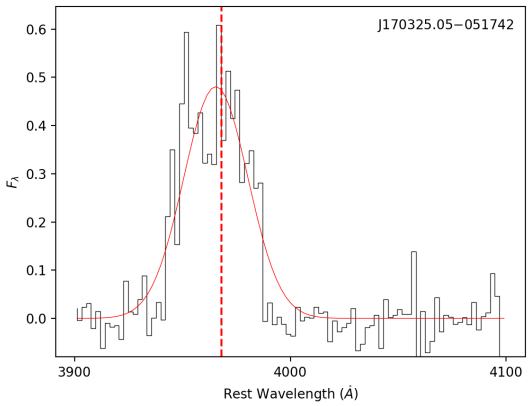

Figure 6.9: The 1D spectra in the region surrounding the Ca(K) emission line. Flux densities are in the units 10^{-16} erg s^{-1}cm^{-2}Å^{-1}. Reduced spectra and fitted model are represented by black histogram and red lines respectively.

Table 6.10: The line flux and widths measured for the sources with detected Mg emission lines.

WISE designation	Flux (10^{-16} erg s^{-1}cm^{-2})	log Luminosity (erg s^{-1})	FWHM (kms^{-1})
J140050.13−291924	5.86 ± 0.83	43.03 ± 0.06	1720 ± 410
J150048.73−064939	8.70 ± 1.68	43.09 ± 0.08	2120 ± 490
J204049.51−390400	3.24 ± 1.61	42.97 ± 0.18	1970 ± 1100

Table 6.11: The line flux and widths measured for the sources with detected Ca_{II} emission lines.

WISE designation	Flux (10^{-16} erg s^{-1}cm^{-2})	log Luminosity (erg s^{-1})	FWHM (kms^{-1})
J140050.13−291924	10.48 ± 2.96	43.28 ± 0.11	1480 ± 560

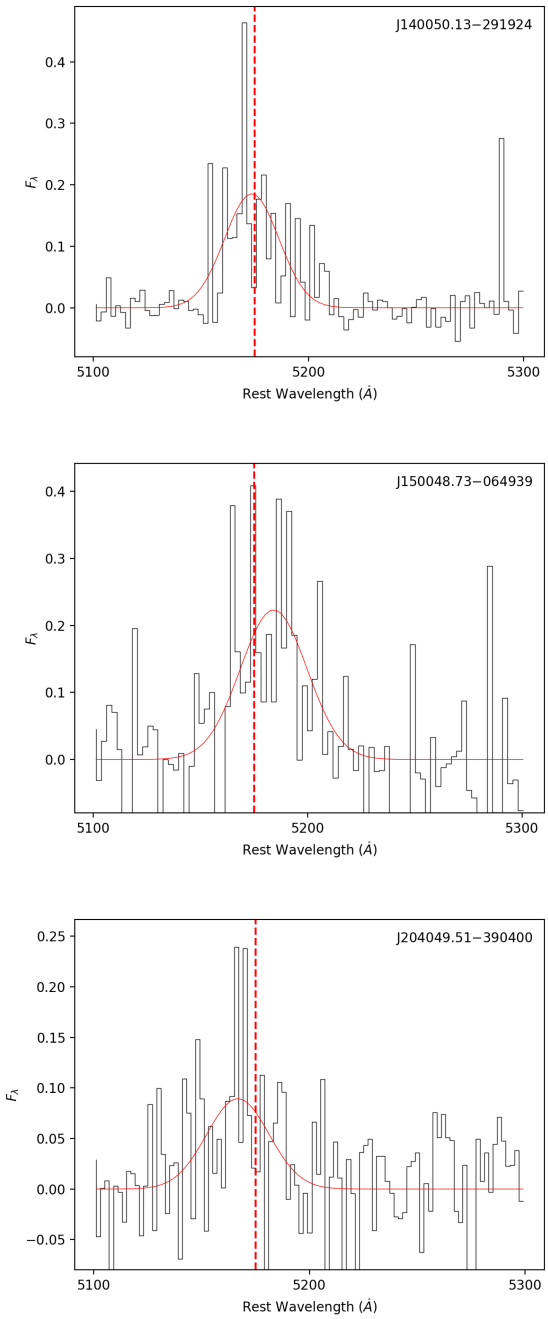

Figure 6.10: The 1D spectra in the region surrounding the Mg emission line. Flux densities are in the units 10^{-16} erg s^{-1}cm^{-2}Å^{-1}. Reduced spectra and fitted model are represented by black histogram and red lines respectively.

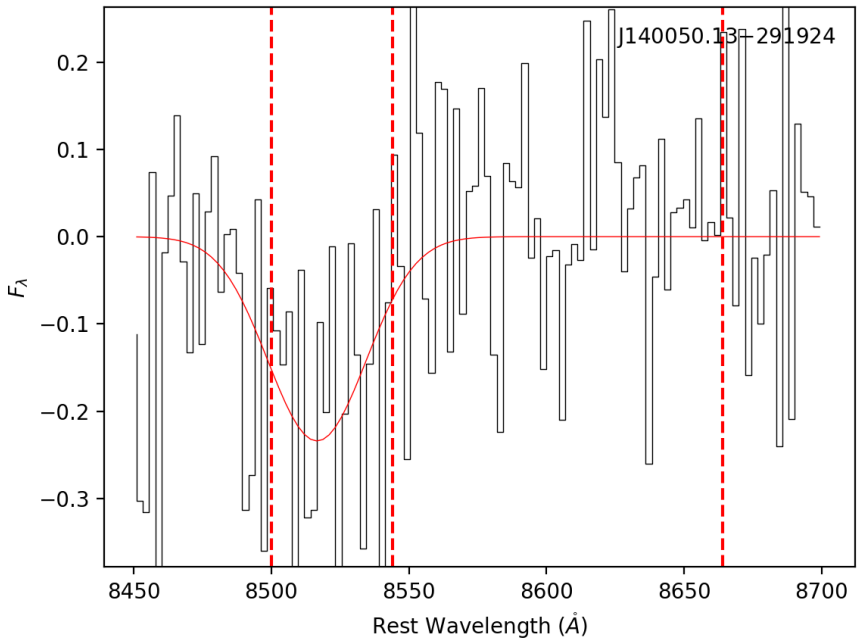

Figure 6.11: The 1D spectra in the region surrounding the Ca_{II} absorption line. Flux densities are in the units 10^{-16} erg s^{-1}cm^{-2}Å^{-1}. Reduced spectra and fitted model are represented by black histogram and red lines respectively.

the errors on my measured spectral properties. Whilst most lines where acceptably fitted by a maximum of two Gaussian components, there is noticeable asymmetry in the Lyα emission line of W108 and my detected Hα emission lines.

In total I now have detections of 12 different emission lines, and three common absorption lines across 23 RWGs out of the 27 possible sources observed. A summary of my 12 detected emission lines is given by Table 6.12, including which X-shooter arm the emission line wavelengths fall in. Details of the three absorption lines detected is given by Table 6.13. These tables will allow for quick reference as to how many detection of each line were made and for comparison of which sources had the largest number of detections.

The four sources without any detected emission lines are W1521, W1641, W1653 and W2021. The first three of these sources were only observed by ISAAC in the K_S band which may have affected the amount of positional information available leading to a possible missed observation, however for W2021 was observed in both the J and K_S bands of ISAAC. These sources are at the higher end of the redshift range of my RWG sample, measuring $z \geq 1.83$ and with the exception of the OVI emission line of W1641, all 12 emission lines searched for were within the observed wavelength range. Examining the spectra of these four sources for visible continuum, I measured no discernible continuum in the spectra of W1521 and W1641. It is therefore likely

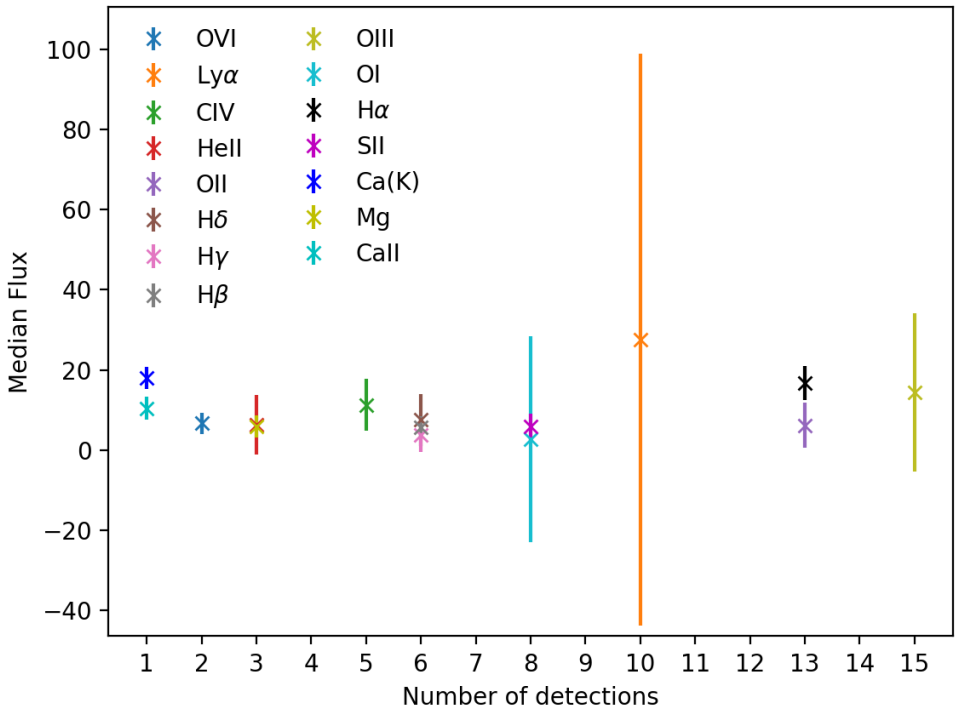

Figure 6.12: The number of detections of each line against the median measured flux.

that these two sources were not successfully observed. There is however measurable continuum in the spectra of W1653 and W2021, so it is very unlikely that my lack of measurable emission lines is due to a misplaced slit. It is possible that these emission lines lie in regions of strong sky absorption lines or there is higher noise levels in the spectra, but I can not be certain why I detected no emission lines among these four sources.

Figure 6.12 shows the number of detections of each emission/absorption line plotted against my median measured flux, in an aim to determine whether there is a correlation between the number of detections and the line luminosity. Whilst for two of these data points, I only have one detection such that the plotted median flux is the singular measured flux, there appears to be little correlation. The top four detected lines do have the highest measured individual fluxes however with a large measured flux range no clear correlation can be found.

In summary, I measured emission and absorption lines at 15 different wavelengths across all three arms of the X-shooter spectograph. These lines were measured across 23 RWGs out of the full observed sample of 27 galaxies. There was no measurable continuum for two of these four sources without any detections, though a misplaced slit is unlikely. For the remaining two sources, it is also uncertain why there are no detected lines, there weren't high levels of noise nor did they align with regions of strong sky absorption.

Table 6.12: All sources with X-Shooter spectra marked as to whether these emission lines are detected in the spectra. Y = detection, N = no detection, with a blank space representing where the wavelength of the emission line was not covered by the spectra. The superscript represents which arm the emission line wavelength falls in with 1 = UVB, 2 = VIS and 3 = NIR.

WISE Designation	Emission Line Name and Rest Wavelength											
	OVI	Lyα	CIV	HeII	OII	Hδ	Hγ	Hβ	OIII	OI	Hα	SII
	1034 Å	1216 Å	1549 Å	1640 Å	3727 Å	4103 Å	4340 Å	4861 Å	4959, 5007 Å	6302, 6365 Å	6562 Å	6732 Å
J071912.58−334944	-	N^1	-	-	N^2	N^3	N^3	N^3	N^3	Y^3	N^3	N^3
J081131.61−222522	-	-	N^1	N^1	Y^2	N^2	N^2	N^3	Y^3	N^3	Y^3	N^3
J082311.24−062408	-	Y^1	Y^1	N^1	N^3	N^3	Y^3	Y^3	Y^3	N^3	Y^3	N^3
J130817.00−344754	-	Y^1	Y^1	Y^1	Y^2	Y^3	N^3	Y^3	Y^3	Y^3	Y^3	Y^3
J134331.37−113609	Y^1	Y^1	Y^1	-	Y^3	N^3	N^3	N^3	Y^3	N^3	N^3	N^3
J140050.13−291924	-	Y^1	Y^1	Y^1	Y^2	N^3	Y^3	Y^3	Y^3	Y^3	Y^3	Y^3
J141243.15−202011	-	Y^1	N^1	N^1	Y^3	N^3	N^3	N^3	Y^3	N^3	Y^3	N^3
J143419.59−023543	N^1	Y^1	N^1	N^1	N^3	Y^3	N^3	N^3	Y^3	Y^3	Y^3	N^3
J143931.76−372523	-	-	N^1	N^1	-	-	-	N^3	N^3	N^3	Y^3	Y^3
J150048.73−064939	-	Y^1	N^1	N^1	Y^2	Y^3	N^3	Y^3	Y^3	Y^3	Y^3	Y^3
J151003.71−220311	-	-	N^1	N^1	Y^2	N^2	N^2	N^2	Y^2	N^3	Y^3	N^3
J151310.42−221004	N^1	Y^1	N^1	N^1	Y^3	N^3	N^3	N^3	N^3	N^3	Y^3	N^3
J151424.12−341100	-	-	N^1	N^1	Y^2	N^2	Y^2	N^3	Y^3	N^3	N^3	N^3
J152116.59+001755	N^1	N^1	N^2	N^2	N^3	N^3	N^3	N^3	N^3	N^3	N^3	N^3
J154141.64−114409	-	Y^1	Y^1	N^1	Y^2	N^3	N^3	N^3	Y^3	Y^3	Y^3	Y^3
J163426.87−172139	N^1	N^1	N^1	N^1	N^3	N^3	N^3	N^3	Y^3	N^3	Y^3	N^3

J164107.22−054827	-	N[1]	N[1]	N[1]	N[3]	N[3]	N[3]	N[3]	N[3]	N[3]	N[3]	N[3]
J165305.40−010230	N[1]	N[1]	N[1]	N[1]	N[3]	N[3]	N[3]	N[3]	N[3]	N[3]	N[3]	N[3]
J170204.65−081108	N[1]	N[1]	N[2]	N[2]	Y[3]	N[3]	N[3]	N[3]	Y[3]	N[3]	N[3]	-
J170325.05−051742	-	N[1]	N[1]	N[1]	N[3]	Y[3]	Y[3]	N[3]	N[3]	N[3]	N[3]	N[3]
J193622.58−335420	N[1]	N[1]	N[1]	N[1]	N[3]	Y[3]	N[3]	N[3]	N[3]	N[3]	N[3]	Y[3]
J195141.22−042024	-	N[1]	N[1]	N[1]	Y[2]	Y[3]	Y[3]	Y[3]	Y[3]	Y[3]	Y[3]	Y[3]
J195801.72−074609	-	N[1]	N[1]	N[1]	N[3]	N[3]	N[3]	N[3]	N[3]	Y[3]	N[3]	Y[3]
J200048.58−280251	N[1]	Y[1]	N[1]	N[1]	N[3]	N[3]	Y[3]	N[3]	Y[3]	N[3]	N[3]	N[3]
J202148.06−261159	N[1]	N[1]	N[1]	N[2]	N[3]	N[3]	N[3]	N[3]	N[3]	N[3]	N[3]	N[3]
J204049.51−390400	N[1]	N[1]	N[1]	N[1]	N[3]	N[3]	N[3]	Y[3]	N[3]	N[3]	N[3]	N[3]
J205946.93−354134	Y[1]	N[1]	N[1]	Y[2]	Y[3]	N[3]	N[3]	N[3]	N[3]	N[3]	N[3]	N[3]

6.3 Classifying RWGs using BPT Diagrams

With nine extra emission lines now measured, and three additional absorption lines, I measured at least one out of 15 different line fluxes across 23 RWGs. I now aim to utilise these extra line detections to help classify my subset of RWGs by placing them on BPT diagrams (Baldwin et al., 1981). BPT diagrams are a set of three different plots that use nuclear emission line ratios to distinguish between the ionisation mechanism of nuclear gas. Through a sources placement onto one, or all, BPT diagrams you can infer the mechanism that powers galaxies. BPT diagrams allow you to distinguish between AGN and star forming galaxies, which then allows for comparisons with other similar populations. The dividing lines of these BPT diagrams (Baldwin et al., 1981; Kauffmann et al., 2003c,a,b; Kewley et al., 2001) were derived through fitting correlations between observed and known sources, using catalogued data. BPT diagrams can therefore be used as a tool to infer the nature of an observed source, through emission line measurements, rather than using more difficult SED fitting. If a population of sources is situated within a unique position on the BPT diagrams, they could also be used as a source classification tool for future RWG observations, or using previously observed survey data. Through the placement of RWGs galaxies onto BPT diagrams I therefore aimed to confirm the AGN nature of these RWGs and compare their position to previously measured HotDOG sources, aiming to see of they occupy the same space.

The first BPT diagram (BPT1, Baldwin et al., 1981) compares the ratios of [NII]$\lambda\lambda 6548, 6563$/H$\alpha$ and [OIII]$\lambda 5007$/Hβ emission lines with two dividing lines derived by Kauffmann et al. (2003a,b,c) and Kewley et al. (2001) provided in Equations 6.1 and 6.2.

$$\log\left(\frac{\mathrm{OIII}}{\mathrm{H}\beta}\right) = 0.61/\left(\log\left(\frac{\mathrm{NII}}{\mathrm{H}\alpha}\right) - 0.05\right) + 1.30 \tag{6.1}$$

$$\log\left(\frac{\mathrm{OIII}}{\mathrm{H}\beta}\right) = 0.61/\left(\log\left(\frac{\mathrm{NII}}{\mathrm{H}\alpha}\right) - 0.47\right) + 1.19 \tag{6.2}$$

Galaxies that lie above both of these lines are thought to be AGN rather than dominated by star formation with sources that lie between the lines likely a composite of the two. The second BPT diagram (BPT2) compares the ratios of SII/Hα to [OIII]$\lambda 5007$/Hβ and is separated with dividing lines given by Equations 6.3 and 6.4 (Kewley et al., 2006). Sources that lie above the dividing line given by Equation 6.3 are again dominated by AGN emission rather than star formation, whereas Equation 6.4 separates these AGN dominated sources into Seyferts or LINERs, with sources lying below the line classified as LINERs.

Table 6.13: All sources with X-Shooter spectra marked as to whether these absorption lines are detected in the spectra. Y = detection, N = no detection, with a blank space representing where the wavelength of the absorption line was not covered by the spectra. The superscript represents which arm the emission line wavelength falls in with 1 = UVB, 2 = VIS and 3 = NIR. Note that I also searched for the lines Ca(H) ($\lambda = 3933$ Å) , Ca(G) ($\lambda = 4305$ Å) and Na ($\lambda = 5894$ Å) with no detections across all sources.

WISE Designation	Absorption Lines		
	Ca(K)	Mg	CaII
	$\lambda = 3969$ Å	$\lambda = 5175$ Å	$\lambda = 8500$ Å
J071912.58−334944	N^3	N^3	N^3
J081131.61−222522	N^2	N^3	N^3
J082311.24−062408	N^3	N^3	N^3
J130817.00−344754	N^3	N^3	N^3
J134331.37−113609	N^3	N^3	-
J140050.13−291924	N^3	Y^3	Y^3
J141243.15−202011	N^3	N^3	N^3
J143419.59−023543	N^3	N^3	-
J143931.76−372523	-	N^3	N^3
J150048.73−064939	N^2	Y^3	N^3
J151003.71−220311	N^2	N^3	N^3
J151310.42−221004	N^2	N^3	-
J151424.12−341100	N^2	N^3	N^3
J152116.59+001755	N^3	N^3	-
J154141.64−114409	N^3	N^3	N^3
J163426.87−172139	N^3	N^3	-
J164107.22−054827	N^3	N^3	N^3
J165305.40−010230	N^3	N^3	-
J170204.65−081108	N^3	N^3	-
J170325.05−051742	Y^3	N^3	N^3
J193622.58−335420	N^3	N^3	-
J195141.22−042024	N^3	N^3	N^3
J195801.72−074609	N^3	N^3	N^3
J200048.58−280251	N^3	N^3	-
J202148.06−261159	N^3	N^3	-
J204049.51−390400	N^3	Y^3	-
J205946.93−354134	N^3	N^3	-

$$\log\left(\frac{\mathrm{OIII}}{\mathrm{H}\beta}\right) = 0.72/\left(\log\left(\frac{\mathrm{SII}}{\mathrm{H}\alpha}\right) - 0.32\right) + 1.30 \tag{6.3}$$

$$\log\left(\frac{\mathrm{OIII}}{\mathrm{H}\beta}\right) = 1.89 \times \log\left(\frac{\mathrm{SII}}{\mathrm{H}\alpha}\right) + 0.76 \tag{6.4}$$

The third BPT diagram (BPT3) again uses two dividing lines to separate between AGN and star forming galaxies and then between Seyferts and LINERs. It compares the ratios of OI/Hα to [OIII]λ5007/Hβ with the dividing lines given by Equations 6.5 and 6.6 (Kewley et al., 2006). Again sources that lie above Equation 6.5 are dominated by AGN emission not star formation, with sources that lie above Equation 6.6 classified as Seyferts not LINER AGNs.

$$\log\left(\frac{\mathrm{OIII}}{\mathrm{H}\beta}\right) = 0.73/(\log\left(\frac{OI}{H\alpha}\right) + 0.59) + 1.33 \tag{6.5}$$

$$\log\left(\frac{\mathrm{OIII}}{\mathrm{H}\beta}\right) = 1.18 \times \log\left(\frac{\mathrm{OI}}{\mathrm{H}\alpha}\right) + 1.30 \tag{6.6}$$

Though derived at different times, with dividing lines added as new observations were made, these three BPT diagrams can be combined with the aim of classifying the nature of a source. This should allow me to confirm the AGN nature of RWGs, but though the comparison of source positions on the three BPT diagrams to HotDOGs (Jun et al., 2020) I aimed to see where the two populations may differ, or if they do not, question whether RWGs and HotDOGs are the same population of sources selected using different criteria. Figure 6.13 shows an example of these three BPT diagrams, with no added sources, in order to show how the dividing lines separate the AGN and star forming galaxy classifications. I aimed to use the measured emission lines to determine the classification of my RWGs. I used all available emission lines, plotting my sources and others for comparison, both before and after extinction corrections are applied.

All of the three BPT diagrams use the measured flux ratios of the Hβ emission line compared to the measured emission line fluxes of the [OIII]λ5007 line. The [OIII]λ5007 emission line is my most successfully detected, with 15 detections, however I have only six detections of the Hβ emission line, five of which correspond with detected [OIII]λ5007 emission lines. The lack of Hβ emission line detections was discussed thoroughly in Chapter 4, and theorised as being due to the comparably fainter fluxes of the Hβ lines combined with the higher levels of noise at these spectral wavelengths. In order to bypass this issue, I described my methods used to create a

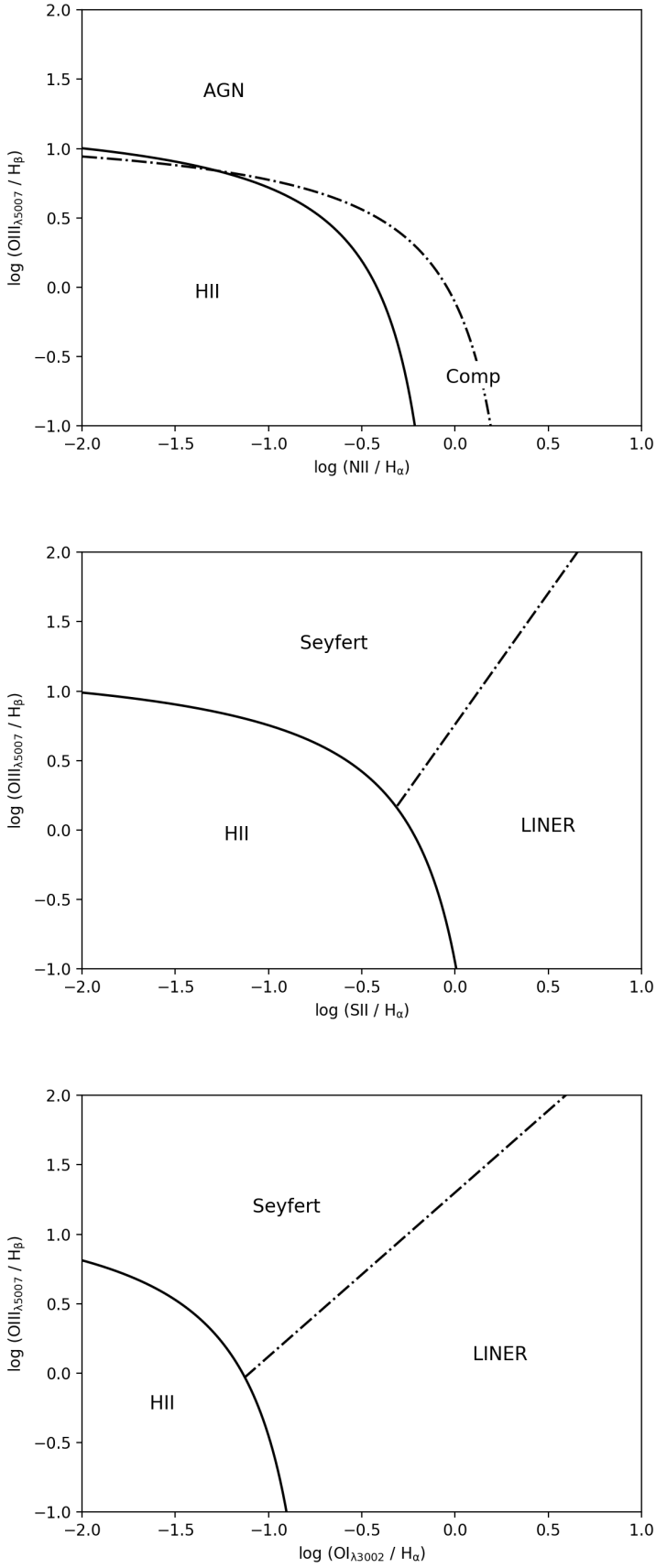

Figure 6.13: The three BPT diagrams (ordered vertically from BPT1 to BPT3) comparing nuclear emission line ratios, with the dividing lines and galaxy categorisations, including AGN and star formation dominated, shown.

simulated realistic Hβ emission line, based on my calculated Hα BH masses, in Chapter 5. In order to be able to place more sources onto a BPT diagram, I again utilised this method, in a separate section further on. With use of both my measured and simulated Hβ emission lines I was able to place 11 RWGs on to a BPT diagram, more than doubling my sample size, and be able to compare the difference between the simulated and real values.

The first BPT diagram compares the flux of the [NII]$\lambda\lambda 6548, 6563$ doublet to that of Hα. I have however been unable to distinguish the underlying [NII]$\lambda\lambda 6548, 6563$ doublet from the broad Hα line measurements. I therefore assumed a ratio of $[N_{II}]/\mathrm{H}_\alpha = 0.83 \pm 0.42$ as in Kim et al. (2013). Using this assumption I placed five RWGs on a BPT1 diagram, or 11 sources if I use a simulated Hβ line. Whilst when using the Hα flux to estimate BH masses in Chapter 4 I assumed the flux and width to be dominated by Hα as confirmed through attempts to simulate and fit the [NII]$\lambda\lambda 6548, 6563$ doublet. These simulations showed that for the broad nature of these sources the Hα profile is dominant. It will however be possible to see where my sources would lie assuming Hα » [NII]$\lambda\lambda 6548, 6563$, through plotting them using this assumed ratio.

BPT2 instead uses a detected SII emission line in the place on [NII]$\lambda\lambda 6548, 6563$. I have detected eight SII lines, and can place four sources on a BPT diagram using my measured Hβ emission lines, or five sources if I use a simulated Hβ line. Finally the third BPT diagrams depends on the ratio of OI/Hα. I have again measured eight detected OI emission lines and can place four RWGs onto BPT3 if I use my measured Hβ fluxes and six RWGs if I use my simulated Hβ flux.

One other factor to consider is that as shown in Chapter 5, these RWGs are affected by dust extinction, meaning that the intrinsic fluxes are more luminous than I observe. As the BPT diagrams plot flux ratios, the extinction corrections at a fixed value of A_V will depend on the different rest wavelengths of the emission lines and the extinction law used (see section 5.4). These following sections aim to classify as many RWGs as possible by using my detected emission line fluxes to place them on the three BPT diagrams. This will be done firstly using my measured Hβ emission lines, then with my simulated lines. I will also do this before and after extinction corrections have been applied.

6.3.1 Using Measured Hβ Lines to place RWGs on BPT Diagrams

Firstly I used my measured Hβ emission lines to place five, four and four sources onto BPT diagrams 1, 2 and 3 respectively, in the aim to distinguish between whether they are dominated by AGN activity and star formation.

Classifications Before Extinction Corrections

Figure 6.14 shows the three BPT diagrams plotted with my measured emission lines. I have also included another set of example galaxies for comparison purposes. Marked in purple are HotDOGs as presented in Jun et al. (2020), and as a similarly selected population these sources are likely to lie in similar regions to my RWGs.

As mentioned before, I couldn't distinguish between the [NII]$\lambda\lambda 6548, 6563$ doublet and the broad line components of the Hα emission lines, so an assumed ratio of $[\mathrm{N_{II}}]/\mathrm{H}_\alpha = 0.83 \pm 0.42$ (Kim et al., 2013) has been used. The central vertical red line in the BPT1 diagrams (Figure 6.14) represents this assumed ratio with the two lines either side representing the given error on this assumed ratio. The need to assume this ratio introduces a level of uncertainty in my RWGs placement on the x-axis however any sources with $\log\left(\frac{OIII}{\mathrm{H}\beta}\right) \geq 1$ will fall under AGN classification no matter the ratio of [NII]$\lambda\lambda 6548, 6563/\mathrm{H}\alpha$ assumed or measured.

Jun et al. (2020) classify only one of their HotDOGs as star forming with the rest being classified as AGN. The HotDOGs lie in a similar region as the RWGs on the first BPT diagram with five out of eight sources lying within the vertical red lines that represent the assumed [NII]$\lambda\lambda 6548, 6563/\mathrm{H}\alpha$ ratio. This similarity allows more confidence in the placement of the RWGs and with two other BPT diagrams to aide in classification, I was confident in the results.

In Section B, Figure 6.14 is re-plotted to also include 20000 example QSOs from SDSS DR7 at redshifts of $1.5 > z > 5$ (Shen et al., 2011) in the first two BPT diagrams. Unfortunately with no measured detections of the OI emission line there are no example SDSS QSOs on BPT3. Notable across the first two BPT diagrams in Figure B.1 is the placement of the SDSS QSOs (Shen et al., 2011). Lying in the bottom left quadrant of both diagrams it is clear that the vast majority of these QSOs are powered by star formation with < 0.1 % of sources lying outside of this region. This may change depending on line width, with a mean FWHM of this SDSS sample of $\sim 570\,\mathrm{km\,s^{-1}}$. This was a surprising result, as due to their selection criteria it would be expected that the majority of these sources lie in the AGN region of the diagram. Due to this uncertainty, example QSO's are not plotted in the remaining figures in this section, just briefly discussed. However, it is clear that RWGs and HotDOGs occupy a unique position on these diagrams.

Table 6.14 shows the classifications of my five RWGs with both Balmer lines detected, based on their positioning on the three BPT diagrams. The final column shows my classification made through combining the results of BPT diagrams one, two and three. Three of my RWGs are classified as AGN, with two of these further classified as Seyfert galaxies. I determine one RWG to be dominated by star formation, but do not manage to classify W1400. Comparing its location

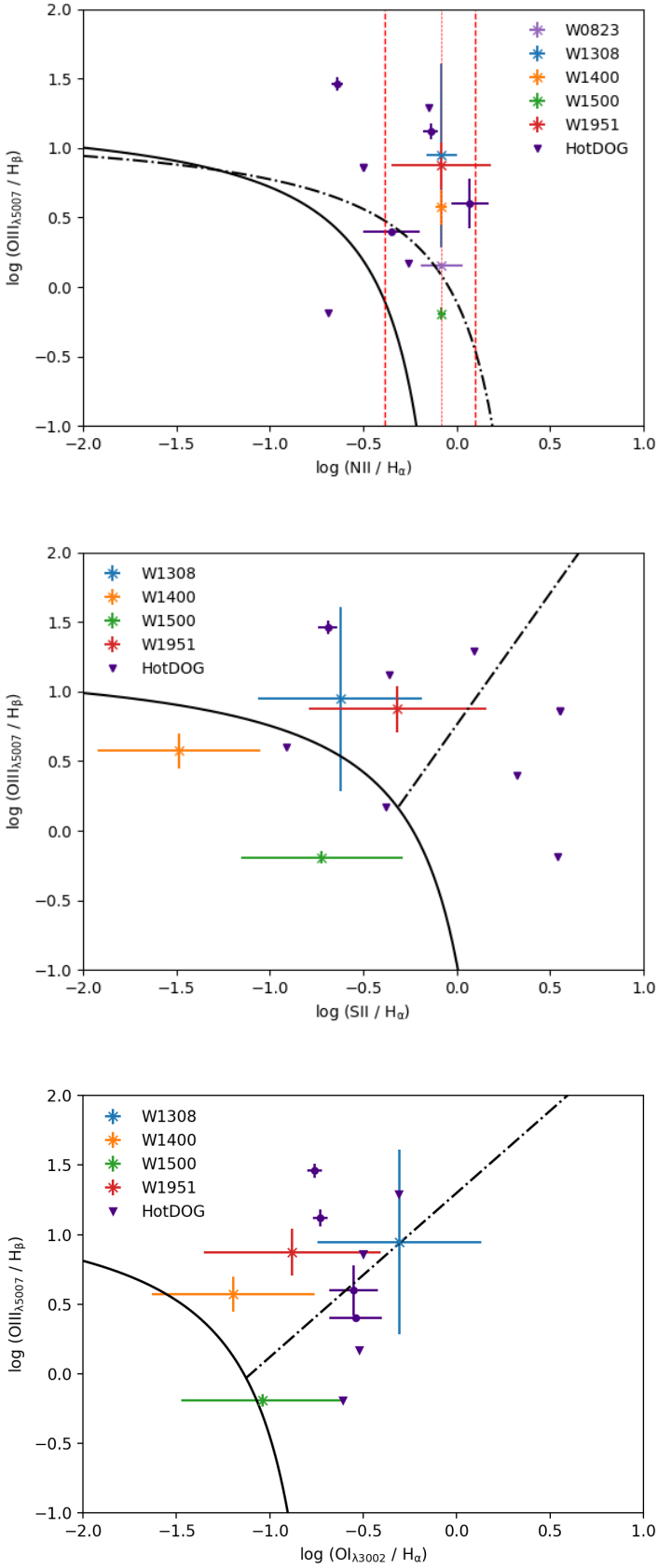

Figure 6.14: Three BPT diagrams comparing nuclear emission line ratios with added dividing lines. Plotted is a maximum of five RWGs based on my measured emission line fluxes. Also included are example HotDOG (Jun et al., 2020) measurements.

Table 6.14: The classifications of the 5 sources with measured Hβ lines based on their BPT diagrams.

WISE designation	BPT 1	BPT 2	BPT 3	Combined
J082311.24−062408	AGN	-	-	AGN
J130817.00−344754	AGN	Sy	Sy	Sy
J140050.13−291924	AGN	HII	Sy	Any
J150048.73−064939	Comp	HII	LI/HII	HII
J195141.22−042024	AGN	Sy	Sy	Sy

across the three BPT diagrams in Figure 6.14, it does not have a consistent location, lying just inside the AGN classification region on BPT1, the HII region of BPT2 and mainly in the Seyfert region in BPT3. Whilst I expected W1400 to be dominated by AGN emission, based on its selection criteria, I can't show this based on BPT diagram placement.

Through its placement on BPT2, and overall, W1500 would appear to be classified as a star forming galaxy, though this initially sounds unlikely. This source does however lie on the border of AGN/ star forming regions in diagrams one and three with AGN classification being within error on BPT3. Due to the original selection criteria, and the poor SED fitting with `MAGPHYS` templates, an AGN powered source is the most likely conclusion. Otherwise I would have expected the lack of AGN templates to not affect the SED fit of W1500, whereas in reality I measured a poor SED fit with a value of $\chi^2_\nu = 5.91$. In order to classify W1500 as AGN powered I would require greater measured flux of the SII emission line or a higher ratio of [OIII]λ5007/Hβ to be measured. It would therefore be interesting to see how W1500 is classified when using a simulated Hβ profile instead.

Classifications After Extinction Corrections

As expected by the given selection criteria, I have shown in Section 5.3 that for 80% of my sources with both Balmer lines detected, I measured $A_V > 1.8$ magnitudes with $A_V > 0$ being within error for my fifth source. I used a simulated Hβ emission line at four different assumed widths (3000, 1480, 1315 km s^{-1} and the corresponding Hα FWHM). As the BPT diagrams depend on ratios of emission line fluxes, with effect of extinction will depend on the relative wavelengths and the extinction law (Cardelli et al., 1989) used.

Figure 6.15 shows the positioning of my five RWGs on BPT diagrams after correcting my measured fluxes for extinction. In order to equally compare figures across this and the next section, I have used my simulated A_V values from Section 5.3 to correct my measured fluxes. This simulation assumes that the Hβ BH mass is equal to my calculated Hα BH mass, at four different assumed Hβ FWHMs. Figure 6.15 shows one BPT diagram per row, with each vertical

column using a different assumed width; 3000 km s^{-1}, the corresponding Hα FWHM, 1480 km s^{-1} and 1315 km s^{-1}.

Comparing Figure 6.15 to Figure 6.14, there initially appears to be little difference. For the first BPT diagram, without extinction corrections I placed four RWGs in the AGN section with one RWG which lies in the combination region. After extinction corrections I still placed three sources firmly in the AGN region of the diagram, with W1500 still placed in the combination region of the diagram. The only change is for W0823 which previously sat just in the AGN region of the diagram. After extinction correction the value of $\log\left(\frac{\mathrm{OIII}}{\mathrm{H}\beta}\right)$ is reduced by a factor of 1.4 at the maximum assumed FWHM. With extinction corrections I measure W0823 to be AGN at assumed width of 1480 and 1315 km s^{-1} but a combination of AGN and star formation at the two wider assumed widths.

For the second BPT diagram, without extinction corrections, I placed two RWGs in the Seyfert region of the BPT diagram with the other two galaxies lying in the HII region. After extinction corrections at all assumed widths, the four RWGs all still classified as the same. As the assumed FWHM increases the data points shift down and left, with decreased SII/Hα and [OIII]λ5007/Hβ ratios. In order to place all four RWGs in the HII region of the second BPT diagram, an unreasonably large assumed FWHM would be needed, with a value of $A_V > 15$ magnitudes required.

I classified three RWGs as Seyfert galaxies before extinction correction with W1500 being on the border of HII/LINER. After extinction corrections are applied the data points are shifted to left classifying now only two RWGs as Seyfert galaxies with both W1308 and W1500 as LINERS.

In comparison to the classifications before extinction corrections, there is little difference. Source W0823 still lies on the border of AGN/Comp no matter the extinction correction made. For W1308 the only classification difference is on BPT3 where the data point has been shifted downwards and now is classified as a LINER. There is no change in the classification of W1400 across all three diagrams with the only change for W1500 on BPT3 where it now is placed in the LINER region of the diagram. This is however a more likely placement as previously W1500 was classified as star forming. Finally there was no change in the classification or BPT positioning of W1951.

With only five measured RWGs with both Hα and Hβ I could only place a maximum of five RWGs onto BPT diagrams. In order to apply extinction corrections I used an assumed FWHM to simulate a Hβ emission line in order to use the Balmer decrement. Now I used these simulated Hβ emission lines with the aim of placing more RWGs onto BPT diagrams.

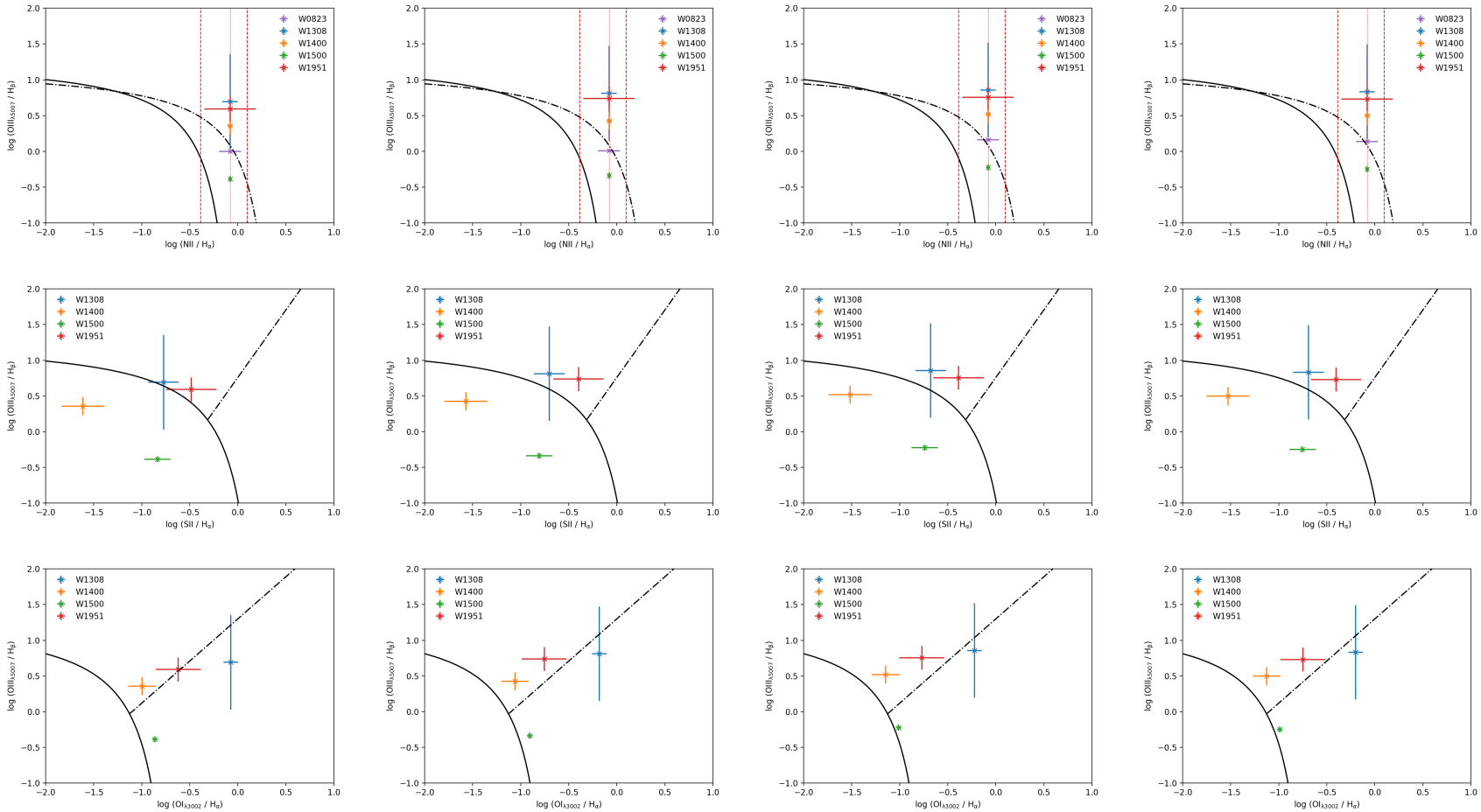

Figure 6.15: BPT diagrams comparing nuclear emission line ratios with added dividing lines. Plotted is a maximum of five RWGs based on my extinction corrected emission line fluxes. These extinction corrections are based on a simulated Hβ line of FWHM 3000, Hα, 1480 and 1315 km s^{-1} going left to right.

6.3.2 Using Simulated Hβ Lines to place RWGs on BPT Diagrams

With only five measurements of both Balmer lines I could only place a maximum of five RWGs on to the three BPT diagrams. However based on the work done in Chapter 5 I have simulated Hβ emission lines. Under the assumption that both the Hβ and Hα BH mass formulas should calculate the same result, I could simulate a realistic Hβ emission line at a given FWHM. For full details on how this is done see Section 5.3. Whilst I did not have many detections of the Hβ emission line, each BPT diagram relies on needed four measured emission line fluxes for the same source. I could now place 11 RWGs on to the first BPT diagram, five on the second and six RWGs onto the third BPT diagram. Using these simulated emission line fluxes allowed me to double my classification sample size, with a lack of Hβ spectral information available. It also helped for comparison with the results presented above to see whether the classification of W1500 as star formation was an anomaly.

These simulations were done in the following sections before and after extinction corrections are applied.

Classifications Before Extinction Corrections

Figures 6.16, 6.17 and 6.18 shows four different variations for all three BPT diagrams based on different assumed FWHMs of my simulated Hβ emission lines. Again I have plotted example HotDOGs from Jun et al. (2020) to allow for comparison. A comparison of the positioning to QSOs from SDSS DR7 was made, but not included in these figures due to uncertainty in their positioning.

Looking at Figure 6.16, all 11 RWGs lie outside of the star formation region[2] due to the assumed [NII]$\lambda\lambda 6548, 6563$/H$\alpha$ used, as all the sources lie in a 'channel' defined by this assumed ratio. The assumed Hβ FWHM just shifts my data points along the y-axis. At the largest assumed FWHM of 3000 km s^{-1} I measured 10 of the 11 RWGs as powered by AGN with W1500 again sitting in the composite region and W1634 being located on this border. This is almost identical to my original results (with detected Hβ lines) where I only placed W1500 in this composite region. In fact, at this width the ratio of $\log\left(\frac{\mathrm{OIII}}{\mathrm{H}\beta}\right)$ is such that I placed six of the RWGs in the AGN region of BPT1, no matter their x-axis value.

As the assumed width decreases, I simulated greater Hβ emission line fluxes, hence the ratio $\log\left(\frac{\mathrm{OIII}}{\mathrm{H}\beta}\right)$ decreases. At my lowest assumed FWHM, 1315 km s^{-1} (the mean FWHM present in all my detected Hβ lines), I placed five sources in this composite region, with one source, W1434, hovering on the composite/AGN border. No matter my measured ratios however, it is clear that

[2] Again showing how the RWGs sit apart from SDSS QSOs of a similar redshift.

based on the first BPT diagram, and the underlying assumptions, that I do not predict any of the sources to be dominated by star formation. This is in comparison to the positioning of W1500 on BPT diagrams two or three where it again appears to be dominated by star formation at all assumed widths.

Even with the additional sources granted via simulating Hβ emission lines, I could still only place five RWGs on to BPT2, only gaining the placement of W1541. Previously, using my detected Hβ emission line fluxes, I placed two sources in the HII region and two into the Seyfert region of the diagram. I agreed with the previous placement of W1500 in the HII region, no matter the FWHM I assume, and am similarly confident with the placements of W1308 and W1951 in the Seyfert region of the diagram. I placed W1400 as a Seyfert at my two largest assumed widths, and the in the HII region at the two lowest widths, however with the Seyfert region still lying within error. My newly placed source, W1541, identically depends on the assumed width, falling into the HII region at my two lowest assumed widths. The placement of this source is uncertain as the same happened with its placement onto BPT1.

I gained the placement of an additional two sources with my simulated Hβ emission lines on BPT3. I placed five of the six RWGs plotted in the Seyfert region at the largest assumed width of $3000\,\mathrm{km\,s^{-1}}$. Two of these sources, W1400 and W1951, remain in this region no matter the assumed FWHM. Similarly, W1500 remains on the border of the HII/LINER regions no mater which width is assumed. Based on its placement on the previous diagrams it appears that W1500 is powered by star formation and belongs in the HII region of BPT3. This however still seems unlikely as raises additional questions including whether any AGN activity is hidden. The placement of the other three is however dependent on the width assumed. As on BPT2, the placement of W1541 switches between Seyfert and HII as the assumed width decreases. The remaining two sources lie confidently outside the HII region, changing between Seyferts and LINERs as the assumed width decreases.

Example galaxies (Jun et al., 2020) are included on all these figures for comparison. As expected the HotDOGs observed by Jun et al. (2020) lie in a very similar position to my RWGs, with the majority of them likely to be dominated by AGN, though equally split between placement in the Seyfert or LINER region. This shows that a sources positioning on the BPT diagrams could be used as a tool to aid in future source classification. Though not shown, example QSOs (Shen et al., 2011) sit in the HII region, with my RWGs placed outside of this population. This again demonstrates the obscure nature of RWGs as suggested by their placements on Figure 5.2, though I would have expected the majority of the QSO's to lie in the AGN regions of the diagrams can't explain their positioning. However, their is a clear difference between the standard

QSO's and extreme populations of RWGs and HotDOGs.

Table 6.15 shows my classification of these sources with simulated Hβ emission line at different assumed widths. The furthest right column gives my final classification based on the average position across all the figures.

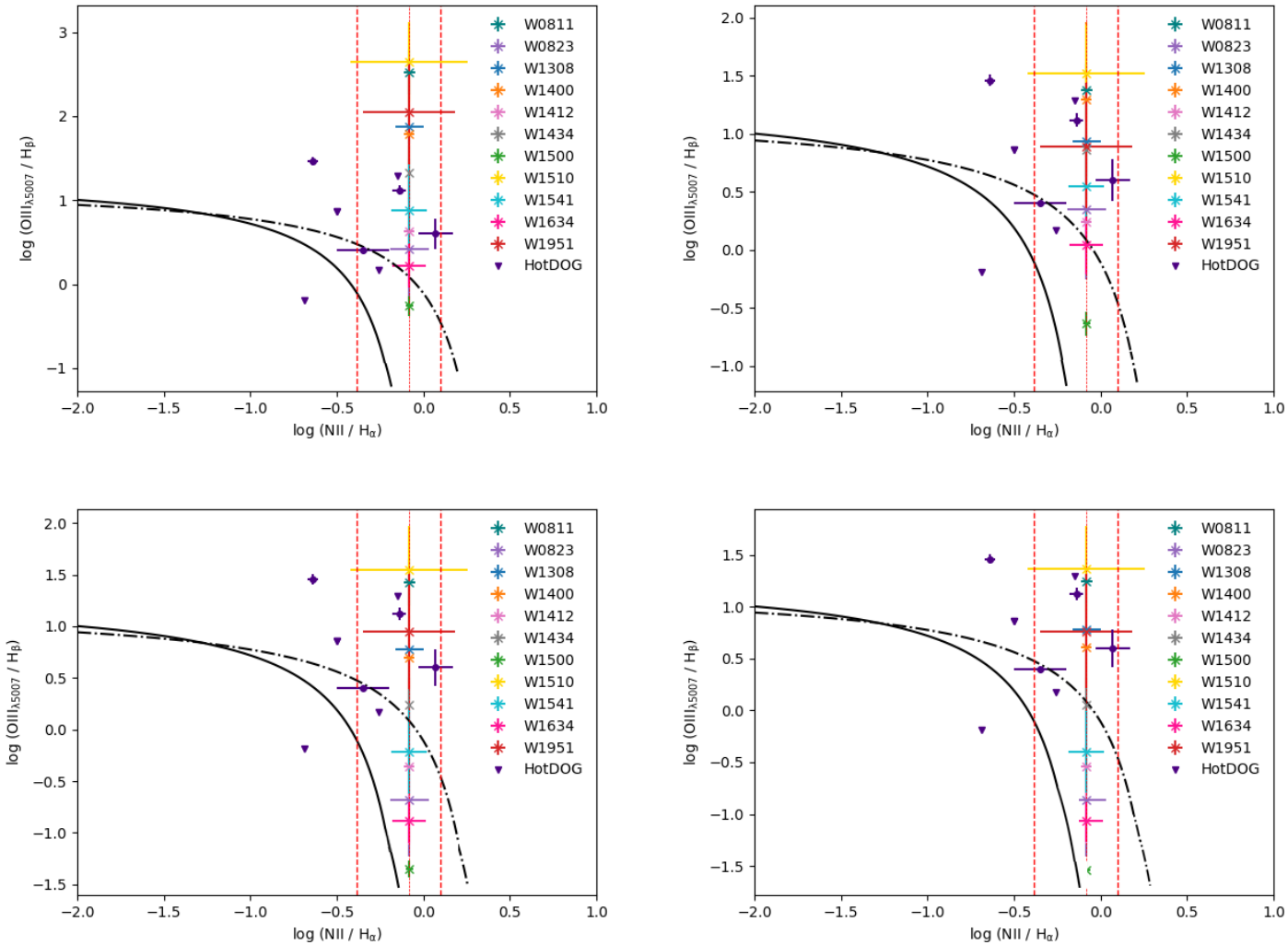

Figure 6.16: BPT1 diagrams comparing nuclear emission line ratios with added dividing lines. Plotted is 11 RWGs based on my measured simulated Hβ line fluxes. The assumed FWHMs of the Hβ line is 3000 km s^{-1}, the Hα width, 1480 and 1315 km s^{-1} from top to bottom. Also included are example HotDOG (Jun et al., 2020) measurements.

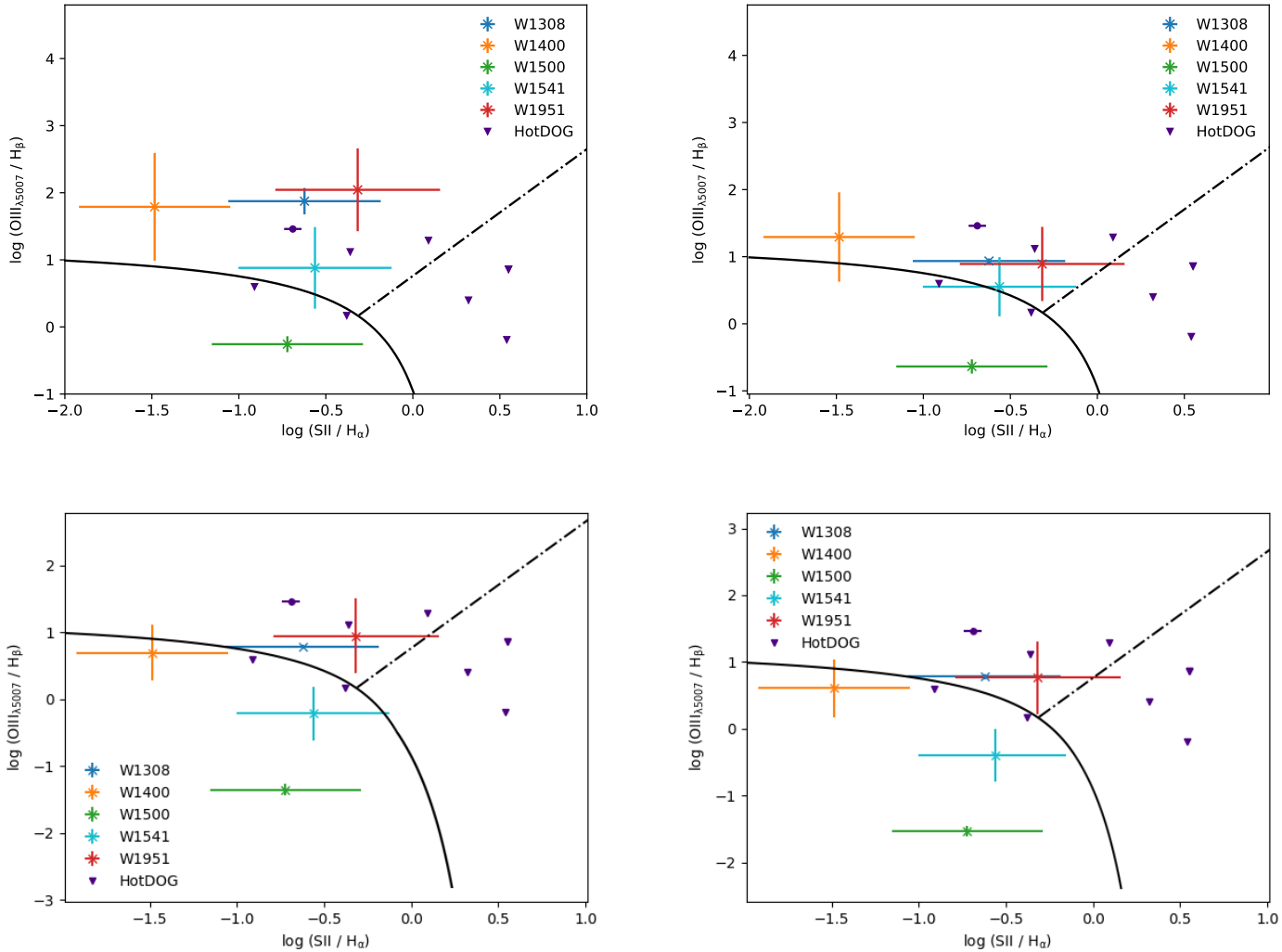

Figure 6.17: BPT2 diagrams comparing nuclear emission line ratios with added dividing lines. Plotted is five RWGs based on my measured simulated Hβ line fluxes. The assumed FWHMs of the Hβ line is 3000 km s^{-1}, the Hα width, 1480 and 1315 km s^{-1} from top to bottom. Also included are example HotDOG (Jun et al., 2020) measurements.

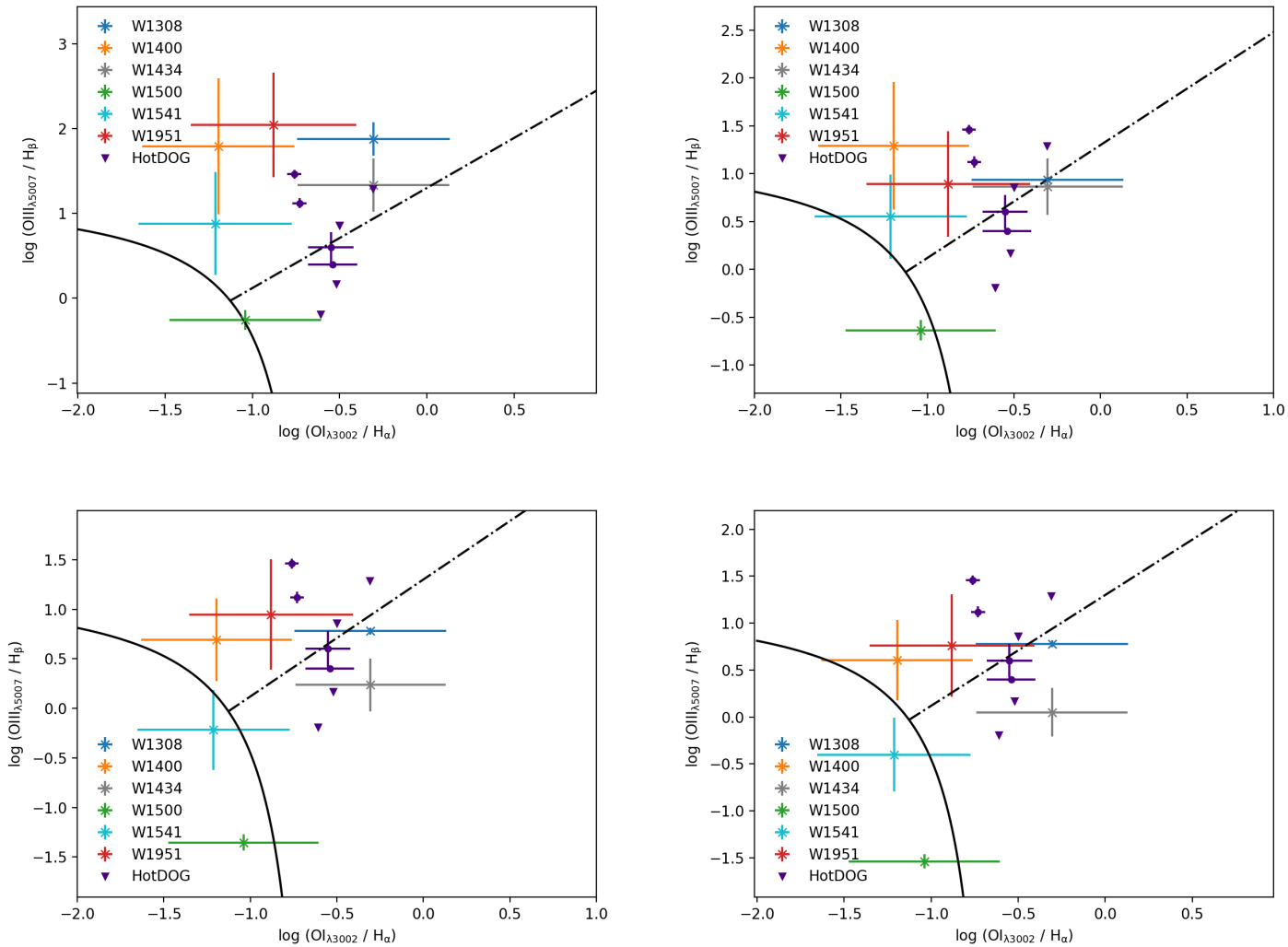

Figure 6.18: BPT3 diagrams comparing nuclear emission line ratios with added dividing lines. Plotted is six RWGs based on my measured simulated Hβ line fluxes. The assumed FWHMs of the Hβ line is 3000 km s^{-1}, the Hα width, 1480 and 1315 km s^{-1} from top to bottom. Also included are example HotDOG (Jun et al., 2020) measurements.

Table 6.15: The classifications of the 11 sources with assumed Hβ lines, at different FWHMs, based on their BPT diagrams. Source name is given instead of the full WISE designation to save space.

Source	BPT 1				BPT 2				BPT 3				Combined				Total
	Assumed FWHM in km s^{-1}				Assumed FWHM in km s^{-1}				Assumed FWHM in km s^{-1}				Assumed FWHM in km s^{-1}				
	3000	Hα	1480	1315	3000	Hα	1480	1315	3000	Hα	1480	1315	3000	Hα	1480	1315	
W0811	AGN	AGN	AGN	AGN	-	-	-	-	-	-	-	-	AGN	AGN	AGN	AGN	AGN
W0823	AGN	AGN	Comp	Comp	-	-	-	-	-	-	-	-	AGN	AGN	Comp	Comp	AGN/Comp
W1308	AGN	AGN	AGN	AGN	Sy	Sy	Sy	Sy	Sy	Sy/LI	Sy/LI	Sy/LIn	Sy	Sy	Sy	Sy	Sy
W1400	AGN	AGN	AGN	AGN	Sy	Sy	HII/Sy	HII/Sy	Sy	Sy	Sy	Sy	Sy	Sy	Sy	Sy	Sy
W1412	AGN	AGN	Comp	Comp	-	-	-	-	-	-	-	-	AGN	AGN	AGN	AGN	AGN
W1434	AGN	AGN	AGN	AGN/Comp	-	-	-	-	Sy	Sy/LI	LI	LI	AGN/Sy	Any	AGN/LI	Any	AGN
W1500	Comp	Comp	Comp	Comp	HII	HII	HII	HII	HII/LIn	HII/LI	HII/LI	HII/LI	HII	HII	HII	HII	HII
W1510	AGN	AGN	AGN	AGN	-	-	-	-	-	-	-	-	AGN	AGN	AGN	AGN	AGN
W1541	AGN	AGN	Comp	Comp	Sy	Sy/ HII	HII	HII	Sy	Sy	Any	HII/LI	Sy	Sy	Any	HII	Sy
W1634	AGN	AGN/Comp	Comp	Comp	-	-	-	-	-	-	-	-	AGN	AGN	Comp	Comp	AGN/Comp
W1951	AGN	AGN	AGN	AGN	Sy	Sy	Sy	Sy	Sy	Sy	Sy	Sy	Sy	Sy	Sy	Sy	Sy

Classifications After Extinction Corrections

Again, the positions of my RWGs on Figures 6.16, 6.17 and 6.18 are dependent on extinction. Figure 6.19 shows the extinction corrected fluxes placed on BPT diagrams. As both the measured flux and the A_V values used for extinction corrections depend on simulated Hβ emission lines, I have used the same assumed FWHM, and simulated line, for both. Shown from left to right are the BPT diagrams based on assumed FWHM of 3000, the Hα width, 1480 and 1315 $\mathrm{km\,s^{-1}}$. As this all depended on two assumptions the results presented in this figure are given as a guide only. I will not discuss them further, but they can provide an idea of how extinction can affect the positioning of my RWGs on BPT diagrams.

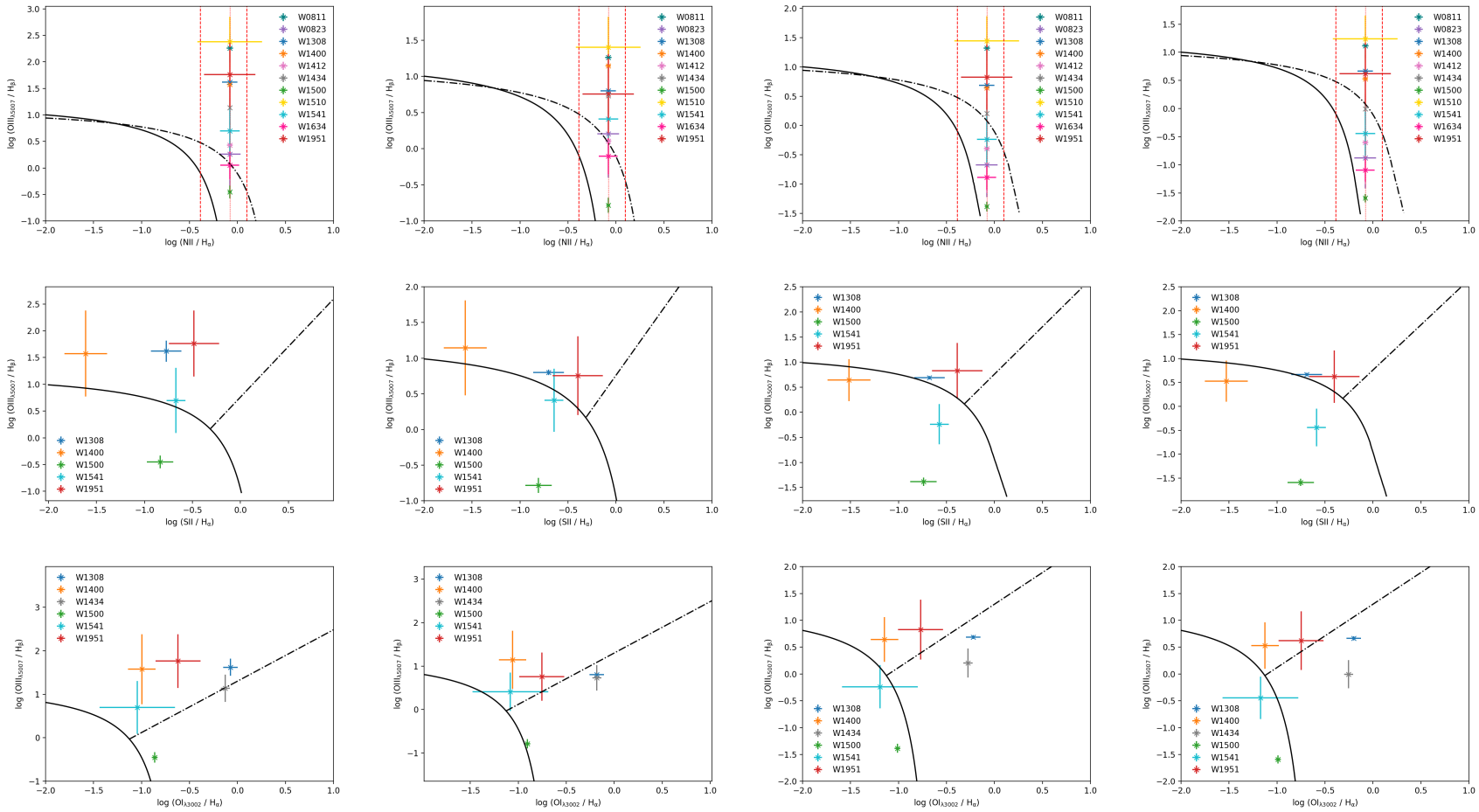

Figure 6.19: BPT diagrams comparing nuclear emission line ratios with added dividing lines. Plotted is a maximum of eleven RWGs based on my extinction corrected emission line fluxes. Both the flux measurements and extinction corrections are based on a simulated Hβ line of assumed FWHM 3000, Hα, 1480 and 1315 km s^{-1} going left to right.

6.3.3 Summary of BPT Diagram Source Classification

The above sections show how BPT diagrams can be used to classify RWGs and compare them with more typical QSOs. I have done this using my detected Hβ emission lines, and those simulated at different assumed FWHM values. Based on all detected emission lines I predict that three RWGs are definitely powered by AGN through their placement on three different BPT diagrams. The vast majority of comparative QSOs are surprisingly placed in the HII region of all three BPT diagrams implying that they are dominated by star formation, whereas, I place only one RWG in this region, suggesting that RWGs are instead dominated by AGN emission. However, due to the uncertainty on the placement of the QSO's this differences may be unreliable. I also show that dust extinction is likely to have little effect on the placement of these five measured RWGs, and therefore this method could be used to assist in classifying RWGs without extinction corrections needed and used a future tool for source classification. Finally I used a simulated Hβ emission line at four assumed FWHM values to gain the placement of at least one extra RWG per BPT diagram and double my sample size. Through these simulations I predict that 10 RWGs are dominated by AGN emission, but the positioning of W1500 still indicates unlikely star formation. As RWGs are classified as AGN through their placement on BPT diagrams, this methodology could in the future be used to select RWG candidates out of previously observed sources, by looking for sources with similar emission line ratios. They additionally lie in a similar region to the HotDOGs from Jun et al. (2020) implying that this methodology would work well at selecting these extreme and obscured AGN, without needing extinction corrections to be made. These measured emission line ratios provide details about the surrounding environment during this extremely active phase of evolution, whilst this confirmation will assist in future SED fitting, with AGN templates definitely needed.

6.4 Investigating the $\mathrm{M_{BH}} - \mathrm{M_{sph}}$ Relation

Part of being able to classify RWGs is seeing how they fit standard relations compared to typical QSOs of similar redshifts. Previously I found that RWG accrete at significantly higher than average and likely at super Eddington rates, and in this chapter I found that the positioning of RWGs to that of QSOs from Shen et al. (2011) differs across BPT diagrams. In this section I briefly discuss the positioning of RWGs on the $\mathrm{M_{BH}} - \mathrm{M_{sph}}$ relation, aiming to determine whether they fit this standard relation and to see how they compare to the similar population of HotDOGs. It also allowed me to compare the size of RWGs to HotDOGs, in order to see if this characteristic is shared between these populations, helping to answer whether any source could

fall under both categorisations.

The $M_{BH} - M_{sph}$ relation from Bennert et al. (2011) relates the BH mass to the spheroidal component of the host mass. This relation was derived from VLT and HST observations of broad line AGN with 1< z <2, and therefore the relation should be reliable for this similar population source. For the similarly selected population of HotDOGs, Wu et al. (2018) find that their sources lie closer to this relation compared to z $\sim$ 1.3 quasars, with Tsai et al. (2018) finding this true for the extremely luminous HotDOG W2246. They measured a spheroidal bulge mass of $M_{sph} = 1.1 \times 10^{12}\, M_{\odot}$ comparable to the value of $\log(M_{sph}/M_{\odot}) = 11.9$ as expected from the $M_{BH} - M_{sph}$ relation.

6.4.1 Applying the $M_{BH} - M_{sph}$ Relation

The $M_{BH} - M_{sph}$ relation (Bennert et al., 2011) is given by Equation 6.7 and allows determination of a BH mass from the spheroidal host mass. Previous works (Assef et al., 2015; Tsai et al., 2018; Wu et al., 2018) have determined M_{sph} through SED fitting, however as discussed in Chapter 4 the SED fitting of RWGs is unreliable with the template by Polletta et al. (2007) being the most reliable. I used the `MAGPHYS` (da Cunha et al., 2008) SED fitting package in order to calculate the stellar masses of my RWGs based on ISAAC, WISE and ALMA fluxes. Along with a small number of data points to fit and a lack of suitable broad line AGN components in the provided `MAGPHYS` templates, they do not fit M_{sph} as a parameter.

$$\log\left(\frac{M_{BH}}{M_{\odot}}\right) = -3.34 \pm 1.19 + (1.09 \pm 0.18) \times \log\left(\frac{M_{sph}}{M_{\odot}}\right) \tag{6.7}$$

I therefore can only compare the likely positioning of my RWGs in comparison to HotDOGs, rather than compare the RWGs to the positioning of the $M_{BH} - M_{sph}$ relation. Using Equation 6.7, allowed me to calculate M_{sph} under the assumption that, similarly to the HotDOGs, RWGs fit the $M_{BH} - M_{sph}$ relation.

6.4.2 Deriving M_{sph} from the $M_{BH} - M_{sph}$ Relation

Figure 6.20 shows 13 RWGs plotted on to the $M_{BH} - M_{sph}$ relation. Shown is the Hα determined BH mass and the corresponding M_{sph} assuming that RWGs fit the relation from Bennert et al. (2011). Also shown on this plot are HotDOGs from Assef et al. (2015) and Wu et al. (2018). With BH masses $\sim$ 1 dex lower my RWGs lie to the right of the previously measured HotDOGs. If this were not the case, it would cause a horizontal shift in my data points. This placement of HotDOGs shows that they are $\sim$ 1 dex larger than RWGs, which indicates that they may not

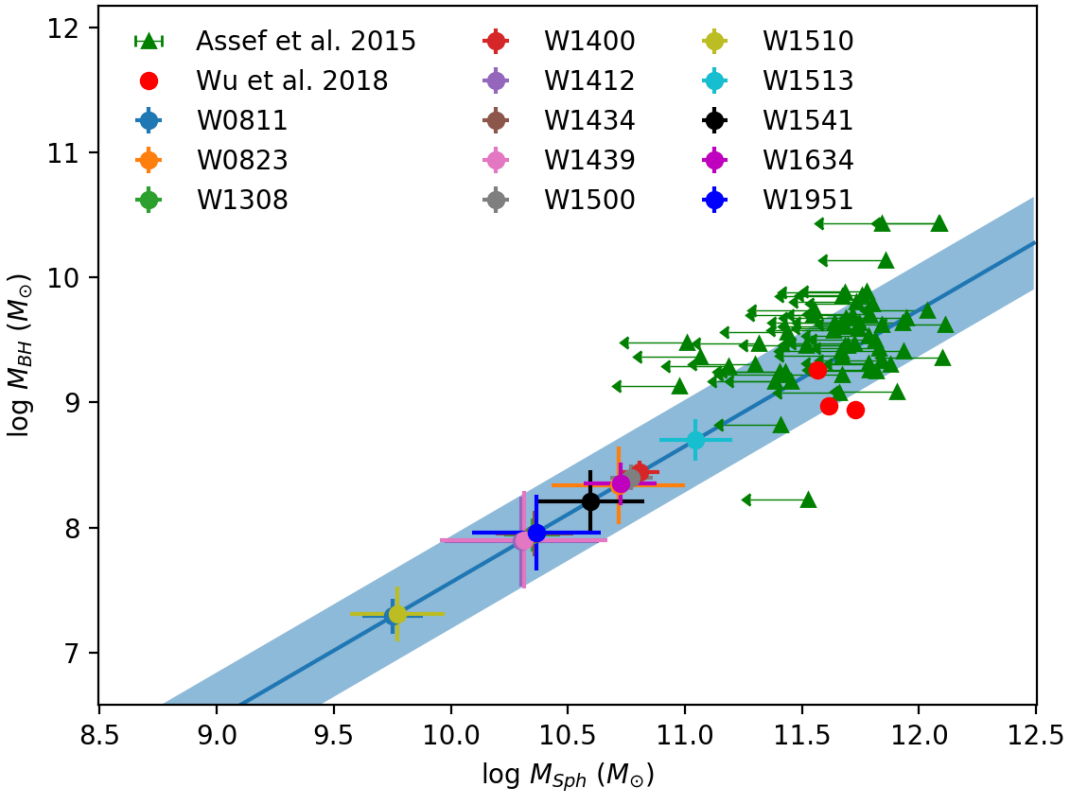

Figure 6.20: Thirteen RWGs with Hα BH mass estimates plotted on to the $M_{BH} - M_{sph}$ relation. Also shown are HotDOGs from Assef et al. (2015) and Wu et al. (2018).

be the same population, but possibly a slightly different, but still active, phase in evolution. I measured $\log\left(\frac{M_{sph}}{M_{\odot}}\right) = 9.5$ - 11.2, in the same order of magnitude as my measured host masses. With 2/3 HotDOGs from Wu et al. (2018) and $\sim 71\%$ of the HotDOGs from Assef et al. (2015) agreeing within error to the $M_{BH} - M_{sph}$ relation I can be confident that 2/3 of my RWGs will also fit this relation. This thought process can be reinforced by the similar positioning of RWGs and HotDOGs on my BPT diagrams.

Table 6.16 gives the exact M_{sph} in $M_{\odot}$ values plotted in Figure 6.20 for my RWGs, with this measured range of $\log\left(\frac{M_{sph}}{M_{\odot}}\right) = 9.5$ - 11.2 based on my previously calculated Hα based BH masses. Here I also gave an estimate for M_{sph}, assuming RWGs follow the (Bennert et al., 2011) relation as with HotDOGs, based on an additional three different BH mass measurements. Included are the results based on my Hα and [OIII]λ5007 (with an assumed $\lambda_{Edd} = 1$) BH masses, along with those calculated by Lonsdale et al. (2015) and Kim et al. (2013). This is shown for a maximum of 18 sources, based on the detected emission lines/those previously observed. With no dependence on a value of λ_{Edd}, the Hα derived masses have been shown in Figure 6.20, though these are the smallest mass estimates measured. With measured masses > 1 magnitude larger than derived from my Hα emission lines, a different used BH mass would place my galaxies in the same region as the HotDOGs from Wu et al. (2018) and Assef et al. (2015) increasing the measured M_{sph} values by ~ 1.5 dex.

6.4.3 Summary of M_{sph} Values Derived

As $\sim$ 2/3 of previous HotDOG estimates (Assef et al., 2015; Wu et al., 2018) agree within error to the $M_{BH} - M_{sph}$ relation from Bennert et al. (2011), as shown in Figure 6.20, I can be confident in the placement of my 13 RWGs on to this relation. I measured $\log\left(\frac{M_{sph}}{M_{\odot}}\right) =$ 9.5 - 11.2, placing my sources ~ 1.1 dex smaller than the HotDOGs from Assef et al. (2015). Whilst I cannot comment on whether my RWGs fit the $M_{BH} - M_{sph}$ relation, the positioning difference between RWGs and HotDogs implied that they are not the same population, with RWGs being $\sim$ 1 magnitude smaller, confirming the results found in Chapters 4 and 5. This is an important distinction between RWGs and HotDOGs and along with showing that they are likely not the exact same population it showed their selection criteria will likely select unique sources. Additionally if RWGs are smaller than HotDOGs they will likely undergo a shorter super-Eddington phase implying that they are a rarer and unique population of galaxies, and therefore demonstrating why there are currently more observations of HotDOGs.

Table 6.16: The M_{sph} derived using the (Bennert et al., 2011) relation. This is calculated using different versions of the BH mass.

WISE Designation	M_{sph} ($M_{\odot}$)			
	Hα	OIII	(Lonsdale et al., 2015)	(Kim et al., 2013)
J081131.61−222522	9.615 - 9.881	10.761 - 10.789	11.055 - 11.055	-
J082311.24−062408	10.358 - 11.000	10.990 - 11.018	11.495 - 11.596	-
J130817.00−344754	10.229 - 10.468	11.605 - 11.661	11.385 - 11.385	11.183 - 11.880
J134331.37−113609	-	11.467 - 11.788	11.394 - 11.412	11.560 - 11.633
J140050.13−291924	10.725 - 10.889	11.339 - 11.577	11.486 - 11.495	11.376 -11.981
J141243.15−202011	9.844 - 10.633	10.550 - 10.633	11.412 - 11.550	11.248 - 11.991
J143419.59−023543	10.174 - 10.522	11.239 - 11.358	11.293 - 11.293	-
J143931.76−372523	-	-	10.743 - 10.743	-
J150048.73−064939	10.669 - 10.862	10.302 - 10.376	11.458 - 11.853	-
J151003.71−220311	9.495 - 9.972	10.743 - 10.789	11.027 - 11.036	-
J151310.42−221004	10.880 - 11.202	-	11.633 - 11.633	-
J151424.12−341100	-	11.064 - 11.165	10.880 - 10.917	-
J154141.64−114409	10.330 - 10.827	11.064 - 11.165	11.220 - 11.339	11.385 - 11.412
J163426.87−172139	10.550 - 10.880	11.005 - 11.018	11.238 - 11.238	-
J170204.65−081108	-	11.37 - 11.8346	11.944 - 11.944	-
J195141.22−042024	10.027 - 10.642	11.779 - 11.779	11.211 - 11.238	11.385 - 11.743
J200048.58−280251	-	10.771 - 10.972	11.165 - 11.302	11.807 - 11.807
J204049.51−390400	-	-	11.321 - 11.532	-

6.5 Investigating Asymmetry in my fitted Emission Lines.

The two final sections of this chapter focus on the shape and offsets in my detected NIR, UVB and VIS emission lines. With an asymmetric emission line hinting at the possibility of a spatially extended structure, this investigation should help in understanding the nature of these galaxies. Jun et al. (2020) found that for their HotDOGs an asymmetric line (Crenshaw et al., 2010; Zakamska & Greene, 2014; Bae & Woo, 2016) profile was caused by outflows broadening the [OIII]λ5007 and Balmer emission lines. In this section I investigated the presence of an asymmetric line profile in my detected Hα emission lines [3].

Previously I used a multiple Gaussian component model to fit my measured emission lines in order to separate the underlying broad and narrow components present, with no velocity component fixed for any of the emission lines. Throughout this fitting I adopted the principle of using as many Gaussians needed to improve the reliability of my model. In practice this meant adding an increasing number of components until this stopped reducing my measured value of χ^2_ν. For most of my measured emission lines a single Gaussian was able to contain all of the present flux of my emission lines. However for some sources a maximum of four different components was required with a mean of two components fitted across all emission lines and all sources.

Across the 15 different emission/absorption lines that I fitted to 23 sources, the emission line which required the largest number of components to produce an optimal fit was the Hα emission line. As described in detail in Chapter 4, this was the first emission line that I fitted, with detections in 13 RWGs. I modelled this emission line independently fitting as many components as necessary to the detected peak. I fitted a mean 1.84 ($\sim$ 2) Gaussian components to my detected Hα profile in order to include all of the flux present.

6.5.1 Comparison of Percentage Flux

In order to investigate whether there was any asymmetry present in my detected emission lines, I adopted a simple method of comparing the ratios of measured fluxes to either side of the centre of my emission lines. Taking the central wavelength[4] of my fitted multi-component Gaussian model, I integrated my flux density model from 645 nm to this central wavelength and then from this wavelength to 675 nm in order to calculate the flux present either side of this central wavelength. The central wavelength of my fitted Gaussian model was used, rather than the emission line rest

[3] These were chosen due to the larger number of components required in my multi Gaussian fitting and by a visual inspection.

[4] Note that the centre of my fitted Gaussian model was not necessarily equal to the rest wavelength of the emission line that I fitted.

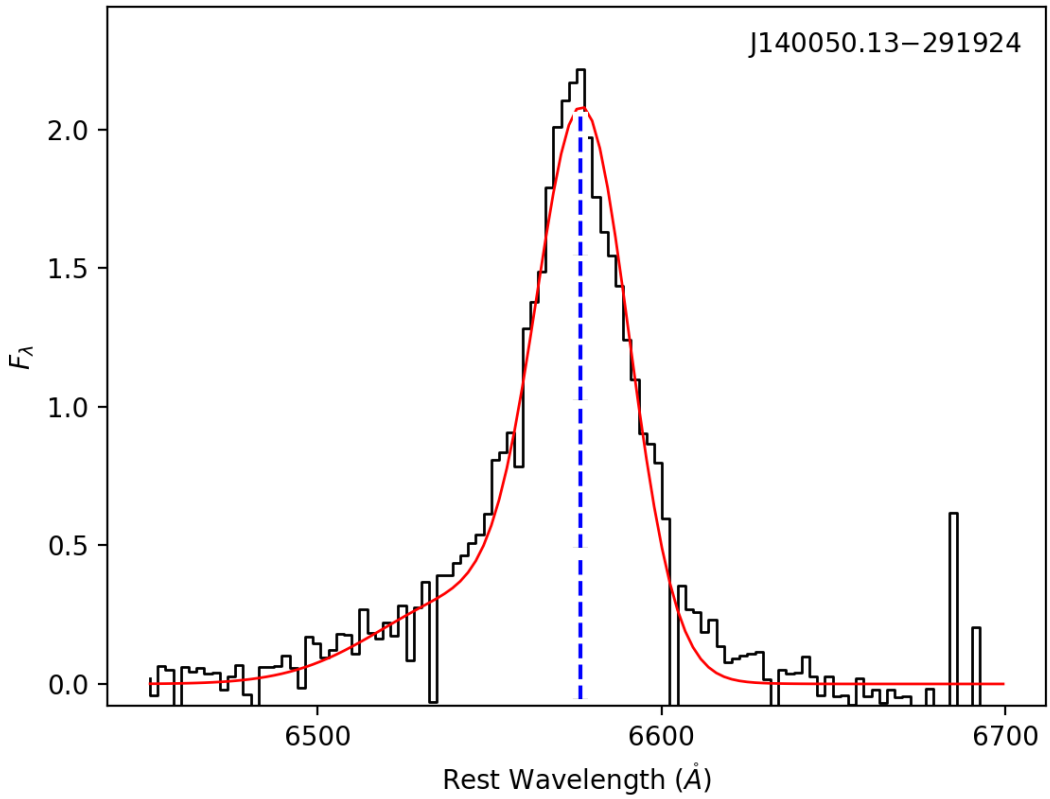

Figure 6.21: Rest frame X-shooter spectra in the region surrounding the Hα emission line. Flux densities are in the units 10^{-16} erg s^{-1}cm^{-2}Å^{-1}. Reduced spectra and fitted model are represented by black histogram and red lines respectively. The dashed blue line shows the centre of my fitted Gaussian model.

wavelength, in order to account for any potential velocity offsets, or redshift errors, as the peak of my measured emission lines do not all fall at this central wavelength.

Figure 6.21 shows an example of this process on the detected Hα emission line of W1400. The dashed blue line in this figure shows the placement of the central wavelength of my fitted multi Gaussian model to the Hα profile. This model is made up of two components in order to fit the broad and narrow line features. However the asymmetric nature of this emission line is clear just from looking at Figure 6.21 with a larger proportion of the detected flux lying to the left (blue-wards) of this centrally fitted line. In fact I measured flux of $56.11 \pm 0.58 \times 10^{-16}$ erg s^{-1}cm^{-2} to the left of this dashed blue line and only $39.19 \pm 0.25 \times 10^{-16}$ erg s^{-1}cm^{-2} worth of flux to the right (redwards) of the line, demonstrating this visible asymmetric nature with a 1.43:1 ratio.

Throughout this chapter, and including the work done in the previous chapters, I searched for the presence of 18 different emission/absorption lines and detected 15 of these across the 27 RWGs observed by X-shooter. Across these detected emission lines, the most noticeable visual

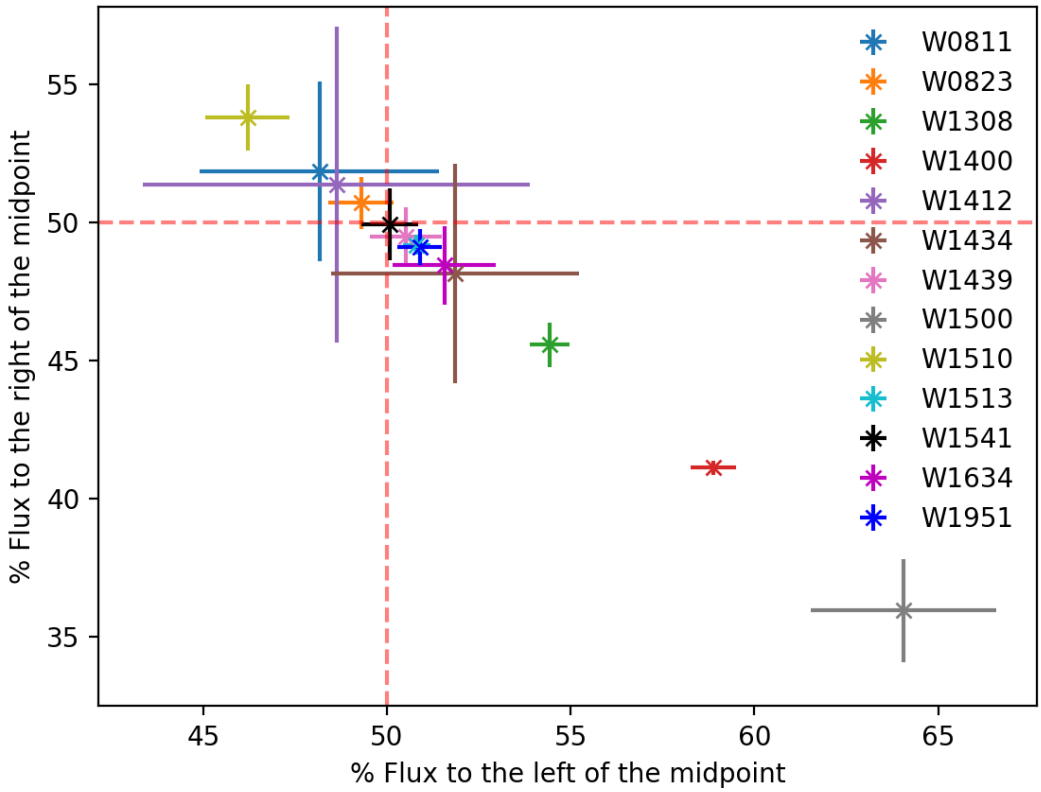

Figure 6.22: The percentages of measured flux to the left (bluewards) and right (redwards) of the central wavelength of my fitted multi-component model. Red dashed lines show the 50% mark.

asymmetry was present in the Hα emission line. This is reinforced by comparing the mean number of Gaussian components needed to successfully fit each emission line. A mean of 1.84 components required for the Hα emission line is greater than the mean number of components; 1.16 and 1.72, required to fit the Hβ and [OIII]λ5007 emission lines respectively.

6.5.2 Derived Asymmetry from Percentage Flux Differences.

Figure 6.22 shows the percentage of fluxes measured to the left and right of the central wavelength of my fitted Gaussian models. This is shown for the 13 RWGs with detected Hα emission lines. I measured a greater amount to the left of the model mid point for 9 of these 13 sources with a mean flux of $14.57 \pm 0.58 \times 10^{-16}\,\mathrm{erg\,s^{-1}cm^{-2}}$ in comparison with a mean flux of $11.88 \pm 0.58 \times 10^{-16}\,\mathrm{erg\,s^{-1}cm^{-2}}$ to the right of the midpoint, an $\sim 18\%$ flux decrease.

I measured a flux differential of $\geq 5\%$[5] for only four of the 13 sources, showing that whilst a greater number of components was required to to fit the Hα emission line, only $\sim 31\%$ of these

[5] 5% was chosen here as a significant flux difference here as it is greater difference caused by noise in the emission line spectra and therefore is likely indicative of asymmetry.

sources have a noticeable asymmetry to their fitted emission lines. Out of these four sources, W1308, W1400, W1500 and W1510, only W1510 has a larger amount of flux to the right of the midpoint compared to the left. These four sources were noticeably separated from the main population in Figure 6.22 where the majority of sources are clustered around the 50% : 50% midpoint.

Only two sources, W1400 and W1500 have an asymmetry $\geq$ 10%, however these sources were reliably fitted by combining multiple Gaussian components. The significantly asymmetric nature of these two sources may hint at a spatially extended structure present in the Hα emission lines, though this likely would require a measurable outflow. These two sources both have broad components ($> 2000\,\mathrm{km\,s^{-1}}$), though are not the broadest of all my measured Hα emission lines.

This analysis of the measured flux either side of the central fitted wavelength is a comparison of the flux encompassed by the Gaussian fitted spectra. However for those sources with visible asymmetry, multiple fitted Gaussians still may leave a fraction of the flux which is not taken into account, possibly skewing the above results for the most asymmetric cases. Therefore this process was again repeated but through a comparison of the original data points rather than the fitted flux. This new comparison led to no change to the original results, with all measured percentages being within error to those presented in Figure 6.22. This allowed both confidence in my measured values of asymmetry and my spectral fitting process.

6.5.3 Summary of Measured Asymmetry

The asymmetric nature of an emission line can hint at a spatially extended structure though detailed analysis of 2D spectra would be needed to confirm this. Through comparing the percentages of flux to the left and the right of the midpoint of my fitted multi-component Gaussian models, I detected asymmetry greater $> 5\%$ in four of the 13 detected Hα emission lines. Three of these sources have their larger amount of flux measured to the left of the fitted midpoint with two of these sources having an asymmetric offset $> 10\%$ of the total measured flux. These specific sources would therefore be among those most interesting for further observation[6], as confirmation of outflows present will provide more evidence for super-Eddington accretion.

6.6 Investigating Velocity Offsets

The final section of this chapter again focuses on properties of my detected emission lines. Whilst in the previous section I investigated whether the flux of the Hα emission line is asymmetrically spread across the fitted emission lines, and found that for 4 out of the 13 sources it is, now I

[6]See Chapter 7 for details on further observations.

investigate the possibility of outflows broadening my measured widths through detecting velocity offsets.

Previously I have briefly discussed the possibility of outflows being present in RWGs in the context of galactic evolution and super Eddington accretion. It is thought that the evolution of BHs and their hosts appearing closely linked, feedback and outflows may be the crucial joining mechanism. Outflows have also been suggested as a mechanism for broadening measured emission lines and therefore evidence for super Eddington accretion being present in certain galaxies.

Through comparing the widths of my measured emission, I found that in some cases the [OIII]λ5007 lines are comparably broad, if not broader, than the Balmer line widths. This has been suggested as caused by outflows broadening some of my measured line widths, which may also be indicative of super Eddington accretion as required by simulations by Kitaki et al. (2021). Previous works (Nesvadba et al., 2007; Harrison et al., 2012) have discussed this mechanism of AGN driven outflows broadening [OIII]λ5007 emission lines with Nesvadba et al. (2011a) and Cano-Díaz et al. (2012) suggesting that for high redshift AGNs broad [OIII]λ5007 emission lines are associated with extended outflows of ionised gas. This has been previously investigated both for the similarly selected WISE population of HotDOGs (Kim et al., 2013; Jun et al., 2020) and similarly obscured AGN (Zakamska et al., 2015). The broadening of Hα emission lines has also been suggested for HotDOGs by Wu et al. (2018).

Measurement of velocity offsets and/or asymmetric emission line profiles does not always indicate the detection of outflows. An asymmetric emission line profile may also be caused by excess noise in the spectra or differential levels of extinction across the broader line profiles, whilst a symmetric profile may still have been broadened by outflows. Similarly offsets of detected emission lines from their expected rest wavelengths may instead be indicators of required redshift corrections. Whilst confirmation of outflows would require individual comparison of sources, which is beyond the scope of this section, detection of any velocity offsets will be a good indicator of which sources may have been broadened by outflows.

In order to investigate possible indicators of outflows I have measured the velocity offsets of the 15 detected emission/absorption lines by comparing the central wavelength of my complete fitted Gaussian model to the rest, and expected, wavelength of the detected emission lines. In order to shift the 1D X-shooter spectra from the observed to the rest wavelength reference frame I performed a redshift correction. Therefore the exact wavelength positioning of my emission lines is affected by the redshift used. In order to perform this correction I use the VLT determined redshifts determined by Lonsdale et al. (2015). Whilst an error in these redshift values used will equally shift both the 'true' rest wavelength of the emission line and my measured emission

line centre, a constant offset between the two across all sources of the detected line is likely to be indicative of an incorrect redshift. Measuring this offset can therefore allow me to make a correction to the redshift values used.

I measured the velocity offsets across all my detected emission lines and sources, in the search for indicators of potential outflows. Whilst I searched across all detections, I focused my results on those most interesting. In addition I followed the work done by Jun et al. (2020) and aim to quantify the outflow properties of the broad OIII emission lines using the equations derived in Maiolino et al. (2012). These properties include the mass outflow rate $\dot{M}_{out}$, energy injection rate $\dot{E}_{out}$ and momentum flux $\dot{P}_{out}$.

6.6.1 Quantifying Velocity Offsets and Outflow Properties

I detected 15 emission/absorption lines across 23 of the 27 RWGs observed across the three arms of X-shooter. In order to measure the velocity offsets of each source, per line detected, I compared the rest wavelength of the detected emission line, to the wavelength of the centre of the multi-Gaussian model fitted to the data points[7]. Figure 6.23 shows an example of this with the Hα emission line of W1634. The red and blue vertical lines show the Hα rest wavelength and fitted model central wavelength respectively (at the peak flux), where there is a clear offset of 17 Å between the two lines. Here the blue line represents the central wavelength of the compound multi Gaussian model not any individual components, therefore measuring the offset from the centre of the fitted line to the expected rest wavelength. The central wavelength of my compound model may be affected by the low SNR of some spectra (see 6.23) but should still give a good indicator of any offsets with the example spectra given in Figure 4.9 to show the SNR of the detected emission lines.

Through quantifying this velocity offset for all emission lines I could determine whether an outflow is likely. In the case that I measured an equal velocity offset across all detected lines of a source an incorrect redshift may have been used to correct the spectra from observed to rest wavelength. If this was the case then a measurement of the velocity offsets allowed me to estimate the redshift correction needed on the z values I have used (Lonsdale et al., 2015).

Additionally to measuring the velocity offsets of all of my emission lines, I also aimed to quantify the outflow properties of the broad [OIII]λ5007 emission line. Following the work done by Jun et al. (2020) and using the equations derived by Maiolino et al. (2012). Assuming a uniform and filled spherical/bi-conical outflow geometry, the mass outflow rate $\dot{M}_{out}$ (Equation 6.8), energy injection rate $\dot{E}_{out}$ (Equation 6.9) and momentum flux $\dot{P}_{out}$ (Equation 6.10) can be

[7]During the multi Gaussian fitting process each individual component is allowed a velocity offset.

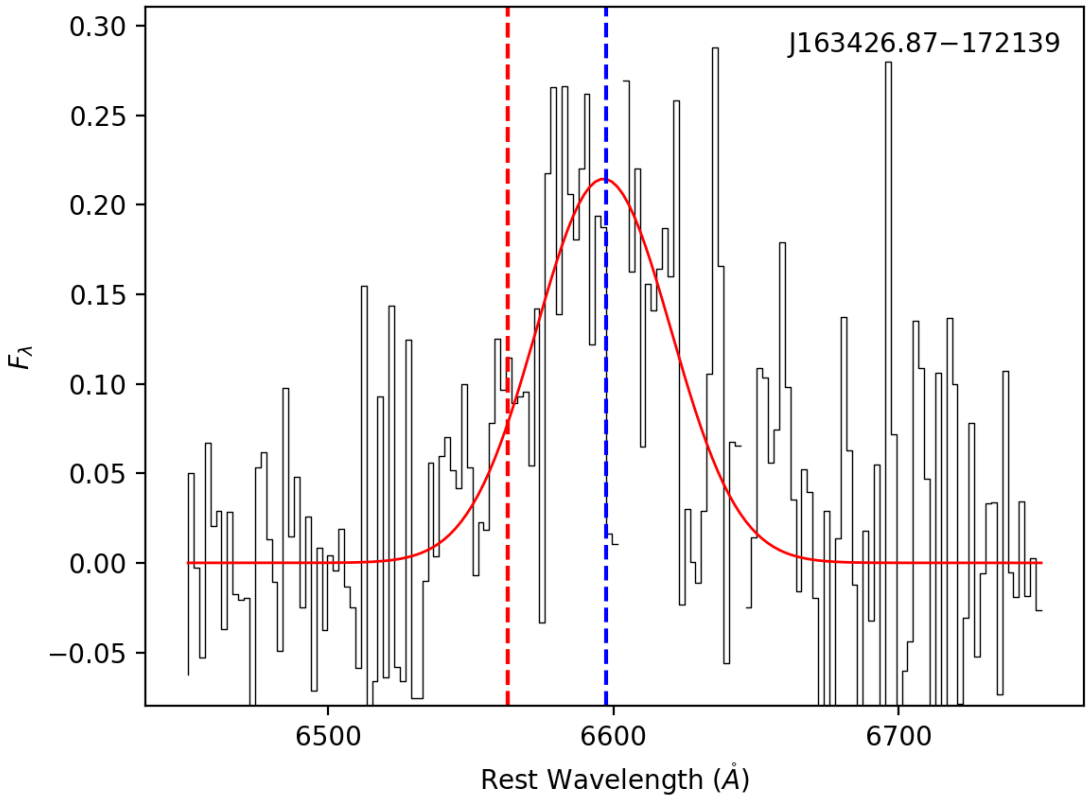

Figure 6.23: The Hα emission line (black) of W1634 fitted with a multi component Gaussian emission line (red). The rest wavelength of the Hα emission line is shown by the vertical red line, whereas the vertical blue line shows the rest wavelength of the centre of the fitted model. Note that flux densities are given in units of 10^{-16} erg s^{-1}cm^{-2}Å^{-1}.

estimated.

$$\dot{\mathrm{M}}_{\mathrm{out}} = \frac{3\mathrm{M}_{\mathrm{gas}}\mathrm{v}_{\mathrm{out}}}{\mathrm{R}_{\mathrm{out}}} \tag{6.8}$$

$$\dot{\mathrm{E}}_{\mathrm{out}} = \frac{1}{2}\dot{\mathrm{M}}_{\mathrm{out}}\mathrm{v}_{\mathrm{out}}^2 = \frac{3\mathrm{M}_{\mathrm{gas}}\mathrm{v}_{\mathrm{out}}^3}{2\mathrm{R}_{\mathrm{out}}} \tag{6.9}$$

$$\dot{\mathrm{P}}_{\mathrm{out}} = \dot{\mathrm{M}}_{\mathrm{out}}\mathrm{v}_{\mathrm{out}} = \frac{3\mathrm{M}_{\mathrm{gas}}\mathrm{v}_{\mathrm{out}}^2}{\mathrm{R}_{\mathrm{out}}} \tag{6.10}$$

The ionised gas mass can be derived using Equation 6.11 (Nesvadba et al., 2011b; Carniani et al., 2015) assuming $C/10^{[O/H]} = 1$ where $C =< n_e >^2 / < n_e^2 >$, n_e is the electron density and [O/H] is the metallicity of the gas. Following Jun et al. (2020), I assume that the outflow size $\mathrm{R}_{\mathrm{out}} = 3\,\mathrm{kpc}$ and that the outflow velocity, $\mathrm{v}_{\mathrm{out}}$, can be derived from Equation 6.12, where v is the velocity dispersion and σ is the velocity offset.

$$\mathrm{M}_{\mathrm{gas}} = 4.0 \times 10^7 \mathrm{M}_\odot \times \left(\frac{\mathrm{C}}{10^{[\mathrm{O/H}]}}\right)\left(\frac{\mathrm{L}_{[\mathrm{OIII}]}}{10^{44}\,\mathrm{erg\,s^{-1}}}\right)\left(\frac{<\mathrm{n_e}>}{10^3\,\mathrm{cm^{-3}}}\right)^{-1} \tag{6.11}$$

$$\mathrm{v}_{\mathrm{out}} = 2\sigma_0 = 2\sqrt{\sigma_{[\mathrm{OIII}]}^2 + \mathrm{v}_{[\mathrm{OIII}]}^2} \tag{6.12}$$

6.6.2 Detected Velocity Offsets

In total I have 100 detections of emission/absorption lines across 23 different RWGs. 62 of these detections were redshifted with respect to the line rest wavelength[8] with a mean offset of 6.52 ± 7.20 Å equivalent to $439.27 \pm 387.40\,\mathrm{km\,s^{-1}}$. The other 38 detections were blue shifted in comparison to the line rest wavelength by a factor of -4.42 ± 3.71 Å or $-341.06 \pm 504.80\,\mathrm{km\,s^{-1}}$. Figure 6.24 presents this information as a histogram showing the distribution of my measured velocity offsets.

Across the 15 different lines I detected, only four emission lines are detected in ≥ 10 sources. These four emission lines, Lyα, OII, OIII and Hα are summarised in Table 6.17. Across all four of these sources I measure $> 70\,\%$ of their offsets to be redshifted with all of the offsets $> 350\,\mathrm{km\,s^{-1}}$. In order to define an offset as significant (greater than an offset caused by a likely redshift error of z $\pm$ 0.001) I set a criterion of $> 600\,\mathrm{km\,s^{-1}}$, to exclude any offsets caused by errors in the Lonsdale et al. (2015) redshifts. Whilst consistent offsets for all sources may be

[8]The rest wavelengths of the detected emission lines are all given in Table D.1.

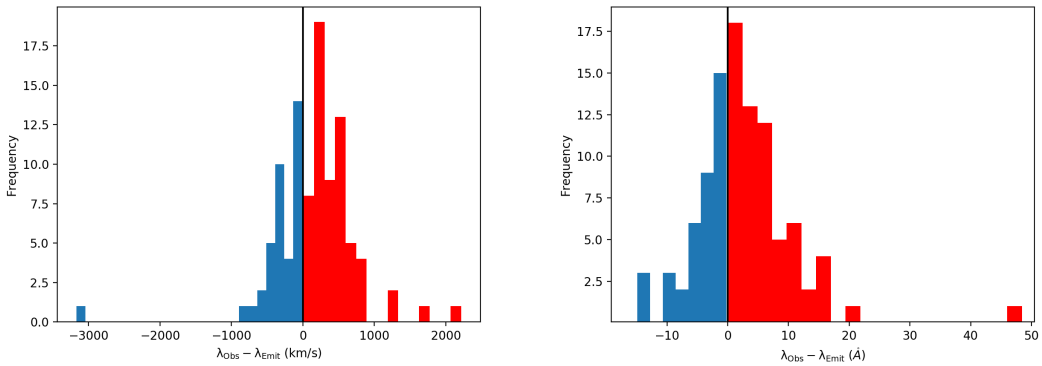

Figure 6.24: The measured velocity offsets across all 100 line detections plotted in both Å and $\mathrm{km\,s^{-1}}$.

indicative of a systematic error, this high offset threshold should exclude them. For the Lyα emission lines I measured an offset of this magnitude for two sources, W1412 with an offset of $\sim 1750\,\mathrm{km\,s^{-1}}$ and W1500 with a blue shifted offset of $\sim -3150\,\mathrm{km\,s^{-1}}$.

I measured an OII velocity offset $> 600\,\mathrm{km\,s^{-1}}$ for three sources W1400, W1412 and W1513 all of which are redshifted. For [OIII]λ5007 I measure two redshifted sources, $> 600\,\mathrm{km\,s^{-1}}$, W1412 and W1634 and four sources W1400, W1412, W1541 and W1634 with a redshifted Hα emission line.

Next I investigated the velocity offsets in terms of individual sources rather than individual emission lines. Out of the total 27 sources observed with X-shooter, I detected emission/absorption lines in 23 of these sources, four of which have detections of $> 50\,\%$ (>8) of my detected lines. Table 6.18 summarises these four emission lines along with two extra sources W1412 and W1634 with solely redshifted emission lines detected.

Figure 6.25 more clearly shows this information, showing the red and blue shifted emission lines for each source. The shaded region represents a velocity offset $< 600\,\mathrm{km\,s^{-1}}$ which is within a redshift difference of $z \pm 0.001$ and can be used to determine which offsets are significant. The other two sources in Table 6.18 are W1412 and W1634. These two sources only have four and two detected emission lines respectively, but all of these detections have offsets which are redshifted with a difference $>600\,\mathrm{km\,s^{-1}}$. These two sources therefore stand out as the only sources whose detections have significant offsets in the same direction. These offsets are shown in Figure 6.26 where it is clear that they all lie outside of the region defined by a redshift error of z $\pm$0.001 and this consistency is likely caused by a redshift shift to the entire spectra rather than specific line offsets.

As these two sources have consistent velocity offsets $> 600\,\mathrm{km\,s^{-1}}$, it is likely that these offsets are due to a redshift error and by fitting a liner relation to the offsets I can estimate a needed redshift correction. Fitting the four offsets of W1412, I measured a redshift offset of

Table 6.17: The number of detections and mean offsets (difference between the emission line rest wavelength and the central wavelength of the fitted model) based of the emission lines with > 10 detections.

Emission Line	Number of Detections	Mean Offset	
		Å	$\mathrm{km\,s^{-1}}$
Lyα	10	0.38 ± 4.81	94.2 ± 1180
Red shift (+)	8	2.11 ± 2.00	520 ± 493
Blue shift (-)	2	-6.52 ± 6.32	-1610 ± 1560
OII	13	3.48 ± 5.55	280 ± 447
Red shift (+)	9	4.60 ± 6.08	370 ± 489
Blue shift (-)	4	-2.36 ± 1.84	-190 ± 148
OIII	15	3.56 ± 7.59	214 ± 454
Red shift (+)	11	7.23 ± 5.17	433 ± 309
Blue shift (-)	4	-6.52 ± 1.97	-390 ± 118
Hα	13	10.70 ± 12.48	488 ± 570
Red shift (+)	11	13.17 ± 12.01	601 ± 548
Blue shift (-)	2	-2.91 ± 0.86	-133 ± 39.5

Table 6.18: The number of detections and mean offset (difference between the emission line rest wavelength and the central wavelength of the fitted model) of the sources with 8 line detections. Also included are the 2 sources with only significant outflows.

WISE Designation	Number of Detections	Mean Offset	
		Å	kms^{-1}
J130817.00−344754	10	1.18 ± 4.65	63.6 ± 287
Red shift (+)	5	5.00 ± 3.07	326 ± 114
Blue shift (-)	5	-2.65 ± 2.12	-199 ± 119
J140050.13−291924	12	2.74 ± 5.59	202 ± 387
Red shift (+)	8	5.73 ± 4.24	427 ± 243
Blue shift (-)	4	-3.26 ± 1.90	-247 ± 166
J141243.15−202011	4	22.9 ± 15.5	1610 ± 409
Red shift (+)	4	22.9 ± 15.5	1610 ± 409
Blue shift (-)	0	-	-
J150048.73−064939	9	-0.37 ± 6.74	-275 ± 1060
Red shift (+)	4	5.66 ± 2.88	331 ± 168
Blue shift (-)	5	-5.19 ± 4.79	-761 ± 1210
J163426.87−172139	2	15.9 ± 1.13	828 ± 52.6
Red shift (+)	2	15.8 ± 1.13	828 ± 52.7
Blue shift (-)	0	-	-
J195141.22−042024	8	5.96 ± 4.10	339 ± 255
Red shift (+)	7	7.32 ± 2.09	425 ± 125
Blue shift (-)	1	3.58 ± 0.00	-262 ± 0

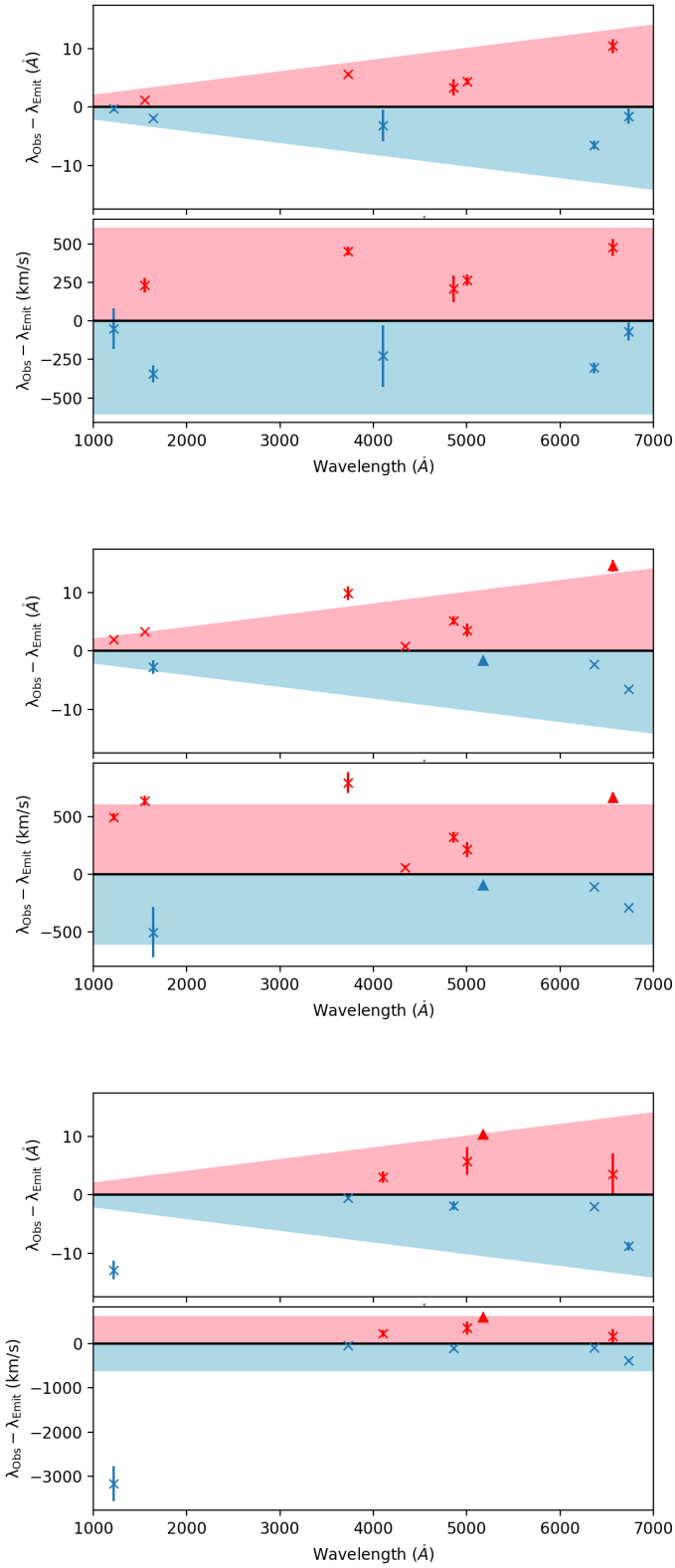

Figure 6.25: The velocity offsets in Å and $\mathrm{km\,s^{-1}}$ for sources W1308, W1400, W1500 and W1951 arranged from top to bottom. The shaded region represents a typical redshift difference of $z \pm 0.001$ applied when converting the spectra from observed to rest wavelengths. Absorption lines are plotted with a triangular marker whilst emission lines use a x shaped marker. Tables 6.12 and 6.13 can be used to determine all the detected lines for these sources.

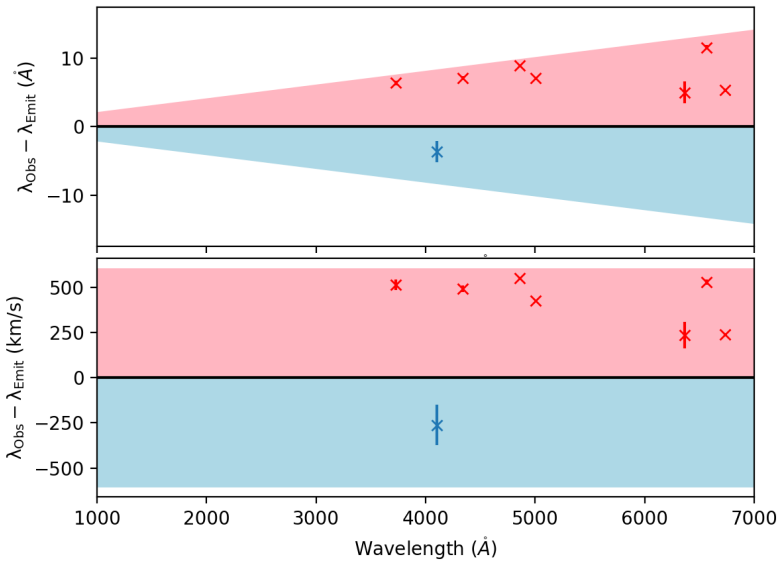

Figure 6.25: Continued.

0.005 ± 0.002 increasing the measured values from Lonsdale et al. of z = 1.808 to z = 1.813. For W1634, I predicted a redshift correction of 0.003 ± 0.0002 leaving an updated redshift of z = 2.703.

The redshifts used in the thesis are those derived by Lonsdale et al. (2015) using the same spectra that is presented in this thesis. They use three different sets of spectroscopic observations to derive the redshift of all sources in their sample, using this VLT X-shooter spectroscopy to derive the redshifts of the 30 RWGs presented here. Rather than independently measuring the redshifts of these RWGs I used the Lonsdale et al. redshifts, as they used the same methods and same data, and therefore I did not expect to measure any differences. They were unable to determine accurate redshifts for three RWGs (W1657, W1707, W2040) instead assuming their redshifts to be 2.0. Before performing any analysis I searched for the Balmer emission lines of these three sources aiming to measure a more exact redshift. For W1657 and W1707 I detect zero emission lines[9] and therefore take the Lonsdale et al. redshift value of 2.0. For W2040 I detect three emission lines and use this to infer a redshift of 2.02, within error to that assumed by Lonsdale et al. (2015). With this similarity I was therefore confident in using these derived redshifts for SED fitting and searching for emission lines. I remained confident with the decision as above I detected only two sources with a likely redshift offset, both whose offsets are less than 5% of the used value, and any offset due to this error is less than the width of the narrowest emission line measured. A redshift error was therefore highly unlikely to be the cause of some

[9]No emission lines are detected for these two sources in this work.

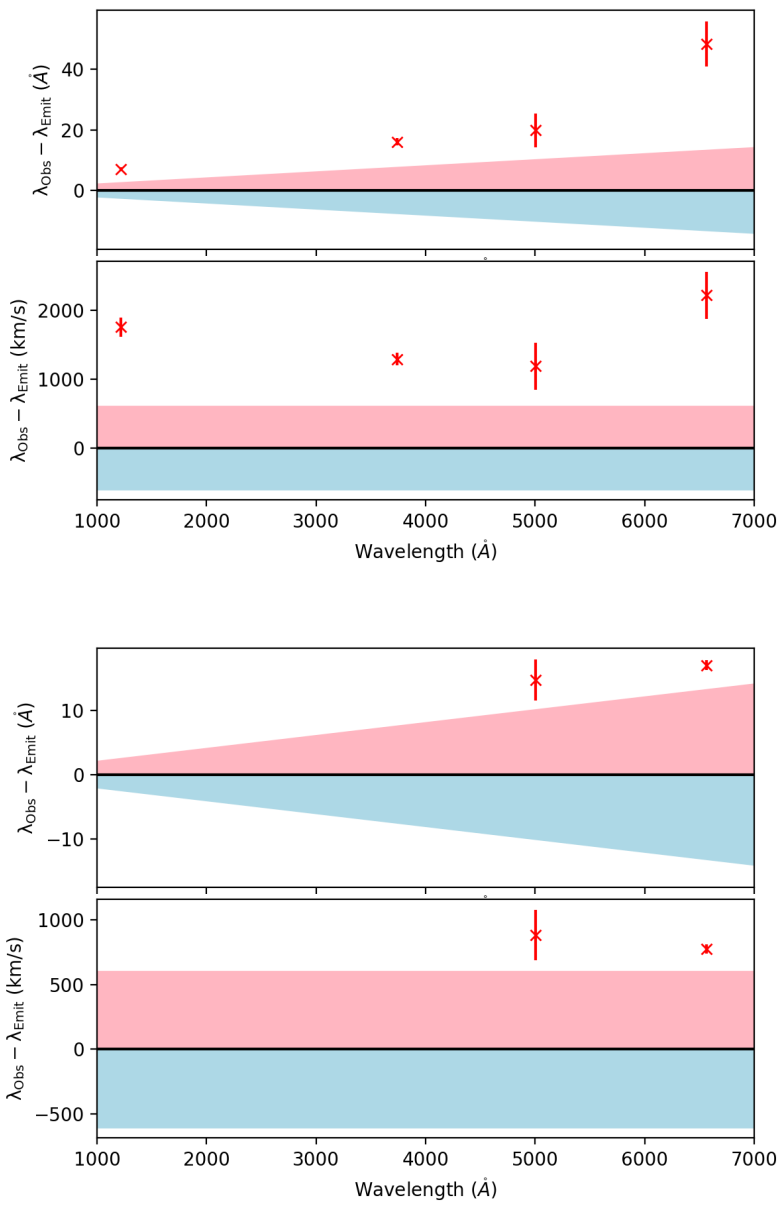

Figure 6.26: The velocity offsets in Å and $\mathrm{km\,s^{-1}}$ for sources W1412 and W1634 arranged from top to bottom. The shaded region represents a typical redshift error of $z \pm 0.001$.

Table 6.19: The outflow quantities based on the OIII emission lines.

WISE designation	$\log M_{gas}$ ($M_\odot$)	v_{out} (kms^{-1})	$\dot{M}_{out}$ ($M_\odot yr^{-1}$)	$\log \dot{E}_{out}$ ($ergs^{-1}$)	$\log \dot{P}_{out}$ (dyn)
J081131.61−222522	7.12 ± 0.02	2702 ± 256	37 ± 5	43.93 ± 0.42	35.8 ± 0.09
J082311.24−062408	7.38 ± 0.02	2229 ± 1007	54 ± 27	43.93 ± 0.79	35.88 ± 0.34
J130817.00−344754	8.06 ± 0.03	2339 ± 253	276 ± 52	44.68 ± 0.44	36.61 ± 0.12
J134331.37−113609	8.09 ± 0.14	4083 ± 1116	510 ± 386	45.43 ± 0.62	37.12 ± 0.35
J140050.13−291924	7.89 ± 0.11	3264 ± 101	261 ± 86	44.94 ± 0.34	36.73 ± 0.14
J141243.15−202011	6.93 ± 0.04	2728 ± 307	24 ± 5	43.75 ± 0.44	35.61 ± 0.14
J143419.59−023543	7.70 ± 0.06	1591 ± 137	81 ± 20	43.81 ± 0.41	35.91 ± 0.13
J150048.73−064939	6.65 ± 0.04	3435 ± 1019	16 ± 7	43.77 ± 0.64	35.53 ± 0.26
J151003.71−220311	7.11 ± 0.02	1141 ± 44	15 ± 1	42.79 ± 0.35	35.04 ± 0.06
J151424.12−341100	7.08 ± 0.14	2335 ± 591	28 ± 21	43.69 ± 0.59	35.62 ± 0.33
J154141.64−114409	7.50 ± 0.05	3006 ± 534	98 ± 32	44.45 ± 0.51	36.27 ± 0.19
J163426.87−172139	7.38 ± 0.01	3223 ± 347	78 ± 11	44.41 ± 0.43	36.20 ± 0.10
J170204.65−081108	8.10 ± 0.18	3179 ± 987	410 ± 407	45.12 ± 0.65	36.92 ± 0.42
J195141.22−042024	8.22 ± 0.01	2347 ± 48	397 ± 9	44.84 ± 0.33	36.77 ± 0.02
J200048.58−280251	7.24 ± 0.10	3402 ± 5422	61 ± 135	44.35 ± 1.54	36.12 ± 0.92

missing emission lines.

Finally, I used Equations 6.8 - 6.12 to measure the outflow properties of the [OIII]λ5007 emission line. I have 15 detections of the [OIII]λ5007 emission line, only two of which show significant velocity offsets. Table 6.19 however gives the measured outflow quantities for all 15 sources with detected emission lines.

I measured a mean outflow gas mass $\log\left(\frac{M_{gas}}{M_\odot}\right) = 7.50$ across the 15 RWGs with detected [OIII]λ5007 emission lines. This is ~ 1 order of magnitude smaller than the mean $\log\left(\frac{M_{gas}}{M_\odot}\right) = 8.53$ measured by Jun et al. (2020) for their eight HotDOGs. I measured a substantially lower mass outflow rate of $\sim 126\,M_\odot yr^{-1}$ in comparison to $\sim 1250\,M_\odot yr^{-1}$, though my mean momentum flux $\log \dot{P}_{out} = 36.14$ dyn agrees within error to the value of $\log \dot{P}_{out} = 37.17$ dyn found by Jun et al. (2020). It is unsurprising that I measured lower outflow properties with my RWGs, as I only measured a substantial velocity offset for two [OIII]λ5007 emission lines out of the 15 I detect. Additionally, these two significant [OIII]λ5007 outflows are detected in sources W1412 and W1634, all of whose detected emission lines have velocity offsets $> 600\,km\,s^{-1}$. With all detected emission lines having offsets, it is likely that this is due to a redshift error and above I measured redshift corrections of 0.005 ± 0.002 and 0.003 ± 0.0002 respectively. This may therefore explain why I measured outflow properties ~ 1 magnitude lower than Jun et al. (2020)

as I actually detect no significant velocity offsets or outflows in my [OIII]λ5007 emission line detections.

6.6.3 Summary of Velocity Offsets and Outflow Properties

I investigated the velocity offsets of my detected emission lines by comparing the rest wavelength at the centre of my fitted model to the rest wavelength of the emission line which I detected. In total I detected 15 different emission/absorption lines across 23 RWGs with a total of 100 individual detections. I measured 62 of these detections to be redshifted by a mean $\sim 440\,\mathrm{km\,s^{-1}}$, with the other 38 detections shifted by a mean $\sim -340\,\mathrm{km\,s^{-1}}$. With the 1D spectra initially converted from observed to rest wavelength with a redshift correction, it is likely that consistent velocity offsets are due to redshift error. I measured velocity offsets $> 600\,\mathrm{km\,s^{-1}}$ in all detected emission lines for two sources, W1412 and W1634, consistent with a redshift corrections of 0.005 ± 0.002 and 0.003 ± 0.0002 respectively.

6.7 Conclusions

The main focus of this chapter was to make use of the additional X-shooter spectroscopy with the aim of using these extra line detections to help classify my observed RWGs and investigate how they compare to other similarly selected populations. Any similar characteristics will help with identifying further RWGs whilst expanding our knowledge on the environment surrounding these sources. Across the previous two chapters I investigated the NIR arm of X-shooter where I detected three different emission lines, Hα, Hβ and [OIII]λ5007 in a respective 13, 6 and 15 RWGs or in a total of 18/27 sources observed.

The X-shooter spectograph observes across a total wavelength range of 300 - 2480 nm split into three different arms UVB (300-560 nm), VIS (550-1020 nm) and NIR (1020-2480 nm). With previous focus on the NIR arm, I now detect an additional 12 emission/absorption lines in this chapter with a total of 23/27 sources having at least one line detection. Firstly I searched for five new emission lines in the NIR wavelength range detecting 13 OII emission lines, six Hδ lines, six Hγ lines, eight OI lines and eight SII emission lines. This led to a total of eight different emission lines detected across the NIR arm and a total of 23 RWGs with a least one detection.

In addition to the NIR arm, I detected additional emission lines in the VIS arm of X-shooter measuring three HeII emission lines. Similarly in the UVB arms wavelength range I detected two OVI and 10 Lyα emission lines. Including results from these two extra wavelength ranges has given me results for an additional three emission lines though all were present in sources with previous detections.

Finally I searched for six common absorption lines across the entirety of X-shooters wavelength range. I detected zero Ca(H), Ca(G) and Na absorption lines though do detected one emission line at the Ca(K) rest wavelength. I detected one absorption line at the CaII wavelength and three additional Mg lines. Overall this led to a total of 15 detected lines, 23 RWGs with a line detection and 100 measured line profiles. These emission line detections will help with identifying future RWGs in previously observed sources, whilst detailing the environment around these highly active sources.

I used these newly measured emission lines to place the RWGs on BPT diagrams with the aim of classifying them as AGN and finding a unique position where RWGs lie and therefore could be used to select additional RWGs. Using my measured Hβ emission lines I placed five RWGs on to the three BPT diagrams showing that three RWGs are powered by AGN. Another is likely dominated by star formation whilst the positioning of the last source was uncertain. Correcting for the extinction measured in the Chapter 5 shifted the placement of these five RWGs though with mixed results across the three BPT diagrams. I additionally used a simulated Hβ emission line with the aim of classifying more than five sources. Classifying RWGs as AGN confirms that future SED fitting attempts will need to include AGN templates and due to the similar positioning of HotDogs and RWGs on BPT diagrams, BPT position could be used to identify these populations of extremely luminous and active AGN in the future.

I used the $\mathrm{M_{BH}} - \mathrm{M_{sph}}$ relation from Bennert et al. (2011) to compare my RWGs to similarly selected HotDOGs (Assef et al., 2015; Wu et al., 2018) and measured $\log\left(\frac{\mathrm{M_{sph}}}{\mathrm{M_{\odot}}}\right) = 9.5$ - 11.2, placing my sources ~ 1.1 dex smaller than the HotDOGs from Assef et al. (2015). Most importantly, this implies that HotDOGs and RWGs are not the same extreme population, and are likely to be different evolutionary stages.

Finally, I focused on the emission line profiles themselves, investigating and potential asymmetry and velocity offsets shown in my measured emission lines. Through comparing the measured flux to the right and left of the central wavelength of my fitted Gaussians, I measured an asymmetry $> 5\%$ for four of 13 detected Hα emission lines hinting at a spatially extended structure and providing additional evidence for the super Eddington accretion of RWGs as found in Chapter 5. Three of these sources were dominated by flux on their left hand side with $\geq 10\%$ of their total flux measured here.

I measured 62/100 total line detections to be redshifted by a mean factor of $\sim 440\,\mathrm{km\,s^{-1}}$, though any velocity offset < 600 $\mathrm{km\,s^{-1}}$ is within a redshift error of $z \pm 0.001$. An offset $>$ 600 $\mathrm{km\,s^{-1}}$ was measured in all detected emission lines of two sources, W1412 and W1634, leading to redshift corrections of 0.005 ± 0.002 and 0.003 ± 0.0002. Finally I used the equations

from Maiolino et al. (2012) and Nesvadba et al. (2011b) to estimate the outflow properties of the [OIII]λ5007 emission line. With no significant outflows detected for [OIII]λ5007 I measured outflow gas mass and momentum flux $\sim$ 1 dex lower than measured for HotDOGs (Jun et al., 2020), again implying they are separate populations, with RWGs having $\sim$ 1 dex smaller masses.

The results in this chapter have shown that source positioning on a BPT diagram may be used as an additional selection/classification method to select extremely luminous and active galaxies. They have confirmed the AGN nature of RWGs, whilst measured asymmetry in the detected emission lines provides more evidence for super Eddington accretion. Finally, the difference in mass between RWGs and HotDOGs implies they are not the same population, and that RWGs may be a shorter, yet just as active phase of galactic evolution.

Chapter 7

Final Conclusions and Future Prospects

RWGs are extremely luminous and obscured radio intermediate AGN selected through a cross match (Lonsdale et al., 2015) between NVSS radio sources (Becker et al., 1995) and the WISE All-sky survey catalogue (Cutri et al., 2013). They are a unique population of galaxies, even including then new WISE galaxy populations, with intermediate radio emission and possess WISE band colours distinctly redder than the main WISE population. This thesis aimed to analyse NIR photometric and multi wavelength spectroscopic observations of 30 RWGs obtained at the VLT, expanding on, and including the work presented in Ferris et al. (2021). I aimed to determine additional and unknown properties of RWGs in order to compare them to existing galaxy populations. Similar characteristics would provide additional characteristics to help detect and classify future RWGs expanding our known population. If, on the other hand, RWGs do not fit existing relations or match other galaxy populations, are they a new phase of galaxy evolution and if so what can they tell us about the universe at that time.

In Chapter 4, I aimed to determine the SED shape and size of my sample of RWGs. I presented measured J and K_s band flux densities, taken from ISAAC imaging, for selected, luminous IR WISE galaxies, alongside WISE and ALMA flux densities previously obtained. Using these flux densities and the `MAGPHYS` SED fitting package, I measured a relatively consistent SED shape of a steep red IR power law, mid-IR peak and flatter mid-IR to sub mm though not all sources were successfully modelled. This SED shape confirmed that RWGs are AGN, as the can not be fitted without AGN templates. It also showed that the are likely a different population to HotDOGs which had a noticeably different SED shape. I measured stellar masses $\log\left(\frac{\mathrm{M}_*}{\mathrm{M}_\odot}\right) = 9.97$ - 11.99, lower than previous measuremnets of HotDOGs and provided χ^2_ν as a guide to their reliability. I then took X-shooter observations of 27 selected RWGs and detected 15 [OIII]λ5007, 13 Hα and six Hβ emission lines across 18 different RWGs in the NIR. The properties of these emission lines were then used to estimate BH and host galaxy masses. Under the assumption of λ_{Edd}

= 1, I derived $\log\left(\frac{M_{BH}}{M_\odot}\right)$ = 7.9 - 9.4 using the [OIII]λ5007 emission line luminosity as a proxy for bolometric luminosity. Furthermore, I used the Hα emission line FWHM and luminosity to derive BH masses of $\log\left(\frac{M_{BH}}{M_\odot}\right)$ = 7.3 - 8.7, with the Hβ lines providing uncertain masses of up to a magnitude lower. Finally, I additionally used the FWHM of five detected CIV emission lines and the luminosity of [OIII]λ5007 as a proxy for $L_{1350\text{Å}}$ to measure $\log\left(\frac{M_{BH}}{M_\odot}\right)$ = 8.3 - 9.6 agreeing with other estimates within error for four of the five sources. All these black hole masses led to measured host masses in the range $\log\left(\frac{M_{Host}}{M_\odot}\right)$ = 10.4 - 12.0. These were again $\sim$ 1 dex lower than previously measured for HotDOGs leading me to conclude that the are not the same exact galaxy population.

Next in Chapter 5, I aimed to investigate the assumptions of $\lambda_{\rm Edd} = 1$ and $A_V = 0$ I made above in order to calculate the correct size of these obscured sources. I measured a mean value of $\lambda_{\rm Edd} = 10.12$ across the 11 sources with both Hα and [OIII]λ5007 line detections in an attempt to rectify the previous assumptions made, reducing my measured [OIII]λ5007 BH masses by $\sim$ 0.68 dex. My $\lambda_{\rm Edd}$ values ranged from $\lambda_{\rm Edd} = 0.34 - 34.59$, with 10/11 sources measuring super Eddington rates and these findings being statistically significant for five sources. I therefore conclude that some RWG's are in a super Eddington phase of their evolution, which will be a short lived phase, and therefore these observations have provided insight into the properties of galaxies at a previously unseen evolutionary phase. I additionally calculated the expected extinction and reddening affecting my measured emission line fluxes in order to determine the true masses of my sources. With five sources having detections of both the Hα and Hβ emission lines, I used the Balmer decrement and the Cardelli et al. (1989) extinction law to measure a mean value of A_V = 2.68 mag and E(B-V) = 0.86 magnitudes. With measurements of $A_V > 0$ mag for four sources, this increased my Hα BH and host galaxy mass measurements by $\sim$ 0.8 dex. As the Hβ was sparsely detected, I then used a simulated Hβ emission line at four different assumed FWHM values (3000, 1480, 1315 km s^{-1} and the FWHM of the corresponding Hα profile) to predict the effect of extinction on those sources without Hβ detections. Assuming that the Hα and Hβ BH mass calculations are equivalent and that the FWHM of Hβ = 1480 km s^{-1}, I measured $A_V > 0$ mag for 12/13 sources with a mean value of A_V = 3.62 magnitudes. For a complete investigation I repeated this calculation using all known BH mass measurements for sources with a Hα detection. However I concluded that RWG's are sources heavily extinguished by dust, with similar levels of extinction measured to HotDOGs, and correction for this extinction increased the measured masses by at least one order of magnitude.

In Chapter 6, I aimed to make full use of the full wavelength range of spectroscopic data provided by X-shooter and measured the properties of an additionally detected 12 emission

and three absorption lines. These detections will allow comparisons to non RWGs to look for environmental comparisons and assist in future selections. This led to a total of 15 separate line detections, 23 RWGs with ≥ 1 line detection and 100 total measured line profiles presented in this thesis. I used these newly detected emission lines to place my RWGs onto BPT diagrams in order to determine their dominant mechanism. Out of the five RWGs with both Balmer lines detected, I determined three sources to be dominated by AGN activity, one source by star formation and the last a combination of the two. The tight placement of RWGs on BPT diagrams can now be used to help classify further RWGs from spectroscopic observations or at least select possible RWG candidates from large scale surveys. I then used the $\mathrm{M_{BH}} - \mathrm{M_{sph}}$ relation from Bennert et al. (2011) to calculate $\log\left(\frac{\mathrm{M_{sph}}}{\mathrm{M_{\odot}}}\right) = 9.5$ - 11.2, measuring my sources ~ 1.1 dex smaller than the HotDOG sample from Assef et al. (2015), agin implying that they are not the same population of galaxies. My final analysis focused on the emission line profiles themselves, where I detected an asymmetric Hα emission line profile for four sources with a $\geq 5\%$ flux difference between the flux densities to the left and right of the central wavelength, another possible indicator of super Eddington accretion. I also detected redshifted line profiles for 62/100 line detections. With offsets $> 600\,\mathrm{km\,s^{-1}}$ in all detected lines, I measured redshift corrections for W1412 and W1634 of 0.005 ± 0.002 and 0.003 ± 0.0002 respectively. Finally I used the equations from Maiolino et al. (2012) and Nesvadba et al. (2011b) to measure outflow gas mass and momentum flux ~ 1 magnitude lower than X-shooter observed HotDOGs (Jun et al., 2020) leading me to conclude that they are separate galaxy populations, though both are likely to be extreme phases of galactic evolution. As RWGs are smaller, they will not be able to maintain their super-Eddington phase for as long, and therefore will be a shorter evolutionary phase. This implies that compared to HotDOGs they are a rarer population, and provide a unique view into the history if the universe.

Through measuring the photometric and spectral properties of RWGs, I have been able to determine various masses, Eddington rates and dust extinction levels allowing for comparison with the similarly selected population of HotDOGs. This has allowed the differences between the populations to be noted with future observations and analysis that needs to be made highlighted so we can truly understand these new galaxy populations. The results and analysis presented in this thesis have extended our knowledge of RWGs, through using novel methods to determine previously unknown properties. I have shown that RWGs are a unique population of AGN and conclude that they are not the same population as HotDOGs. They can accrete at super Eddington rates and suffer from an average 2.7 magnitudes of dust extinction. They are therefore likely to be a short lived and extremely active phase of galaxy evolution and therefore provide

insight into the history of other galaxies, with RWGs providing us with a snapshot of the universe in an extremely active phase. I have also shown that the placement of previously observed AGN on to BPT diagrams is a good criterion to help select future AGN, and their narrow placement means that future RWGs could be determined using catalogue data.

This work has however led to many more questions needed to be answered in the future. These include whether the differences between HotDOGs and RWGs are actually due to changes in selection criteria and whether these new populations of extremely luminous and obscured WISE galaxies are a previously unknown stage of galaxy evolution or do other active galaxies belong to this same phase, but have different properties to RWGs. There also remain open questions around the correct SED shape of RWGs, as these are still not accurately fitted, and for the understanding of why common templates and relations do not always give reliable results for these specific galaxies.

Following on directly from this work, further spectroscopy is required in order to accurately predict the level of dust extinction affecting the whole population of RWGs, with corrections necessary for true comparisons with other populations. High resolution spectroscopy of the Hα and the Hβ emission lines with an instrument such as VLT's KMOS would provide higher S/N observations of the Balmer lines, allowing for tighter constraints on measured extinction values. It would also allow for the measurement of extinction values for those sources without current Hβ detections. These new extinction measuremnets would allow for an increased number of BH mass corrections, but also assist in further source placement on BPT diagrams he;ping place tighter constraints on new RWG selection criteria.

In total, further high resolution NIR spectroscopy will allows for exact values of masses, Eddington ratios and BPT diagram placement to be calculated rather than having to rely on limits taken from simulated spectra. This will reduce the error on my measured values, though some systematic error will remain. Further photometric observations (with a high resolution NIR images such as VLT's HAWK-I) of RWGs would also assist with more reliable SED fitting though the creation of further templates. Without additional photometic data points and new SED templates created it is unlikely that a reliable SED fit will be obtained, though model used in the future will need to include an AGN template.

Finally, with the upcoming launch of the James Webb Space Telescope (JWST, Gardner et al., 2006) in December, the availability of new high resolution NIR spectra should allow fast advancements in this field. This will allow further RWGs to be selected either through their SED shape or RWG placement and accurately calculate their extinction measurements. This will allow us to further investigate the properties and surrounding environments of these extreme and

obscured galaxies in order to confidently determine the exact luminosities, BH masses and other vital galaxy properties of RWGs, and therefore increase our understanding of an extremely active and short lived phase of galaxy evolution - properties that may be true for all AGN at some phase in their evolution.

Appendix A

Deriving Extinction Corrections with Previously Determined BH Masses

In this section I used previously published BH mass estimates (Lonsdale et al., 2015; Kim et al., 2013) derived independently from my spectroscopic measurements, to estimate the extinction of RWGs. These BH mass estimates used different data used and different assumptions, including the $\lambda_{\rm Edd}$ value used. The analytic methods used are again identical to those presented in Chapter 5, but here I present the results in more detail.

A.1 Using the Lonsdale et al. (2015) BH Mass to Simulate a Hβ Line Profile

The Lonsdale et al. (2015) BH masses are $\sim$ 0.9 dex greater than my Hα based BH mass results and I require a mean extinction correction of $A_V = 6.13$ magnitudes for my Hα BH masses to align with them. Lonsdale et al. use an assumed value of $\lambda_{\rm Edd} = 0.25$ increasing their mass measurements through this choice. These larger BH mass estimates require broad (2150 - 4125 $\rm km\,s^{-1}$) Hβ lines to be simulated in order to measure a flux ratio of Hα/H$\beta > 2.86$. Table A.1 gives my measured A_V and E(B-V) values using four different assumed FWHMs for the 13 sources with detected Hα emission lines. Across my four assumed FWHMs of 3000, Hα FWHM, 1480 and 1315 $\rm km\,s^{-1}$ I measured eight, two, zero, and zero visual extinction values greater than zero and mean values of A_V of 0.48, -3.1, -7.4 and -8.7 magnitudes respectively.

The range of corrected BH masses for all 13 sources is shown in Figure A.1 where I measured $\log\left(\frac{\rm M_{BH}}{\rm M_\odot}\right) = 4.9$ - 7.3. With a majority (10/52) of visual extinction measurements made here being negative, $> 80\%$ of my BH mass estimates have been reduced by $\sim$ 1 dex through these particular extinction corrections. Most noticeably in comparison to the corrections made using

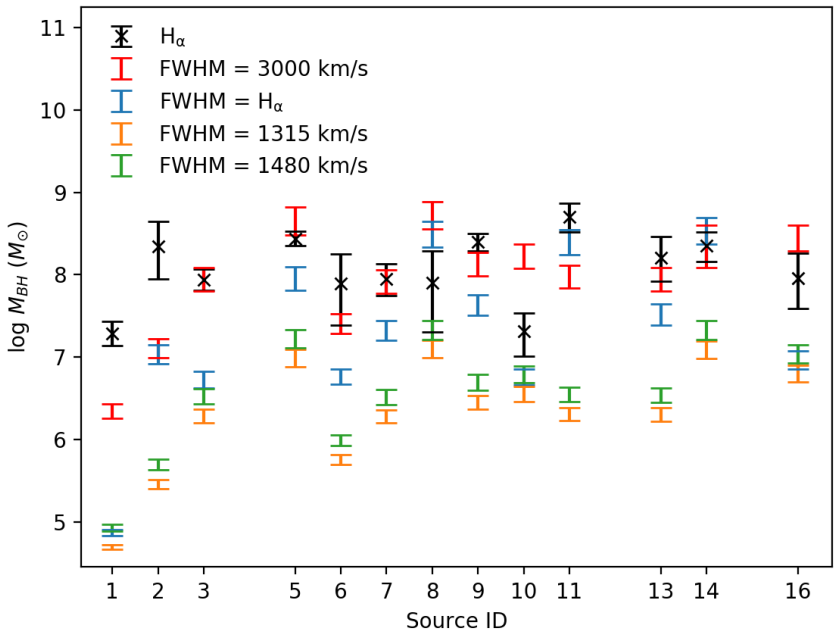

Figure A.1: The corrected Hα derived BH masses when I use the Lonsdale et al. (2015) BH mass to predict the expected measures of extinction. Source ID corresponds to the source labelling system given in Table 4.2.

my measured BH masses in Figure A.1, is the smaller error range due to the low error margins given on Lonsdale et al.'s BH masses.

The minimum FWHM required to measure a positive value for visual extinction is given in Table A.2 where I require a simulated Hβ emission line with a mean FWHM of 2955 km s^{-1} in order to measure $A_V > 0$ magnitudes. The whole distribution is shown later in Figure 5.19. This required width is $> 2\times$ as broad as the mean of my measured broad Hβ FWHMs, and I would require a value of FWHM = 12,984 km s^{-1} in order to measure an A_V value in agreement with Kim et al. (2013) for W1400. As RWGs are selected to be highly obscured sources, these broad FWHM required to measure $A_V > 0$ mean that the BH masses calculated in Lonsdale et al. (2015) are highly likely be overestimates of the true values. This is in agreement with the arguments made above and is likely due to their choice of $\lambda_{\rm Edd} = 0.25$, whilst I measure 10/11 RWGs accreting at super Eddington rates.

Table A.1: The calculated reddening and extinction for my 13 sources with detected Hα emission lines, assuming different FWHMs and that the Hβ and Lonsdale et al. (2015) BH masses are the same. Results are given in magnitudes.

WISE Designation	FWHM = 3000 km s^{-1}		FWHM = Hα		FWHM = 1480 km s^{-1}		FWHM = 1315 km s^{-1}	
	A_V	E(B-V)	A_V	E(B-V)	A_V	E(B-V)	A_V	E(B-V)
J081131.61−222522	$-1.55^{+1.14}_{-0.86}$	$-0.50^{+0.37}_{-0.28}$	$-9.79^{+0.72}_{-0.61}$	$-3.16^{+0.23}_{-0.2}$	$-9.45^{+0.74}_{-0.62}$	$-3.05^{+0.24}_{-0.2}$	$-10.77^{+0.54}_{-0.68}$	$-3.48^{+0.17}_{-0.22}$
J082311.24−062408	$-1.18^{+0.26}_{-0.25}$	$-0.38^{+0.08}_{-0.08}$	$-1.62^{+0.24}_{-0.24}$	$-0.52^{+0.08}_{-0.08}$	$-9.09^{+0.09}_{-0.1}$	$-2.93^{+0.03}_{-0.03}$	$-10.41^{+0.15}_{-0.16}$	$-3.36^{+0.05}_{-0.05}$
J130817.00−344754	$0.42^{+1.04}_{-0.87}$	$0.14^{+0.34}_{-0.28}$	$-6.35^{+0.72}_{-0.66}$	$-2.05^{+0.23}_{-0.21}$	$-7.49^{+0.67}_{-0.62}$	$-2.42^{+0.22}_{-0.20}$	$-8.81^{+0.55}_{-0.76}$	$-2.84^{+0.18}_{-0.25}$
J140050.13−291924	$2.6^{+0.92}_{-0.72}$	$0.84^{+0.3}_{-0.23}$	$-1.26^{+0.73}_{-0.6}$	$-0.41^{+0.23}_{-0.19}$	$-5.31^{+0.54}_{-0.47}$	$-1.71^{+0.18}_{-0.15}$	$-6.63^{+0.68}_{-0.90}$	$-2.14^{+0.22}_{-0.29}$
J141243.15−202011	$-3.57^{+0.5}_{-0.44}$	$-1.15^{+0.16}_{-0.14}$	$-7.15^{+0.34}_{-0.31}$	$-2.31^{+0.11}_{-0.1}$	$-11.47^{+0.15}_{-0.14}$	$-3.7^{+0.05}_{-0.05}$	$-12.8^{+0.09}_{-0.09}$	$-4.13^{+0.03}_{-0.03}$
J143419.59−023543	$0.13^{+1.2}_{-1.02}$	$0.04^{+0.39}_{-0.33}$	$-3.23^{+1.04}_{-0.92}$	$-1.04^{+0.34}_{-0.3}$	$-7.78^{+0.83}_{-0.78}$	$-2.51^{+0.27}_{-0.25}$	$-9.1^{+0.41}_{-0.58}$	$-2.94^{+0.13}_{-0.19}$
J143419.59−023543	$2.45^{+1.48}_{-1.11}$	$0.79^{+0.48}_{-0.36}$	$1.18^{+1.41}_{-1.07}$	$0.38^{+0.45}_{-0.35}$	$-5.46^{+1.05}_{-0.88}$	$-1.76^{+0.34}_{-0.28}$	$-6.78^{+0.29}_{-0.36}$	$-2.19^{+0.09}_{-0.12}$
J150048.73−064939	$-1.54^{+2.87}_{-1.53}$	$-0.5^{+0.93}_{-0.49}$	$-4.27^{+2.63}_{-1.47}$	$-1.38^{+0.85}_{-0.47}$	$-9.45^{+2.22}_{-1.34}$	$-3.05^{+0.72}_{-0.43}$	$-10.77^{+2.13}_{-1.31}$	$-3.47^{+0.69}_{-0.42}$
J151003.71−220311	$1.2^{+1.21}_{-0.89}$	$0.39^{+0.39}_{-0.29}$	$-6.89^{+0.79}_{-0.64}$	$-2.22^{+0.25}_{-0.21}$	$-6.71^{+0.8}_{-0.65}$	$-2.16^{+0.26}_{-0.21}$	$-8.03^{+0.51}_{-0.62}$	$-2.59^{+0.16}_{-0.2}$
J151310.42−221004	$-2.82^{+0.73}_{-0.6}$	$-0.91^{+0.24}_{-0.19}$	$-0.5^{+0.84}_{-0.67}$	$-0.16^{+0.27}_{-0.22}$	$-10.72^{+0.38}_{-0.34}$	$-3.46^{+0.12}_{-0.11}$	$-12.05^{+0.8}_{-1.1}$	$-3.89^{+0.26}_{-0.36}$
J154141.64−114409	$0.6^{+0.42}_{-0.37}$	$0.19^{+0.14}_{-0.12}$	$-1.78^{+0.32}_{-0.29}$	$-0.57^{+0.1}_{-0.09}$	$-7.3^{+0.09}_{-0.09}$	$-2.36^{+0.03}_{-0.03}$	$-8.63^{+0.04}_{-0.04}$	$-2.78^{+0.01}_{-0.01}$
J163426.87−172139	$1.82^{+1.05}_{-0.83}$	$0.59^{+0.34}_{-0.27}$	$0.55^{+0.99}_{-0.79}$	$0.18^{+0.32}_{-0.26}$	$-6.08^{+0.67}_{-0.58}$	$-1.96^{+0.22}_{-0.19}$	$-7.41^{+0.58}_{-0.76}$	$-2.39^{+0.19}_{-0.24}$
J195141.22−042024	$4.01^{+0.16}_{-0.17}$	$1.3^{+0.05}_{-0.05}$	$-4.29^{+0.44}_{-0.52}$	$-1.38^{+0.14}_{-0.17}$	$-3.89^{+0.42}_{-0.5}$	$-1.26^{+0.14}_{-0.16}$	$-5.21^{+0.47}_{-0.56}$	$-1.68^{+0.15}_{-0.18}$

A.2 Using the Kim et al. (2013) BH Mass to Simulate a Hβ Line Profile

I finally use the assumption that my Hβ derived BH masses should be equal to the BH masses presented in Kim et al. (2013). These BH mass measurements are again derived completely independently from my own, using spectroscopy from FIRE (Simcoe et al., 2013). They also use an assumed Eddington ratio meaning they will also be increased uncertainties. We use identical methods assuming that the [OIII]λ5007 emission line luminosity can be used as a proxy for the bolometric luminosity and that $\lambda_{\rm Edd} = 1$. However, despite the identical methods Kim et al. measure BH masses ~ 0.46 dex greater than my own.

Table A.3 gives the measured A_V and E(B-V) magnitudes for the five sources observed by Kim et al. with corresponding Hα line detections in my VLT spectroscopy. Across the four assumed emission lines of FWHM = 3000, Hα width, 1480 and 1315 km s^{-1} I measured $A_V > 0$ for two, zero, zero and zero sources with mean visual extinction values of -0.47, -4.86, -8.82 and -9.39 magnitudes respectively. These negative measures of A_V will again mean a reduction in my recalculated BH masses in comparison to those originally measured.

Table A.2: The minimum FWHMs required for different values of visual extinction, based on the Lonsdale et al. (2015) calculated BH masses

WISE Designation	Minimum FWHM ($\mathrm{km\,s^{-1}}$) required				
	$A_v = 0$ mag	$A_v = 3$ mag	$A_v = 5$ mag	$A_v = 10$ mag	$A_v = 15$ mag
J081131.61−222522	3447	4503	5385	8421	13142
J082311.24−062408	3337	4360	5214	8153	12724
J130817.00−344754	2893	3778	4518	7065	11027
J140050.13−291924	2381	3094	3720	5816	9095
J141243.15−202011	4126	3110	6448	10076	15744
J143419.59−023543	2969	3878	4637	7252	11318
J143931.76−372523	2412	3151	3768	5892	9214
J150048.73−064939	3446	4502	5383	8418	13138
J151003.71−220311	2698	3525	4215	6591	10287
J151310.42−221004	3862	5046	6034	9436	14726
J154141.64−114409	2845	3716	4444	6950	10846
J163426.87−172139	2551	3332	3985	6231	9744
J195141.22−042024	2097	2740	3276	5123	8012

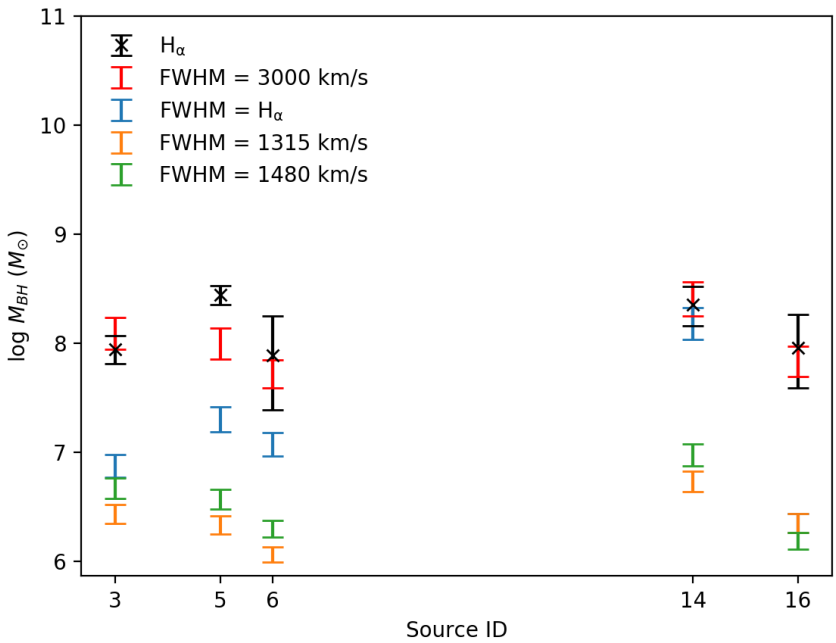

Figure A.2: The corrected Hα derived BH masses when I use the Kim et al. (2013) BH mass to predict the expected measures of extinction. Source ID corresponds to the source labelling system given in Table 4.2.

Table A.3: The calculated reddening and extinction for my 13 sources with detected Hα emission lines, assuming different FWHMs and that the Hβ and Kim et al. (2013) BH masses are the same. Results are given in magnitudes.

WISE Designation	FWHM = 3000 km s^{-1}		FWHM = Hα		FWHM = 1480 km s^{-1}		FWHM = 1315 km s^{-1}	
	A_V	E(B-V)	A_V	E(B-V)	A_V	E(B-V)	A_V	E(B-V)
J130817.00−344754	$1.22^{+5.04}_{-5.04}$	$0.39^{+1.63}_{-1.63}$	$-5.55^{+4.81}_{-4.82}$	$-1.79^{+1.55}_{-1.55}$	$-6.68^{+4.80}_{-4.78}$	$-2.16^{+1.55}_{-1.54}$	$-8.0^{+4.74}_{-4.74}$	$-2.58^{+1.53}_{-1.53}$
J140050.13−291924	$-1.03^{+5.58}_{-1.93}$	$-0.33^{+1.8}_{-0.62}$	$-4.88^{+4.85}_{-1.85}$	$-1.57^{+1.56}_{-0.60}$	$-8.93^{+4.24}_{-1.77}$	$-2.88^{+1.37}_{-0.57}$	$-10.26^{+4.07}_{-1.75}$	$-3.31^{+1.31}_{-0.56}$
J141243.15−202011	$-1.84^{+6.01}_{-6.00}$	$-0.59^{+1.93}_{-1.94}$	$-5.43^{+5.89}_{-5.88}$	$-1.75^{+1.91}_{-1.90}$	$-9.75^{+5.70}_{-5.73}$	$-3.14^{+1.84}_{-1.85}$	$-11.07^{+5.45}_{-5.68}$	$-3.57^{+1.75}_{-1.83}$
J163426.87−172139	$-0.13^{+0.18}_{-0.21}$	$-0.04^{+0.06}_{-0.07}$	$-1.4^{+0.23}_{-0.26}$	$-0.45^{+0.07}_{-0.08}$	$-8.04^{+0.45}_{-0.57}$	$-2.59^{+0.15}_{-0.18}$	$-9.36^{+0.50}_{-0.63}$	$-3.02^{+0.16}_{-0.2}$
J195141.22−042024	$0.56^{+4.51}_{-1.81}$	$0.18^{+1.45}_{-0.58}$	$-7.74^{+3.08}_{-1.55}$	$-2.5^{+0.99}_{-0.5}$	$-8.67^{+2.96}_{-1.52}$	$-2.8^{+0.96}_{-0.49}$	$-7.74^{+3.08}_{-1.55}$	$-2.5^{+0.99}_{-0.50}$

Table A.4: The minimum FWHMs required for different values of visual extinction, based on the Kim et al. (2013) calculated BH masses

WISE Designation	Minimum FWHM ($\mathrm{km\,s^{-1}}$) required				
	$A_v = 0$ mag	$A_v = 3$ mag	$A_v = 5$ mag	$A_v = 10$ mag	$A_v = 15$ mag
J130817.00−344754	2691	3516	4205	6577	10138
J140050.13−291924	3291	4300	5143	8044	12399
J141243.15−202011	3539	4625	5531	8650	13333
J163426.87−172139	3038	3969	4747	7425	11444
J195141.22−042024	2855	3730	4461	6977	10754

A comparison of the recalculated BH masses for all sources in shown by Figure A.2. With the Kim et al. (2013) BH masses again being greater than my originally measured masses, the FWHM of my simulated Hβ emission lines have to be broader in order to measure the same Hβ luminosity. This means that FWHMs $\sim 2.3\times$ broader than I originally measure are required to measure the Hα fluxes 2.86 $\times$ greater than those measured from my simulated Hβ emission lines.

This relation between the minimum FWHM required and measured A_V value for the five sources with measured Hα and Kim et al. (2013) BH masses is shown in the next section by Figure 5.19 where minimum FWHM required increases with measured A_V. The minimum FWHM values required to measure values of $A_V = 0$, 3, 5, 10 and 15 magnitudes are given in Table A.4. A mean FWHM of 3144 $\mathrm{km\,s^{-1}}$ is required to required to measure a simulated Hβ flux $<$ Hα flux / 2.86, which is greater than all of my measured Hβ FWHMs and $> 2\times$ my mean measured FWHM. This broad FWHM requirement is again due to their assumed value of $\lambda_{\mathrm{Edd}} = 1$, whilst both my above work and that by Kim et al. (2013) show that some RWGs accrete at super Eddington rates.

Appendix B

BPT diagrams including example QSOs

Figure B.1 shows three BPT diagrams, with the emission line ratios of five RWGs plotted. Unlike the image given in Chapter 6, here I have included 2000 QSO's from SDSS DR7. In this figure the majority of the QSO's are situated in the star formation region of the diagrams, contradicting what I would have expected from their selection criteria.

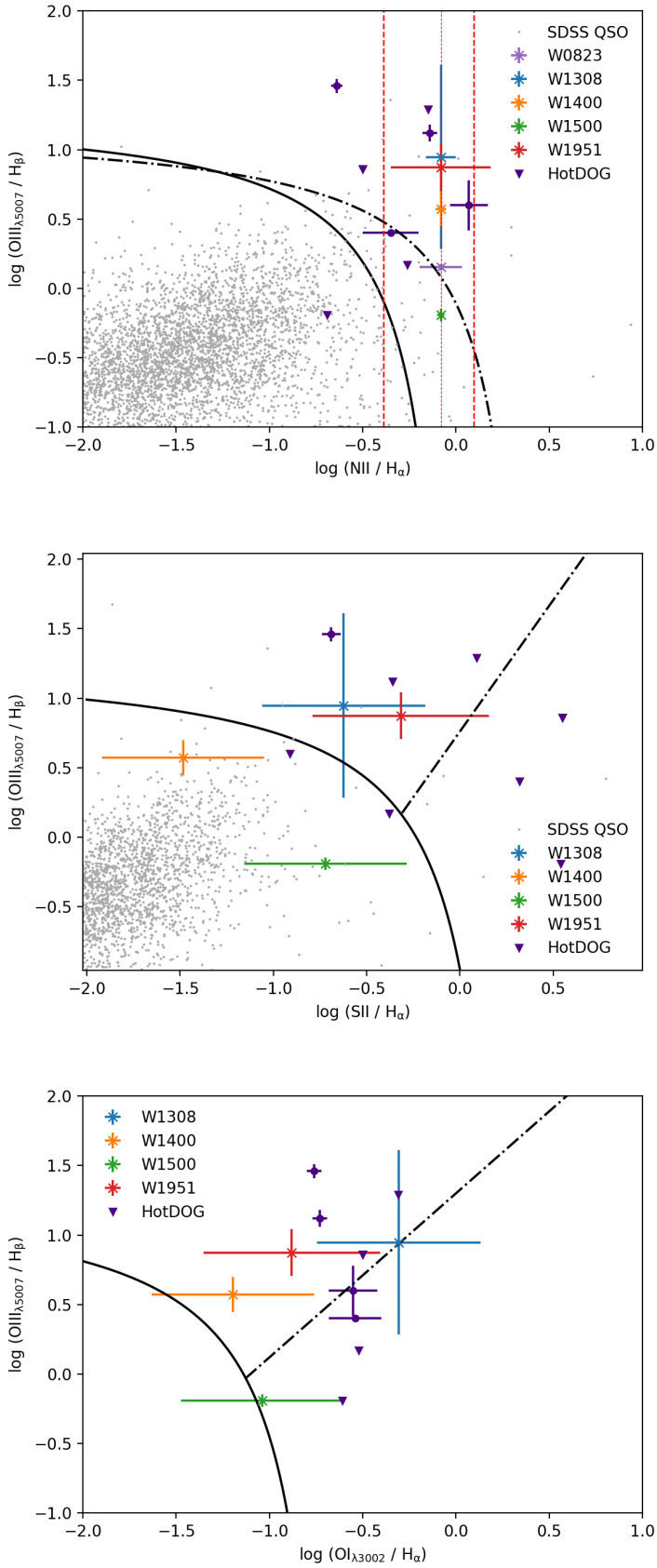

Figure B.1: Three BPT diagrams comparing nuclear emission line ratios with added dividing lines. Plotted is a maximum of five RWGs based on my measured emission line fluxes. Also included are example QSOs (Shen et al., 2011) and HotDOG (Jun et al., 2020) measurements.

Appendix C

Abbreviations and Units

C.1 Abreviations

AGN - Active Galactic Nuclei

ALMA - Atacama Large Millimeter/submillimeter Array

BL Lac - BL Lacertae

BLR - Broad Line Region

BH - Black Hole

BPT - Baldwin, Phillips and Terlevich

CCD- Charge Coupled Device

CDM - Cold Dark Matter

ELIRGs - Extremely Luminous Infra Red Galaxies

ESO - European Southern Observatory

EVLA - Expanded Very Large Array

EW - Equivalent Width

FIR - Far Infra-Red

FIRE - Folded Port Infra-red Echellette

FIRST - First Images of the Radio Sky at Twenty centimetres

FWHM - Full Width Half Maximum

IR - Infra Red

IRAF - Image Reduction and Analysis Facility

IGM - Inter-Galactic Medium

ISAAC - Infrared Spectrometer And Array Camera

ISM - Inter Stellar Medium

IRAC - Infra Red Array Camera

IRAS - Infra-red Astronomical Satellite

HotDOG - Hot Dust Obscured Galaxy

HST - Hubble Space Telescope

HyLIRGs - Hyper Luminous IR Galaxies

LAB - Lyα Blob

LAE - Lyα Emitter

LINER - Low-ionisation nuclear emission-line region

LRIS - Low Resolution Imaging Spectrometer

OVV - Optically Violently Variable quasars

MAGPHYS - Multi-wavelength Analysis of Galaxy Physical Properties

MIR - Mid Infra Red

MOSAIC - Multi-Object Spectrograph for Astrophysics, Intergalactic medium studies and Cosmology

NASA - National Aeronautics and Space Administration

NEOWISE - Near Earth Object Wide Field Infra-red Explorer

NIR - Near Infra Red

NRAO - National Radio Astronomy Observatory

NVSS - NRAO VLA Sky Survey

QSO - Quasi Stellar Object

RA - Right Ascension

RWGs - Radio WISE Galaxies

SCUBA - Submillimetre Common-User Bolometer Array

SDSS - Sloan Digital Sky Survey

SED - Spectral Energy Distribution

SFR - Star Formation Rate

SHARC - Submillimeter High Angular Resolution Camera

SIMBAD - Set of Identifications, Measurements and Bibliography for Astronomical Data

SMBH - Super Massive Black Hole

SMG - Sub Millimetre Galaxy

SNR - Signal to Noise Ratio

SPHERE - Spectro-Polarimetric High-contrast Exoplanet REsearch instrument

ULIRG - Ultra Luminous IR Galaxy

UT - Unit Telescope

UV - Ultra Violet

VISA - VLT Interferometer Small Array

VLA - Very Large Array

VLT - Very Large Telescope

VLTI - Very Large Telescope Interferometer

WCS - World Coordinate System

WIRC - Wide Field IR Camera

WISE - Wide field Infra-red Survey Explorer

WLAB - WISE Lyα Blob

WLAE - WISE Lyα Emitter

2MASS - 2 Micron All Sky Survey

4LGSF - 4 Laser Guide Star Facility

C.2 Units

Å - Angstrom

ADU - Analogue Digital Unit

as - Arc Second

g - Gram

Hz - Hertz

Jy - Jansky

$L_\odot$ - Solar Luminosity = 3.83×10^{26} W = 3.84×10^{33} erg s^{-1}

$M_\odot$ - Solar Mass = 1.99×10^{30} kg

m - Metre

pc - Parsec = 3.09×10^{16} m

s - Second

W - Watt

yr - Year

C.3 Prefixes

M - Mega = 1×10^6

k - Kilo = 1×10^3

c - Centi = 1×10^2

m - Milli $= 1 \times 10^{-3}$

μ - Micro $= 1 \times 10^{-6}$

n - Nano $= 1 \times 10^{-9}$

Appendix D

Emission and Absorption Line Rest Wavelengths

Table D.1 gives the rest wavelengths and corresponding frequencies of the emission and absorption lines detected in the spectra of my RWGs.

Table D.1: The wavelength and frequency of the emission and absorption lines found in this thesis.

Line	Rest Wavelength λ (Å)	Frequency f (Hz)
OVI	1034	2.90×10^{15}
Lyα	1216	2.47×10^{15}
CIV	1549	1.94×10^{15}
HeII	1640	1.83×10^{15}
OII	3727	8.05×10^{14}
Ca(K)	3933	7.63×10^{14}
Hδ	4103	7.31×10^{14}
Hγ	4340	6.91×10^{14}
Hβ	4861	6.17×10^{14}
[OIII]	4959, 5007	6.05×10^{14}, 5.99×10^{15}
Mg	5175	5.80×10^{14}
[OI]	6302, 6365	4.67×10^{14}, 4.71×10^{14}
Hα	6562	4.57×10^{14}
SII	6732	4.46×10^{14}
CaII	8500	3.53×10^{14}

Bibliography

Alonso S., Mesa V., Padilla N., Lambas D. G., 2012, Astronomy and Astrophysics, 539, A46

Antonucci R., 1993, Annual Review of Astronomy and Astrophysics, 31, 473

Assef R. J., et al., 2011, The Astrophysical Journal, 728, 56

Assef R. J., et al., 2015, The Astrophysical Journal, 804, 27

Assef R. J., et al., 2020, The Astrophysical Journal, 897, 112

Bañados E., et al., 2021, The Astrophysical Journal, 909, 80

Bae H.-J., Woo J.-H., 2016, The Astrophysical Journal, 828, 97

Bahcall J. N., Kirhakos S., Saxe D. H., Schneider D. P., 1997, The Astrophysical Journal, 479, 642

Bailey J., Axon D. J., Hough J. H., Ward M. J., McLean I., Heathcote S. R., 1988, Monthly Notices of the Royal Astronomical Society, 234, 899

Baldwin J. A., Phillips M. M., Terlevich R., 1981, Publications of the Astronomical Society of the Pacific, 93, 5

Barbary K., 2016, extinction v0.3.0, doi:10.5281/zenodo.804967, `https://doi.org/10.5281/zenodo.804967`

Barnes J. E., 1989, Nature, 338, 123

Barnes J. E., Hernquist L., 1992, Annual Review of Astronomy and Astrophysics, 30, 705

Barnes J. E., Hernquist L., 1996, The Astrophysical Journal, 471, 115

Baskin A., Laor A., 2005, Monthly Notices of the Royal Astronomy Society, 356, 1029

Becker R. H., White R. L., Helfand D. J., 1995, The Astrophysical Journal, 450, 559

Bennert V. N., Auger M. W., Treu T., Woo J.-H., Malkan M. A., 2011, The Astrophysical Journal, 726, 59

Bentz M. C., et al., 2009, The Astrophysical Journal, 705, 199

Bertin E., Arnouts S., 1996, Astronomy and Astrophysics Supplement, 117, 393

Blain A. W., Smail I., Ivison R., Kneib J.-P., Frayer D. T., 2002, Physics Reports, 369, 111

Blandford R. D., McKee C. F., 1982, The Astrophysical Journal, 255, 419

Blanton M. R., 2006, The Astrophysical Journal, 648, 268

Bohren C. F., Huffman D. R., 1983, Absorption and scattering of light by small particles

Bridge C. R., et al., 2013, The Astrophysical Journal, 769, 91

Brotherton M. S., Runnoe J. C., Shang Z., DiPompeo M. A., 2015, Monthly Notices of the Royal Astronomy Society, 451, 1290

Bussmann R. S., et al., 2012, The Astrophysical Journal, 744, 150

Calzetti D., Armus L., Bohlin R. C., Kinney A. L., Koornneef J., Storchi-Bergmann T., 2000, The Astrophysical Journal, 533, 682

Cano-Díaz M., Maiolino R., Marconi A., Netzer H., Shemmer O., Cresci G., 2012, Astronomy and Astrophysics, 537, L8

Cardelli J. A., Clayton G. C., Mathis J. S., 1989, The Astrophysical Journal, 345, 245

Carniani S., et al., 2015, Astronomy and Astrophysics, 580, A102

Casey C. M., Narayanan D., Cooray A., 2014, Physics Report, 541, 45

Chapman S. C., et al., 2010, Monthly Notices of the Royal Astronomy Society, 409, L13

Chiang Y.-K., Overzier R. A., Gebhardt K., Henriques B., 2017, The Astrophysical Journal, 844, L23

Chiu H.-Y., 1964, Physics Today, 17, 21

Coatman L., Hewett P. C., Banerji M., Richards G. T., 2016, Monthly Notices of the Royal Astronomy Society, 461, 647

Coatman L., Hewett P. C., Banerji M., Richards G. T., Hennawi J. F., Prochaska J. X., 2017, Monthly Notices of the Royal Astronomy Society, 465, 2120

Collin S., Kawaguchi T., Peterson B. M., Vestergaard M., 2006, Astronomy and Astrophysics, 456, 75

Condon J. J., Cotton W. D., Greisen E. W., Yin Q. F., Perley R. A., Taylor G. B., Broderick J. J., 1998, The Astrophysical Journal, 115, 1693

Cooray A., et al., 2010, Astronomy and Astrophysics, 518, L22

Crenshaw D. M., Schmitt H. R., Kraemer S. B., Mushotzky R. F., Dunn J. P., 2010, The Astrophysical Journal, 708, 419

Cutri R. M., et al., 2013, VizieR Online Data Catalog, 2328

Davy Kirkpatrick J., et al., 2011, The Astrophysical Journal Supplement Series, 197, 19

Di Matteo T., Springel V., Hernquist L., 2005, Nature, 433, 604

Díaz-Santos T., et al., 2016, Astrophysical Journal Letters, 816, L6

Díaz-Santos T., et al., 2018, Science, 362, 1034

Domínguez A., et al., 2013, The Astrophysical Journal, 763, 145

Donoso E., Yan L., Stern D., Assef R. J., 2014, The Astrophysical Journal, 789, 44

Dowell C. D., et al., 2003, in Phillips T. G., Zmuidzinas J., eds, Society of Photo-Optical Instrumentation Engineers (SPIE) Conference Series Vol. 4855, Millimeter and Submillimeter Detectors for Astronomy. pp 73–87, doi:10.1117/12.459360

Eggen O. J., Lynden-Bell D., Sandage A. R., 1962, The Astrophysical Journal, 136, 748

Eisenhardt P. R. M., et al., 2012, The Astrophysical Journal, 755, 173

European Southern Observatory 1998, The VLT White Book

Faber S. M., et al., 2007, The Astrophysical Journal, 665, 265

Fanaroff B. L., Riley J. M., 1974, Monthly Notices of the Royal Astronomy Society, 167, 31P

Fath E. A., 1909, Lick Observatory Bulletin, 149, 71

Ferrarese L., Merritt D., 2000, Astrophysical Journal Letters, 539, L9

Ferris E. R., et al., 2021, Monthly Notices of the Royal Astronomy Society, 502, 1527

Fitzpatrick E. L., 1999, Publications of the Astronomical Society of the Pacific, 111, 63

Fitzpatrick E. L., Massa D., 2007, The Astrophysical Journal, 663, 320

Forbes D. A., Proctor R., Strader J., Brodie J. P., 2007, The Astrophysical Journal, 659, 188

Gabor J. M., Davé R., Finlator K., Oppenheimer B. D., 2010, Monthly Notices of the Royal Astronomy Society, 407, 749

Gardner J. P., et al., 2006, Space Science Review, 123, 485

Gaskell C. M., 1982, The Astrophysical Journal, 263, 79

Geach J. E., et al., 2013, Monthly Notices of the Royal Astronomy Society, 432, 53

Gebhardt K., et al., 2000, Astrophysical Journal Letters, 539, L13

Glenn J., et al., 1998, in Phillips T. G., ed., Society of Photo-Optical Instrumentation Engineers (SPIE) Conference Series Vol. 3357, Advanced Technology MMW, Radio, and Terahertz Telescopes. pp 326–334, doi:10.1117/12.317418

Gordon K. D., Clayton G. C., 1998, The Astrophysical Journal, 500, 816

Greene J. E., Ho L. C., 2005, The Astrophysical Journal, 630, 122

Harrison C. M., et al., 2012, Monthly Notices of the Royal Astronomy Society, 426, 1073

Hatch N. A., et al., 2014, Monthly Notices of the Royal Astronomy Society, 445, 280

Heckman T. M., 1980, Astronomy and Astrophysics, 500, 187

Ho L. C., 1996, in Eracleous M., Koratkar A., Leitherer C., Ho L., eds, Astronomical Society of the Pacific Conference Series Vol. 103, The Physics of Liners in View of Recent Observations. p. 103 (`arXiv:astro-ph/9605190`)

Ho L. C., Filippenko A. V., Sargent W. L. W., 1997, The Astrophysical Journal, 487, 568

Holmberg E., 1941, The Astrophysical Journal, 94, 385

Hopkins P. F., Hernquist L., Cox T. J., Matteo T. D., Robertson B., Springel V., 2006, The Astrophysical Journal Supplement Series, 163, 1

Hubble E. P., 1926, The Astrophysical Journal, 64, 321

Hubble E., 1929, Proceedings of the National Academy of Sciences, 15, 168

Hubble E., 1936, The Astrophysical Journal, 84, 270

Humason M. L., 1932, Publications of the Astronomical Society of the Pacific, 44, 267

IceCube Collaboration 2018, Science, 361, 147

Jones S. F., et al., 2014, Monthly Notices of the Royal Astronomy Society, 443, 146

Jones S. F., et al., 2015, Monthly Notices of the Royal Astronomy Society, 448, 3325

Jones S. F., et al., 2017, Monthly Notices of the Royal Astronomy Society, 469, 4565

Jun H. D., Im M., Kim D., Stern D., 2017, The Astrophysical Journal, 838, 41

Jun H. D., et al., 2020, The Astrophysical Journal, 888, 110

Kaspi S., Smith P. S., Netzer H., Maoz D., Jannuzi B. T., Giveon U., 2000, The Astrophysical Journal, 533, 631

Kauffmann G., White S. D. M., Guiderdoni B., 1993, Monthly Notices of the Royal Astronomy Society, 264, 201

Kauffmann G., et al., 2003a, Monthly Notices of the Royal Astronomy Society, 341, 33

Kauffmann G., et al., 2003b, Monthly Notices of the Royal Astronomy Society, 341, 54

Kauffmann G., et al., 2003c, Monthly Notices of the Royal Astronomy Society, 346, 1055

Kereš D., Katz N., Fardal M., Davé R., Weinberg D. H., 2009, Monthly Notices of the Royal Astronomy Society, 395, 160

Kewley L. J., Dopita M. A., Sutherland R. S., Heisler C. A., Trevena J., 2001, The Astrophysical Journal, 556, 121

Kewley L. J., Groves B., Kauffmann G., Heckman T., 2006, Monthly Notices of the Royal Astronomy Society, 372, 961

Kim M., Ho L. C., Lonsdale C. J., Lacy M., Blain A. W., Kimball A. E., 2013, Astrophysical Journal Letters, 768, L9

King A., 2003, Astrophysical Journal Letters, 596, L27

Kitaki T., Mineshige S., Ohsuga K., Kawashima T., 2021, arXiv e-prints, p. arXiv:2101.11028

Kong M., Ho L. C., 2018, The Astrophysical Journal, 859, 116

Kormendy J., Ho L. C., 2013, Annual Review of Astronomy and Astrophysics, 51, 511

Kurk J., et al., 2008, The Astrophysical Journal, 669, 32

Labita M., Decarli R., Treves A., Falomo R., Kotilainen J. K., Scarpa R., 2010, Monthly Notices of the Royal Astronomy Society, 402, 2453

Lacey C., Cole S., 1993, Monthly Notices of the Royal Astronomy Society, 262, 627

Lambas D. G., Alonso S., Mesa V., O'Mill A. L., 2012, Astronomy and Astrophysics, 539, A45

Laor A., Stern J., 2012, Monthly Notices of the Royal Astronomy Society, 426, 2703

Lauer T., et al., 2021, The Astrophysical Journal, 906, 77

Leighly K. M., 2004, The Astrophysical Journal, 611, 125

Levan A., et al., 2015, The Astrophysical Journal, 819

Lin L., et al., 2008, The Astrophysical Journal, 681, 232

Lonsdale C. J., et al., 2015, The Astrophysical Journal, 813, 45

Lonsdale C., et al., 2016, Astronomische Nachrichten, 337, 194

Loveday J., 1996, Monthly Notices of the Royal Astronomy Society, 278, 1025

Lyke B. W., et al., 2020, The Astrophysical Journal Supplement, 250, 8

Lynden-Bell D., 1969, Nature, 223, 690

Magnelli B., et al., 2012, Astronomy and Astrophysics, 539, A155

Magorrian J., et al., 1998a, The Astrophysical Journal, 115, 2285

Magorrian J., et al., 1998b, The Astrophysical Journal, 115, 2285

Maiolino R., Rieke G. H., 1995, The Astrophysical Journal, 454, 95

Maiolino R., et al., 2012, Monthly Notices of the Royal Astronomy Society, 425, L66

Maire, A.-L. et al., 2016, A&A, 587, A56

Marov M. Y., 2015, The Structure of the Universe. Springer New York, New York, NY, pp 279–294, doi:10.1007/978-1-4614-8730-2_10, https://doi.org/10.1007/978-1-4614-8730-2_10

Matthews T. A., Sandage A. R., 1963, The Astrophysical Journal, 138, 30

Mayall N. U., 1934, Publications of the Astronomical Society of the Pacific, 46, 134

Mayall N. U., 1939, Lick Observatory Bulletin, 497, 33

Moorwood A., et al., 1998, The Messenger, 94, 7

Murray N., Chiang J., 1997, The Astrophysical Journal, 474, 91

Narayanan D., Hayward C. C., Cox T. J., Hernquist L., Jonsson P., Younger J. D., Groves B., 2010, Monthly Notices of the Royal Astronomical Society, 401, 1613

Nesvadba N. P. H., Lehnert M. D., De Breuck C., Gilbert A., van Breugel W., 2007, Astronomy and Astrophysics, 475, 145

Nesvadba N. P. H., Polletta M., Lehnert M. D., Bergeron J., De Breuck C., Lagache G., Omont A., 2011a, Monthly Notices of the Royal Astronomy Society, 415, 2359

Nesvadba N. P. H., Polletta M., Lehnert M. D., Bergeron J., De Breuck C., Lagache G., Omont A., 2011b, Monthly Notices of the Royal Astronomical Society, 415, 2359

Netzer H., 2013, The Physics and Evolution of Active Galactic Nuclei

Neugebauer G., et al., 1984, Astrophysical Journal Letters, 278, L1

O'Donnell J. E., 1994, The Astrophysical Journal, 422, 158

Orellana, G. Nagar, N. M. Isaak, K. G. Priddey, R. Maiolino, R. McMahon, R. Marconi, A. Oliva, E. 2011, A&A, 531, A128

Osterbrock D. E., 1989, Astrophysics of gaseous nebulae and active galactic nuclei

Peng Y., Maiolino R., Cochrane R., 2015, Nature, 521, 192

Penney J. I., et al., 2019a, Monthly Notices of the Royal Astronomy Society, 483, 514

Penney J. I., et al., 2019b, Monthly Notices of the Royal Astronomy Society, 483, 514

Picogna, Giovanni Kley, Wilhelm 2015, A&A, 584, A110

Polletta M. d. C., et al., 2006, The Astrophysical Journal, 642, 673

Polletta M., et al., 2007, The Astrophysical Journal, 663, 81

Raimundo S. I., Fabian A. C., 2009, Monthly Notices of the Royal Astronomical Society, 396, 1217

Rees M. J., 1978, Nature, 275, 516

Richards G. T., Berk D. E. V., Reichard T. A., Hall P. B., Schneider D. P., SubbaRao M., Thakar A. R., York D. G., 2002, The Astronomical Journal, 124, 1

Richards G. T., et al., 2006, The Astrophysical Journal Supplement, 166, 470

Roebuck E., Sajina A., Hayward C. C., Martis N., Marchesini D., Krefting N., Pope A., 2019, The Astrophysical Journal, 881, 18

Roukema B. F., Quinn P. J., Peterson B. A., 1993, in Chincarini G. L., Iovino A., Maccacaro T., Maccagni D., eds, Astronomical Society of the Pacific Conference Series Vol. 51, Observational Cosmology. p. 298

Roukema B. F., Quinn P. J., Peterson B. A., Rocca-Volmerange B., 1997, Monthly Notices of the Royal Astronomy Society, 292, 835

Salpeter E. E., 1964, The Astrophysical Journal, 140, 796

Schmidt M., 1963a, Nature, 197, 1040

Schmidt M., 1963b, Nature, 197, 1040

Searle L., Zinn R., 1978, The Astrophysical Journal, 225, 357

Seyfert C. K., 1943, The Astrophysical Journal, 97, 28

Shankar F., Weinberg D. H., Miralda-Escudé J., 2008, The Astrophysical Journal, 690, 20

Shen Y., et al., 2011, The Astrophysical Journal Supplement, 194, 45

Shields G. A., 1999, Publications of the Astronomical Society of the Pacific, 111, 661

Silva A., Sajina A., Lonsdale C., Lacy M., 2015, Astrophysical Journal Letters, 806, L25

Simcoe R., et al., 2013, Publications of the Astronomical Society of the Pacific, 125, 270

Singh V., Shastri P., Risaliti G., 2011, Astronomy and Astrophysics, 532, A84

Skrutskie M. F., et al., 2006, The Astrophysical Journal, 131, 1163

Slipher V. M., 1917, Lowell Observatory Bulletin, 3, 59

Smith D. J. B., Jarvis M. J., Simpson C., Martínez-Sansigre A., 2009, Monthly Notices of the Royal Astronomy Society, 393, 309

Sparks W. B., Fraix-Burnet D., Macchetto F., Owen F. N., 1992, Nature, 355, 804

Steinmetz M., Navarro J. F., 2002, New Astronomy, 7, 155

Stern D., et al., 2014, The Astrophysical Journal, 794, 102

Tacconi L. J., et al., 2008, The Astrophysical Journal, 680, 246

The Astropy Collaboration et al., 2018, preprint, (arXiv:1801.02634)

Tody D., 1986, in Crawford D. L., ed., Vol. 627, Instrumentation in astronomy VI. p. 733, doi:10.1117/12.968154

Toomre A., Toomre J., 1972, The Astrophysical Journal, 178, 623

Tsai C.-W., et al., 2015, The Astrophysical Journal, 805, 90

Tsai C.-W., et al., 2018, The Astrophysical Journal, 868, 15

Urry C. M., Padovani P., 1995, Publications of the Astronomical Society of the Pacific, 107, 803

Vernet J., et al., 2011, Astronomy and Astrophysics, 536, A105

Villarroel B., Korn A. J., 2014, Nature Physics, 10, 417

Vlahakis C., et al., 2015, The Astrophysical Journal, 808, L4

Wenger M., et al., 2000, Astronomy and Astrophysics Supplement, 143, 9

White S. D. M., Rees M. J., 1978, Monthly Notices of the Royal Astronomy Society, 183, 341

Willott C., Rawlings S., Blundell K., Lacy M., Eales S., 2000, Monthly Notices of the Royal Astronomical Society, 322

Wootten A., Thompson A. R., 2009, Proceedings of the IEEE, 97, 1463

Wright E. L., et al., 2010, The Astrophysical Journal, 140, 1868

Wu J., et al., 2012, The Astrophysical Journal, 756, 96

Wu J., et al., 2014, The Astrophysical Journal, 793, 8

Wu J., et al., 2018, The Astrophysical Journal, 852, 96

Wylezalek D., et al., 2013, The Astrophysical Journal, 769, 79

York D. G., et al., 2000, The Astrophysical Journal, 120, 1579

Zakamska N. L., Greene J. E., 2014, Monthly Notices of the Royal Astronomical Society, 442, 784

Zakamska N., et al., 2015, Monthly Notices of the Royal Astronomy Society, 458

Zou F., Yang G., Brandt W. N., Xue Y., 2019, The Astrophysical Journal, 878, 11

Zwicky F., 1959, Handbuch der Physik, 53, 373

da Cunha E., Charlot S., Elbaz D., 2008, Monthly Notices of the Royal Astronomy Society, 388, 1595